

**PHARMACOKINETIC ANALYSIS OF THE POSITRON EMISSION TOMOGRAPHY
RADIOTRACER [¹⁸F]ML-10 IN GLIOBLASTOMA MULTIFORME BRAIN TUMORS**

by

Matthew John Oborski

Bachelor of Science, Mathematics, University of Pittsburgh, 2008

Bachelor of Science, Physics, University of Pittsburgh, 2008

Master of Science, Physics, Carnegie Mellon University, 2010

Submitted to the Graduate Faculty of
the Swanson School of Engineering, Department of Bioengineering,
in partial fulfillment
of the requirements for the degree of
Doctor of Philosophy

University of Pittsburgh

2018

UNIVERSITY OF PITTSBURGH
SWANSON SCHOOL OF ENGINEERING

This dissertation was presented

by

Matthew John Oborski

It was defended on

June 29, 2018

and approved by

Robert L. Ferris, M.D. Ph.D., Professor,
Department of Otolaryngology and Immunology, University of Pittsburgh

Tamer S. Ibrahim, Ph.D., Associate Professor,
Department of Bioengineering, University of Pittsburgh

Patrick J. Loughlin, Ph.D., Professor,
Department of Bioengineering, University of Pittsburgh

James M. Mountz, M.D. Ph.D., Professor,
Department of Radiology, University of Pittsburgh

Julie C. Price, Ph.D., Professor,
Department of Radiology, Harvard Medical School

Dissertation Director: Charles M. Laymon, Ph.D., Research Assistant Professor,
Department of Radiology and Bioengineering, University of Pittsburgh

Copyright © by Matthew John Oborski

2018

**PHARMACOKINETIC ANALYSIS OF THE POSITRON EMISSION
TOMOGRAPHY RADIOTRACER [¹⁸F]ML-10 IN GLIOBLASTOMA MULTIFORME
BRAIN TUMORS**

Matthew John Oborski, Ph.D.

University of Pittsburgh, 2018

Conventional approaches to radiologic response assessment are inadequate for *early* therapy response assessment (ETRA) of glioblastoma multiforme (GBM), as they rely on slowly changing measures of therapeutic effect, e.g., changes in tumor size or in contrast enhancement on magnetic resonance imaging (MRI). Positron emission tomography (PET) imaging of GBM glucose metabolism using 2-[¹⁸F]fluoro-2-deoxy-D-glucose ([¹⁸F]FDG) has exhibited some success in diagnostic imaging of GBM; however, false-positive uptake caused by inflammation at the tumor site as well as high background uptake in uninvolved brain tissue limits its use for ETRA.

2-(5-[¹⁸F]fluoro-pentyl)-2-methylmalonic acid ([¹⁸F]ML-10) has recently been proposed as a PET radiotracer for imaging apoptosis. Molecular imaging of apoptosis is an attractive approach to ETRA of GBM, as it would provide a direct measure of therapeutic effect and a framework within which to interpret and compare efficacies of competing therapies. Previous studies have demonstrated the safety and bioavailability of [¹⁸F]ML-10 in healthy humans. However, the pharmacokinetic (PK) properties of [¹⁸F]ML-10 have not been evaluated.

This dissertation examines the PK properties of [^{18}F]ML-10 in a cohort of human subjects receiving treatment for GBM. [^{18}F]ML-10 time-course in GBM was studied on a whole tumor and voxelwise level. [^{18}F]ML-10 uptake was modeled as the response of a linear system using the radiotracer concentration in blood (measured from the PET image) as the input function (IF). In the whole tumor analysis, candidate models for the IF and GBM impulse response function (IRF) were fit simultaneously using a maximum likelihood approach. The relative merits of the joint IF/IRF models were compared using the Akaike information criterion and model parameter estimability considerations. Spectral analysis was performed to support model selection and provide alternative estimates of standard PK uptake measures. The selected IF/IRF models were further interpreted through tissue compartmental modeling. Standard PK measures of radiotracer uptake derived from models were evaluated for their utility in ETRA for a limited number of subjects. Finally, GBM heterogeneity in response to therapy was evaluated through a voxelwise analysis of [^{18}F]ML-10 uptake. Comparison was made between [^{18}F]ML-10 uptake at an ETRA time-point and later change in tumor cellularity measured using diffusion weighted MRI.

TABLE OF CONTENTS

LIST OF TABLES	X
LIST OF FIGURES	XII
LIST OF ABBREVIATIONS	XV
ACKNOWLEDGEMENTS	XVIII
1.0 INTRODUCTION.....	1
1.1 PURPOSE OF THIS DISSERTATION	3
2.0 PET PHYSICS	5
2.1 THE BASIC MATHEMATICS OF IMAGE RECONSTRUCTION FROM PROJECTION DATA	8
2.1.1 The Fourier Slice Theorem	11
2.1.2 Filtered Backprojection.....	13
2.1.3 Convolution Backprojection	14
2.2 METHODS OF PET IMAGE RECONSTRUCTION	15
2.3 SOME IMPORTANT CORRECTIONS APPLIED TO PET DATA.....	17
2.3.1 PET Photon Attenuation Correction	17
2.3.1.1 Approaches to MR-Based Attenuation Correction (MRAC)	18
2.3.2 Corrections for Scatter and Random Coincidences	23
2.3.3 Correcting for Scanner Dead Time	24
2.3.4 Scanner Normalization	25

2.4	TIME ACTIVITY CURVE MEASUREMENT FROM DYNAMIC PET ACQUISITIONS.....	25
2.4.1	Approximate Model for Measurement Noise of Time-Activity Curve Data in PET	29
2.4.2	Partial Volume Effect is a Practical Limiter of PET Resolution.....	31
3.0	APOPTOSIS IMAGING IN HUMAN CANCER RESPONSE ASSESSMENT: CURRENT STATE OF THE ART	34
3.1	THE PROCESS OF APOPTOSIS: AN OVERVIEW.....	35
3.1.1	The Intrinsic Pathway	36
3.1.2	The Extrinsic Pathway	37
3.1.3	Alternative Forms of Cell Death: Necrosis	38
3.2	CELL DEATH IMAGING USING RADIOLABELD ANNEXIN-V	38
3.2.1	Therapy Response Assessment using ^{99m} Tc-labeled Annexin-V.....	39
3.2.2	Measuring Chemo-/Radio-Sensitivity using ^{99m} Tc-labeled Annexin-V Imaging	45
3.3	2-(5-FLUORO-PENTYL)-2-METHYLMALONIC ACID (ML-10) AS A TRACER FOR EARLY STAGE APOPTOSIS	48
3.3.1	Therapy Response Assessment using [¹⁸ F]ML-10.....	50
4.0	STUDY SUBJECTS AND PET IMAGING PROTOCOL	54
4.1	STUDY SUBJECTS.....	54
4.2	STUDY IMAGING PROTOCOL	57
4.2.1	Attenuation Correction Methods Applied to Study PET Images.....	62
5.0	ANALYSIS OF [¹⁸ F]ML-10 TISSUE UPTAKE PROPERTIES IN GBM AND NORMAL BRAIN TISSUE	64
5.1	INPUT FUNCTION MODELING	65
5.1.1	Background: Image Based Input Functions.....	65
5.1.2	Background: Evaluation of Model Parameter Uncertainty.....	68

5.1.3 Methods.....	71
5.1.3.1 Subjects	71
5.1.3.2 PET Image Processing	72
5.1.3.3 Volume of Interest Definition and Image Based Input Function Measurement	72
5.1.3.4 Proposed Input Function Models and Selection Criteria.....	74
5.1.3.5 Input Function Model Fitting	78
5.1.3.6 Input Function Model Selection.....	86
5.1.4 Results	87
5.1.5 IBIF Model Selection Discussion	93
5.2 CHARACTERIZATION OF REGIONAL TUMOR TISSUE TIME-ACTIVITY CURVES	99
5.2.1 Background: Tracer Compartmental Modeling in PET	99
5.2.2 Background: Spectral Analysis of Tracer Uptake in PET.....	119
5.2.2.1 Limitations of Spectral Analysis.....	127
5.2.3 Methods.....	132
5.2.3.1 PET Image Processing	132
5.2.3.2 Whole Tumor Tissue Time Activity Curve Extraction	133
5.2.3.3 Healthy Tissue Time Activity Curve Extraction.....	133
5.2.3.4 Joint IBIF & Tumor IRF Model Order Selection.....	134
5.2.3.5 Estimating the Compartmental Rate Constants	146
5.2.3.6 Exploratory Spectral Analysis	150
5.2.3.7 Voxelwise Impulse Response Function Modeling	159
5.2.4 Results	163
5.2.4.1 Time Activity Curve Analysis	163

5.2.4.2	Model Selection via Simultaneous Estimation of IBIF and Tumor Tissue IRF Model Parameters	165
5.2.4.3	Spectral Analysis of Tumor Tissue TACs.....	190
5.2.4.4	Compartmental Modeling	209
5.2.4.5	Response Evaluation using Compartmental Modeling of [¹⁸ F]ML-10. 225	
5.2.4.6	Voxelwise Compartmental Modeling.....	230
5.2.5	Discussion and Conclusions: Tumor Tissue Modeling and Response Assessment	247
5.2.5.1	[¹⁸ F]ML-10 Uptake Profile in Healthy Brain Tissue.....	248
5.2.5.2	Tumor TAC Discussion	249
5.2.5.3	PK Modeling of the Tumor Tissue Impulse Response Function ..	251
5.2.6	Evaluation of Local Heterogeneity in Apoptosis Rate via Voxelwise PK Modeling	262
5.2.6.1	Study Limitations.....	264
5.2.7	[¹⁸ F]ML-10 Pharmacokinetic Modeling Conclusions.....	267
6.0	FUTURE DIRECTIONS.....	269
6.1	OPTIMAL IMAGE TIMING	269
6.2	STRATEGIES FOR NORMALIZATION OF MEASURES OF OVERALL APOPTOSIS.....	271
6.3	FUTURE DIRECTIONS SPECIFIC TO [¹⁸ F]ML-10 AND GBM.....	272
APPENDIX A		275
BIBLIOGRAPHY		318

LIST OF TABLES

Table 4-1. Study Enrollment Table.....	55
Table 4-2. Subject Treatment and Outcome.	57
Table 4-3. Subject Imaging Schedule.	59
Table 4-4. PET Scanner Used for Data Acquisition.	61
Table 4-5. Attenuation Correction Method used for PET Data.	63
Table 5-1. Candidate Input Function Model Forms.....	74
Table 5-2. List of Candidate Input Function Models Tested.	77
Table 5-3. ML-10 #5 Baseline Scan Input Function Model Selection Results.	90
Table 5-4. ML-10 #6 Early Therapy Assessment Scan Input Function Model Selection Results.	91
Table 5-5. Selected IBIF Model for each [¹⁸ F]ML-10 PET Acquisition.....	93
Table 5-6. Candidate Impulse Response Models.....	135
Table 5-7. List of Candidate IBIF Models.....	136
Table 5-8. Joint IBIF-Tumor IRF Model Selection Results for ML-10 #6 at Early Therapy Response Assessment.	170
Table 5-9. Joint IBIF tumor IRF Model Selection Results for ML-10 #13 at Baseline.	175
Table 5-10. Joint IBIF-Tissue Model Selected using AICc Alone.....	177
Table 5-11. Joint IBIF tumor IRF Model Selection Results for ML-10 #14 at Early Therapy Assessment.....	181

Table 5-12. Joint IBIF-Tissue Model Selected using AICc and Parameter Estimability Considerations.....	183
Table 5-13. Estimated Macroparameter Values for Each Subject and Time-point using the Corresponding Selected IBIF and IRF Models in Table 5-12.	189
Table 5-14. Summary of Macroparameter Estimates for NNLS and L_1 Norm Spectral Analysis Methods.....	202
Table 5-15. Number of Detected Spectral Components using NNLS SA Method.	204
Table 5-16. Number of Detected Spectral Components using L_1 Norm SA Method.	204
Table 5-17. Macroparameter Estimates Obtained from Spectral Analysis using NNLS Method.	207
Table 5-18. Macroparameter Estimates Obtained from Spectral Analysis using L_1 Norm Method.	208
Table 5-19. 2-Tissue Reversible Tracer Kinetics: Blood Volume Fraction V_B	221
Table 5-20. 2-Tissue Reversible Tracer Kinetics: Compartmental Rate Constants.	222
Table 5-21. 2-Tissue Reversible Tracer Kinetics: Total Volume of Distribution V_T	223
Table 5-22. 2-Tissue Irreversible Kinetics: Compartmental Rate Constants.	224
Table 5-23. 2-Tissue Irreversible Kinetics: Influx Rate K_i	225
Table 5-24. Percent Change in V_T Compared to Subject Clinical End-points.	228
Table 5-25. Percent Change in K_i Compared to Subject Clinical End-points.	229
Table 5-26. Percent Change in K_i^* Compared to Subject Clinical End-points.....	229

LIST OF FIGURES

Figure 2-1. Two-Dimensional Cross-Section of PET Scanner with Coordinates System.....	10
Figure 4-1. [¹⁸ F]ML-10 PET Acquisition Protocol After Initial Injection of [¹⁸ F]ML-10.	58
Figure 5-1. Example [¹⁸ F]ML-10 PET Image Section Showing IBIF VOI Defined on the Internal Carotid Arteries of the Brain.....	73
Figure 5-2. Example IBIF model curves with N=2 decaying exponentials.....	76
Figure 5-3. IBIF Model 1 Optimization Workflow.	82
Figure 5-4. IBIF Model 2 Optimization Workflow.	85
Figure 5-5. Example Comparison of IBIF Model Selection Fit Results for ML-10 #5 at BL.....	89
Figure 5-6. Comparison of IBIF Model Fits for ML-10 #6 at ETA: IBIF Model 1b versus IBIF Model 2a.	91
Figure 5-7. 2-Tissue Compartmental Model Structure Appropriate for PET.....	102
Figure 5-8. 3-Tissue Compartmental Model with Reversible Pharmacokinetics.	108
Figure 5-9. 1-Tissue Compartmental Model.....	112
Figure 5-10. Procedure for Generating Initial Tissue Model Parameter Guesses for Maximization of the Joint IBIF and Tissue Model Log-Likelihood Function.....	142
Figure 5-11. Coordinate Descent Procedure for Maximizing Joint IBIF and Tissue Model Log-Likelihood Function.....	143
Figure 5-12. Representative IBIF, Tumor, and Healthy Tissue PET Time-Activity Curves.	164
Figure 5-13. Representative IBIF Model Fits for ML-10 #6 at ETA Assuming a 3α - 2β Tumor IRF Model.	167

Figure 5-14. Representative Candidate IRF Model Fits for ML-10 #6 at ETA Assuming IBIF Model 1b as the Selected Input Model.	168
Figure 5-15. Representative IBIF Model Fits for ML-10 #13 at BL Assuming a $2\alpha-1\beta$ Tumor IRF Model.	172
Figure 5-16. Representative Candidate IRF Model Fits for ML-10 #13 at BL Assuming IBIF Model 1b as the Selected Input Model.	173
Figure 5-17. Comparison of IRF Model Parameter Fits for ML-10 #14 at ETA Assuming Joint Estimation using IBIF Model 1c.	179
Figure 5-18. Comparison of the IBIF Model 1c Fits Obtained through Simultaneous Estimation with the $3\alpha-3\beta$, $3\alpha-2\beta$, and $2\alpha-2\beta$ tumor IRF Models for ML-10 #14 at ETA.	180
Figure 5-19. IRF model fits for ML-10 #11 at ETA Assuming Joint Maximum Likelihood Estimation with IBIF Model 2b.	185
Figure 5-20. Comparison of fits for IBIF Model 2b to Measured Blood TAC Data for ML-10 #11 at ETA Assuming Joint Estimation with Different IRF Models.	187
Figure 5-21. Tumor TAC Spectra for ML-10 # 6 at ETA using IBIF Model 1b.	192
Figure 5-22. Tumor TAC Spectra for ML-10 # 12 at BL using IBIF Model 2b.	194
Figure 5-23. Tumor TAC Spectra for ML-10 # 14 at FUA using IBIF Model 1c.	196
Figure 5-24. Tumor TAC Spectra for ML-10 # 11 at ETA using IBIF Model 2b.	199
Figure 5-25. Tumor TAC Spectra for ML-10 # 14 at ETA using IBIF Model 1c.	200
Figure 5-26. Tumor TAC Spectra for ML-10 # 5 at BL using IBIF Model 1b.	205
Figure 5-27. Example 2-Tissue Compartment Model Fit Obtained from Joint Maximum Likelihood Estimation with IBIF Model 1b for ML-10 #5 at BL.	210
Figure 5-28. Comparison of 2T-4K and 2T-3K Compartmental Model Fit Results from Joint Maximum Likelihood Estimation with IBIF Model 2b for ML-10 #12 at BL.	212
Figure 5-29. Comparison of 3T-5K, 2T-4K and 2T-3K Compartmental Model Fit Results from Joint Maximum Likelihood Estimation with IBIF Model 1b for ML-10 #2 at ETA.	214
Figure 5-30. Comparison of 3T-5K, 2T-4K and 2T-3K Compartmental Model Fit Results from Joint Maximum Likelihood Estimation with IBIF Model 1b for ML-10 #6 at ETA.	216
Figure 5-31. Comparison of 3T-5K, 2T-4K and 2T-3K Compartmental Model Fit Results from Joint Maximum Likelihood Estimation with IBIF Model 1b for ML-10 #6 at FUA.	218

Figure 5-32. Example Voxelwise Fits for Subject ML-10 #6 at ETA using the 2α - 2β and 2α - 1β IRF models.....	231
Figure 5-33. Example Voxelwise Analysis for ML-10 #6.	233
Figure 5-34. Histograms of Voxelwise V_T and K_i for ML-10 #6 Across Imaging Time-points.	234
Figure 5-35. Example Voxelwise Analysis for ML-10 #5.	236
Figure 5-36. Histograms of Voxelwise V_T and K_i for ML-10 #5 Across Imaging Time-Points.	237
Figure 5-37. Example Voxelwise Maps of V_T at ETA Compared to ADC Change on Diffusion MRI for ML-10 #10 and ML-10 #14.....	241
Figure 5-38. Example Voxelwise Maps of K_i at ETA Compared to ADC Change on Diffusion MRI for ML-10 #10 and ML-10 #14.	243
Figure 5-39. Histograms of Voxelwise V_T Over Time for ML-10 #10 and ML-10 #14.....	245
Figure 5-40. Histograms of Voxelwise K_i Over Time for ML-10 #10 and ML-10 #14.....	246

LIST OF ABBREVIATIONS

Abbreviations:

PET	positron emission tomography
[¹⁸F]ML-10	2-(5-[¹⁸ F]fluoro-pentyl)-2-methylmalonic acid
[¹⁸F]FDG	2-[¹⁸ F]fluoro-2-deoxy-D-glucose
[¹⁸F]FLT	3'-deoxy-3'-[¹⁸ F]fluorothymidine
min	minutes
sec	seconds
SUV	standard uptake value
TAC	time-activity curve
IBIF	image-based input function
GBM	glioblastoma multiforme
RT	radiation therapy
TMZ	temozolomide chemotherapy
PFS	progression-free survival
OS	overall survival
RECIST	response evaluation criteria in solid tumors
RANO	response assessment in neuro-oncology criteria

BL	baseline
ETA	early therapy assessment
FUA	follow-up assessment
BBB	blood-brain barrier
MR	magnetic resonance
MRI	magnetic resonance imaging
UTE	ultrashort echo time
CE	contrast enhanced
MPRAGE	magnetization-prepared rapid gradient-echo
MRSI	magnetic resonance spectroscopic imaging
ADC	apparent diffusion coefficient
SPECT	single photon emission computed tomography
CT	computed tomography
WHO	World Health Organization
PK	pharmacokinetic/pharmacokinetics
IRF	impulse response function
AIC	Akaike information criterion
AIC_c	Akaike information criterion adjusted for small samples
MLE	maximum likelihood estimate
COV	coefficient of variation
VOI	volume of interest
ROI	region of interest
FWHM	full width at half maximum

AC	attenuation correction
SAC	source-based attenuation correction
CTAC	CT-based attenuation correction
MRAC	MRI-based attenuation correction
PVE	partial volume effect
PVC	partial volume correction
PSF	point spread function
PSFR	point spread function recovery
FOV	field of view
TBkgR	tumor-to-background ratio
TBR	tumor-to-blood ratio
CRLB	Cramer-Rao lower bound

ACKNOWLEDGEMENTS

First, I would like to thank my dissertation advisor, Dr. Charles M. Laymon, for his time, patience, and guidance throughout the course of my Ph.D. training as well as during my 2 years as a data analyst at the PET center. I would also like to thank him for his willingness to be my Ph.D. advisor, as it was through his initial encouragement that I started down the path of a Ph.D. in Bioengineering. I would also like to thank Dr. James M. Mountz for initially hiring me as a PET research data analyst when I had no previous experience, as well as for providing me with opportunities to both present research findings at conferences and write scientific publications before I started graduate school. I also want to thank Dr. Julie C. Price for her support, guidance, and willingness to make time for me even when she didn't have the time to give. I would also like to thank the remaining dissertation committee members: Dr. Robert L. Ferris, Dr. Tamer S. Ibrahim, and Dr. Patrick J. Loughlin for their time, effort, and helpful suggestions.

I would also like to express my sincere gratitude and thanks to the many faculty mentors at the University of Pittsburgh for their help and guidance during my undergraduate and graduate careers. I would especially like to thank Dr. Murat Akcakaya for many helpful discussions on detection and estimation methodology as well as for his unwavering belief in my ability to succeed. I would like to thank Dr. Vladimir Savinov for his support and guidance in the classroom and in

the lab. I would also like to thank Dr. Alison Slinsky Legg for her help, encouragement, and guidance when I needed it most as an undecided freshman.

I would also like to express my thanks to the IEEE NPSS Awards Committee for selecting me as the first Ronald J. Jaszczak Graduate Award recipient. This award allowed me to attend several conferences including 2 IEEE NSS/MIC conferences where I was able to present research results and network with leading researchers in medical imaging from both academia and industry.

Additionally, I would like to express my appreciation to the faculty and staff of the University of Pittsburgh Medical Center PET-Cyclotron facility for their patience and support. I would also like to extend my thanks to our collaborators at Aposense Ltd. and Siemens Medical Solutions USA, Inc. I would especially like to thank Dr. Judson Jones and Dr. Paul Schleyer of Siemens Medical Solutions USA, Inc. for their time and patience, which lead to many helpful conversations regarding the use of the e7tools for reconstruction of PET images acquired using the Siemens Biograph mMR scanner. Additionally, I would like to thank the study subjects and their families for their time and effort in participating in our [^{18}F]ML-10 PET imaging trial.

Finally, I would like to thank family and friends for their love and support. I would especially like to thank my mother, Kathleen Oborski, who instilled in me the importance and power of education at an early age. I would also like to thank my Aunt Rita and Uncle Gerald for their love and patience in guiding me from adolescence to adulthood after the death of my mother. It's difficult to imagine where I would be without them. Lastly, I would like to thank my wife,

Laura, for the love, support, and patience she has given me since we met in the Summer of 2005.

It is through her support that I find my courage.

1.0 INTRODUCTION

Glioblastoma multiforme (GBM) is a World Health Organization (WHO) grade IV astrocytoma and is the most common and most aggressive form of primary brain tumor [1]. In the United States alone, GBM account for 60-70% of primary brain tumors diagnosed each year [1-3]. The current standard of care for newly diagnosed GBM patients typically includes tumor debulking surgery followed by radiotherapy (RT) plus concomitant temozolomide (TMZ) chemotherapy [4]. Despite treatment, overall prognosis for patients suffering from GBM remains poor with tumor recurrence occurring in approximately 90% of patients [4]. Median overall survival for GBM patients enrolled in clinical trials is approximately 15-18 months, with a 5-year overall survival of less than 5% [4-6].

Image based biomarkers that quantify GBM response to therapy early after therapy institution may increase overall survival by quickly identifying patients that are not responding to a particular therapy, thereby providing radiologists and oncologists with a rationale for therapy modulation. Furthermore, methods for evaluation of therapeutic efficacy *early* after therapy institution are essential for reducing systemic toxicity, treatment delays, and drug trial expense.

Current methods for evaluating GBM response to therapy rely largely on assessing changes in tumor morphology on contrast enhanced (CE) magnetic resonance imaging (MRI) and then classifying tumor size reduction according to standard criteria such as the Response Evaluation Criteria in Solid Tumors (RECIST) [7] and the Response Assessment in Neuro-Oncology (RANO) [8]. However, such methodology for response assessment is limited, as changes in tumor size can be slow relative to the time scale of the underlying molecular physiology. Moreover, the degree of contrast enhancement by a GBM can be influenced by several non-tumor processes, including ischemia, radiation necrosis, and blood-brain-barrier breakdown, all of which can contribute to a transient increase in contrast enhancement on MRI mimicking true progression [9, 10]. In general, patients exhibiting this apparent radiologic progression, or “pseudoprogression”, on CE-MRI report no worsening of neurologic symptoms [11]. At present, there are no imaging methods that can reliably discern pseudoprogression from true progression. As a result, some radiologists have suggested that contrast enhancement observed on MRI in previously radiation treated regions should not be diagnosed as progression if the enhancement is observed less than 3 months after completion of radiotherapy [12, 13]. This represents a significant shortcoming in the management of GBM.

Positron emission tomography (PET) imaging of GBM glucose metabolism using 2-¹⁸F-fluoro-2-deoxy-D-glucose (¹⁸F)FDG) has exhibited some success in diagnostic imaging of GBM; however, false-positive uptake caused by inflammation at the tumor site as well as overall high background uptake in uninvolved brain tissue limits the use of ¹⁸F)FDG PET for GBM early therapy response assessment [14].

1.1 PURPOSE OF THIS DISSERTATION

2-(5-[^{18}F]fluoro-pentyl)-2-methylmalonic acid ([^{18}F]ML-10) has recently been proposed as a PET radiotracer for imaging apoptosis. Molecular imaging of apoptosis is an attractive approach to early therapy response assessment of GBM, as it would: a) provide a direct measure of therapeutic effect (thereby potentially providing the earliest possible indication of therapy response) and b) provide a framework within which to interpret and compare efficacies of competing therapies. Previous studies have demonstrated the safety and bioavailability of [^{18}F]ML-10 in healthy humans. However, the pharmacokinetic (PK) properties of [^{18}F]ML-10 have not been reported for healthy or diseased tissue anywhere in the body.

This dissertation examines the PK and brain distribution properties of the novel PET apoptosis tracer [^{18}F]ML-10 in a cohort of human GBM subjects receiving treatment for GBM. A detailed understanding of these properties is essential to the development of patient imaging protocols and accurate quantitative methodology. Moreover, evidence of favorable [^{18}F]ML-10 PK in GBM at either the whole tumor or voxelwise level will be used as support for future studies that address more specific questions regarding radiotracer uptake.

As stated above, the PK of [^{18}F]ML-10 have not been previously investigated. Therefore, a major focus of this study is on development of quantitative methodology. To this end, [^{18}F]ML-10 time-course in GBM was studied on a whole tumor and voxelwise level. In both cases, [^{18}F]ML-10 uptake was modeled as the response of a linear time-invariant system using the radiotracer concentration in blood as the input function. No arterial blood sampling was performed. Therefore,

for each [^{18}F]ML-10 PET scan the radiotracer concentration in the blood was measured directly from the image, yielding an image-based input function (IBIF).

In the whole tumor analysis, candidate models for the IBIF and GBM impulse response function (IRF) were fit simultaneously using a maximum likelihood approach. The relative merits of the joint IBIF/IRF models were compared using the Akaike information criterion and model parameter estimability considerations. Spectral analysis was performed to support model selection and provide alternative estimates of standard PK uptake measures. The selected IBIF/IRF models were further interpreted through tissue compartmental modeling. PK measures of radiotracer uptake derived from fitted joint IBIF/IRF models were evaluated for their utility in early therapy response assessment for a limited number of subjects using progression-free survival (PFS) and overall survival (OS) as clinical endpoints. Finally, the potential to quantify heterogeneity in GBM treatment response is explored through voxelwise modeling of [^{18}F]ML-10 uptake measures.

2.0 PET PHYSICS

As described in the following paragraphs, positron emission tomography (PET) is a method for producing an image of the distribution of positron emitting radioactivity in an object. The technique requires a scanner to detect the radiation and the implementation of processing algorithms to produce the image. Important to this work, PET allows the production of a time-sequence of images from which the changing distribution of radioactivity can be determined.

A positron is the antimatter conjugate of an electron. When an electron and a positron meet they interact and annihilate to produce 2 coincident photons, each with energy 511 keV, that are emitted at 180 degrees apart in the center-of-mass system [15]. Positron emission tomography imaging platforms are outfitted with detectors optimized for detecting 511 keV photons [15]. Generally, these detectors consist of scintillator elements (typical size 4 mm x 4 mm face, 20 mm depth) arranged in a grid pattern or “block” (64 or more elements per block, typical) with blocks (72 or more) arranged in a ring [16-18]. Several rings of block detectors (e.g. 4 or more) are arranged one after another creating a cylindrical field of view (FOV). The subject being imaged is placed in the cylinder so that the rings of detectors surround the subject [15]. Typical axial FOVs are: 15.5 cm for Siemens HR+ [16] and 25.8 cm for Siemens mMR [17, 18]. The cylindrical arrangement of detectors in PET scanners allows for the detection of both emitted photons in

coincidence in separate detectors [15]. The line defined by the two detectors is known as a line of response (LOR) and the various combinations of pairs detectors form a set of LORs [15]. Collection of annihilation count rates along the various LORs produces sufficient information to reconstruct an image of the distribution of radioactivity in the [15].

511 keV positrons have sufficiently high energy to penetrate bone, including the skull. This property allows for real-time, *in vivo* measurement of biologic processes using PET through use of radio-labeled probes that follow (or “trace”) the process of interest. In a typical PET experiment, a small amount of tracer labeled with a positron emitting nuclide is injected into the subject and the time-course of tracer radioactivity concentration (also called a time-activity curve) in the target region is measured and quantified. Essentially any biologic process, for which a suitable probe can be isolated/synthesized and labeled with a positron emitting isotope, can be quantified using PET. Some examples include: glucose metabolism using [^{18}F]FDG [19, 20], dopamine receptor density in brain tissue using [^{11}C]raclopride [21], and protein formation using methyl- ^{11}C -L-methionine [22].

Lassen and Perl [23] define a tracer as a molecular indicator that exactly follows (i.e. traces) the path of the systemic substance (i.e. the tracee) of interest (e.g. albumin). As far as the body system is concerned, the tracer is indistinguishable from the tracee [23]. In practice this definition of tracer is often relaxed to include both radio-labeled molecules that only proceed through a portion of the metabolic pathway of the tracee, as well as radio-labeled indicator molecules that bind to systemic receptors. For example, [^{18}F]FDG is by far the most commonly used PET radio-labeled compound for cancer staging and follow-up, acting as a tracer for glucose metabolism in

the tumor. However once in the cell [^{18}F]FDG gets phosphorylated by hexokinase to form [^{18}F]FDG-6-phosphate, which is unable to continue through the Krebs cycle, in contrast to the tracee (i.e. glucose); effectively trapping the now ^{18}F -labeled metabolite in the cell [19, 20]. Hence, by strict definition [^{18}F]FDG is not a tracer, though it is commonly used as such.

The Becquerel (Bq) is the unit of radioactivity in the International System of Units [24]. 1 Bq is equal to 1 disintegration per second [24]. The Curie is also a commonly used unit of radioactivity in PET imaging ($1\text{mCi} = 37\text{MBq}$). In research applications typical injected doses of radioactivity are between 5-15mCi, with the administered mass of tracer being on the order of 20 μg or less. Generally, a standard with known radioactivity concentration is used to convert the count-rate of detected annihilation events by the PET scanner to concentration of radioactivity. As such, the final reconstructed PET image will typically have units of kilobecquerel per milliliter (kBq/ml).

Commonly used positron emitting radionuclides in PET imaging are ^{18}F , ^{11}C , ^{13}N , and ^{15}O though there are others [24]. Depending on the energy of the emitted positron, which depends on radionuclide, the emitted positron may travel a few millimeters from the emission site before interacting with an electron and annihilating (an effect known as positron range) [25]. Positron range is one effect that fundamentally limits the resolution of PET imaging. Additional fundamental limiters of PET resolution are non-collinearity of the emitted 511 keV photons, and scanner geometry/hardware.

In PET image reconstruction algorithms, the coincident photons are commonly approximated as having been emitted 180 degrees apart (i.e. along a line) producing the LOR for that annihilation event. However, this is only true if the annihilation event occurs with both the positron and electron at rest. In general, the center of mass of the electron-positron pair will have some non-zero momentum at the time of the annihilation event. Hence the 2 emitted 511 keV photons are generally not emitted at a perfect 180 degrees apart (i.e. they are not co-linear) as is approximated. This produces additional uncertainty in the location of the annihilation event, and has been estimated to reduce image resolution by an additional 1.5 mm [26, 27]. Moreover, the impact of noncollinearity on image resolution is greater as the radius of the detector rings gets larger [26, 27].

Finally, the design and arrangement of the detectors, the scintillation material used for stopping the emitted photons, and the scanner electronics used to process detected events all affect the fundamental resolution of the PET scanner.

2.1 THE BASIC MATHEMATICS OF IMAGE RECONSTRUCTION FROM PROJECTION DATA

Fundamentally, PET scanners measure the count rate of coincident 511keV photons along the LOR between each pair of detectors. The basic mathematics required for reconstruction of a PET image is most easily explained in 2-dimensions (2D); hence that will be the approach used in this dissertation. However, in practice PET projection data are generally acquired in 3-dimensions

(3D) and require some pre-processing before the reconstruction algorithms can begin. Further details on the processing required to prepare measured PET projection data for reconstruction as well as the mathematics required for image reconstruction of 3D projection data can be found in the following references [26, 28, 29].

Figure 2-1 shows a simplified cartoon of a PET scanner in 2D with Cartesian x-y coordinate system. The rectangles arranged along the perimeter of a circle represent individual PET detectors. The large blue-oval in the center of the PET scanner represents an object with a uniform amount of radioactivity, while the smaller gray and orange ovals represent objects that attenuate the transit of emitted photons; though they are assumed to contain no radioactivity themselves. The black-dotted lines represent two LORs through the object that cross the line ℓ at right-angles. Mathematically, these two LORs represent individual line integrals of radioactivity that intersect the line ℓ at points ρ_1 and ρ_2 . The angle θ_0 that the lateral line ℓ makes with the x-y axis is called the projection angle. The set of all possible line integrals that cross the lateral line ℓ at right-angles is called the projection of the object at angle θ_0 , and denoted $\phi(\ell, \theta_0)$. In the continuous case, $\phi(\ell, \theta_0)$ has the form of a continuous distribution of line-integral values as shown in figure 2-1.

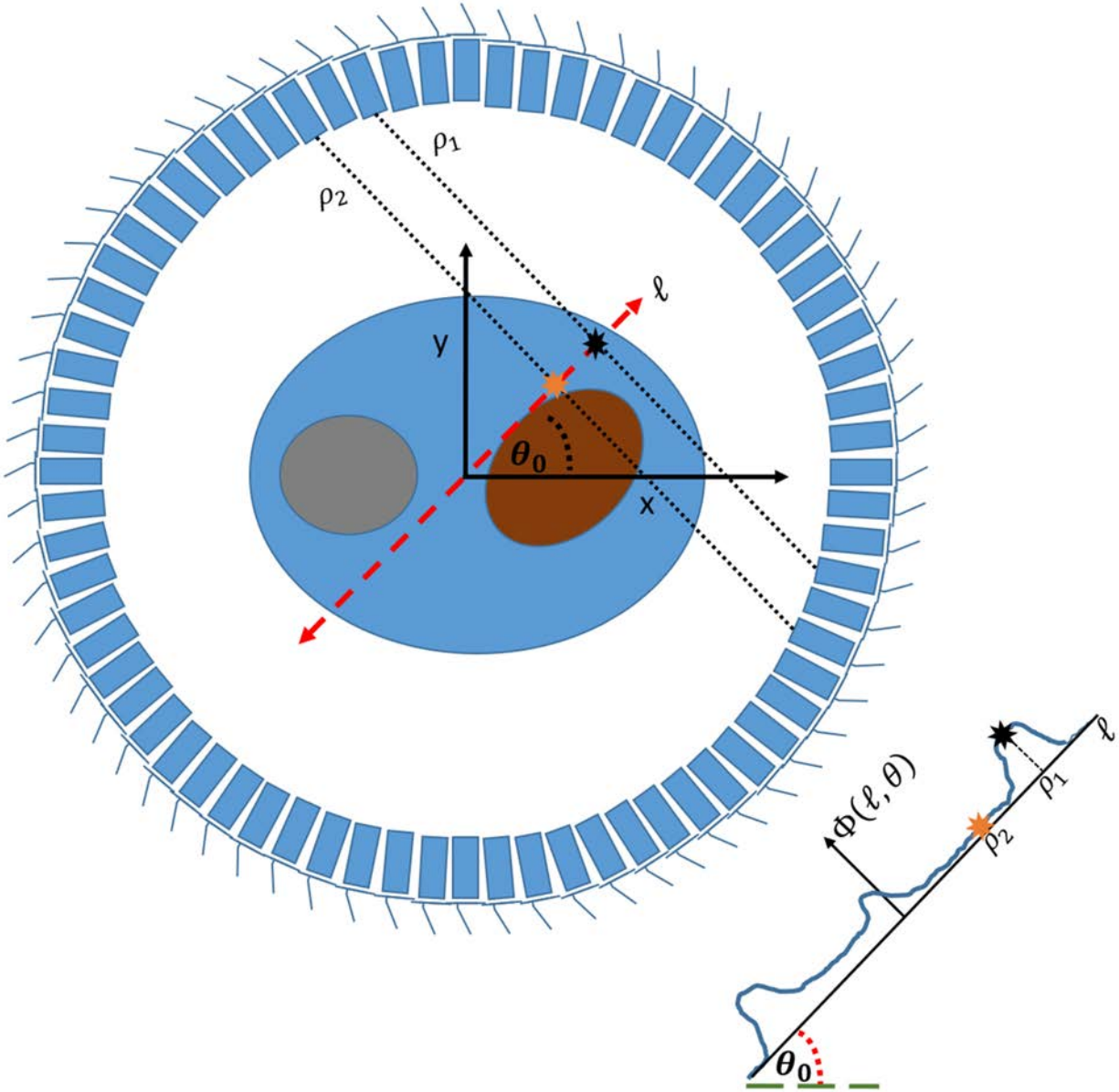


Figure 2-1. Two-Dimensional Cross-Section of PET Scanner with Coordinates System.

The collection of individual projections $\phi(\ell, \theta)$ over the angular range $\theta \in [0, \pi]$ comprise the measured data in PET. Given the measured projection data, two common analytic methods of reconstructing the generating radioactivity distribution are: filtered back projection (Section 2.1.2) and convolution back projection (Section 2.1.3). However, both of these reconstruction methods make use of the Fourier slice theorem, which is describe in the next section.

2.1.1 The Fourier Slice Theorem

The Fourier slice theorem is the fundamental relationship on which all projection-based image reconstruction methods are reliant [29-31]. It relates the Fourier transform of each 1D projection to the 2D Fourier transform of the activity distribution. Specifically, (Eqn. 2.1.1) gives the general equation for all possible 2D projections through the image data $f(x, y)$. Using figure 2-1 above as a guide, ℓ represents the position along a lateral line with angle θ in the x-y coordinate system, \bar{x} denotes the vector of x and y coordinates (i.e. $\bar{x} = [x, y]^T$), and \hat{n} denotes the unit vector $[\cos(\theta), \sin(\theta)]^T$ that mathematically describes the angle θ that the line ℓ makes with the x-y axis.

$$\left\{ \begin{array}{l} \Phi(\ell, \theta) = \int_{-\infty}^{\infty} \int_{-\infty}^{\infty} f(x, y) \delta(\bar{x}^T \cdot \hat{n} - \ell) dx dy \\ \text{where, } \hat{n} = [\cos(\theta), \sin(\theta)]^T \end{array} \right. \quad (\text{Eqn. 2.1.1})$$

The 1D Fourier transform of (Eqn. 2.1.1) with respect to ℓ is given in (Eqn. 2.1.2).

$$\Phi(\rho, \theta) = \mathcal{F}_{1D}\{\Phi(\ell, \theta)\} = \int_{-\infty}^{\infty} \Phi(\ell, \theta) e^{-2\pi j \rho \ell} d\ell \quad (\text{Eqn. 2.1.2})$$

Substitution of (Eqn. 2.1.2) into (Eqn. 2.1.1) gives (Eqn. 2.1.3), which yields (Eqn. 2.1.4) by the sifting property of the Dirac delta-function.

2.1.2 Filtered Backprojection

(Eqn. 2.1.7) gives the general equation for the 2D inverse Fourier transform of the activity distribution $f(x, y)$, which can be transformed using polar coordinates to give (Eqn. 2.1.8).

$$f(x, y) = \int_{-\infty}^{\infty} \int_{-\infty}^{\infty} F(u, v) e^{2\pi j(xu+yv)} du dv \quad (\text{Eqn. 2.1.7})$$

$$f(x, y) = \int_0^{2\pi} \int_0^{\infty} \rho F(\rho \cos(\theta), \rho \sin(\theta)) e^{2\pi j\rho(x\cos(\theta)+y\sin(\theta))} d\rho d\theta \quad (\text{Eqn. 2.1.8})$$

As a result of the cylindrical symmetry of the PET scanner, (Eqn. 2.1.8) can be re-cast as (Eqn. 2.1.9) below.

$$f(x, y) = \int_0^{\pi} \int_{-\infty}^{\infty} |\rho| F(\rho \cos(\theta), \rho \sin(\theta)) e^{2\pi j\rho(x\cos(\theta)+y\sin(\theta))} d\rho d\theta \quad (\text{Eqn. 2.1.9})$$

From the Fourier slice theorem in (Eqn. 2.1.6), $F(\rho \cos(\theta), \rho \sin(\theta))$ can be replaced by the 1D Fourier transform of the projection data $\Phi(\rho, \theta)$ yielding (Eqn. 2.1.10).

$$f(x, y) = \int_0^{\pi} \int_{-\infty}^{\infty} |\rho| \Phi(\rho, \theta) e^{2\pi j\rho(x\cos(\theta)+y\sin(\theta))} d\rho d\theta \quad (\text{Eqn. 2.1.10})$$

(Eqn. 2.1.10) can be further simplified by defining $\ell(\bar{x}, \theta) \triangleq x\cos(\theta) + y\sin(\theta)$, to produce (Eqn. 2.1.11). (Eqn. 2.1.11) gives the general form of the filtered backprojection equation in 2D. The equation in brackets is called the filtering equation. From (Eqn. 2.1.11) it can be observed that the radioactivity distribution $f(x, y)$ can be reconstructed by filtering the 1D Fourier transform of each projection with a ramp filter $|\rho|$.

$$f(x, y) = \int_0^\pi d\theta \left[\int_{-\infty}^{\infty} |\rho| \Phi(\rho, \theta) e^{2\pi j \rho \ell} d\rho \right]_{\ell(\bar{x}, \theta) = x\cos(\theta) + y\sin(\theta)} \quad (\text{Eqn. 2.1.11})$$

2.1.3 Convolution Backprojection

(Eqn. 2.1.11) above gives the general formula for reconstructing the 2D radioactivity distribution $f(x, y)$ from its corresponding set of projections. However, using the convolution theorem of Fourier transforms, the filtering equation can be re-written in terms the convolution operation as in (Eqn. 2.1.12), where $\mathcal{F}_{1D}^{-1}\{|\rho|\}$ denotes the 1D inverse Fourier transform of the ramp filter $|\rho|$, $\Phi(\rho, \theta)$ denotes the set of projections obtained from $f(x, y)$, and \otimes denotes the convolution operation. Defining $c(\ell) \triangleq \mathcal{F}_{1D}^{-1}\{|\rho|\}$ gives the general equation for convolution backprojection in 2D, (Eqn. 2.1.13).

$$f(x, y) = \int_0^\pi d\theta \left[\mathcal{F}_{1D}^{-1}\{|\rho|\} \otimes \Phi(\ell, \theta) \right]_{\ell = x\cos(\theta) + y\sin(\theta)} \quad (\text{Eqn. 2.1.12})$$

$$\left\{ \begin{array}{l} f(x, y) = \int_0^\pi \left[\int_{-\infty}^{\infty} \Phi(\ell, \theta) c(x\cos(\theta) + y\sin(\theta) - \ell) d\ell \right] d\theta \\ \text{where, } c(\ell) = \mathcal{F}_{1D}^{-1}\{|\rho|\} \end{array} \right. \quad (\text{Eqn. 2.1.13})$$

However, the ramp filter $|\rho|$ is non-integrable and hence does not have an inverse Fourier transform. Therefore, in practice, the ramp filter $|\rho|$ is multiplied by an apodizing window function $W(\rho)$, such that the inverse Fourier transform of the product $|\rho|W(\rho)$ exists. That is, in practice, the 2D radioactivity distribution is approximated by (Eqn. 2.1.14). Typical window functions $W(\rho)$ used in PET image reconstruction are the square, Hann, and Gaussian windows [26, 29, 31].

$$\left\{ \begin{array}{l} f(x, y) \approx \int_0^\pi [\tilde{c}(\ell) \circledast \Phi(\ell, \theta)]_{\ell=x\cos(\theta)+y\sin(\theta)} d\theta \\ \text{where, } \tilde{c}(\ell) = \mathcal{F}_{1D}^{-1}\{|\rho|W(\rho)\} \end{array} \right. \quad (\text{Eqn. 2.1.14})$$

2.2 METHODS OF PET IMAGE RECONSTRUCTION

Several algorithms exist for reconstructing PET projection data, and can be broadly classified into two categories: analytic or iterative methods [30, 32]. The most commonly used methods for analytic image reconstruction are filtered back projection (FBP) or convolution back-projection (CBP) [26, 30]. Analytic reconstruction methods essentially work to apply the inverse Radon transform to the measure projection data and generate the corresponding distribution of radioactivity [26, 30]. As a result, analytic methods are less computationally intensive compared to their iterative counter-parts and produce images for which their noise properties are easily evaluated, since each voxel represents the sum of a large number of random variables. However, the principal drawback of these methods is that they treat each measured projection as if it were,

in fact, a true (i.e. a non-random) projection of the tracer distribution; thereby ignoring the random nature of the radio-active decay processes that produced the measured LORs [26, 29, 30, 32].

In contrast, iterative reconstruction methods treat the set of measured projections as a single random realization of the set of true projections and explicitly include the randomness of the count rates as part of the reconstruction algorithm [26, 32]. Generally, these approaches involve optimization of a cost-function that contains information about the scanner hardware properties, the injected tracer, and the attenuation properties of the subject being scanned; though, additional information can also be included [26, 32]. The most popular method of iterative reconstruction is based on maximizing a log-likelihood function for which the detected coincident photons are assumed to follow a Poisson distribution [26, 32]. The most widely used optimization algorithms for maximizing this log-likelihood function are: expectation-maximization (EM) and its accelerated version ordered subset expectation maximization (OSEM) [26, 32].

Iterative methods generally have the advantage of producing images with less streaking artifacts as well as better contrast in regions of low tracer uptake (especially with regard to PET imaging of the body) [26, 32]. Moreover, iterative methods that utilize Bayesian approaches can readily incorporate prior information about the tracer into image reconstruction [26, 32]. For example, iterative methods can be used to generate parametric maps of tracer pharmacokinetic model parameters as part of the image reconstruction process [33]. However, some disadvantages of iterative methods include high computational burden and the noise properties of the resulting images can be difficult to evaluate [26, 32].

2.3 SOME IMPORTANT CORRECTIONS APPLIED TO PET DATA

As part of the image reconstruction process, PET data need to be corrected for several degrading effects to produce an image set that can be accurately quantified. These include corrections for: photon attenuation, scatter and random coincidences, detector dead time, and detector normalization. The final reconstructed resolution of a PET scan is typically ~5-6 mm full width at half maximum (FWHM) and may vary as a function of position and direction in the FOV.

2.3.1 PET Photon Attenuation Correction

In order to be counted by the PET scanner both photons from an annihilation event must be detected. When one or both photons originating from an annihilation event are “lost” the photon/photons are said to have been attenuated. The probability of a photon being attenuated before reaching a detector increases with tissue density and distance traveled through a medium. Failure to account for photon attenuation in PET data will result in a gradual increase in underestimation of radioactivity from edge of skull/body to the center [31]. The underestimation of tracer activity concentration is especially dramatic in dense tissue. Therefore, without an accurate knowledge of attenuation, correctness of the final PET image is compromised.

Attenuation measurements are a routine part of a PET imaging protocol. Because both annihilation photons are detected in coincidence, attenuation correction of PET data can be implemented via multiplication of the appropriate correction factors along each LOR. In standalone PET, attenuation factors are usually measured directly using a positron-emitting source [source-based attenuation correction (SAC)], e.g. $^{68}\text{Ge}/^{68}\text{Ga}$. More recently, with the advent of

dual modality PET/CT [34], the required attenuation information is obtained from CT data [CT-based attenuation correction CTAC)]. The CTAC method is an indirect method in which attenuation is measured at CT energies and then transformed to values appropriate for 511 keV using some simple assumptions about the atomic make-up of the body [35-42].

2.3.1.1 Approaches to MR-Based Attenuation Correction (MRAC)

While the availability of dual modality PET/MR imaging provides opportunities in clinical oncology for and clinical trials, MRI-AC is fundamentally different from either of these approaches in that no actual measurement of attenuation is performed. In the Siemens mMR, MRI-AC is implemented using the Dixon method [43, 44], in which both “in phase” and “opposed” T₁ spin echo images are acquired, from which are derived fat and water images. The manufacturer-supplied software uses this data to classify voxels into one of 3 segments: air, fat, or soft tissue. Each of these segments is assigned a fixed 511 keV attenuation value. Because of the difficulty in imaging cortical bone, no such segment is included in the standard-release software.

The review of Bezrukov et al [45] contains an in depth discussion of the state-of-the-art in production of a PET attenuation correction starting with MR data as well a concise summary of methods used in the head and body. Wagenknecht et al [46] provide an overview of methods with a special emphasis on the advantages and disadvantages of each. Here the two main approaches toward improving Dixon-based MRAC are summarized.

MR Pulse Sequence Based Methods

In this approach, MR pulse sequences and methodologies are used to deduce attenuation properties given some assumptions about body makeup but without recourse to anatomical images from other modalities. Mainly, this work is based on the use of ultrashort echo time (UTE) pulse sequences to identify and characterize cortical bone. Historically, UTE has been evaluated as a method for MR-based assessment of bone-disease states e.g. [47]. Efforts are underway to adapt this method for improving MRAC in PET/MR. Assessment of MRAC employing UTE has been almost exclusively limited to the head, e.g., [48-50]. Application of UTE for whole-body scanning is technically difficult [51-53] although some authors have commented about the potential of MRAC/UTE in the body, e.g. [54]. Alternative pulse sequences and methodologies providing similar information to UTE, again, mainly in the head, are also being studied, e.g., the combination of short- and long-echo times [55].

Atlas-Based and Template-Based Methods

In this approach, an attenuation map is transformed to match the patient's anatomy. A typical method employs an atlas of CT-based attenuation maps, each with a co-registered MR image. A subset of MR images is chosen from the atlas and warped to the patient's MR. Each of the coregistered attenuation maps is warped using the transformation determined in MR warping process. The resulting patient aligned attenuation maps are then combined, for example, by averaging, to produce a patient-specific attenuation map. Additional operations may be used to improve the attenuation-map quality.

For example, Izquierdo-Garcia et al [56] developed a sophisticated atlas approach from 15 subjects who had both a magnetization-prepared rapid gradient-echo (MPRAGE) MRI and a CT scan. Production of the atlas was accomplished using the freely available software SPM8 (Wellcome Trust Centre for Neuroimaging <http://www.fil.ion.ucl.ac.uk/spm/software/spm8/>). The steps involved were to register each CT with the corresponding MPRAGE image, segment the MPRAGE images into 6 tissue classes with the assistance of a set of tissue priors contained within SPM8, warp the 15 subject segmentations into a common space, and co-warp the CTs. The resulting atlas consists of a tissue-class template and an averaged CT both in the same space. The atlas is used to generate a “pseudoCT” of a study-subject, again employing SPM8, by segmenting the study subject’s MPRAGE into tissue classes and warping this into the template space. The inverse transformation is then applied to the atlas CT to bring it into the study-subject’s space. This pseudoCT is then converted to a 511 keV linear attenuation coefficient image by scaling the pseudoCT values [57].

In 2017, Ladefoged et al [58] published a report comparing 11 *post hoc* attenuation correction methods for PET images acquired on integrated PET/MRI scanners. Their study concluded that all 11 tested AC method exhibited an acceptable average global performance [58]. However, they selected 5 of the tested methods as the best performing methods based on robustness, outlier analysis, and clinical feasibility [58]. The method of Izquierdo-Garcia *et al* [56] was selected as one of the 5 best performing post hoc AC methods [58].

A Substitution Based Method Developed at the University of Pittsburgh

Dual modality PET/MR, in which MR and PET data are acquired simultaneously is of great current interest in both the clinical and research domain. As noted elsewhere, quantitative PET requires compensation for events that are lost (or attenuated) due to the medium being imaged. In PET an exact compensation can be made for attenuated events. The correction requires a knowledge of the 511 keV attenuation factor along each LOR. The attenuation factor can be determined by placing a source at one end of the line of response and measuring the count rate in a detector at the other end of the LOR with attenuating material present and normalizing to the rate with attenuation material absent. Thus, attenuation factors range from 0-1. Attenuation information can also be encoded as an image of specific 511 keV attenuation or “ μ -value” at each pixel (typical units, cm^{-1}). In standalone PET, scanners typically are equipped with 511 keV radiation sources (e.g. $^{68}\text{Ge}/^{68}\text{Ga}$) that can be used to make the required “transmission” measurements. In PET/CT, the CT data are used to generate a 511 keV μ -image by scaling the CT-image [37-40].

In contrast to standalone PET or PET/CT, in PET/MR attenuation information is deduced from the MR data and is not based on a transmission measurement. A common method of MR-based attenuation correction uses the Dixon procedure [43, 44] in which fat and water images are used to classify voxels into one of several segments, typically air, fat, or soft tissue. Importantly, this method does not include a bone segment. Thus, while the method produces an overall useable attenuation correction, it does result in artifacts, particularly in the vicinity of bone. For example, in neuroimaging, Dixon MRAC has been shown [59, 60] to result in a bias that takes the form of a spatial gradient increasing from the skull (where attenuation is underestimated) toward the center of the head. However, improved algorithms for producing μ -images from MR are being developed.

Recently, our facility has been producing μ -images from MR data using the method of Izquierdo-Garcia et al. [61] to replace the native μ -images produced by our Siemens mMR PET/MR scanner. The method has been shown to perform well in a multisite evaluation of proposed techniques [62]. The PET/MR images in this dissertation have all been produced using μ -images generated using the method of ref. [61]. Thus, each μ -image was created offline at some point after the original data acquisition.

A complication of using a new attenuation correction is that it requires a new reconstruction, which itself requires the availability of the raw PET sinogram data, the scanner normalization, access to the manufacturer's reconstruction engine, and the ability to load the new μ -image into the scanner's database in a usable way. Due to initial problems with the Siemens mMR, a new product at the time of scan acquisition for this project, some blocks of sinogram data were lost. To remedy this particular situation as well as to generally provide a more usable pathway to attenuation replacement, we developed a new image-based 2D reprojection method, implemented in MATLAB, which does not require sinogram data or access to scanner software, for substituting one attenuation correction for another [63]. Briefly, approximate 2D sinograms are regenerated by applying the Radon transform (forward projection) to each plane of the PET image, performing the attenuation substitution, and then performing the inverse Radon transform (filtered back-projection). Additional details relating to this AC procedure can be found in Laymon et al [63]. The method was tested with both [^{18}F]FDG [63] and [^{18}F]ML-10 (unpublished) and found to provide accurate results.

2.3.2 Corrections for Scatter and Random Coincidences

After the annihilation event, a coincident 511 keV photon may interact with an outer-shell electron of an atom in the tissue causing the photon to lose some fraction of its initial energy and deviate from its initial trajectory [31]. In this case, the photon is said to have undergone Compton scattering. If the scattered photon has not lost too much energy during the interaction with the electron and is detected within the coincidence window of the detector pair, the un-scattered photon and the scattered photon will be counted as an annihilation event along the wrong LOR.

A random detection event refers to the accidental counting of non-paired photons in coincidence [31]. Random events can occur if two annihilation events occur near simultaneously creating 2-pairs of annihilation photons. If one photon from each pair is lost due to attenuation, the two remaining photons may be detected in coincidence and, therefore, considered by the PET scanner to form a valid LOR. As in the case of photon scatter, the detection of random coincidence events leads to incorrect assignment of counts to a LOR and a general decrease in image contrast.

A common approach to scatter correction in PET is to model it based on the attenuation map and the known behavior/properties of electromagnetic interactions [64, 65]. Additionally, one can set an energy threshold because the photons should be 511 keV but could be lower if scattered (could lose energy). The rate of random coincidences is generally estimated during each PET acquisition by using a delayed coincidence timing window or utilizing an approximation that relates the singles rate (i.e. the rate at which single un-paired photons are being detected) to the random coincidence rate [27].

Finally, an additional degrading effect is the detection of multiple coincidence events. That is, the simultaneous detection of 3 or more annihilation photons within the coincidence detection window of the scanner. Similar to random coincidence events, a multiple coincidence event may occur when two annihilation events occur at near simultaneous times producing 2-pairs of annihilation photons. However, if only one photon is lost to attenuation, then the remaining 3 photons may be detected in coincidence; thereby producing more than one plausible LOR. The occurrence of multiple coincidence events ultimately leads to a loss of counts because the scanner throws them out when they occur.

2.3.3 Correcting for Scanner Dead Time

There is a non-zero minimum amount of time required by sub-systems within the PET scanner to process events, during which the system cannot process new events. The time window during which the scanner cannot process a new event is called “dead time”. Dead time depends on count-rate and the architecture of the PET system. Dead time models are routinely built into the scanner software by the manufacturer, and correction for loss of events due to scanner dead time is performed automatically. A more detailed discussion of detector dead-time and methods of correction can be found in the textbook by Knoll [66] as well as the review by Meikle and Badawi [27].

2.3.4 Scanner Normalization

As a result of several factors (e.g. differences in detector efficiencies), each LOR in a PET scanner will in general have differing detection sensitivities. Failure to account for these differences will result in several image artifacts, and, ultimately, prevent reconstruction of a quantitatively accurate image. The process of correcting for differences in LOR detection sensitivities is called normalization. Indeed, normalization correction of the measure projection data is required before most reconstruction algorithms can begin. The simplest approach to normalization, is to measure the individual correction factors for each LOR using a rotating positron line source (typically ^{68}Ge); though other approaches can be followed [27].

2.4 TIME ACTIVITY CURVE MEASUREMENT FROM DYNAMIC PET ACQUISITIONS

PET imaging allows for the study of physiologic processes *in vivo* through the acquisition of a time-series of images that each represent the distribution of radioactivity in the tissue of interest over a finite dwell time (or “frame”). Using the appropriate tracer, measures can be developed to quantify pathological changes in the physiologic process of interest. The principal means by which these measures are obtained and evaluated is via pharmacokinetic analysis of the time-course of radioactivity concentration in the tissue containing the physiologic process of interest.

The previous section detailed corrections that must be applied for accurate reconstruction of PET sinogram into a quantifiable image. However, from the stand-point of modeling the temporal profile of tracer uptake in tissue, additional corrections may be warranted to facilitate accurate quantification. These include correcting for contribution of radio-labeled metabolites to the tissue time-activity curve (TAC) as well as correction for radioactive decay.

As mentioned above, PET detects annihilation events *in vivo*. This means that two tracers labeled with the same positron emitting radionuclide will be indistinguishable to the scanner, and, hence, the cumulative radioactivity from both tracers would be reconstructed into the same PET image. This feature of PET imaging is particularly important for tracers that undergo significant metabolism by the body, which results in the production of several different chemical species distinct from the parent tracer but are nonetheless labeled with a positron emitting nuclide. The effects of tracer metabolism are to reduce the overall concentration of parent tracer available for imaging, as well as to corrupt the true temporal profile of parent tracer concentration in the target tissue. Moreover, the effect of radio-labeled metabolites (or radio-metabolites) may be especially important in the blood as the blood tracer concentration is commonly used as the input tracer concentration for pharmacokinetic modeling. Thus, incorrect accounting of radio-metabolites in the blood may severely bias pharmacokinetic model parameters as well as any derived measures.

Several approaches exist for identifying radio-metabolites from blood and tissue samples (e.g. high-performance liquid chromatography (HPLC) analysis) [67]. If a tracer is known to undergo significant metabolism *in vivo* and yield an appreciable concentration of radio-labeled biochemical species, then some method of correcting the blood and tissue TACs for radio-

metabolites will be required. In the brain, the blood-brain-barrier (BBB) often prevents radio-metabolites from leaving the vasculature and entering the tissue due to their usual high polarity, though exceptions do exist [68]. Approaches to metabolite correction can range from including radio-metabolite formation as part of the pharmacokinetic model of the tracer as in Price et al [68], to applying a population based correction [69]. However, caution is required when using a population-based metabolite correction for oncologic applications as the toxic effects of anti-cancer therapy may modulate metabolite production [70, 71].

A second important consideration in the analysis of the time-course of tracer uptake is that of correcting measured TACs for radioactive decay. Often this correction is made during the image reconstruction process but is discussed here because of its importance in quantification of tracer uptake. The general equation describing the radioactive decay of a radioactive sample is given below in (Eqn. 2.4.1), where A_0 denotes the initial radioactivity at time $t = 0$, and λ denotes the radioactive decay rate of the radionuclide. However, it is important to point out that this equation describes the instantaneous decay of a radioactive sample. This is a critical point since PET cannot reliably measure instantaneous radioactivity concentration, and, as a result, each PET frame is typically acquired over a finite time duration (e.g. minimum duration is typically 6 sec).

$$A(t) = A_0 e^{-\lambda t} \tag{Eqn. 2.4.1}$$

Therefore, in practice decay correction is applied to each PET frame by calculating the time of average decay for each frame dwell time. Specifically, let $\tilde{A}_k(t)$ denote the time-averaged

activity of the sample measured during the k^{th} PET frame with corresponding frame start and end times denoted t_k^s and t_k^e , respectively. Then, based on (Eqn. 2.4.1), the radioactivity at the start of the k^{th} frame (decay corrected to the time of injection), A_0^k , is given by (Eqn. 2.4.2), which yields (Eqn. 2.4.3).

$$A_0^k = \tilde{A}_k(t) \left[\frac{1}{(t_k^e - t_k^s)} \int_{t_k^s}^{t_k^e} e^{\lambda t} dt \right] \quad (\text{Eqn. 2.4.2})$$

$$A_0^k = \tilde{A}_k(t) \left[\frac{(e^{\lambda t_k^e} - e^{\lambda t_k^s})}{\lambda(t_k^e - t_k^s)} \right] \quad (\text{Eqn. 2.4.3})$$

For decay correction of PET data, the final decay correction factor for the k^{th} frame, $e^{\lambda \bar{t}_k}$, is obtained by defining a “time of average decay” \bar{t}_k as shown in (Eqn. 2.4.4), from which the value of \bar{t}_k for the k^{th} frame is obtained: (Eqn. 2.4.5).

$$e^{\lambda \bar{t}_k} = \left[\frac{(e^{\lambda t_k^e} - e^{\lambda t_k^s})}{\lambda(t_k^e - t_k^s)} \right] \quad (\text{Eqn. 2.4.4})$$

$$\bar{t}_k = \frac{1}{\lambda} \ln \left\{ \frac{(e^{\lambda t_k^e} - e^{\lambda t_k^s})}{\lambda(t_k^e - t_k^s)} \right\} \quad (\text{Eqn. 2.4.5})$$

With the definition of \bar{t}_k in (Eqn. 2.4.5) the measured sample activity $\tilde{A}_k(t)$ can be decay corrected back to the injection time of the radiotracer using (Eqn. 2.4.6) below.

$$A_0^k = \tilde{A}_k(t) e^{\lambda \tilde{t}_k} \quad (\text{Eqn. 2.4.6})$$

2.4.1 Approximate Model for Measurement Noise of Time-Activity Curve Data in PET

A common assumption in PET quantification is to assume the measurement errors are independent and normally distributed with zero mean and individual variances proportional to the measured activity. This proposed error model is based on the Gaussian approximation to the Poisson distribution [66] as well as a heuristic argument relating the measured activity in a particular PET frame to an effective count-rate [72]. Moreover, the assumption of the measurement errors following a multivariate Gaussian distribution is particularly relevant when the PET image data have been re-constructed using filtered-backprojection and is based on the Central Limit Theorem, which states that the distribution of a sum of random variables converges to a Gaussian distribution with probability equal to one, independent of the distributions of the individual random variables being summed [73, 74].

Specifically, let N_i^{counts} represent the number of effective counts that would have been emitted from a particular volume of interest during the i^{th} PET frame of duration $\Delta_i T$, then the corresponding effective count-rate count rate, R_i , for the i^{th} frame in that volume of interest is given by $R_i = \frac{N_i^{counts}}{\Delta_i T}$, which has variance equal to $var\{R_i\} = var\left\{\frac{N_i^{counts}}{\Delta_i T}\right\} = \left(\frac{1}{\Delta_i T}\right)^2 var\{N_i^{counts}\} = \frac{N_i^{counts}}{\Delta_i T^2}$ under the assumption of Poisson counting noise. However, for each time window, the number of detected counts is proportional to the measured concentration multiplied by the time-length of the PET frame when no decay correction is applied.

Nevertheless, most PET imaging platforms automatically decay correct the reconstructed images, thus the final derivation of the sample variances of the time-activity curve will be presented in terms of the non-decay corrected signal, y_i , and the decay corrected signal, x_i . That is $x_i = y_i * e^{(\bar{t}_i * \lambda)}$, $\forall i$ where \bar{t}_i denotes the time of average radioactive decay over the i^{th} PET frame, and λ denotes the decay rate of the positron emitter (e.g. for ^{18}F , $\lambda = 0.00631 \text{ min}^{-1}$). Following this notation then, the effective measured counts in a particular volume of interest during the i^{th} frame, N_i^{counts} , is proportional to the non-decay corrected activity multiplied by the corresponding frame length, that is: $N_i^{\text{counts}} \propto y_i * \Delta_i T = [x_i * e^{-(\bar{t}_i * \lambda)}] * \Delta_i T$. Therefore, an approximate formula for the noise variance of the non-decay corrected count rate in the i^{th} frame is given by (Eqn. 2.4.7), where α is a positive constant of proportionality.

$$\sigma_{NC,i}^2 \triangleq \text{var}_{NC}\{R_i\} = \frac{N_i^{\text{counts}}}{\Delta_i T^2} = \alpha^2 \left(\frac{[x(\bar{t}_i) * e^{-\lambda \bar{t}_i}] * \Delta_i T}{\Delta_i T^2} \right) = \alpha^2 \left(\frac{[x_i * e^{-\lambda \bar{t}_i}]}{\Delta_i T} \right)$$

$$\sigma_{NC,i}^2 = \alpha^2 \left(\frac{[x_i * e^{\lambda \bar{t}_i}]}{\Delta_i T} \right) \quad (\text{Eqn. 2.4.7})$$

While (Eqn. 2.4.7) gives an equation for the measurement variance associated with the non-decay corrected PET time-activity curve data, it is often useful to have an expression for the variance of the decay-corrected data. Since the decay corrected data are obtained by multiplying the uncorrected data by a factor of $e^{\lambda \bar{t}_i}$, the variance of the decay corrected data can be obtained by multiplying the variance of the uncorrected data by a factor of $(e^{\lambda \bar{t}_i})^2$ resulting in (Eqn. 2.4.8) and (Eqn. 2.4.9) for the variance of the decay corrected data samples.

$$\sigma_{Cor,i}^2 = \alpha^2 \left(\frac{[x_i * e^{\lambda \bar{t}_i}]}{\Delta_i T} \right) \quad (\text{Eqn. 2.4.8})$$

$$\sigma_{Cor,i}^2 = \alpha^2 v_i^2; \quad \text{where, } v_i^2 \triangleq \frac{[x_i * e^{\lambda \bar{t}_i}]}{\Delta_i T} \quad (\text{Eqn. 2.4.9})$$

2.4.2 Partial Volume Effect is a Practical Limiter of PET Resolution

In PET, the partial volume effect (PVE), sometimes called partial volume averaging, refers to a size dependent bias between the apparent radioactivity concentration in reconstructed voxel values on PET and the true radioactivity concentration [27, 75]. The PVE is a result of 2 separate effects that conspire to distort reconstructed voxel values from their true values [75]. The first effect is that of finite PET scanner resolution, which results in an overall blurring of the PET image [75]. The second contributor to PVE is the voxel sampling grid [75]. Specifically, the contours of the rectangular voxels will not in general match the contours of the radioactivity distribution [75]. As a result, most image voxels will contain more than one tissue type, each of which may have a different radioactivity concentration [75]. The observed activity in these voxels will be the average activity of the underlying tissue types [75].

Many methods have been suggested to correct brain PET images for PVE [76]. For example, the Meltzer method [77] treats each brain PET image as being composed of matter (MA, the combination of gray and white matter) from which PET signal originates or “not matter” (NM; the rest of the PET FOV). The measured concentration (C^{PET}) within a VOI is assumed to have contributions from both MA and NM described by (Eqn. 2.4.10):

$$C^{PET} = \lambda^{MA}f + \lambda^{NM}(1 - f), \quad (\text{Eqn. 2.4.10})$$

where λ^{MA} and λ^{NM} are the true tracer concentrations in MA and NM respectively. The goal is to correct C^{PET} to obtain the desired quantity λ^{MA} . The quantities f and $(1-f)$ are the “signal weights” of MA and NM respectively. To determine these weights, the subject’s T₁ MR is segmented into MA and NM and blurred by the assumed PET resolution. The Meltzer method has the advantage of being easily implemented but does not distinguish between GM and WM within an analysis region. An extended version of the Meltzer method has been proposed by Müller-Gärtner et al [78] that explicitly includes white matter (WM) as part of partial volume correction (PVC). However, the method is subtractive in nature and can result in increased PET image noise in cases of high white matter signal.

The Geometric Transfer Matrix (GTM) method [79] requires that the entire brain be segmented into a set of contiguous regions with the assumption that each region has a uniform tracer concentration but that concentrations in the different regions can be different. The blurring produced by the imaging process results in the measured concentration being a weighted average of the true concentrations in each region: $\lambda_i^{PET} = \sum_j G_{ij}\lambda_j$ where λ_i^{PET} is the measured concentration in region i , λ_j is the true concentration in region j (the things we wish to know) and G_{ij} is the matrix of weights (the geometric transfer matrix) connecting the true concentrations to the measured concentration. The G_{ij} values are determined from blurred (by the PET resolution) maps of the different regions. Once determined G_{ij} is inverted, allowing the recovery of the λ_j values from the λ_i^{PET} .

Finally, modern scanners offer point spread function recovery (PSFR) reconstruction [80, 81] as an option (Siemens: TrueX, GE: SharpIR, Philips: xSharp). Manufacturers make painstaking PSF measurements as a function of position throughout the FOV of the scanner. The PSF can then be modeled in the reconstruction with the goal of undoing the blurring inherent in the imaging process. PSFR is fundamentally different from the partial volume correction methods described above. While the other methods are applied post-reconstruction, PSFR is incorporated into the manufacturer's reconstruction software. Further, PSFR knows nothing about the imaged object; it operates completely based on well-measured characteristics of the imaging process. The PVC methods on the other hand, employ both a measured PSF and an *a priori* model of tracer distribution. In particular, the PVC methods assume uniform tracer distributions within each of a set of anatomically defined regions of interest. It should be noted that the PSF model incorporated into PSFR reconstruction by the manufacturer is far more sophisticated than that used in practice in Meltzer, MG, or GTM.

3.0 APOPTOSIS IMAGING IN HUMAN CANCER RESPONSE ASSESSMENT: CURRENT STATE OF THE ART

Non-invasive and early assessment of the efficacy of anticancer agents is a highly desirable and a generally unmet need in clinical oncology. Current methods for radiologic response assessment rely largely on measuring change in tumor morphology on CT or MRI [82, 83]. However, this approach to response assessment is limited as change in tumor size is a late indication of response. Furthermore, therapy induced scarring and fibrosis confound accurate assessment of viable tumor at early response assessment times.

The major mechanism of cell kill by many chemotherapeutic agents is the induction of apoptosis in rapidly proliferating cells [84]. Doxorubicin (an intercalating agent that inhibits topoisomerase II), cisplatin (an interstrand DNA cross-linking agent), temozolomide (a DNA methylating agent), and 5-fluorouracil (anti-metabolite) are all commonly used chemotherapeutics that have been shown to cause apoptosis in cells cultured in vitro [85, 86]. Moreover, proposed mechanisms of resistance to many chemotherapeutics often include loss of function of pro-apoptotic pathways [87]. Given the central role of apoptosis, it would be desirable to have a noninvasive imaging method to serially detect and monitor the extent of this process in cancer

patients undergoing conventional radiation and chemotherapy treatments as well as for the development and testing of new drugs [88, 89].

To date, in human apoptosis imaging trials have focused on evaluating the utility of radiolabeled Annexin V [90] and [^{18}F]ML-10 [91] for therapy response assessment, with the majority of clinical imaging trials being performed using $^{99\text{m}}\text{Tc}$ -labeled Annexin V [92].

3.1 THE PROCESS OF APOPTOSIS: AN OVERVIEW

The process of apoptosis (or type I cell death) refers to a regulated, energy-dependent procedure, initiated by either intrinsic or extrinsic signals, that culminates in the death and removal of a cell [93, 94]. Hallmarks of apoptosis include: DNA cleavage, chromatin condensation in the cell nucleus, and plasma membrane blebbing [93, 94]. Another distinguishing trademark of apoptosis is the depolarization of the plasma membrane without loss of membrane integrity [93, 94]. Specifically, in a non-apoptosing cell, the transmembrane protein flippase restricts the anionic phospholipids phosphatidylserine (PS) and Phosphatidylethanolamine (PE) to the inner leaflet of the cell, while cationic phospholipids such as phosphatidylcholine (PC) are transported to the outer membrane of the cell by the transport protein floppase [95]. In this way, a normal cell maintains an asymmetric distribution of anionic and cationic phospholipids in the inner and outer leaflets of the plasma membrane [95]. However, the process of apoptosis leads to a rapid redistribution of these membrane phospholipids, facilitated by Ca^{2+} dependent activation of a family of scramblase

phospholipids [96], resulting in loss of asymmetry of plasma membrane phospholipids [96] and ultimately plasma membrane depolarization [95].

The two best characterized pathways of apoptosis are the mitochondrial (or intrinsic) and death receptor (or extrinsic) pathways; though other pathways have been reported (e.g. host defense pathway) [94]. The enzymes responsible for the physiological and morphological cell changes that characterize apoptosis are a family of cysteine-aspartic proteases called caspases [94, 97]. In humans, these caspases can be further divided into at least two groups: initiator caspases (caspase-8 and caspase-9) and executioner caspases (caspase-3, caspase-6, and caspase-7) [94, 97]. The initiator caspases exist in an inactive form in the most cells but become activated when two identical chains are brought together to form a protein dimer [94, 97]. This dimerization and subsequent activation of the initiator caspase is facilitated by adapter proteins [94, 97]. It is the unique adapter protein/initiator caspase relationship that distinguishes each of the pathways of apoptosis [94, 97]. Once activated, the initiator caspases activate the executioner caspases, which also preexist in almost all cells in an inactivated form, through proteolytic cleavage and apoptosis proceeds [94, 97]. As a further consequence of apoptosis, cells undergoing apoptosis produce “bind-me signals” (PS externalization is one of these) that promote rapid clearance of the dying cell by phagocytes [94].

3.1.1 The Intrinsic Pathway

The mitochondrial pathway is orchestrated by the BCL-2 family of proteins, which are responsible for managing the integrity of the outer membranes of mitochondria [94]. This family of proteins is composed of three sub-groups: pro-apoptotic BCL-2 proteins, which act to disrupt

the outer membrane of mitochondria, anti-apoptotic BCL-2 proteins, which work to preserve mitochondria outer membrane integrity, and a group of regulatory proteins (the BH3-only proteins), which promote apoptosis through regulation of the pro-apoptotic and anti-apoptotic BCL-2 protein sub-families [94]. Once the pro-apoptotic BCL-2 proteins have been activated, they insert themselves into the mitochondria outer-membrane where they oligomerize forming holes in the membrane [94]. The formation of these opening facilitates mitochondrial outer-membrane permeabilization, which then allows for the release of cytochrome-c (and other soluble proteins) from the intermembrane space of the mitochondria into the cell cytosol [94]. Once released, cytochrome-c interacts with an adapter protein (apoptotic protease activating factor-1, APAF-1) causing this protein to oligomerize and bind to caspase-9 resulting in the activation of the initiator caspase, which proceeds to activate the executioner caspases and apoptosis proceeds [94].

Most events that stress the cell induce the mitochondrial pathway of apoptosis [94]. These cell stressors include excessive DNA damage, loss of growth factors, and cytoskeleton disruption [94]. However, the mitochondrial pathway can also be initiated through tumor-suppression mechanisms and by developmental signals (i.e. programmed cell death) [94].

3.1.2 The Extrinsic Pathway

In the case of the death receptor pathway, death ligands originating from outside the cell bind to death receptors found on the outer leaflet of cell plasma membrane [94]. These death ligands and their corresponding death receptors are all members of the tumor necrosis factor (TNF) and TNF receptor families, respectively [94]. The major members of the TNF receptor family include: tumor necrosis factor receptor-1 (TNFR1), CD95 (also called Fas and APO-1), death

receptor 3 (DR3), and the TNF-related apoptosis-inducing ligand (TRAIL) receptors (TRAIL receptor-1 and TRAIL receptor-2), and death receptor 6 (DR6) [94]. Once a death ligand is bound to its corresponding receptor, this induces conformational changes in the intracellular region of the death receptor protein, which then engages an adaptor protein that activates a specific initiator caspase (caspase-8) [94]. The activated caspase-8 then cleaves and activates the executioner caspases, thereby initiating the apoptosis process [94].

3.1.3 Alternative Forms of Cell Death: Necrosis

Finally, it should be mentioned that there are several forms of cell death in addition to apoptosis that have been discovered and characterized to varying degrees of detail in the literature [94]. In the context of anticancer treatment, necrosis (type III cell death) is probably the most important as this form of cell death has been associated with radiation therapy [94]. Necrosis refers to a form of cell death in which the cell swells, bursts and decomposes [94]. Necrosis is characterized by a loss of plasma membrane integrity resulting in the spilling of the cell contents into its surroundings [94]. As a result, necrosis often elicits an immune response, in contrast with apoptosis [94].

3.2 CELL DEATH IMAGING USING RADIOLABELD ANNEXIN-V

One of the best characterized markers of cell death is annexin-V. Numerous *in vitro* studies have demonstrated that annexin-V binds to membrane bound PS with high affinity ($K_d = 7$ nmol) [98], and have validated annexin-V binding as a marker for cell death [99-101], with the potential

for up to 8 Annexin V molecules being able to bind to a single PS molecule [102]. However, while PS functions as a “bind me” signal for phagocytic cells, annexin-V has not been shown to have any involvement in the process of apoptosis [94]. To date, the exact physiologic role of annexin-V remains largely unclear. The protein has been found in the placenta, umbilical vessels, liver, spleen, kidney, heart and others [103].

In human imaging of radio-labeled annexin-V has primarily focused on the development of single photon emission computed tomography (SPECT) compounds, generally differing by which chelator is used for attaching the ^{99m}Tc label. To date, all clinical studies evaluating the prognostic or predictive value of radio-labeled annexin-V imaging have used a ^{99m}Tc label; though other radiolabels appropriate for SPECT have been investigated [104, 105]. By far the most common chelator has been hydrazinonicotinamide (HYNIC), though other chelators such as 4,5-bis(thioacetamido)pentanoic acid (BTAP) and ethylenedicysteine (EC) have also been used [98, 106, 107]. Biodistribution studies for these compounds have generally shown physiologic uptake in the gut, spleen, kidney, and salivary glands, in addition to high liver and bone marrow uptake, common sites of metastasis for many cancers; though the degree of physiologic uptake depends on the chelator [98, 105, 106].

3.2.1 Therapy Response Assessment using ^{99m}Tc -labeled Annexin-V

The first in human study specifically designed to evaluate the feasibility and potential utility of using radiolabeled-Annexin-V for predicting response to therapy in oncology was performed by Belhocine et al in 2002 [90], which was expanded upon in [108]. In this study, 15

subjects (10 lung cancer, 3 lymphoma, and 2 breast cancer) received ^{99m}Tc -BTAP Annexin-V (Apopmate; Theseus Imaging Corporation, Boston, MA) planar scintigraphy before and within 72h of receiving anti-cancer therapy [90, 108]. For each subject, change in ^{99m}Tc -BTAP Annexin-V uptake between pre- and post-therapy time-points was quantified through calculation of relative tumor ratios and by evaluating change in tumor-to-background ratios (TBkgRs) [90]. No pre-therapy ^{99m}Tc -BTAP Annexin-V uptake was observed at tumor sites for any subjects [90, 108]. 7 subjects showed at least a 10% increase in TBkgR within 72 hr of completing first course of therapy compared to baseline, of which all demonstrated a partial or complete response [90, 108]. Of the remaining 8 subjects that showed no change in uptake between imaging time-points, 2 exhibited a partial response to therapy and 6 demonstrated progressive disease [90, 108].

Since the publication of the aforementioned initial feasibility study, several in human studies have followed which investigate the utility of ^{99m}Tc -labeled-Annexin-V imaging to predict patient response to anti-cancer therapy. For example, Haas et al. [109] investigate the utility of ^{99m}Tc -labeled Annexin-V SPECT for predicting response to radiotherapy in a cohort of recurrent follicular lymphoma patients (FL) [109]. Specifically, 11 histologically confirmed FL subjects received a baseline (no more than 1-week prior to therapy institution) and post-therapy (24hr after completion of therapy) ^{99m}Tc -labeled Annexin-V SPECT scan [109]. For each subject therapy consisted of involved field radiotherapy to total dose 4 Gy in 2 Gy fractions with a 48 hr interval between radiotherapy doses [109]. 5 subjects received ^{99m}Tc -Phentitotate-rh Annexin-V, while remaining subjects received ^{99m}Tc -HYNIC-rh Annexin-V [109]. FL uptake was evaluated using a visual grading method that comprised four classifications: absent, weak, present or intense [109]. Weak uptake was reported in pre-therapy images of 5 subjects, while ^{99m}Tc -labeled Annexin-V

uptake was reported as visually undetectable in FL sites for the remaining 6 subjects [109]. A visual concordance between change in cell death on cytology and change in apparent ^{99m}Tc -labeled Annexin-V uptake on SPECT was reported [109]. Moreover, pathology scoring was found to be consistent with patient outcome for all 11 subjects, while change in visual scoring of SPECT images was determined to be inconsistent with outcome for only a single subject [109].

Using a similar scoring method, Kartachova et al. [110] investigated a relationship between change in ^{99m}Tc -HYNIC Annexin-V tumor uptake after therapy administration and tumor response assessed on anatomical imaging acquired 1-3 months after treatment initiation [110]. To this end, 29 subjects (23 malignant lymphoma, 5 NSCLC, 1 SCCHN) received baseline and post-therapy (within 72hrs of initiating therapy) ^{99m}Tc -HYNIC Annexin-V SPECT imaging [110]. Therapy for these subjects consisted of either radiotherapy, platinum-based chemotherapy, or concurrent chemoradiation protocols [110]. Each visual grade category was assigned a numerical value (absent = 0, weak = 1, moderate = 2, and intense = 3) [110]. A significant correlation (Spearman rank test; = 0.62, $P \leq 0.001$) was reported between change in tumor uptake grade and tumor response (RECIST criteria) [82, 110].

One of the first studies to evaluate the feasibility of quantitative response prediction was performed by Rottey et al [111], which used TBkgRs as a measure of ^{99m}Tc -HYNIC Annexin-V uptake [111]. Specifically, a sequential imaging protocol was used that consisted of a baseline time-point followed by 2 additional scans acquired at 5-7hrs and 40-44hrs post therapy initiation [111]. Results demonstrate that a greater than or equal to 25% increase occurring at one of or both of the post-therapy scans is predictive for tumor response (assessed using RECIST [82]) at 3

months (and 6 months for some subjects) post-therapy initiation [111]. The authors were able to correctly predict response in 16/17 subjects using this sequential imaging protocol [111]. However, the acquisition and quantification of both the 5-7 hrs and 40-44 hrs post-therapy initiation scans are required to obtain this prediction accuracy compared to acquisition and interpretation of either scan alone (table 1) [111].

In addition to TBkgR, percent injected dose of ^{99m}Tc -labeled Annexin-V has also been investigated as a response measure. For example, Kartachova et al. [112] investigated the utility of sequential ^{99m}Tc -HYNIC Annexin-V SPECT in predicting therapy response in 14 subjects with advanced lung cancer receiving platinum-based chemotherapy [112]. Subjects received ^{99m}Tc -HYNIC Annexin-V SPECT scans prior to therapy initiation (baseline) and 24-48 hrs after injection of the first dose of therapy [112]. Radiotracer uptake was quantified by measuring the maximum pixel count within a tumor volume and normalizing this value by the injected dose and the corresponding subject's weight (denoted C_{\max}) [112]. All therapy responders exhibited an increase in tumor C_{\max} at the post-therapy time-point relative to baseline (range of percent increase: [16%, 121%]) [112]. In contrast, the group of non-responders showed both decreases and increases in post-therapy C_{\max} compared to baseline (range in percent change: [-30%, 24%]) [112]. A significant correlation (linear regression analysis; $r^2 = 0.86$; $P \leq 0.001$) was reported between tumor size change and percent increase in C_{\max} [112].

In a follow-up study, Kartachova et al. [113] investigated and compared the value of visual and quantitative response assessment approaches to predict treatment outcome using ^{99m}Tc -HYNIC Annexin-V SPECT [113]. Specifically, 33 subjects (25 fNHL, 4 NSCLC, 3 SCCHN, 1

mantel cell NHL) received ^{99m}Tc -HYNIC Annexin-V SPECT scans before and at either 24 hrs (NSCLC subjects only) or 48 hrs (remaining NHL and SCCHN subjects) post-therapy initiation [113]. Subjects that showed either a partial-response or complete-response to therapy exhibited a visual increase in ^{99m}Tc -HYNIC Annexin-V uptake at post-therapy compared to baseline [113]. Moreover, subjects with stable-disease or progressive-disease visually exhibited either a decrease or no change in radiotracer uptake at post-therapy compared to baseline [113]. Response using C_{max} was determined by first calculating percent change in C_{max} between corresponding pre- and post-therapy images, and then histogramming the calculated percent change values into one of four possible grades (or bins): grade = -1 if tumor uptake decrease by greater than 25%, grade = 0 if tumor uptake decreased by between 1% and 25%, grade = 1 if tumor uptake increased by between 1% and 25%, and grade = 3 if tumor uptake increased by more than 25% [113]. When this maximum pixel count-based grading scheme was used to predict response, 4 subjects demonstrated an increase in tumor uptake but were determined to have either stable-disease or progressive-disease (see figure 3b), while all subjects that showed partial-response or complete-response exhibited an increase in C_{max} grade [113]. Change in ^{99m}Tc -HYNIC Annexin-V tumor uptake between pre- and post-therapy time-points showed a significant correlation with subject outcome using either the visual (Spearman's rank test; $r = 0.97$; $P \leq 0.001$) or quantitative response (Spearman's rank test; $r = 0.99$; $P \leq 0.001$) assessment methods [113].

In an effort to account for tumor response heterogeneity between pre- and post-therapy time-points, Hoebbers et al [114] measured the mean and maximum voxelwise change in tumor uptake of ^{99m}Tc -HYNIC Annexin-V uptake on SPECT in a cohort of 13 advanced stage inoperable SCCHN patients [114]. Clinical response to therapy was determined 6-8 weeks after completion

of each subject's prescribed therapy regimen (overall treatment duration was 7 weeks) using anatomical imaging as well as examination under anesthesia and biopsy in the case of suspicious findings [114]. Using this subtraction method, no significant correlation was found between change in ^{99m}Tc -HYNIC Annexin-V uptake by primary tumor and response rate, recurrence or overall survival [114]. Moreover, no significant correlation was found between ^{99m}Tc -HYNIC Annexin-V uptake and differences in treatment schedule or tumor volume (data not shown) [114].

In an effort to reconcile the results of the above response assessment trials with each other, Belhocine et al [92] performed a meta-analysis on dedicated response assessment studies, for which the imaging protocol consisted of a pre-therapy and at least one post-therapy assessment scan, and for which response to therapy was evaluated quantitatively [92]. Specifically, they evaluated the pooled positive predictive value (PPV) and pooled negative predictive value (NPV) for six ^{99m}Tc -labeled Annexin V clinical imaging studies (5 single-center, 1 multi-center), for which uptake was quantified at baseline and after therapy administration [92]. However, for the purposes of calculating pooled PPV and NPV estimates only the 5 single-center studies were considered for analysis, as the inclusion of the PPV and NPV values estimated from the multi-center study had been determined to create significant heterogeneity [92]. The reported pooled PPV and NPV estimates were 100% (95% CI: 92 – 100 %) and 70% (95% CI: 55 – 82 %), respectively [92]. These pooled estimates suggest that patients exhibiting a significant increase in ^{99m}Tc -labeled Annexin V uptake are very likely to demonstrate a response to therapy, while approximately 30% of subjects exhibiting no significant increase in ^{99m}Tc -labeled Annexin V but may still demonstrate a complete or partial response to therapy [92]. However, when using PPV and NPV one has to

consider the prevalence of response versus non-response in these studies as a possible driver for these estimates.

3.2.2 Measuring Chemo-/Radio-Sensitivity using ^{99m}Tc-labeled Annexin-V Imaging

In addition to investigating the predictive utility of Annexin V imaging, several studies have also evaluated the feasibility of Annexin V imaging to measure tumor chemo-/radio-sensitivity at baseline and predict patient therapy response. For example, Rottey et al [115] investigated a relationship between TBkgR evaluated prior to therapy initiation on ^{99m}Tc-HYNIC Annexin-V SPECT and tumor response (RECIST) at approximately 2-3 months and 5-6 months post-therapy initiation in a cohort of 23 subjects suffering from a variety of malignancies [115]. Therapy for each subject was not homogeneous, 3 subjects received radiotherapy only, 3 subjects received concurrent radiation and chemotherapy, and the remaining 17 subjects received chemotherapy alone (table 1) [115]. Results showed that subjects treated with radiation alone or concomitant radiation and chemotherapy that also demonstrated a partial-response or complete-response at response assessment had TBkgRs ≥ 2.3 prior to therapy start [115]. Moreover, subjects showing progressive-disease at response assessment had no detectable tumor uptake on pre-therapy SPECT imaging [115]. In the group that received chemotherapy alone, 8 were determined to be responders (partial-response or complete-response) to therapy [115]. It was reported that pre-therapy TBkgRs in these responders were significantly higher [median 2.5, range: 0.3-4.2] compared to non-responders (stable-disease/progressive-disease) [median = 1, range: 0.1-1.4] using an unpaired Wilcoxon test ($P \leq .001$) [115].

In a separate study, Loose et al [116] evaluated the prognostic potential of ^{99m}Tc -HYNIC Annexin-V SPECT in a cohort of 29 SCCHN subjects each receiving a single ^{99m}Tc -HYNIC Annexin-V SPECT scan prior to therapy institution [116]. Primary tumor uptake was quantified via TBkgRs and compared to each subject's disease free and overall survival [116]. Results of this analysis revealed an inverse correlation between TBkgR and both disease free and overall survival [116]. Moreover, Loose et al [116] were able to determine a cut-point based on the sample TBkgR median (median = 2; range = 1.0 - 5.1), such that subjects exhibiting a TBkgR < 2 had a median disease free survival of 32.8 months and a median overall survival of 55.8 months compared to the subgroup of patients with a TBkgR > 2, which had a median disease free survival and median overall survival of 8.9 months and 12.9 months, respectively [116]. Moreover using the same TBkgR cut-point of TBkgR = 2, the authors were able to dichotomize lymph node status according to N0 versus N1-N2-N3 disease and found this threshold to be prognostic for both disease free and overall survival [116]. However, it is important to note that all study subjects received therapy (radiotherapy and/or chemotherapy) after SPECT imaging, and, in most cases (27 out of total 29 subjects), subjects received a resection of their primary tumors [116].

Furthermore, Kurihara et al [107] evaluated the feasibility of using ^{99m}Tc -ethylenedicycysteine (^{99m}Tc -EC) Annexin V to image cell death in women with primary breast cancer [107]. A total of 9 women received a single ^{99m}Tc -EC Annexin V SPECT scan either before therapy initiation (4 subjects) or 16 hrs after chemotherapy initiation (5 subjects) [107]. In this study, it was found that the mean TBkgR for the subjects who received therapy (mean = 2.6; standard deviation = 0.5; range: 2.1 - 3.3) was larger than the average TBkgR between subjects

that had not received therapy prior to imaging (mean = 1.5; standard deviation = 0.2; range: 1.3 - 1.7) [107].

However, not all studies have observed a correlation between baseline ^{99m}Tc -HYNIC Annexin-V uptake and patient response. Specifically, as part of their analysis Kartachova et al. [112] observed measurable ^{99m}Tc -HYNIC Annexin-V uptake in all tumors prior to therapy initiation. However, it was reported that no significant correlation between baseline C_{\max} and subject outcome was found [112].

One potential explanation for this disagreement in predicting response to therapy based on pre-therapy ^{99m}Tc -HYNIC Annexin-V uptake may be that tumors in these studies had differing levels of necrosis. For example, van de Wiele et al. [117] performed a study to investigate a relationship between the degree of ^{99m}Tc -HYNIC Annexin-V uptake on SPECT and number of tumor cells undergoing apoptosis determined by histology. In this study 20 head and neck carcinoma subjects received pre-therapy ^{99m}Tc -HYNIC Annexin-V SPECT scans at 1 hr and 5-6 hr post radio-pharmaceutical injection [117]. Results from this analysis revealed a significant ($p \leq .03$) linear correlation between percent uptake of injected dose per cubic centimeter tumor volume assessed on SPECT and percent of apoptotic cells evaluated on histology when only the 11 subjects with the smallest corresponding percent necrosis were included [117]. However, progressive inclusion of tumors with increasing percent necrosis resulted in loss of correlation significance between percent apoptotic cells and image measures [117].

A second hurdle to using baseline ^{99m}Tc -labeled Annexin V imaging to presage patient therapy response is the inconsistent degree of radiotracer uptake at pre-therapy time-points [90, 107-118]. For example, in their seminal study Belhocine et al [90] evaluated 15 subjects with various malignancies (10 lung cancer, 3 lymphoma, and 2 breast cancer) prior to therapy start and observed no pre-therapy ^{99m}Tc -BTAP Annexin-V uptake on planar scintigraphy [90]. In contrast, measurable ^{99m}Tc -HYNIC Annexin-V uptake was reported prior therapy for all 14 advanced lung cancer subjects evaluated by Kartachova et al [112]. Moreover, differences in the degree of ^{99m}Tc -HYNIC Annexin-V pre-therapy accumulation have been observed between the primary tumor site and involved lymph nodes of subjects suffering from head and neck carcinoma [118]. Specifically, in a study that included 18 head and neck carcinoma patients, in which 7 subjects had associated lymph node involvement, Vermeersch et al [118] were able to visualize the primary tumor in nearly all subjects (17 out of 18 total) on SPECT; however, uptake was observed in involved lymph nodes for only 2 of 7 subjects [118].

3.3 2-(5-FLUORO-PENTYL)-2-METHYLMALONIC ACID (ML-10) AS A TRACER FOR EARLY STAGE APOPTOSIS

Currently the only PET radiotracer to be evaluated in humans for imaging apoptosis is [^{18}F]ML-10. *In vitro* assays performed using ^3H -labeled ML-10 ([^3H]ML10) have shown that [^3H]ML10 accumulates within cells (60% cytoplasm, 30% nucleus) that have permanently depolarized cell membranes, a signature of early phase apoptosis [119, 120]. Moreover, a positive correlation between [^3H]ML-10 accumulation and validated markers of apoptosis including:

caspase-3 activity, mitochondrial membrane depolarization, and phosphatidylserine externalization was observed using Jurkat cells (human adult leukemia T-lymphocyte cells) incubated with anti-Fas antibody [97, 119]. Moreover, simultaneous incubation of Jurkat cells with anti-Fas antibody and Z-VAD-FMK (Z-Val-Ala-Asp-fluoromethyl ketone), a pan-caspase inhibitor, exhibited low, near control levels of [³H]ML-10 accumulation showing that [³H]ML-10 accumulation could be significantly reduced via inhibition of caspase activation [119].

[³H]ML-10 accumulation has been shown to occur prior to loss of plasma membrane integrity [119]. Moreover, subjection of untreated Jurkat T-cells to three cycles of freeze-thaw, which disrupts plasma membrane integrity, did not result in [³H]ML-10 accumulation above normal control [119], suggesting that [³H]ML-10 may be able to distinguish cells undergoing apoptosis from necrotic and non-viable cells. This hypothesis is further supported by fluorescence microscopy imaging of HeLa cells (human cervix carcinoma) and CT26 cells (murine colon carcinoma) treated with cisplatin and taxotere, respectively [119]. In both cases increased dansyl-ML-10 accumulation was observed after treatment; however, propidium iodide positive cells (indicating non-viable cells) did not show fluorescence [119]. It should be noted that there is not uniform agreement as to the degree that labeled ML-10 can indicate cells proceeding through apoptosis; though some of this disagreement may be a result of differences in *in vitro* assays and pre-clinical imaging protocols [119, 121-128]

In healthy humans, [¹⁸F]ML-10 exhibits a rapid clearance from blood and normal tissue, with low tracer metabolism and no defluorination [129]. Specifically, an analysis of plasma samples from 8 human subjects found a 97.5% ± 0.4% unchanged [¹⁸F]ML-10 fraction 150 min

post-injection [129]. In the same biodistribution study, selective accumulation of [^{18}F]ML-10 was observed on PET in the testes of male humans and mice [129], a known site of apoptosis as a result of processes related to spermatogenesis [130]. Further investigation of this phenomenon using fluorescent microscopy imaging revealed that cells exhibiting dansyl-ML-10 fluorescence in the testicular tissue of male mice were positive for characteristic apoptotic DNA fragmentation assessed via terminal deoxynucleotidyl transferase (TdT) dUTP nick-end labeling (TUNEL) staining [129].

3.3.1 Therapy Response Assessment using [^{18}F]ML-10

While PET imaging of glucose metabolism in both brain metastasis and high grade primary brain tumors, including GBM, using [^{18}F]FDG has exhibited some success in diagnostic imaging, false-positive uptake caused by inflammation at the tumor site as well as overall high background uptake in uninvolved brain tissue limits the use of [^{18}F]FDG PET for early therapy response assessment. Moreover, in the case of GBM conventional approaches to radiologic response assessment are particularly inadequate for *early* therapy response assessment as they rely on slowly changing measures of therapeutic effect, i.e., changes in tumor size and degree of contrast enhancement on contrast enhanced MRI.

As a result, in human PET imaging of using [^{18}F]ML-10 has primarily focused on therapy response assessment of brain metastasis and GBM brain tumors. Allen et al [91] published the first phase 1 trial investigating the feasibility of [^{18}F]ML-10 PET for early therapy response assessment of brain metastasis [91]. A total of 10 subjects with newly diagnosed brain metastases schedule to

receive whole brain radiation therapy (WBRT; total dose of 30 Gy in 2 Gy fractions over 2-weeks) were prospectively enrolled in this study [91]. Additionally, all were required 1) to have at least one brain metastasis ≥ 1.5 cm in diameter, 2) no previous history of brain irradiation, and 3) have their primary tumors under control [91]. Each subject received 2 [^{18}F]ML-10 scans; one prior to therapy (baseline) and a second, therapy response scan, after administration of WBRT to a total dose of 27-30 Gy [91]. Each PET scanning session consisted of three 16-20 min acquisitions, the first session initiating 20 min after intravenous injection of [^{18}F]ML-10 (maximum dose 13.5 mCi) [91]. Response to therapy was assessed via evaluation of tumor size change on contrast enhanced MRI or CT obtained at baseline and at 6-8 weeks post-therapy completion using WHO-based [83] and volumetric based response criteria [91].

In this study, quantification consisted of measures of average overall radiotracer accumulation as well as a voxelwise change analysis [91]. Specifically, all PET voxels were converted to standardized uptake values (SUVs) and normalized to blood pool uptake [91]. Tumor-to-background (contra-lateral healthy brain tissue) ratios were evaluated for each PET acquisition (total 3 per scanning time-point) and averaged across scanning time-points and subjects [91]. Results of this analysis revealed an overall increasing trend in average tumor-to-background ratios as a function of time post-tracer injection, consistent with [^{18}F]ML-10 accumulation in the target tumor with simultaneous clearance in normal brain tissue [91]. Voxelwise quantification was based on approaches developed for quantification of MRI based parametric maps [131-133], and consisted of calculating percent change in normalized uptake between corresponding baseline and therapy response time points for each voxel [91]. Voxels were then categorized as having increased, decreased or not changed in normalized uptake based on a threshold [91]. Results

revealed a strong correlation between the percentage of voxels that increased between PET imaging time-points with percent reduction in tumor size using either the WHO ($R = .92$) or the volumetric based ($R = .91$) methods [91].

The first report using [^{18}F]ML-10 for imaging response to therapy of primary brain tumors was published by Oborski et al [134]. In this case report, a single subject with newly diagnosed GBM received [^{18}F]ML-10 imaging at baseline and after 3-weeks of concomitant radiation therapy (2 Gy fractions daily) and temozolomide (75 mg/m² daily) [134]. In order to facilitate voxelwise comparison, all PET images were normalized to the maximum voxel value within a defined region of the superior sagittal sinus. Baseline PET imaging showed therapy naive uptake localized at the site of the GBM on contrast enhanced MRI [134]. Moreover, TUNEL staining performed on biopsied tumor tissue obtained via fine-needle MRI guided stereotactic biopsy confirmed the presence of cells undergoing apoptosis prior to therapy administration [134]. Visual comparison between pre- and post-therapy initiation time-points revealed new regions of [^{18}F]ML-10 uptake at early therapy response assessment that had not previously existed at baseline [134].

Later a second report investigated a correspondence between changes in [^{18}F]ML-10 uptake and progression-free survival (PFS) for 4 GBM subjects [135]. Following a similar imaging schedule as that of Allen et al. [91], study subjects were scanned at baseline and at 2-3 weeks of post-therapy institution [135]. Each scanning session lasted for 30 min (5 min/frame) initiating 120 min after injection of 10 mCi of [^{18}F]ML-10. Each set of dynamic PET frames was averaged to form a single frame static image, which could be quantified using SUVs [135]. Findings were interpreted on a case-by-case basis for each subject, with each subject's time-to-radiologic

progression serving as the clinical end-point [135]. Overall, this limited study did not clearly demonstrate an ability to predict time-to-radiologic progression based on maximum SUV evaluated between 120 min-150 min post-injection [135].

The apparent incongruity in the ability to predict therapeutic response of brain metastasis [91] versus GBM [134-136] using [^{18}F]ML-10 PET may be due to the different patho-physiologies of brain metastasis versus GBM. For example, brain metastases generally form in the vasculature of the brain, and thus the blood-brain-barrier (BBB) does not provide as much of an impediment to radiotracer delivery to the target tumor as it does for primary brain tumors. Unfortunately, limited published data is available regarding the clearance of [^{18}F]ML-10 in normal human brain tissue. However preclinical studies using a mouse ischemic cerebral stroke model, induced by surgical occlusion of the middle cerebral artery (MCA), have observed areas of dansyl-ML-10 accumulation that were simultaneously negative for Evans blue autofluorescence in the transition zones between healthy and infarct tissues on fluorescence microscopy [124]. This observation is consistent with the hypothesis that [^{18}F]ML-10 can reach cells undergoing apoptosis in normal brain tissue through an intact BBB; however, further investigation is required to confirm this hypothesis in humans.

4.0 STUDY SUBJECTS AND PET IMAGING PROTOCOL

Section 4.1 presents the recruitment and follow-up information for all study subjects. Section 4.2 presents the study design and imaging protocol for study subjects. The imaging study was designed such that each subject received a total of 3 [¹⁸F]ML-10 PET scans, 1 pre-therapy scan and 2 post-therapy administration scans.

4.1 STUDY SUBJECTS

Table 4-1 contains the full-list of subjects that were enrolled in the imaging study as well as subject demographics, and a record of which scanning sessions were completed by the enrolled subject. This research study was performed under the U.S. Food and Drug Administration Investigational New Drug program (Application #: 106662; Sponsor Investigator: James M. Mountz M.D., Ph.D.) with University of Pittsburgh Institutional Review Board (IRB) approval. The associated study subject cohort was accrued and imaged under a National Institutes of Health (NIH) grant awarded to Dr. James M. Mountz (Grant #: U01 CA140230) following a University of Pittsburgh IRB approved protocol. Written consent forms were signed by all study participants. The radiochemical synthesis process of [¹⁸F]ML-10 from precursor is described in Oborski et al [135].

A total of 14 subjects (9 male; 5 female) with histologically confirmed high grade (WHO grade 3 or grade 4) astrocytoma were enrolled in this study. Of these subjects 1 did not report for imaging after enrollment. Of the 13 subjects that received a baseline scan, 11 subjects received an ETA PET scan, while 9 subjects received both ETA and FUA PET scans.

Table 4-1. Study Enrollment Table.

Subject ID	Gender (M/F)	*Age (Years)	WHO Grade	Subject History	BL Scan Completed	ETA Scan Completed	FUA Scan Completed
ML-10 #1	F	64	Grade 4	newly diagnosed	Yes	No	No
ML-10 #2	M	72	Grade 4	newly diagnosed	¥Yes	Yes	No
ML-10 #3	M	63	Grade 4	newly diagnosed	No	No	No
ML-10 #4	M	54	Grade 4	newly diagnosed	Yes	Yes	Yes
ML-10 #5	F	58	Grade 4	newly diagnosed	Yes	Yes	Yes
ML-10 #6	F	57	Grade 4	recurrent	Yes	Yes	Yes
ML-10 #7	M	60	Grade 4	newly diagnosed	Yes	Yes	Yes
ML-10 #8	F	34	Grade 3	recurrent	Yes	Yes	▼Yes
ML-10 #9	M	60	Grade 4	newly diagnosed	Yes	Yes	Yes
ML-10 #10	M	57	Grade 4	newly diagnosed	Yes	‡Yes	Yes
ML-10 #11	M	49	Grade 4	recurrent	Yes	Yes	Yes
ML-10 #12	F	33	Grade 3	recurrent	Yes	No	No
ML-10 #13	M	72	Grade 4	recurrent	^a Yes	Yes	No
ML-10 #14	M	66	Grade 4	newly diagnosed	Yes	Yes	Yes

* Subject age refers to their age at time of enrollment into study.
 ¥ Subject missing first 67 sec dynamic data.
 ▼ Subject's second acquisition acquired on HR+ due to mMR scanner failure; second scan started 34 min and 21 sec late.
 ‡ Subject's second acquisition started 54 min and 30 sec late.
^a Subject's second acquisition started 68 sec late.

Table 4-2 contains therapy administered at time of enrollment, progression-free survival (PFS; assessed on subject contrast enhanced MRI scans) in months and overall survival (OS) data (in months) for all 13 subjects that received BL PET imaging. 8 subjects received standard of care for newly diagnosed GBM, which consisted of fractionated external beam radiation therapy (RT) to a total dose of 60Gy, in daily 2Gy fractions, with concomitant temozolomide (TMZ) at a dose of 75mg/kg/day (5 days/week for 6-weeks followed by a 4-week break), followed by adjuvant TMZ at 150-200mg/m² per day on days 1-5 of 28-day cycles (starting at week 10). Therapies for the remaining 3 recurrent GBM and 2 recurrent grade 3 astrocytoma subjects varied between subjects. For example, ML-10 # 13 received the same TMZ regimen as the 8 newly diagnosed GBM subjects, but did not receive RT. In the specific case of ML-10 #12, they received craniotomy surgery with placement of Gliadel wafer after their first [¹⁸F]ML-10 PET scan, which resulted in their removal from our study.

Table 4-2. Subject Treatment and Outcome.

Subject ID	*Therapy	†PFS (months)	‡OS (months)
ML-10 #1	RT+TMZ	^Δ N/F	N/F
ML-10 #2	RT+TMZ	1	2
ML-10 #4	RT+TMZ	4	5
ML-10 #5	RT+TMZ	15	25
ML-10 #6	ABT-888/TMZ	11	22
ML-10 #7	RT+TMZ	11	26
ML-10 #8	ANG1005	7	22
ML-10 #9	RT+TMZ	25	35
ML-10 #10	RT+TMZ	18	19
ML-10 #11	ANG1005	<1	14
ML-10 #12	Craniotomy Surgery with placement of Gliadel wafer	N/F	N/F
ML-10 #13	TMZ	2	13
ML-10 #14	RT+TMZ	3	9

* Initial therapy regimen prescribes prior to acquisition of BL PET scan.
† PFS = Progression-free survival (in months from therapy initiation). PFS of more than 15 days in a month equals 1 month.
‡ OS = Overall survival (in months from therapy initiation). Survival of more than 15 days in a month equals 1 month.
^Δ N/F = No follow-up available.

4.2 STUDY IMAGING PROTOCOL

The [¹⁸F]ML-10 imaging study was designed such that subjects would receive PET and MRI scans at three time-points: baseline (BL, prior to therapy initiation), early therapy assessment (ETA, approximately 14 ± 3 days after therapy initiation), and follow-up assessment (FUA,

approximately 72 ± 3 days after therapy initiation). As illustrated in figure 4-1, each PET imaging time-point consisted of two acquisitions (but with a single tracer injection): (i) a 0-45 min scan initiating with intravenous injection of 10 mCi of [^{18}F]ML-10, (ii) followed by a 30 min scan starting 120 min post-injection. Dynamic PET scans were performed on either a Siemens/CTI ECAT HR+ PET scanner (Siemens ECAT HR+; CTI/Siemens, Knoxville, TN), or a Siemens Biograph mMR combined dual modality PET/3T MRI scanner (Siemens, Munich, Germany).

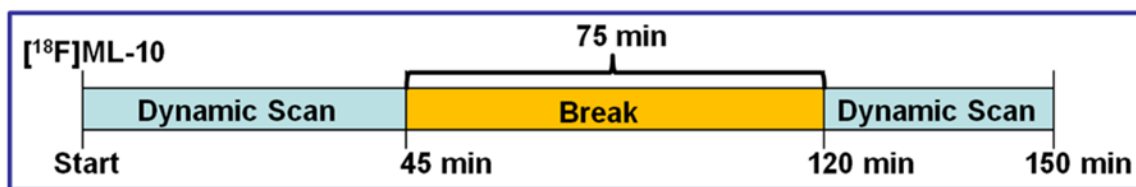


Figure 4-1. [^{18}F]ML-10 PET Acquisition Protocol After Initial Injection of [^{18}F]ML-10.

Table 4-3 contains the number of days between therapy initiation and each subject's BL, ETA, and FUA imaging time-points. For each subject, day 0 corresponds to the day they started therapy. A '-' sign indicates the PET scan was acquired prior to the subject's therapy initiation date, while a '+' sign indicates the PET scan was acquired post-therapy initiation. Two subjects, ML-10 #13 and ML-10 #14 received their first [^{18}F]ML-10 PET scans after already receiving therapy. These 2 subjects are listed in table 4-3 as having BL scans acquired +5 and +6 days prior to therapy, respectively; however, neither scan is a true baseline scan. ML-10 #12 received their BL PET scan 41 days prior to therapy start. However, after receiving their BL PET scan the subject underwent craniotomy surgery for placement of Gliadel wafers and was removed from the [^{18}F]ML-10 PET study as a result.

Table 4-3. Subject Imaging Schedule.

Subject ID	BL PET (days prior to therapy start)	ETA PET (days post therapy start)	FUA PET (days post therapy start)
ML-10 #1	0	†N/A	N/A
ML-10 #2	^a -21	+15	N/A
ML-10 #4	-5	+16	+67
ML-10 #5	0	+9	+72
ML-10 #6	-14	+14	+77
ML-10 #7	-5	+23	+79
ML-10 #8	-2	+18	+41
ML-10 #9	-5	+16	+72
ML-10 #10	-27	+11	+68
ML-10 #11	-10	+24	+55
ML-10 #12	[*] -41	N/A	N/A
ML-10 #13	^b +5	+21	N/A
ML-10 #14	+6	+12	+68

† N/A = Not acquired.
^a Therapy administered on day 0; '-' indicates PET scan acquired prior to therapy initiation date.
^{*} Subject did not receive any [¹⁸F]ML-10 PET scans post-therapy start.
^b Therapy administered on day 0; '+' indicates PET scan acquired after therapy initiation date.

Table 4-4 contains a record of which scanner was used for each subject for each time-point. In general, each subject received their PET scans on the same scanner for all time-points. The only exception is ML-10 #8, who received their BL scan on the HR+, their ETA scan on the mMR, and acquisition 1 (i.e. the 45 min scan) of their FUA scan on the mMR and acquisition 2 (i.e. the 30 min scan, following the 75min break) of the FUA scan on the HR+. ML-10 #8's acquisition 1 and acquisition 2 were performed on two different scanners because the mMR malfunctioned during the FUA time-point after completion of acquisition 1. Due to the inconsistency in scanning, ML-10 #8 was ultimately not considered for PK analysis in Chapter 5.

All PET data were reconstructed using filtered back-projection (Fourier rebinning/2D backprojection, 3 mm Hann filter, zoom = 2.5) with the following framing: 0-45 min acquisition: 10 sec/frame x 12 frames, 15 sec/frame x 8 frames, 30 sec/frame x 8 frames, 60 sec/frame x 12 frames, 300 sec/frame x 5 frames; 120-150 min acquisition: 300 sec/frame x 6 frames. All images were corrected for photon attenuation, scatter, and random coincidences. Moreover, all acquisitions were decay corrected to the time of [¹⁸F]ML-10 injection, that is the 120-150 min acquisition was decay corrected back to the start time of the 0-45 min acquisition. Images acquired on the Siemens/CTI ECAT HR+ PET scanner were reconstructed using manufacturer's software into a final matrix size of 128x128x63. Images acquired on the Siemens Biograph mMR were reconstructed using the manufacturer provided e7Tools software (Siemens Molecular Imaging, Knoxville, USA) into a final matrix size of 128x128x127.

Table 4-4. PET Scanner Used for Data Acquisition.

Subject ID	BL PET Scanner	ETA PET Scanner	FUA PET Scanner
ML-10 #1	HR+	[†] N/A	N/A
ML-10 #2	[¥] HR+	HR+	N/A
ML-10 #4	HR+	HR+	HR+
ML-10 #5	HR+	HR+	HR+
ML-10 #6	HR+	HR+	HR+
ML-10 #7	HR+	HR+	HR+
ML-10 #8	HR+	mMR	mMR/ [∇] HR+
ML-10 #9	mMR	mMR	mMR
ML-10 #10	mMR	[‡] mMR	mMR
ML-10 #11	mMR	mMR	mMR
ML-10 #12	mMR	N/A	N/A
ML-10 #13	^a mMR	mMR	N/A
ML-10 #14	mMR	mMR	mMR

[†] N/A = Not acquired.
[¥] Subject missing first 67 sec of dynamic data.
[∇] Subject's second acquisition acquired on HR+ due to mMR. scanner failure; second scan started 34 min and 21 sec late.
[‡] Subject's second acquisition started 54 min and 30 sec late.
^a Subject's second acquisition started 68 sec late.

While all PET acquisitions were corrected for attenuation, the method of attenuation correction utilized depended on which scanner was used to acquire the PET data (see Section 4.2.1 below). All PET acquisitions were inspected for inter-frame motion, which, if necessary, was corrected for on a frame-by-frame basis. The 120-150 min PET scan was co-registered to the (0-45 min scan) prior to image quantification.

4.2.1 Attenuation Correction Methods Applied to Study PET Images

Table 4-5 contains a catalog of the attenuation correction methods used for reconstructing study PET images. For PET scans acquired on the Siemens/CTI ECAT HR+ PET scanner photon attenuation correction was performed using a 10 min transmission scan ($^{68}\text{Ge}/^{68}\text{Ga}$ rods) prior to tracer injection. Images were then processed via the manufacturer's software. With the exception of subject ML-10 #13, PET acquisitions acquired using the Siemens Biograph mMR were corrected for attenuation using the method of Izquierdo-Garcia et al [56] (referred to as the Pseudo CT attenuation correction method in table 4-5). In this method the attenuation μ -map is generated from the subject's T₁-weighted MPRAGE MRI. The e7tools reconstruction software toolbox provided by Siemens was then used to reconstruct the attenuation corrected PET image.

For the case of ML-10 #13 at BL, a scanner error caused the loss of the PET sinogram data needed to reconstruct the attenuation corrected PET image using the e7tools software. As a result, attenuation correction of both the BL and ETA PET images was performed using the attenuation substitution method (previously described in *Section 2.3.1.1* developed at the University of Pittsburgh Department of Radiology PET Facility [137]). The application of the attenuation substitution method to correct the BL scan was verified using the corresponding ETA time-point, for which both the e7tools and the attenuation substitution reconstructions were available.

Table 4-5. Attenuation Correction Method used for PET Data.

Subject ID	BL PET Scanner	ETA PET Scanner	FUA PET Scanner
ML-10 #1	Transmission Scan	N/A	N/A
ML-10 #2	Transmission Scan	Transmission Scan	N/A
ML-10 #4	Transmission Scan	Transmission Scan	Transmission Scan
ML-10 #5	Transmission Scan	Transmission Scan	Transmission Scan
ML-10 #6	Transmission Scan	Transmission Scan	Transmission Scan
ML-10 #7	Transmission Scan	Transmission Scan	Transmission Scan
ML-10 #8	Transmission Scan	Pseudo CT	[⊖] Pseudo CT (acq. 1) [‡] Transmission Scan (acq. 2)
ML-10 #9	Pseudo CT	Pseudo CT	Pseudo CT
ML-10 #10	Pseudo CT	Pseudo CT	Pseudo CT
ML-10 #11	Pseudo CT	Pseudo CT	Pseudo CT
ML-10 #12	Pseudo CT	N/A	N/A
ML-10 #13[£]	Attenuation Substitution	Attenuation Substitution	N/A
ML-10 #14	Pseudo CT	Pseudo CT	Pseudo CT

* Subject age refers to their age at time of enrollment into study.
† N/A = Not acquired.
⊖ = ML-10 #8 FUA 0-45 min acquisition was acquired on the Siemens Biograph mMR.
‡ = ML-10 #8 FUA 120-150 min acquisition was acquired on the Siemens HR+.
£ = ML-10 #13 ETA binned sinogram data was lost due to mMR technical error preventing use of the Pseudo CT method; for consistency the attenuation substitution method was used for AC of both the BL and ETA PET scanning sessions.

5.0 ANALYSIS OF [¹⁸F]ML-10 TISSUE UPTAKE PROPERTIES IN GBM AND NORMAL BRAIN TISSUE

This chapter presents an analysis of [¹⁸F]ML-10 pharmacokinetics (PK) in GBM and normal brain tissue on a whole tumor and voxelwise level. As the PK of [¹⁸F]ML-10 have not been previously reported in either pre-clinical or clinical studies, the methodology for doing so needs to be developed from the ground-up. This process includes evaluating candidate models to describe both the radiotracer concentration in both the blood and tumor tissue.

[¹⁸F]ML-10 concentration in the blood is measured on each dynamic PET scan from the internal carotid arteries of the brain. *Section 5.1* evaluates a set of 8 candidate models for their ability to parsimoniously describe the image-based blood concentration profile. The goal of this analysis is to find a subset of the 8 candidate models that can be used as image-based input function (IBIF) models for simultaneous IBIF/tumor impulse response function (IRF) modeling (similar to that of Wong et al [138]).

Section 5.2 contains the PK analysis results for [¹⁸F]ML-10 in GBM. Model selection criteria and model parameter estimability considerations are used to evaluate candidate tumor IRF models. Once appropriate IRF models are selected, macroparameters that quantifying radiotracer

uptake are estimated and studied using compartmental modeling. Spectral analysis (SA) is also performed to provide additional support for IRF model selection as well obtain additional macroparameter estimates. The utility of these macroparameters to predict treatment response is investigated in a subset of GBM subjects. Finally, heterogeneity in GBM response to treatment is evaluated through voxelwise analysis of [^{18}F]ML-10 uptake measures. Diffusion MRI imaging was available at the ETA and FUA time-points for 2 subjects, allowing for a preliminary investigation comparing [^{18}F]ML-10 uptake at ETA with later change in tumor density.

5.1 INPUT FUNCTION MODELING

5.1.1 Background: Image Based Input Functions

In order to apply pharmacokinetic modeling to quantify [^{18}F]ML-10 uptake in high grade brain tumors, measurements of the time-courses of tracer concentration in the blood and in the tumor tissue are required. In pharmacokinetic modeling, the concentration of [^{18}F]ML-10 in the blood acts as the input function that perturbs the underlying tumor (treated as a linear system) to produce the measured tumor tissue uptake profile (i.e. the tumor system response function). The theory of pharmacokinetic modeling as well as its application to analyzing [^{18}F]ML-10 uptake in high grade astrocytomas are described below in *Section 5.2*. The focus of this current section is on measuring and modeling the [^{18}F]ML-10 concentration time-course in the blood (i.e. modeling the input function to the tumor system).

In PET, there are three basic approaches to obtaining the input blood tracer concentration. One approach is to insert a catheter into the forearm and draw blood samples from either of the ulna or radial arteries and measure the concentration of radioactivity in the blood directly. In the case of a well-studied tracer, it is sometimes possible to derive a population-based model for tracer concentration in the blood, thereby obviating the need for laborious arterial blood sampling; though a few blood samples are often obtained in order to normalize the population-based curve to the particular study subject [139-142]. The third approach is to measure the activity in the blood directly from the dynamic PET image obtaining what is referred to as an image-based input function (IBIF). Like population-based methods, IBIFs have the potential advantage of requiring no arterial blood sampling.

Although it would be desirable, no arterial blood sampling was performed as part of this study based on the requirements of the referring physicians. Moreover, as this is the first study to evaluate the pharmacokinetics of [^{18}F]ML-10 in humans, there are no established population-based input function models of [^{18}F]ML-10 time-course in the blood. These considerations limit the analysis of [^{18}F]ML-10 to IBIFs. As a result, the remaining background discussion will focus on approaches to modeling IBIFs.

Several studies have demonstrated the capability of input function measurement noise to affect estimates of pharmacokinetic rate constants [143-146]. Moreover, for use in both regional and voxelwise pharmacokinetic analysis in this dissertation values for the IBIF must be available at arbitrary times from injection, which includes during the 75 min break between scanning

sessions. Taken together, these factors motivate the need for fitting a smooth model to the measured IBIF data.

Currently there no uniformly agreed upon methods for modeling an IBIF [71, 147], and often the approaches used are tracer specific and dependent on the IBIF source (e.g. internal carotid arteries of the brain, descending aorta, etc...) [71, 148-150]. However, a popular IBIF model used commonly in exploratory situations is the input function model proposed by Feng et al [151]. The general form of their input function model is given in (*Eqn. 5.1.1*), where θ_0 , θ_1 , and θ_2 denote constant amplitudes, $u(t)$ represents the unit-step function, and the exponential rates: p_0 , p_1 , and p_2 are all non-negative.

$$f(t) = [\theta_0 t - (\theta_1 + \theta_2)]e^{-p_0 t} u(t) + \theta_2 e^{-p_2 t} u(t) + \theta_3 e^{-p_3 t} u(t) \quad (\text{Eqn. 5.1.1})$$

From the stand-point of pharmacokinetic modeling, *Eqn. 5.1.1* has several advantageous properties. For example, because (*Eqn. 5.1.1*) is an analytic function composed of a sum of first and second-order causal exponentials, the gradient with respect to the model parameters of *Eqn. %%* is relatively easy to obtain. This property is greatly beneficial from the stand point of model fitting/optimization as well as obtaining an estimate for the covariance matrix of the model parameters, and linear system modeling. Furthermore, due to the simplicity of (*Eqn. 5.1.1*), additional first order or second order causal exponentials can be added to account for long acquisition times or the presence of a re-circulation peak, respectively. Finally, like many IBIF models the Feng model is physiologically reasonable; the model is zero at time, $t = 0$, and naturally

produces a peak concentration followed by an exponentially decreasing tail. Therefore, due to its simplicity and stated advantages, the model in (Eqn. 5.1.1) will form the basis from which all other candidate IBIF models are derived.

A practical consideration when fitting any model to an IBIF is that the measured IBIF samples are really the time-averages of the true blood activity concentration over corresponding frame dwell times. Therefore, when fitting any model to an IBIF, it is actually the time-averaged version that must be fit to the data. This approach is described in, for example, Simoncic et al [152] at a high level.

5.1.2 Background: Evaluation of Model Parameter Uncertainty

Random fluctuations between different realizations of time-course data due to stochastic noise and measurement errors means that the same estimation procedure applied to two different realizations will produce different parameter estimates for the same model. Ideally these estimates will not deviate significantly from one realization to the next and will on average obtain their true values. For the case of a deterministic signal embedded in noise, a model parameter is said to be ill-determined if the value of its estimate exhibits large changes in response to ostensibly random fluctuations in the measured data [153]. In practical application, this means that a parameter is ill-determined if it has a large variance (or standard deviation) relative to the nominal value of the estimate [153, 154].

When the joint probability distribution, $p(x; \theta)$, of the measured data vector x given the vector of true values of the model parameters θ is exactly known, the distribution can be used to compute the Cramer-Rao lower bound (CRLB) for all possible model parameter estimators. The CRLB provides an important benchmark for evaluating and comparing different estimators for the same model parameters, as the CRLB specifies the minimum possible variance that an unbiased estimator for the model parameters can have given the noise level in the data. For a vector of parameters, the CRLB is equal to the inverse of the Fisher information matrix $I(\theta)$. The Fisher information matrix is defined in (Eqn. 5.1.2), where $\mathcal{E}[\cdot]$ denotes the expected value operation. By definition, an unbiased estimator that achieves the CRLB is termed efficient [155]. Moreover, in some cases an estimator may achieve the CRLB only as the number of data samples N gets large. In this case the estimator is said to be asymptotically efficient [153, 156]. Similarly, an estimator that becomes unbiased for large data records is said to be consistent (or asymptotically unbiased) [153, 156].

$$[I(\theta)]_{ij} = -\mathcal{E} \left[\frac{\partial^2 (\ln\{p(x;\theta)\})}{\partial \theta_i \partial \theta_j} \right] \quad (\text{Eqn. 5.1.2})$$

For the case that the measurement errors follow a Gaussian distribution, the Fisher information matrix takes a particularly simple form given by (Eqn. 5.1.3), where $\Sigma_x(\theta)$ is the covariance matrix of the measured data x (which may depend on the model parameters) and $\mu(t; \theta)$ represents the time-dependent deterministic model being fitted to the data [155].

$$[I(\boldsymbol{\theta})]_{ij} = \left(\frac{\partial \boldsymbol{\mu}(t; \boldsymbol{\theta})}{\partial \theta_i} \right)^T \boldsymbol{\Sigma}_x^{-1}(\boldsymbol{\theta}) \left(\frac{\partial \boldsymbol{\mu}(t; \boldsymbol{\theta})}{\partial \theta_j} \right) + \frac{1}{2} \text{Tr} \left\{ \boldsymbol{\Sigma}_x^{-1}(\boldsymbol{\theta}) \left(\frac{\partial \boldsymbol{\Sigma}(\boldsymbol{\theta})}{\partial \theta_i} \right) \boldsymbol{\Sigma}_x^{-1}(\boldsymbol{\theta}) \left(\frac{\partial \boldsymbol{\Sigma}(\boldsymbol{\theta})}{\partial \theta_j} \right) \right\} \quad (\text{Eqn. 5.1.3})$$

In practice, the general form of $p(x; \boldsymbol{\theta})$ may be known but the true values of the model parameters, $\boldsymbol{\theta}$, are generally unknown and need to be estimated from the measured data. Importantly, different estimators for the same parameter vector will generally produce different sampling distributions [153]. Hence the variance of a parameter estimate depends on the estimation procedure used [153]. However, as stated above, the CRLB specifies the minimum possible variance for an unbiased estimator of a set of model parameters. Therefore, the goal is to find an estimator $\hat{\boldsymbol{\theta}}$ that achieves the CRLB for a given $p(x; \boldsymbol{\theta})$.

In general, determining an efficient estimator (or estimators) for a set of model parameters is a difficult problem. However, defining the likelihood function as $\mathcal{L}(\boldsymbol{\theta}) \triangleq p(x; \boldsymbol{\theta})$, it can be shown that the value of $\boldsymbol{\theta}$ that maximizes the likelihood function for the given data, denoted $\hat{\boldsymbol{\theta}}_{MLE}$, has the properties of being asymptotically unbiased and asymptotically efficient [155, 157]. Therefore, the CRLB can be used as an approximate formula for calculating the covariance matrix, $\boldsymbol{\Sigma}_{\hat{\boldsymbol{\theta}}_{MLE}}$, of the $\hat{\boldsymbol{\theta}}_{MLE}$ estimator (Eqn. 5.1.4).

$$\boldsymbol{\Sigma}_{\hat{\boldsymbol{\theta}}_{MLE}} \approx I(\boldsymbol{\theta})^{-1} \quad (\text{Eqn. 5.1.4})$$

However, since the true values of the model parameters are unknown, only an approximate expression for the covariance matrix in (Eqn. 5.1.4) is calculable and is obtained by substituting

the true value of θ with the most likely value for the model parameters (i.e. by setting θ equal to the MLE estimate $\hat{\theta}_{MLE}$ (Eqn. 5.1.5)). The accuracy of this approximation will depend on the shape of the likelihood function around its maximum (i.e. the quality of the fit); that is, the sharper the peak of the likelihood function is around $\hat{\theta}_{MLE}$ (i.e. the smaller the parameter variance) the better the approximation to the covariance matrix that (Eqn. 5.1.5) will be [153]. For the case of normally distributed errors the approximate formula for $\Sigma_{\hat{\theta}_{MLE}}$ is obtained by substituting $\theta = \hat{\theta}_{MLE}$ into (Eqn. 5.1.3) giving (Eqn. 5.1.6).

$$\Sigma_{\hat{\theta}_{MLE}} \approx [I(\theta)^{-1}]_{\theta = \hat{\theta}_{MLE}} \quad (\text{Eqn. 5.1.5})$$

$$\Sigma_{\hat{\theta}_{MLE}} = \left\{ \left(\frac{\partial \mu(\mathbf{t}; \theta)}{\partial \theta} \right)^T \Sigma_x^{-1}(\theta) \left(\frac{\partial \mu(\mathbf{t}; \theta)}{\partial \theta} \right) + \frac{1}{2} \text{Tr} \left(\left[\Sigma_x^{-1}(\theta) \left(\frac{\partial \Sigma(\theta)}{\partial \theta} \right) \right]^2 \right) \right\}_{\theta = \hat{\theta}_{MLE}} \quad (\text{Eqn. 5.1.6})$$

where, $x \sim N(\mu(\mathbf{t}; \theta), \Sigma_x(\theta))$

5.1.3 Methods

5.1.3.1 Subjects

Study subject characteristics were detailed in Chapter 4. While a total of 32 [¹⁸F]ML-10 PET scans were acquired, only 29 were analyzed for IBIF modeling. As highlighted in table 4-4, subject ML-10 #2's BL scan was started 67 sec after tracer injection making it impossible to model the initial peak tracer concentration in the blood. Additionally, subject ML-10 #8 received their BL, ETA, and FUA PET scans on different PET scanners depending imaging time-point, making

it difficult to compare fit results across time-points. Due to the above reasons, these PET scans were excluded from IBIF model selection analysis

5.1.3.2 PET Image Processing

All PET acquisitions were inspected for inter-frame motion, which, if necessary, was corrected for on a frame-by-frame basis using the motion correction tool available in PMOD 3.6 (PMOD Technologies LLC; Zürich, Switzerland). Because each PET imaging time-point consisted of two PET acquisitions, between which the subject got off the scanner, the 120-150 min scan was co-registered to the 0-45 min scan. To this end, the entire (motion corrected if necessary) 0-45 min acquisition was summed to produce a single static image. Next each frame of the 120-150 min acquisition was individually co-registered to the summed static image derived from the 0-45 min scan using the normalized mutual information method available in PMOD 3.6. The resulting transformation was then applied to each individual frame of the 120-150 min scan, which was then combined with the 0-45 min acquisition to form a single dynamic acquisition volume.

5.1.3.3 Volume of Interest Definition and Image Based Input Function Measurement

As part of the study design (due to clinical requirements) no arterial blood sampling was performed. Therefore, quantification of [¹⁸F]ML-10 kinetics for the GBM subjects in this study is limited to using image-based input functions (IBIFs), obtained from the internal carotid arteries of the brain.

IBIF volumes of interest (VOI) were defined by first summing together the entire 51 frame PET image to create a single static image. Next a single preliminary VOI was defined around each

carotid separately (i.e. each carotid had its own initial loose VOI) with a margin of normal tissue, but not including tumor activity or activity from neighboring vessels. VOIs consisted of closed contours drawn on a set of transaxial imaging planes. Each preliminary carotid VOI spanned at least 4 consecutive planes. Next a 90% of max pixel threshold was applied to each preliminary carotid VOI. That is, the maximum value of the pixels within the preliminary VOI was determined; the final VOI included those pixels that fell within the preliminary VOI and had a value of 90% or greater of the maximum value. The final carotid VOI was generated by taking the union of the two thresholded carotid VOIs. It is from this final carotid ROI that the IBIF was extracted for each imaging time-point. Figure 5-1 shows an example IBIF VOI.

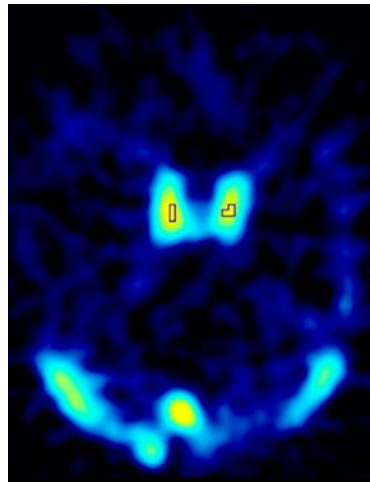


Figure 5-1. Example [¹⁸F]ML-10 PET Image Section Showing IBIF VOI Defined on the Internal Carotid Arteries of the Brain.

Previous studies have shown that [¹⁸F]ML-10 exhibits low tracer metabolism (97.5% ± 0.4% unchanged [¹⁸F]ML-10 fraction 150 min post-injection) with no defluorination in healthy

humans [129]. Therefore, throughout this study no metabolite correction was applied to the IBIF. If it was found that tracer accumulation in the tumor region was touching one of the internal carotid arteries, the carotid touching the tumor activity was excluded from the final IBIF ROI, and thus did not contribute to the measured IBIF.

5.1.3.4 Proposed Input Function Models and Selection Criteria

For use in regional and voxelwise pharmacokinetic analysis, values for the IBIF must be available at arbitrary times from injection, which includes during the 75 min break between scanning sessions. In order to determine an appropriate IBIF model, 2 general input function model forms were evaluated. The two model forms are shown in table 5-1, and were based on a model originally proposed by Feng et al [151]. The principle difference between the two forms is that IBIF Model 2 allows for a second peak in the input function. Both models include a variable number of decaying exponentials.

Table 5-1. Candidate Input Function Model Forms.

IBIF Model	IBIF Model Mathematical Form.
Model 1	$f^{(N)}(t) = \left\{ \left[\theta_0(t - \tau) - \sum_{i=1}^N \theta_i \right] e^{-p_0(t-\tau)} + \sum_{i=1}^N \theta_i e^{-p_i(t-\tau)} \right\} u(t - \tau);$ <p style="text-align: center;">N = 1, 2, 3, 4</p>
Model 2	$g^{(N)}(t) = \{ \alpha_0(t - (\tau + \tau_\alpha)) e^{-\alpha_1(t - (\tau + \tau_\alpha))} \} u(t - (\tau + \tau_\alpha)) + f^{(N)}(t);$ <p style="text-align: center;">N = 1, 2, 3, 4</p>

IBIF Model 1 consists of a second-order pole followed by a variable number of first-order decaying exponentials. For IBIF Model 1 the coefficients $\theta_1 \dots \theta_N$ as well as the washout rates $p_1 \dots p_N$ and the time-delay τ all need to be estimated for each nested model. IBIF Model 2 is essentially IBIF Model 1 ($f^{(N)}(t)$) with an additional second-order pole term that allows for modeling of an additional recirculation peak [23, 158], and requires additional estimation of the parameters α_0, α_1 , and an additional delay term τ_α , which allows independent movement of the additional peak with respect to $f^{(N)}(t)$. Figure 5-2 shows two representative IBIF model forms each composed of $N=2$ decaying exponentials, with IBIF Model 1 shown on the left and IBIF Model 2 shown on the right. Zoomed-in versions of each model are shown in the corresponding insets. Comparison between the two zoomed-in figures highlights corresponding differences in peak shape.

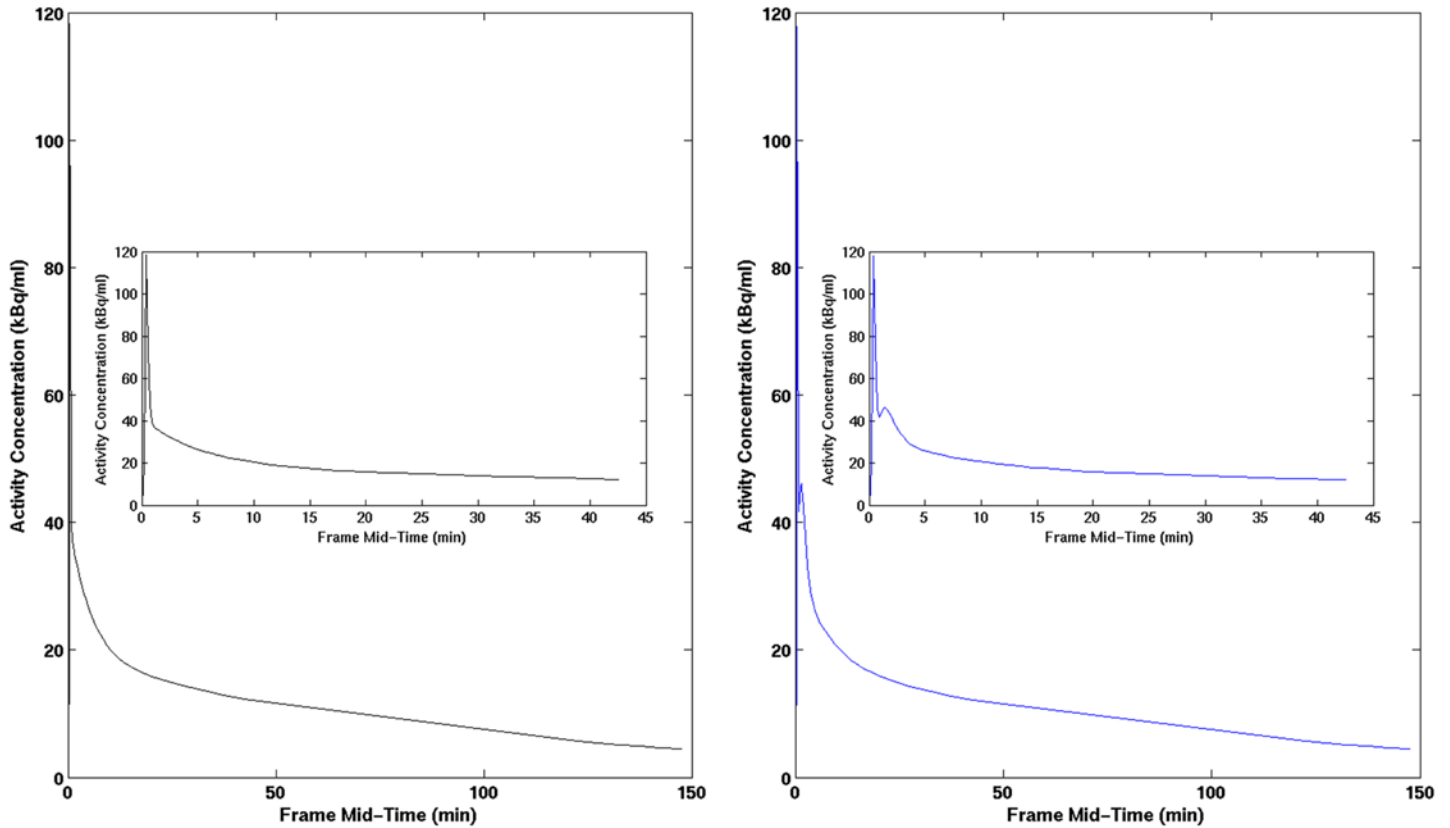


Figure 5-2. Example IBIF model curves with N=2 decaying exponentials. (Left) IBIF Model 1 from 0-150 min with zoomed view of 0-45 min (inset). (Right) shows IBIF Model 2 with corresponding zoomed 0-45 min (inset).

Table 5-2 contains an explicit list of the candidate input function models tested for each subject at each imaging time-point. For the purposes of model selection, as few as 1 and as many as 4 decaying exponentials were tested for each model form, resulting in a total of 8 candidate IBIF models tested per subject per imaging time-point. Despite differences in the number of parameters and the number of second order pole terms, all models in table 5-2 describe a radioactivity concentration profile that is equal to zero prior to tracer injection, and approaches zero as the time following bolus injection of [^{18}F]ML-10 approaches infinity.

Table 5-2. List of Candidate Input Function Models Tested.

IBIF Model	List of Tested Candidate IBIF Models.
Model 1a	$f^{(1)}(t) = \{[\theta_0(t - \tau) - \theta_1]e^{-p_0(t-\tau)} + \theta_1 e^{-p_1(t-\tau)}\}u(t - \tau);$
Model 1b	$f^{(2)}(t) = \left\{ \left[\theta_0(t - \tau) - \sum_{i=1}^2 \theta_i \right] e^{-p_0(t-\tau)} + \sum_{i=1}^2 \theta_i e^{-p_i(t-\tau)} \right\} u(t - \tau);$
Model 1c	$f^{(3)}(t) = \left\{ \left[\theta_0(t - \tau) - \sum_{i=1}^3 \theta_i \right] e^{-p_0(t-\tau)} + \sum_{i=1}^3 \theta_i e^{-p_i(t-\tau)} \right\} u(t - \tau);$
Model 1d	$f^{(4)}(t) = \left\{ \left[\theta_0(t - \tau) - \sum_{i=1}^4 \theta_i \right] e^{-p_0(t-\tau)} + \sum_{i=1}^4 \theta_i e^{-p_i(t-\tau)} \right\} u(t - \tau);$
Model 2a	$g^{(1)}(t) = \{ \alpha_0(t - (\tau + \tau_\alpha)) e^{-\alpha_1(t - (\tau + \tau_\alpha))} \} u(t - (\tau + \tau_\alpha)) + f^{(1)}(t);$
Model 2b	$g^{(2)}(t) = \{ \alpha_0(t - (\tau + \tau_\alpha)) e^{-\alpha_1(t - (\tau + \tau_\alpha))} \} u(t - (\tau + \tau_\alpha)) + f^{(2)}(t);$
Model 2c	$g^{(3)}(t) = \{ \alpha_0(t - (\tau + \tau_\alpha)) e^{-\alpha_1(t - (\tau + \tau_\alpha))} \} u(t - (\tau + \tau_\alpha)) + f^{(3)}(t);$
Model 2d	$g^{(4)}(t) = \{ \alpha_0(t - (\tau + \tau_\alpha)) e^{-\alpha_1(t - (\tau + \tau_\alpha))} \} u(t - (\tau + \tau_\alpha)) + f^{(4)}(t);$

The overall forms of the models in table 5-2 were inspired by previously proposed input function model forms from the literature [151, 158]. Traditionally the Feng model [151], which refers to IBIF Model 1b, has been a common model form adopted by researchers interested in fitting as well as simulating [151] image-based input functions, though several other model forms have been proposed [71, 147, 159]. An advantage that the models in table 5-2 have over more complicated IBIF models, for example [148, 160], is that the models in table 5-2 are composed of sums of first and second-order poles, which have simple and well known Laplace transforms, and thus readily facilitate analytic expressions for compartmental modeling of the tracer in tissue.

Moreover, since the entire IBIF is modeled, not just the portion of the IBIF occurring after the peak blood concentration [140, 160], a simultaneous fitting of the IBIF model and the tissue response can be performed allowing for an investigation of the impact of input function noise on compartmental model parameter estimates.

5.1.3.5 Input Function Model Fitting

Input function model fitting was carried out in two-stages using the optimization toolbox available in MATLAB (R2014a, The MathWorks, Natick, MA., USA). For each stage, a time-averaged version of the input function model under investigation was fitted. Stage one focused on generating a good initial guess for the model parameters, which was then used as the initial starting point for maximization of a Gaussian log-likelihood function. The model parameter estimates obtained by maximizing this log-likelihood were used as the final model parameter estimates for model selection.

Obtaining the Gaussian Likelihood Function to be Maximized

The multivariate Gaussian likelihood function used for IBIF model fitting is given by (Eqn. 5.1.7), where y denotes the (Nx1) column vector of measured samples of the image-based input function, \bar{t} denotes the corresponding (Nx1) column vector of frame mid-times, and $M(\theta; \bar{t})$ represents the candidate input function model being tested with model parameter vector θ .

$$\mathcal{L}(y; \theta) = (2\pi)^{-\frac{N}{2}} |\Sigma|^{-\frac{1}{2}} e^{-\frac{1}{2} [y - M(\theta; \bar{t})]^T \Sigma^{-1} [y - M(\theta; \bar{t})]} \quad (\text{Eqn. 5.1.7})$$

Use of this particular likelihood form assumes the measurement errors are distributed following a multivariate Gaussian distribution with zero-mean. This is a common assumption in PET quantitative methodology when image data have been re-constructed using filtered-backprojection and is based on the Central Limit Theorem, which states that the distribution of a sum of random variables converges to a Gaussian distribution with probability equal to one, independent of the distributions of the individual random variables being summed [73, 74]. However, in order to make the maximization of (Eqn.5.1.7.) more tractable, additional simplifying assumptions were made regarding the measurement noise characteristics. Specifically, it was assumed that the measurement errors were independently distributed and that their individual variances were proportional to the measured blood activity.

Under the simplifying assumptions of: (i) independent errors and (ii) individual variances being proportional to the corresponding measured blood activity, the covariance matrix takes the form of (Eqn. 5.1.8); where $\sigma_{Cor,i}^2$ is as defined by equation (Eqn. 5.1.9), and λ denotes the ^{18}F decay-rate.

$$\Sigma_{ij} = \begin{cases} \sigma_{Cor,i}^2 & \mathbf{i} = \mathbf{j}; \\ \mathbf{0} & \mathbf{i} \neq \mathbf{j}; \end{cases} \quad (\text{Eqn. 5.1.8})$$

$$\sigma_{Cor,i}^2 = \alpha^2 v_i^2; \quad \text{where, } v_i^2 \triangleq \frac{[y_i * e^{\lambda t_i}]}{\Delta_i T} \quad (\text{Eqn. 5.1.9})$$

Inserting (Eqn. 5.1.8) into (Eqn. 5.1.7) gives (Eqn. 5.1.10), which can be further simplified using (Eqn. 5.1.9) yielding (Eqn. 5.1.11), where $v_i^2 \triangleq \frac{[y_i * e^{\lambda \bar{t}_i}]}{\Delta_i T}$ and α is a positive constant (see Chapter 2.4.1).

$$\mathcal{L}(\mathbf{y}; \boldsymbol{\theta}) = \frac{1}{\sqrt{(2\pi)^N \prod_{i=1}^N \sigma_{Cor,i}^2}} \mathbf{e}^{-\frac{1}{2} \sum_{i=1}^N \left[\frac{y_i - M(\boldsymbol{\theta}; \bar{t}_i)}{\sigma_{Cor,i}} \right]^2} \quad (\text{Eqn. 5.1.10})$$

$$\mathcal{L}(\mathbf{y}; \boldsymbol{\theta}) = \frac{1}{\sqrt{(2\pi)^N \prod_{i=1}^N (\alpha v_i)^2}} \mathbf{e}^{-\frac{1}{2} \sum_{i=1}^N \left[\frac{y_i - M(\boldsymbol{\theta}; \bar{t}_i)}{\alpha v_i} \right]^2} \quad (\text{Eqn. 5.1.11})$$

Finally, taking the natural-log of both sides of (Eqn. 5.1.11) and collecting terms gives the log-likelihood function to be maximized, (Eqn. 5.1.12).

$$\ln(\mathcal{L}(\mathbf{y}; \boldsymbol{\theta})) = -\frac{N}{2} \ln(2\pi) - \sum_{i=1}^N \ln(v_i^2) - N \ln(\alpha^2) - \frac{1}{2\alpha^2} \sum_{i=1}^N \left[\frac{y_i - M(\boldsymbol{\theta}; \bar{t}_i)}{v_i} \right]^2 \quad (\text{Eqn. 5.1.12})$$

Note that maximizing (Eqn. 5.1.12) requires estimation of the proportionality constant α , which increases the total number of model parameters by 1 for AIC, and AIC_c calculations. Moreover, estimates of α are required to be positive as the product ($\alpha \sigma_i$) is a standard deviation.

A practical consideration of fitting any of the candidate models in table 5-2 is that the measured IBIF samples are really the time-averages of the true blood activity concentration over corresponding frame dwell times. Therefore, the time-averaged versions of each model in table 5-

2 are actually used during IBIF model selection [152]. The time-averaged versions of input models 1 and 2 and the derivations of these equations are given in *Appendix A.1*.

IBIF Model Parameter Estimation Strategy: IBIF Model 1

Figure 5-3 shows a high-level workflow illustrating the multi-step optimization method used for fitting candidate IBIF models: IBIF Model 1a, IBIF Model 1b, IBIF Model 1c, and IBIF Model 1d. Step 1 was composed of a multi-phase optimization procedure that began with constrained, unweighted (i.e. $\alpha = 1$; $v_i = 1, \forall i$) ordinary least-squares (OLS) fitting of each candidate IBIF model to only the first 0-45 min worth of input function data using 500 random initial guesses. Random start points were generated using the MultiStart.m function in the MATLAB 2014a optimization toolbox. The solution to the OLS maximization from the 0-45 min data was then used as a starting point for un-weighted constrained OLS maximization using the complete set (0-150 min data) of measured blood concentration samples. The solution obtained from the constrained, un-weighted OLS maximization of (*Eqn. 5.1.12*) using the complete 0-150 min data set was then used as the initial guess for a weighted-constrained maximization fit to the complete 0-150min data set. The solution to the weighted and constrained fit, denoted θ_0 , was used as initial guess for the final weighted and unconstrained maximization of the likelihood function in (*Eqn. 5.1.12*), the solution to which was used as the final input function model parameter estimate, denoted $\hat{\theta}$.

All constrained optimization was carried out using the fmincon.m function, while unconstrained optimization was performed using the fminunc.m function, both of which are

available in the MATLAB optimization toolbox (R2014a, The MathWorks, Natick, MA., USA). All constraints consisted of set constraints only, which restricted the possible ranges for the exponential washout-rates and the size of the time-delay, τ . No constraints were placed on the linear coefficients of the IBIF models. Specifically, IBIF models of the form of Model 1 in table 5-1 (i.e. IBIF Models: 1a, 1b, 1c, 1d) the second-order pole was restricted to be in the range $p_1 \in [0, 20] \text{ min}^{-1}$, while all first-order poles were restricted to the range $p_i \in [0, 1] \text{ min}^{-1}$, and the time delay parameter was constrained to be $\tau \in [0, 2] \text{ min}$.

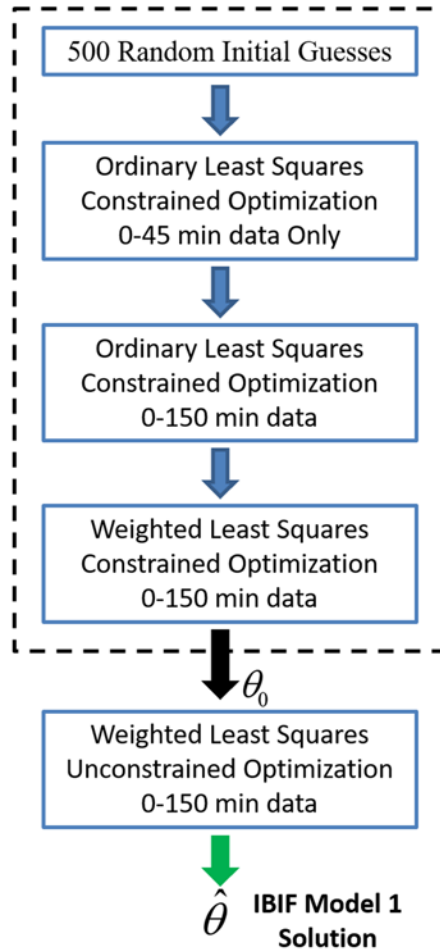


Figure 5-3. IBIF Model 1 Optimization Workflow.

IBIF Model Parameter Estimation Strategy: IBIF Model 2

Figure 5-4 shows a high-level workflow illustrating the multi-step optimization method used for fitting candidate IBIF Models: IBIF Model 2a, IBIF Model 2b, IBIF Model 2c, and IBIF Model 2d. The approach to obtaining initial guesses for IBIF Models: 2a, 2b, 2c, and 2d, consisted of first fitting the corresponding $f^{(N)}(t)$ component (see table 5-1) to the first 0-45 min worth of input function data using the same un-weighted OLS constrained maximization of (Eqn. 5.1.12) procedure as for Model 1 IBIF models with 500 random initial start-points. Next, the solution to the unweighted OLS maximization using only the $f^{(N)}(t)$ component, denoted $\theta_{45min}^{f^{(N)}}$, was used to form an initial guess vector $\theta_{45min}^{g^{(N)}} = \left[\theta_{45min}^{f^{(N)}} \mid \theta_0^{dblPeak} \right]^T$; where $\theta_0^{dblPeak} = [-5, 10, 1.5]^T$ contains the initial starting guesses for the second peak parameters: α_0 , α_1 , and τ_α , respectively. Next, a constrained OLS maximization was performed using only the 0-45min PET data and allowing only the $\theta_0^{dblPeak}$ parameters to float (i.e. the $\theta_{45min}^{f^{(N)}}$ parameters were held fixed during this step). The solution to this step was then used as initial guess for a constrained OLS step that allowed all IBIF model parameters to float, the solution to which is denoted $\theta_{150min}^{g^{(N)}} = \left[\theta_{150min}^{f^{(N)}} \mid \theta_{150}^{dblPeak} \right]^T$.

The OLS solution $\theta_{150min}^{g^{(N)}}$ was then used as an initial guess for a weighted coordinate descent procedure that alternated between optimizing over the $\theta^{f^{(N)}}$ and $\theta^{dblPeak}$ parameters until the relative change in the log-likelihood value was less than or equal to 10^{-5} . Finally, the gradient descent solution, denoted θ_0 , was used as the initial guess for an unconstrained maximization of

the likelihood function in (Eqn. 5.1.12), the solution to which was used as the final input function model parameter estimate, denoted $\hat{\theta}$.

All constrained optimization was carried out using the `fmincon.m` function, while unconstrained optimization was performed using the `fminunc.m` function, both of which are available in the MATLAB optimization toolbox (R2014a, The MathWorks, Natick, MA., USA). All constraints consisted of set constraints only, which restricted the possible ranges for the exponential washout-rates and the size of the time-delays. The set constraints for the $f^{(N)}(t)$ component are the same as in the IBIF Model 1 fitting procedure described in the previous section. The decay rate and time delay of the additional IBIF peak were restricted to the ranges $\alpha_1 \in [0, 20] \text{ min}^{-1}$, and $\tau_\alpha \in [0, 2] \text{ min}$. No constraints were applied to the linear coefficients of any candidate IBIF model.

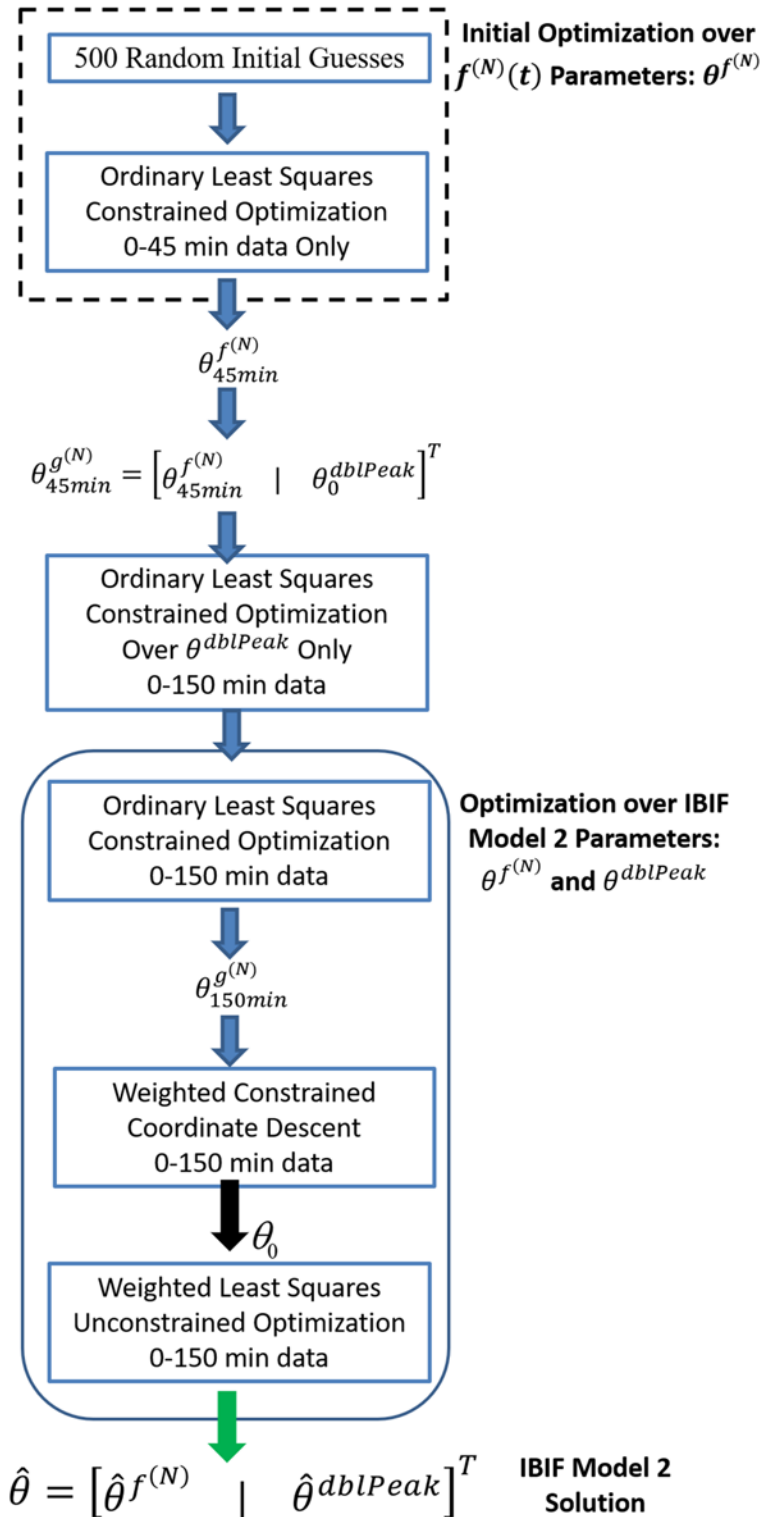


Figure 5-4. IBIF Model 2 Optimization Workflow.

5.1.3.6 Input Function Model Selection

In terms of selecting an IBIF model for a particular acquisition, several criteria were evaluated and the candidate model in table 5-2 that best described the measured IBIF was chosen based on a preponderance of the evidence. Specifically, input models were ranked based on relative differences in the small sample Akaike Information Criteria (denoted AIC_c), where the model with the minimum AIC_c score was taken to be the best model supported by the data. The standard Akaike Information Criteria (AIC) is given by: $AIC = -2 * \log(L(\hat{\theta})) + 2K$; where $L(\hat{\theta})$ denotes the maximum-likelihood value of the model being fitted and K is equal to the number of model parameters (including any associated nuisance parameters). The AIC_c compensates for small sample sizes relative to the number of parameters in the model being fitted, and can be obtained from the AIC as: $AIC_c = AIC + \frac{2K(K+1)}{N-K-1}$ [161]. In cases where the ratio of the number of samples (here, $N = 51$) to number of parameters of the largest model is small (i.e. $\frac{N}{K} < 40$), the AIC_c is generally recommended over the AIC [161].

The differences in AIC_c , denoted by ΔAIC_c^i , and defined as $\Delta AIC_c^i = (AIC_c^i - AIC_c^{\min})$ were computed over all candidate models for the purposes of comparison and ranking of the candidate models [161]. By definition, the model best supported by the measured data will have $\Delta AIC_c^i = 0$ [161].

Statistical Evaluation of IBIF Model Fit & Parameter Estimates

Estimates for parameter variances were obtained by calculating the inverse of the Fisher information matrix for each candidate IBIF model. Specifically, because the measurement errors are assumed to follow a Gaussian distribution, (Eqn. 5.1.6) can be used to compute the form of the Fisher Information matrix for the parameters of each candidate IBIF model. Using (Eqn. 2.4.9) and the formula for the Fisher information matrix in (Eqn. 5.1.6) an estimate of the covariance of model parameters was then obtained for each candidate IBIF function. The explicit equations for the partial derivatives with respect to each parameter are given in *Appendix A.1*.

Based on the obtained estimates of candidate IBIF model covariance matrices, the coefficient of variation (COV) for each model parameter was computed, where the COV of a particular model parameter γ is given by the ratio of the standard deviation of the estimate, $\hat{\sigma}_\gamma$, divided by the estimated value of that parameter, $\hat{\gamma}$, that is $\widehat{COV}_\gamma = \frac{\hat{\sigma}_\gamma}{\hat{\gamma}}$. For the purposes of model fitting, a small COV for each model parameter is desired, as a large COV value for a model parameter suggests poor parameter estimability and can be indicative of model over-fitting and/or high correlation among model parameters [154].

5.1.4 Results

Figure 5-5 shows an example IBIF model selection analysis for subject ML-10 #5 at BL. Figure 5-5A shows the model fits for the IBIF Model 1 (left) candidates (IBIF Model 1a, IBIF Model 1b, IBIF Model 1c, and IBIF Model 1d) and IBIF Model 2 (right) candidates (IBIF Model

2a, IBIF Model 2b, IBIF Model 2c, and IBIF Model 2d) to the measured IBIF data (circles). Figure 5-5B shows IBIF Model 1 (left) and IBIF Model 2 candidate (right) fit results to the first 0-5 min of measured IBIF data. For both the IBIF Model 1 and IBIF Model 2 candidates, increasing the number of component exponentials produced visually better fits to the measured IBIF data. IBIF Model 1a and IBIF Model 2a both are visually poor fits to the IBIF data, while IBIF Model 2c and IBIF Model 2d show signs of overfitting after the peak [¹⁸F]ML-10 concentration.

The corresponding model selection results for subject ML-10 #5 at BL are contained in table 5-3. The weighted residual sum of squares (WRSS), the value of the log-likelihood function for the model estimates ($\log(\mathcal{L}(\hat{\theta}, \hat{\sigma}^2 | data))$), the number of model parameters, K, as well as the AIC and AIC_c are shown for each candidate IBIF model. IBIF Model 1b has the minimum AIC_c value among the tested models, as a result this row of table 5-3 is highlighted in bold.

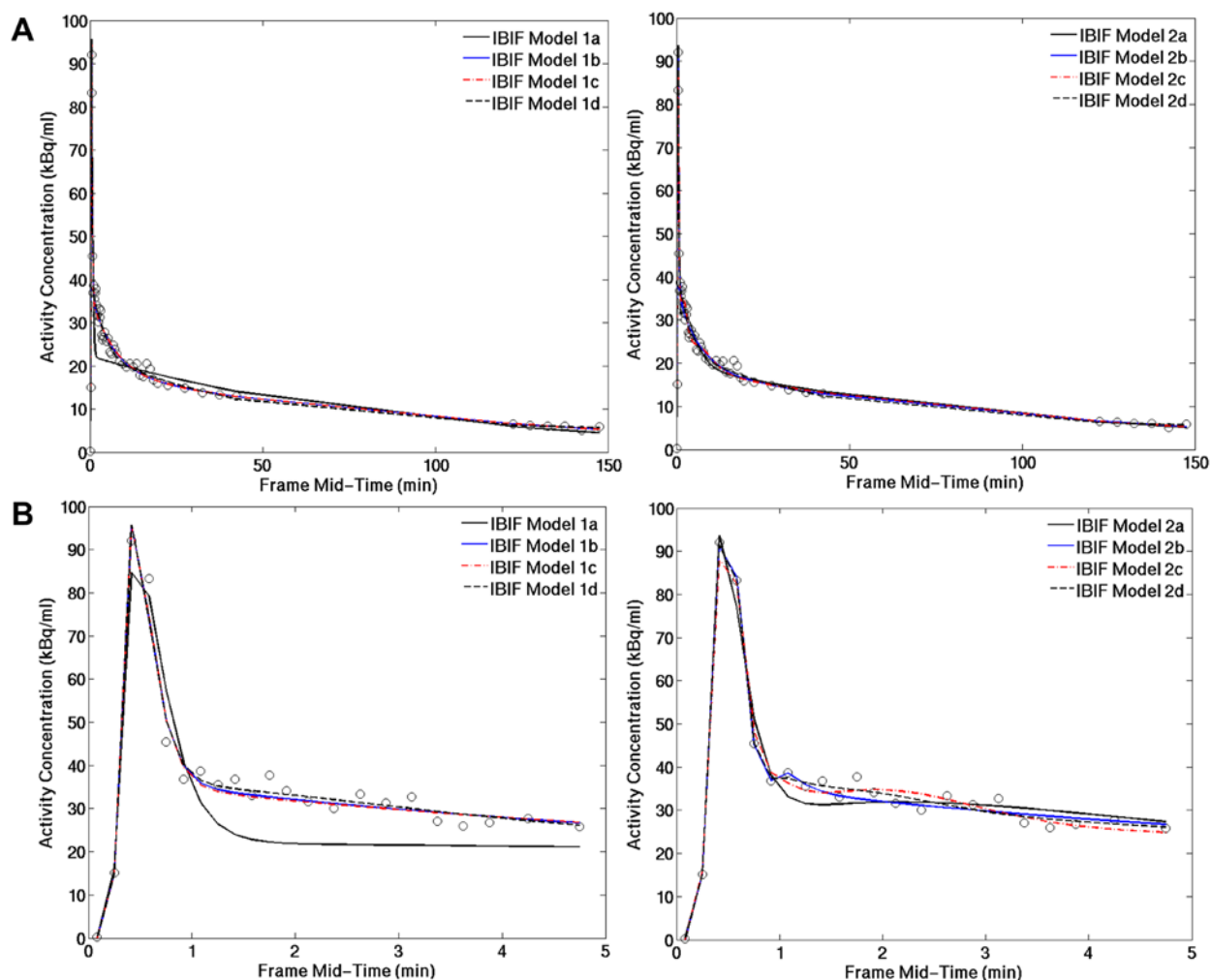


Figure 5-5. Example Comparison of IBIF Model Selection Fit Results for ML-10 #5 at BL. (A) IBIF (circles) with candidate IBIF Model 1 (left) and IBIF Model 2 (right) fits for subject ML-10 #5 at BL over a period of 150 min following injection of [^{18}F]ML-10. (B) shows candidate IBIF Model 1 (left) and IBIF Model 2 (right) fits to the first 0-5 min of measured IBIF data. For both IBIF Model 1 and IBIF Model 2, increasing the number of component exponentials produced visually better fits to the data. Based on minimum AIC_c , IBIF Model 1b was determined to be the overall best fitting IBIF model. For IBIF Model 1b the maximum likelihood parameter estimates and their respective estimated percent coefficients of variation (%COV) were: $\hat{\theta}_0 = -210.247$ kBq/ml (%COV = 7.08%), $\hat{\theta}_1 = -2183.541$ kBq/ml/min $^{-1}$ (%COV = 2.08%), and $\hat{\theta}_2 = -115.537$ kBq/ml/min $^{-1}$ (%COV = 8.48%), while the estimated decay rates and delay parameter τ were: $\hat{p}_0 = 8.498$ min $^{-1}$ (%COV = 7.93%), $\hat{p}_1 = 8.421 \times 10^{-3}$ min $^{-1}$ (%COV = 3.46%),

$\hat{p}_2 = 0.159 \text{ min}^{-1}$ (%COV = 10.57%), and $\hat{\tau} = 0.277 \text{ min}$ (%COV = 2.14%). The estimated value of the noise parameter α^2 was $\widehat{\alpha^2} = 0.0457$ (%COV = 19.80%).

Table 5-3. ML-10 #5 Baseline Scan Input Function Model Selection Results.

IBIF Model	WRSS	$\log(\mathcal{L}(\hat{\theta}, \widehat{\alpha^2} data))$	K	AIC	AIC_c	$\Delta_i \text{AIC}_c$
1a	17.88	-135.5	6	282.9	284.8	98.3
1b	2.333	-83.54	8	183.1	186.5	0
1c	2.388	-84.13	10	188.3	193.8	7.3
1d	2.317	-83.37	12	190.7	198.9	12.4
2a	3.733	-95.53	9	209.1	213.5	27.0
2b	1.956	-79.05	11	180.1	186.9	0.4
2c	2.525	-85.56	13	197.1	207	20.5
2d	1.939	-78.83	15	187.7	201.4	14.9

Across subjects IBIF Model 1a was consistently inadequate in describing the measured IBIFs, and generally exhibited an underestimation of the measured IBIF peak activity concentration as well as long runs of over and underestimation of data at times after the IBIF peak. IBIF Model 2a was determined to have the minimum AIC_c value among the candidate IBIF models only once (ML-10 #6 at ETA). However, IBIF Model 1b, which has 1 less parameter, was also found to visually well describe the IBIF of ML-10 #6 at ETA as illustrated in Figure 5-6. Table 5-4 contains the model selection results for ML-10 #6 at ETA.

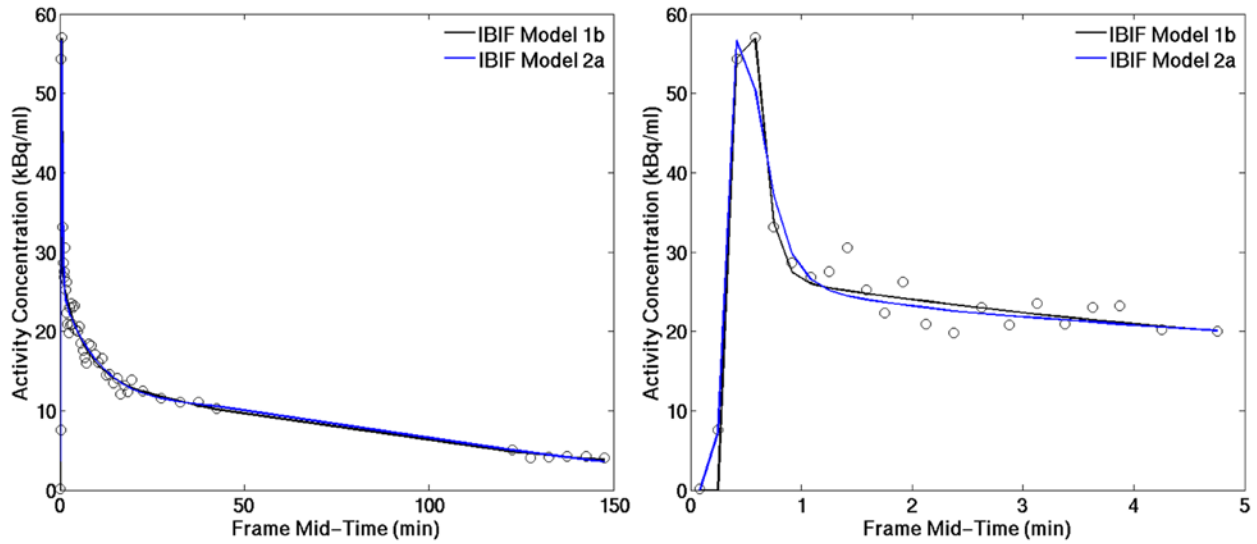


Figure 5-6. Comparison of IBIF Model Fits for ML-10 #6 at ETA: IBIF Model 1b versus IBIF Model 2a. (Left) IBIF (circles) with candidate IBIF Model 1b and IBIF Model 2b for subject ML-10 #6 at ETA over a period of 150 min following injection of [¹⁸F]ML-10. (Right) shows corresponding fits to the first 0-5 min of measured IBIF data (circles). IBIF Model 2a was found to have the minimum AIC_c of all candidate IBIF models. IBIF Model 1b, which has 1 less model parameter, can also be observed to well describe the overall trend in the measured IBIF data, especially near the IBIF peak concentration.

Table 5-4. ML-10 #6 Early Therapy Assessment Scan Input Function Model Selection Results.

IBIF Model	WRSS	$\log(\mathcal{L}(\hat{\theta}, \hat{\alpha}^2 data))$	K	AIC	AIC_c	$\Delta_i AIC_c$
1a	10.017	-112.85	6	237.7	239.6	69.2
1b	3.112	-83.046	8	182.1	185.5	15.1
1c	5.088	-95.579	10	211.2	216.7	46.3
1d	2.962	-81.78	12	187.6	195.8	25.4
2a	2.185	-74.029	9	166.1	170.4	0
2b	2.797	-80.317	11	182.7	189.4	19.0
2c	2.134	-73.422	13	172.9	182.7	12.3
2d	2.577	-78.227	15	186.1	200.2	29.8

Table 5-5 summarizes the IBIF model selected for each time-point. If one or more of the parameters of the minimum AIC_c IBIF model were not estimable the next best estimable model, in terms of minimum ΔAIC_c , is shown in parentheses. Based on the AIC_c criteria alone, the most commonly chosen IBIF model was that of IBIF Model-1b (10 times), while model IBIF Model 1c was selected for 6 acquisitions and IBIF Model 2b was chosen 7 times. In 5 of 6 of the remaining cases, the minimum AIC_c IBIF Model was determined to be either IBIF Model 1d, IBIF Model 2c, or IBIF Model 2d; however, in all cases the associated IBIF model parameter estimates were not statistically estimable. That is, either %COV values on some IBIF model parameters was large (e.g. %COV > 50%) or the estimate for the associated IBIF model parameter covariance matrix was not positive definite.

Table 5-5. Selected IBIF Model for each [¹⁸F]ML-10 PET Acquisition.

Subject ID	BL	ETA	FUA
ML-10 #1	IBIF Model 1b	N/A	N/A
ML-10 #2	‡N/A	†IBIF Model 2d (IBIF Model 1b)	N/A
ML-10 #4	IBIF Model 1b	IBIF Model 1b	IBIF Model 2b
ML-10 #5	IBIF Model 1b	IBIF Model 2b	IBIF Model 2b
ML-10 #6	IBIF Model 1b	IBIF Model 2a	IBIF Model 1b
ML-10 #7	IBIF Model 1b	IBIF Model 1c	IBIF Model 1b
ML-10 #9	IBIF Model 1c	IBIF Model 2b	†IBIF Model 2d (IBIF Model 1b)
ML-10 #10	IBIF Model 1c	IBIF Model 2b	IBIF Model 1c
ML-10 #11	†IBIF Model 1d (IBIF Model 1b)	†IBIF Model-2c (IBIF Model 2b)	IBIF Model 1b
ML-10 #12	IBIF Model 2b	N/A	N/A
ML-10 #13	IBIF Model 1b	†IBIF Model-2c (IBIF Model 1c)	N/A
ML-10 #14	IBIF Model 2b	IBIF Model 1c	IBIF Model 1c
N/A = Data not available ‡ Subject Missing first 67 sec of dynamic data. † Indicates that the model parameters for the minimum AIC _c IBIF model were not estimable. The next best IBIF model in terms of minimum ΔAIC _c that also resulted in estimable model parameters is indicated below in parentheses.			

5.1.5 IBIF Model Selection Discussion

In this section, a set of candidate IBIF models were fit to IBIF data derived from the internal carotid arteries of the brain and the relative support for each model was compared using standard model selection criteria and model parameter estimability considerations. VOI were defined using a manual segmentation approach applied directly to the PET image. Of the 29 [¹⁸F]ML-10 PET scans analyzed, the most commonly chosen models were IBIF Model 1b (selected 10 times), IBIF

Model 1c (selected 6 times), and IBIF Model 2b (selected 7 times). In 5 of the 6 remaining cases, either IBIF Model 1d, IBIF Model 2c, or IBIF Model 2d was selected as the best fitting IBIF model based on minimum AIC_c . However, in all 5 cases estimates for one or more associated model parameters were found to have poor precision (i.e. $\%COV > 50\%$) or resulted in a non-positive definite estimate for the model parameter covariance matrix. For these 5 cases the next best (in terms of minimum ΔAIC_c) estimable model was determined to be one of either IBIF Model 1b, IBIF Model 1c, or IBIF Model 2b as indicated in table 5-5.

The primary appeal of using image-based input functions (IBIFs) is that they, in principle, require no blood sampling from the patient. Gold standard arterial blood sampling is invasive, painful, and often discourages research subjects from enrolling in imaging trials. In many research institutions the procedure is so specialized that it requires the coordination of specialized teams, often including an anesthesiologist, to insert the catheter into one of the two main arteries (i.e. ulna or radial arteries) in the forearm. These factors often raise risk-benefit concerns of arterial blood sampling for the primary investigator and the referring physician. Finally, arterial sampling is a laborious process that exposes the PET technologist to additional radiation as well as to the potential risks associated with handling human blood. These factors combined impose practical challenges to arterial blood sampling in the clinic.

The use of IBIFs removes all of the additional risk associated with arterial blood sampling. Essentially the same kinds of approaches that are used to measure activity in the tissue can be used to measure an IBIF. However, from the stand-point of producing accurate quantification of tracer pharmacokinetics, IBIF models have some drawbacks.

The primary drivers that influence IBIF accuracy are PET scanner spatial and temporal resolution. Specifically, the limited spatial resolution of PET scanners (e.g. $\sim 6\text{mm}$) produces an overall averaging of true activity between neighboring voxels in the PET image. Sometimes the effects of partial volume averaging are discussed from the standpoint of VOI definition, where the effects of spatial resolution are talked about as being a combination of the ‘spill-in’ of activity from neighboring voxels outside of the internal carotid arteries into the IBIF volume of interest as well as the ‘spill-out’ of activity in the internal carotids into the surrounding tissue voxels.

The impact of partial volume on the measured IBIF depends on the size of the source from which the IBIF is being measured. For example, because of their small size ($\sim 5\text{mm}$ in diameter) internal carotid arteries of the brain will be especially affected by partial volume effects, likely resulting in some degree of distortion in the shape and scale of an IBIF measured there compared to the arterially sampled blood concentration. The degree to which this distortion biases compartmental parameter estimates is likely to be tracer and application specific.

Several methods have been proposed for correcting IBIFs obtained from the internal carotid arteries of brain with varying degrees of success [71]. The performance of many of these methods depends on several factors including: the particular tracer, the resolution of the PET scanner used, and the image reconstruction method implemented [71]. Moreover, many of these methods are time consuming and complicated to implement while only providing a marginal improvement in the accuracy of compartmental model parameter estimates (compared to the gold standard arterial blood sampling) [71]. Currently, there does not exist a consensus method for correcting IBIF input functions from the internal carotid arteries of brain [71].

Temporal resolution also greatly influences the shape of the IBIF curve compared to the true arterial concentration, especially with regard to IBIF curve shape around the fast-changing input peak [71]. Specifically, dynamic PET data are generally organized into finite time bins, or frames, where each PET frame contains the time-average of the measured activity during that frame duration. Moreover, below a certain frame duration, quantitative accuracy of the measured tracer concentration is dubious at best [71]. Therefore, it is not possible to recover the true peak tracer concentration in the blood using an IBIF alone. As a result, a mathematical model is often proposed to describe the measured IBIF.

Assuming an accurate description of circulating radio-labeled metabolites, most IBIF models are able to estimate the tail of the input function to within a scale factor [71]. In cases where a limited number of blood samples are taken, this scale factor can be estimated to obtain good agreement between the true tracer concentration in the blood and the proposed IBIF model [71]. The importance of accounting for radio-metabolites in the blood cannot be overstated, since the PET scanner only detects radioactivity and cannot distinguish between the parent tracer and radio-labeled metabolite. Generally, the radio-metabolite concentration in the blood must be measured (which requires blood sampling, though limited) or a model-based metabolite correction must be used to correct the measured IBIF. However, it is not obvious to what degree anticancer therapies will modulate tracer metabolism, which cautions use of a population based approach in oncology applications [70].

Because no blood sampling was performed, it is not possible to compare the model results to the gold standard arterial based input function; nor is it possible to estimate the fraction of tracer

in the blood that is free to transition from the blood into the tissue (e.g. some [^{18}F]ML-10 may become bound to albumin circulating in the blood) or to measure the concentration profile of any radio-labeled [^{18}F]ML-10 metabolites in the blood.

Currently no studies (clinical or pre-clinical) have been performed that quantify the free-fraction of [^{18}F]ML-10 in the blood. Incomplete knowledge of the [^{18}F]ML-10 free fraction, means that the true input tracer concentration can only be estimated up-to to a scale factor, potentially biasing estimates of the rate of tracer transport from the blood into the tissue the described by K_1 below. However, [^{18}F]ML-10 has been shown to exhibit low tracer metabolism (97.5% \pm 0.4% unchanged [^{18}F]ML-10 fraction 150 min post-injection) with no defluorination in healthy humans [129].

Although analysis using image-based input functions has its difficulties as described above, there are some situations in which it is more appropriate to use of an IBIF than others. Properties that appear to be common to tracers that are amenable to accurate IBIF modeling are: i.) low radiolabeled metabolites, and ii.) low tracer accumulation (especially early after injection) in the tissues surrounding the internal carotid arteries [71]. As mentioned [^{18}F]ML-10 has been shown to have limited metabolism in healthy subjects. Moreover, in the above analysis it was observed that [^{18}F]ML-10 exhibits low background tracer uptake in healthy tissue surrounding the internal carotid arteries (see Figure 5-1 for example). From this stand-point, it is encouraging to note that [^{18}F]ML-10 exhibits properties that are consistent with tracers that afford good approximations of arterially sampled input functions using IBIFs.

Some empirical evidence has suggested that methods which simultaneously estimate the input function and the pharmacokinetic model parameters of the tissue model produce better estimates of the input function compared to IBIF from the internal carotids alone [71]. These approaches operate under the assumption that the tracer concentration in the blood is the same everywhere in the body, which includes the vascular bed of the target tissue in the brain (i.e. the brain tumor in the case of this dissertation). In other words, the vascular bed of the tumor provides a second (albeit attenuated) IBIF realization. Therefore, using simultaneous estimation methods, the [^{18}F]ML-10 uptake in the brain tumor can assist in estimating the parameters of the IBIF model, while simultaneously reducing the influence that the uncertainty in the IBIF model parameters has on the estimates of the tumor pharmacokinetic rate constants.

In the next section the pharmacokinetic properties of [^{18}F]ML-10 are evaluated in a cohort of GBM subjects. To this end, a simultaneous estimation approach will be used. The knowledge gained in this current section is used to aid in the selection of minimum AIC_c tumor tissue compartmental model. Specifically, based on the results of this section, the number of candidate IBIF models to be tested simultaneously with the candidate tissue models can be reduced from 8 to 3. Moreover, the IBIF model parameter estimates obtained for IBIF model still under consideration will serve as initial guesses to initiate the maximization of the log like-likelihood function used in the simultaneous estimation approach below.

5.2 CHARACTERIZATION OF REGIONAL TUMOR TISSUE TIME-ACTIVITY CURVES

5.2.1 Background: Tracer Compartmental Modeling in PET

The strength of PET imaging is in being able to measure and quantify physiologic processes *in vivo*. For example, an investigator may be interested in measuring change in the density of a particular neuro-receptor over time, or evaluating change in glucose metabolism by a tumor between follow-up imaging time-points. Pharmacokinetic (PK) modeling of the time-course of tracer concentration in the target tissue is the principle means by which radiotracer performance *in vivo* is evaluated. The results of PK modeling can be used to determine the utility of a novel radiotracer in measuring the target process. If the radiotracer PK results are found to be satisfactory, they can also provide the basis for development of clinically practical quantitative methodology and optimized imaging protocols.

Fundamentally PET images the distribution of radioactivity concentration in the target tissue. This means that while the investigator maybe interested in only measuring radiotracer uptake in a specific cell type or binding at a specific receptor, in practice the measured tissue activity concentration will contain contributions from all tissue types in the region of interest. As a result, the central approach taken in PET PK modeling is to analyze the target tissue as being composed of a finite number of sub-systems, called compartments, that are each kinetically distinct from each other, but are allowed to interact.

Generally, several simplifying assumptions are made about the structure of the compartmental system used to analyze the measured tissue concentration time-course. Specifically, it is assumed that the physiologic system being interrogated is in steady-state, and that the introduction of the tracer does not appreciably perturb the underlying system away from this steady state [23, 162]. Additionally, it is assumed that each compartment is well-mixed, and that when a tracer molecule transits from one compartment to another it is assumed to be immediately spread throughout its new compartment [154, 162]. This assumption makes it so that each tracer molecule within a compartment has the same probability of transitioning to a different compartment as any other tracer molecule in its same compartment [154, 162]. Under these assumptions the target tissue can be treated as a linear system [162, 163], for which the measured tissue concentration curve is the system response function [164]. The overall goal then, is to determine the impulse response function (IRF) of the linear compartmental system.

Two approaches to studying linear systems are commonly employed to quantify tracer PK in PET: input/output (i.e. convolution based) and state-space. In the input/output (I/O) approach, the IRF of the compartmental system is assumed to be composed of a superposition of first-order, causal exponentials, where each exponential mode describes the impulse response of a specific member compartment. (Eqn. 5.2.1) gives the form of the IRF for a general 2-compartment model, where it is assumed that: $\alpha_1, \alpha_2, \beta_1, \beta_2 \geq 0$.

$$\mathbf{h}(t) = \alpha_1 \mathbf{e}^{-\beta_1 t} \mathbf{u}(t) + \alpha_2 \mathbf{e}^{-\beta_2 t} \mathbf{u}(t) \quad (\text{Eqn. 5.2.1})$$

The I/O formalism has several advantages that make it ideal for model development and parameter estimation in the case of investigating a novel radiotracer. For example: if the input function itself is modeled as a sum of exponential terms, then computation of the resulting convolution integral is comparatively easier in the I/O description compared to the state-space representation. This is particularly helpful for model order selection when the number of component exponentials of the tumor tissue IRF is unknown. Moreover, because the IRF, $h(t)$, is the sum of causal exponentials with constant coefficients, calculation of the Fisher information matrix (assuming Gaussian distributed random errors, and an input function model) for IRF model parameters is comparatively straight forward. The disadvantage of this method lies in computing the inter-compartmental transfer rates for multi-compartmental structures. Theoretically, transformation equations can always be derived (see below) relating the IRF model parameters to the transfer rates of the state-space representation (assuming the state-space model parameters are globally identifiable); however, in practice this approach is limited to compartmental models with 3 compartments or less.

In the state-space approach the fractional transfer rates of radiotracer molecules between the individual tissue compartments are estimated; and, because the compartmental system is assumed to be linear and time-invariant, the transfer rates are necessarily constant [162, 165]. Figure 5-7 shows two example connectivity diagrams for a 2-tissue compartmental model appropriate for quantification of reversible (Figure 5-7A) or irreversible (Figure 5-7B) radiotracer pharmacokinetics in PET. The distinguishing feature between the two models is that there is no transfer of radiotracer back from compartment 2 to compartment 1 (i.e. $k_4 = 0$) in the irreversible model, that is, in the irreversible model, compartment 2 is a trap. In contrast, the compartmental

model structure in Figure 5-7A allows for a radiotracer molecule in one compartment to reach the other compartment independent of in which compartment the radiotracer molecule began, that is the compartmental model structure in Figure 5-7A is ‘strongly connected’ [154, 162]. Both compartmental systems are; however, ‘open systems’, since both models allow for excretion of tracer into the surrounding environment (quantified by the fractional rate constant k_2) [154, 162]. Moreover, both compartmental systems are ‘mamillary systems’ in that one compartment acts as the central compartment (compartment 1 in both cases) [154, 162], and radiotracer exchange takes place between the central compartment and each individual peripheral compartment (see figure 5-8, for an example 3-tissue mamillary system).

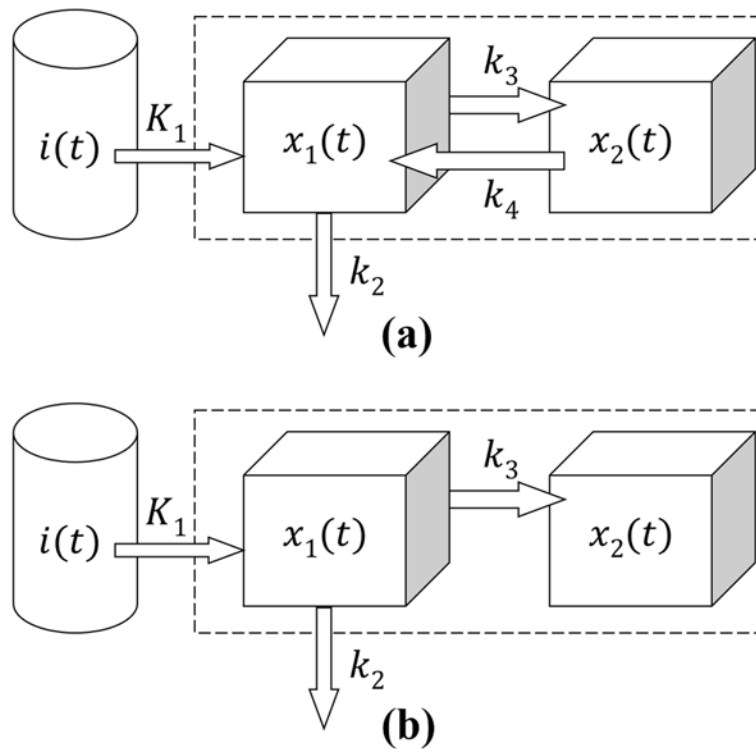


Figure 5-7. 2-Tissue Compartmental Model Structure Appropriate for PET.

(Eqn. 5.2.2) gives the system of first order differential equations that describe tracer kinetics for the 2-tissue, reversible compartmental model shown in figure 6-7A. The system of differential equations in (Eqn. 5.2.2) can be re-expressed in state-space form [154, 163, 165] as in (Eqn. 5.2.3); where $y(t)$ in the observation equation, (ii), is the quantity measurable by PET and is the superposition of the radioactivity profiles of the component compartments.

$$\begin{cases} \frac{dx_1(t)}{dt} = [-(k_2 + k_3)x_1(t) + k_4x_2(t)] + K_1i(t) \\ \frac{dx_2(t)}{dt} = [k_3x_1(t) - k_4x_2(t)] \end{cases} \quad (\text{Eqn. 5.2.2})$$

$$\begin{cases} (i) \begin{bmatrix} \dot{x}_1 \\ \dot{x}_2 \end{bmatrix} = \begin{bmatrix} -(k_2 + k_3) & k_4 \\ k_3 & -k_4 \end{bmatrix} \begin{bmatrix} x_1 \\ x_2 \end{bmatrix} + K_1 \begin{bmatrix} i(t) \\ 0 \end{bmatrix} \\ (ii) \quad y(t) = [1 \quad 1] \begin{bmatrix} x_1 \\ x_2 \end{bmatrix} \end{cases} \quad (\text{Eqn. 5.2.3})$$

As mentioned above, transformations can be derived relating the I/O and state-space representations. However, in order to guarantee that these transformation equations yield unique values for each compartmental rate constant, the proposed connectivity of the compartmental model must be globally identifiable [154, 162, 163]. (Eqn. 5.2.4) gives the general form of the state-space equations appropriate for compartmental modeling of PET data (assuming no direct transfer of the input function), where A denotes the nxn compartmental matrix of rate constants, B is a nx1 column vector with first element equal to K_1 and the rest equal to zero, and C is an nx1 row vector where each entry is equal to unity, and n denotes the number of tissue compartments [164, 165]. If all rate parameters in the compartmental matrix A can be determined uniquely, assuming perfect noise-free observations, given the connectivity of the individual compartments

and the observation matrix C , then the compartmental system is said to be globally identifiable [154, 163]. If there is a finite number of alternative values for the rate constants that explain the noise-free observations, then the system is said to be locally identifiable [154, 163]. Otherwise the compartmental system is said to be unidentifiable [154, 163].

$$\begin{cases} \dot{\mathbf{x}} = \mathbf{A}\mathbf{x} + \mathbf{B}\mathbf{i}(t) \\ \mathbf{y} = \mathbf{C}\mathbf{x} \end{cases} \quad (\text{Eqn. 5.2. 4})$$

Assuming the proposed compartmental model structure is globally identifiable, the transformation equations that relate the I/O description to the state-space fractional rate constants can be obtained by calculating the transfer functions of the linear system under each description and setting them equal to each other [154, 162, 163]. A system of equations is then obtained that can be solved uniquely (because the system is globally identifiable), thereby producing the desired transformations [154, 162, 163]. (Eqn. 5.2.5), (Eqn. 5.2.6), and (Eqn. 5.2.7) give the transformations from I/O representation to state-space representation for the reversible (i.e. well-connected) 1-tissue and 2-tissue compartment models, respectively. The derivations of these equations, and the transformation equations for the 3-tissue compartment model, can be found below. Moreover, the reverse transformations can be found in Gunn et al [164].

$$\begin{cases} K_1 \\ k_2 \end{cases} \rightarrow \begin{cases} \alpha_1 \\ \beta_1 \end{cases} \quad (\text{Eqn. 5.2.5})$$

$$\begin{pmatrix} K_1 \\ k_2 \\ k_3 \\ k_4 \end{pmatrix} \rightarrow \begin{pmatrix} (\alpha_1 + \alpha_2) \\ \frac{(\alpha_1\beta_1 + \alpha_2\beta_2)}{\alpha_1 + \alpha_2} \\ \frac{\alpha_1\alpha_2(\beta_1^2 + \beta_2^2) - 2\alpha_1\alpha_2\beta_1\beta_2}{(\alpha_1 + \alpha_2)(\alpha_1\beta_1 + \alpha_2\beta_2)} \\ \frac{(\alpha_1 + \alpha_2)\beta_1\beta_2}{\alpha_1\beta_1 + \alpha_2\beta_2} \end{pmatrix} \quad (\text{Eqn. 5.2.6})$$

The transformation equations given for the 2-tissue and 3-tissue compartment models assume the systems are open with a single excretion compartment (being the central compartment) and that the peripheral compartments are arranged in a mamillary configuration. Moreover, the measured tissue concentration curve is assumed to be equal to the sum of the individual radiotracer concentration time-courses described by each member compartment, as is appropriate for PK modeling of PET data. If one compartment is turned into a trap in either the 2-tissue or 3-tissue models, the corresponding transform equations can be obtained by setting the appropriate I/O IRF eigenvalues and state-space fractional rate constants to equal 0 (i.e. $\beta_2 = 0$, and $k_4 = 0$ for both models).

While characterization of the target tissue impulse response $h(t)$ and fractional rate constants is useful for evaluation of tracer performance, the individual parameters for each model are difficult to interpret in the context of cancer therapy response assessment. In order to bridge the gap between mathematical description and tumor physiology, derived measures (also called macroparameters) such as the total distribution volume (V_T) and the overall uptake flux (K_i) are

more commonly used to quantify therapeutic response in tumors demonstrating reversible and irreversible radiotracer kinetics, respectively [166-169].

V_T can be conceptualized a few different ways; however, it is generally used as a proxy for the “amount” of tracer that would be in the tissue at equilibrium due to an infusion injection with unit tracer concentration. Said another way, V_T is the equilibrium gain that would be obtained from calculating the step response of the compartmental system. Said one more way, if the radiotracer concentration in the blood was fixed to 1 kBq/cc, and C_∞ equaled the resulting equilibrium concentration in the tissue, then $V_T = \frac{C_\infty}{1 \text{ kBq/cc}}$. Following the convention established by Innis et al [170], the units of V_T are $\text{ml}\cdot\text{cm}^{-3}$. The interpretation of K_i is that it is a measure of overall flux of tracer from the blood into the tissue [19, 23, 168]. Multiplying K_i by the steady-state plasma concentration of the tracee can be used to calculate the physiologic metabolism or clearance rate of a physiologic protein or molecule of interest [23]. For example, glucose metabolism rate using [^{18}F]FDG PET [19, 20, 166, 167]. The units of K_i are $\text{ml}\cdot\text{cm}^{-3}\cdot\text{min}^{-1}$.

The calculation of the macroparameters V_T and K_i requires few assumptions regarding the pharmacokinetic model of the system, and, as a result, they can be obtained using either the I/O or state-space descriptions; in other words, they are robust to misspecification of the compartmental connectivity. Specifically, V_T is equal to the area under the system impulse response function for the reversible kinetics case, while K_i is equal to the coefficient in front of the step-function in the irreversible case (e.g. α_2 in (Eqn. 5.2.1) above when $\beta_2 = 0$). As a result, these measures are much easier to determine accurately compared to the individual fractional rate constants.

(Eqn. 5.2.7) and (Eqn. 5.2.8) give the equations for V_T and K_i for the reversible and irreversible systems in figure 5-7A and figure 5-7B, respectively.

$$V_T = \left(\frac{\alpha_1}{\beta_1} + \frac{\alpha_2}{\beta_2} \right) = \frac{K_1}{k_2} \left(1 + \frac{k_3}{k_4} \right) \quad (\text{Eqn. 5.2.7})$$

$$K_i = \alpha_2 = K_1 \left(\frac{k_3}{k_2 + k_3} \right) \quad (\text{Eqn. 5.2.8})$$

A drawback of estimating the compartmental fractional rate constants (or microparameters), is that the rate constants tend to be strongly correlated with each other, which contributes to relatively higher noise sensitivity and overall larger parameter uncertainty compared to the I/O model parameters. On the other hand, knowledge of the microparameters allows the modeler to separate out the individual contributions of each compartment to the measured tissue activity profile; thereby allowing for investigation of the relative contributions of each component compartment to the total distribution volume, V_T .

For example, figure 5-8 shows the compartmental connectivity diagram for an open, well-connected (i.e. reversible), mamillary 3-tissue compartment model with the central compartment being the only excretion compartment. Assuming this is a neuro-imaging example, the first (or central compartment) typically represents tracer molecules that have crossed the blood-brain-barrier and are free to interact in the tissue (i.e. tracer molecules in the interstitial space). Compartment 2 would represent the specific binding or uptake by the target process, and compartment 3 generally represents non-specific binding of the tracer to non-target

proteins/tissues. Given a measure of V_T , it is useful to know what the fractional contribution of each compartment is to the total distribution volume. That is, one would like to know what the individual volumes of distribution V_{free} , V_{NS} , V_S for the component compartments is, where $V_T = (V_{free} + V_{NS} + V_S)$. Ideally, the volume of distribution of the specific, V_S , will account for the majority of tracer in the tissue at equilibrium. Assuming the compartmental structure in figure 5-8 and that the measured tissue activity is the superposition of the compartmental component concentrations, the individual compartmental volumes are given in (Eqn. 5.2.9).

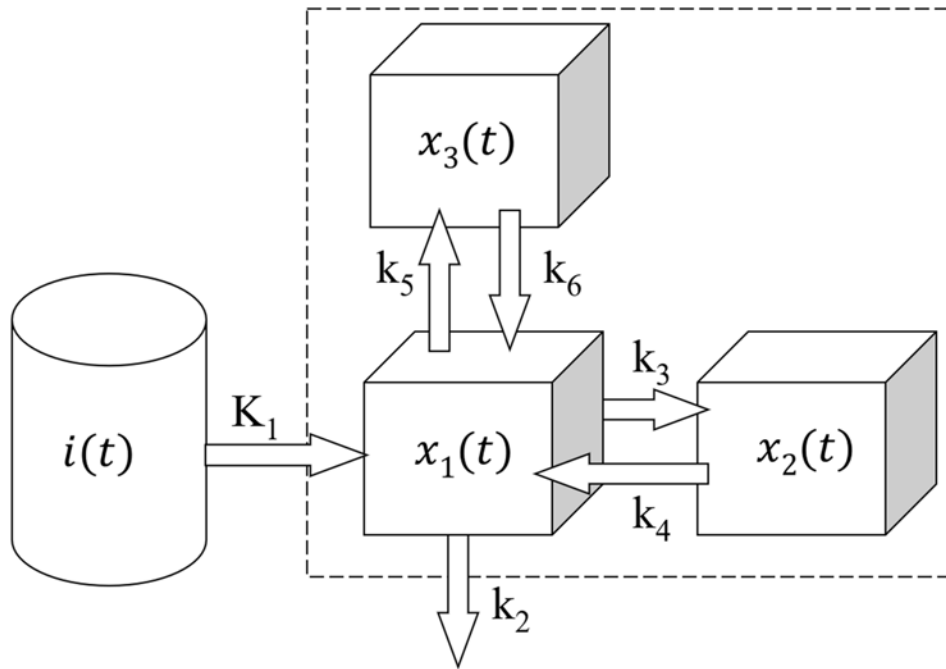


Figure 5-8. 3-Tissue Compartmental Model with Reversible Pharmacokinetics.

$$\begin{cases} V_{free} = \frac{K_1}{k_2} \\ V_{nonSpecific} = \frac{K_1}{k_2} \left(\frac{k_5}{k_6} \right) \\ V_{Specific} = \frac{K_1}{k_2} \left(\frac{k_3}{k_4} \right) \end{cases} \quad (\text{Eqn. 5.2.9})$$

When the pharmacokinetics of the free and non-specific compartments are essentially indistinguishable, the compartmental structure in figure 5-8 reduces to that of a reversible 2-tissue compartmental model (i.e. figure 5-7A), where the central compartment represents the combined free and non-specific component (called non-displaceable component), and compartment 2 represents the specific component [170]. For this case, the individual compartment volumes are given by (Eqn. 5.2.10).

$$\begin{cases} V_{ND} = \frac{K_1}{k_2} \\ V_S = \frac{K_1}{k_2} \left(\frac{k_3}{k_4} \right) \end{cases} \quad (\text{Eqn. 5.2.10})$$

Special Considerations in the Compartmental Modeling of PET Data

The previous section presented the general compartmental modeling approach to modeling the time-course of radioactivity concentration in a target tissue. However, in general a few additional considerations are required including: accounting for radio-labeled metabolites in the target region, as well as the fraction of tracer in the blood that is free to be transported into the

target tissue (i.e. the blood free fraction: f) [72], and the whole body hematocrit (i.e. the volume of the red-blood cells divide by the total blood volume) [23]. The impact of not accounting for these effects on the input function $i(t)$ were discussed in *section 5.1.5*. Essentially the same discussion regarding incorrect metabolite correction applies here for the tissue response function.

In the case of analyzing the radiotracer concentration time-course in the tissue, the free-tracer in the tissue is accounted for as a compartment. However, as mentioned in *section 5.1.5*, if the blood free fraction or hematocrit are not accounted for in the input function, then the effect will be to attenuate the observed input function $i(t)$ by a scalar multiple. Indeed, the true input function, denoted $i'(t)$, will be related to the observed input function as: $i(t) = Mi'(t)$, where M denotes a constant. Ultimately, because the system response is described through the convolution operation, this means that the estimate for K_1 will be biased by a constant M ; that is the observed K_1 will be related to the true value, denoted K'_1 , as: $K_1 = MK'_1$.

An additional consideration when analyzing PET tissue time-activity curves, especially in neuro-oncology imaging, is the contribution of radiotracer in the vascular bed of the tumor to the measured tissue activity concentration. The general approach to accounting for the blood component is to define the blood volume fraction V_B , where $V_B \in [0,1]$, and add a direct transfer component to the impulse response function of the tissue. (*Eqn. 5.2.11*) and (*Eqn. 5.2.12*) give the modified I/O and state-space representations for the case of a 2-tissue compartmental model with reversible tracer kinetics and a non-zero blood component. The blood activity component is accounted for in exactly the same way for the 1-tissue and 3-tissue compartment models.

$$h(t) = V_B \delta(t) + (1 - V_B) [\alpha_1 e^{-\beta_1 t} u(t) + \alpha_2 e^{-\beta_2 t} u(t)] \quad (\text{Eqn. 5.2.11})$$

$$\begin{cases} \begin{bmatrix} \dot{x}_1 \\ \dot{x}_2 \end{bmatrix} = \begin{bmatrix} -(k_2 + k_3) & k_4 \\ k_3 & -k_4 \end{bmatrix} \begin{bmatrix} x_1 \\ x_2 \end{bmatrix} + K_1 \begin{bmatrix} i(t) \\ 0 \end{bmatrix} \\ \mathbf{y}(t) = [(\mathbf{1} - \mathbf{V}_B) \quad (\mathbf{1} - \mathbf{V}_B)] \begin{bmatrix} x_1 \\ x_2 \end{bmatrix} + V_B i(t) \end{cases} \quad (\text{Eqn. 5.2.12})$$

Derivation of 1-Tissue Model Parameter Transformation

The general form state-space representation is given by (Eqn. 5.2.13) below, assuming no direct transfer component [165]. The general form of the transfer function $\hat{G}(s)$ of the system in (Eqn. 5.2.13) is given by (Eqn. 5.2.14) [165].

$$\begin{cases} \dot{\mathbf{x}} = \mathbf{A}\mathbf{x} + \mathbf{B}i(t) \\ \mathbf{y} = \mathbf{C}\mathbf{x} \end{cases} \quad (\text{Eqn. 5.2.13})$$

$$\hat{\mathbf{G}}(s) = \mathbf{C}(s\mathbb{I} - \mathbf{A})^{-1}\mathbf{B} \quad (\text{Eqn. 5.2.14})$$

Figure 5-9 shows the connectivity diagram for a 1-tissue compartmental model. (Eqn. 5.2.15) and (Eqn. 5.2.16) give the impulse response function $h(t)$ (where $u(t)$ denotes the step-function) and state-space equations with corresponding transfer functions $\hat{H}(s)$ and $\hat{G}(s)$ appropriate for the 1-tissue compartmental model, respectively.

$$(i) \quad h(t) = \alpha_1 e^{-\beta_1 t} u(t)$$

$$(ii) \quad \hat{H}(s) = \frac{\alpha_1}{s + \beta_1}$$

(Eqn. 5.2.15)

$$(i) \quad \begin{cases} [\dot{x}_1] = [-k_2][x_1] + [K_1]i(t) \\ y(t) = [1][x_1] \end{cases}$$

$$(ii) \quad \hat{G}(s) = \frac{K_1}{s + k_2}$$

(Eqn. 5.2.16)

In order to obtain the appropriate transformation equations relating IRF parameters $\{\alpha_1, \beta_1\}$ to the state-space parameters $\{K_1, k_2\}$, set the transfer function of the I/O equation, $\hat{H}(s)$, equal to the transfer function of the state-space representation, $\hat{G}(s)$; yielding the system of 2 equations in (Eqn. 5.2.17). For the 1-tissue compartmental model the solution to the system of equations is trivial, and the transformation equations relating the two descriptions is given in (Eqn. 5.2.18).

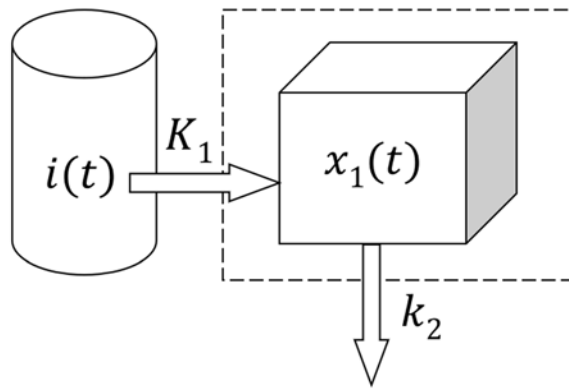


Figure 5-9. 1-Tissue Compartmental Model.

$$\begin{cases} K_1 = \alpha_1 \\ k_2 = \beta_1 \end{cases} \quad (\text{Eqn. 5.2.17})$$

$$\begin{cases} K_1 \\ k_2 \end{cases} \rightarrow \begin{cases} \alpha_1 \\ \beta_1 \end{cases} \quad (\text{Eqn. 5.2.18})$$

Derivation of 2-Tissue Model Parameter Transformation

Figure 6-7A (above) shows the connectivity diagram for an open, reversible 2-tissue compartmental model with central compartment. (Eqn.5.2.19) and (Eqn.5.2.20) give the appropriate impulse response function $h(t)$ (where $u(t)$ denotes the step-function) and state-space equations, respectively, appropriate for the model in Figure 6-7A. The corresponding transfer functions $\hat{H}(s)$ and $\hat{G}(s)$ are given in (Eqn. 6.2.22), where $\hat{G}(s)$ was obtained using (Eqn. 5.2.14) above.

$$h(t) = \alpha_1 e^{-\beta_1 t} u(t) + \alpha_2 e^{-\beta_2 t} u(t) \quad (\text{Eqn. 5.2. 19})$$

$$\begin{cases} \begin{bmatrix} \dot{x}_1 \\ \dot{x}_2 \end{bmatrix} = \begin{bmatrix} -(k_2 + k_3) & k_4 \\ k_3 & -k_4 \end{bmatrix} \begin{bmatrix} x_1 \\ x_2 \end{bmatrix} + K_1 \begin{bmatrix} i(t) \\ 0 \end{bmatrix} \\ y(t) = [1 \quad 1] \begin{bmatrix} x_1 \\ x_2 \end{bmatrix} \end{cases} \quad (\text{Eqn. 5.2.20})$$

$$\begin{cases} \hat{H}(s) = \frac{(\alpha_1 + \alpha_2)s + (\alpha_1\beta_2 + \alpha_2\beta_1)}{s^2 + (\beta_1 + \beta_2)s + \beta_1\beta_2} \\ \hat{G}(s) = \frac{K_1 s + K_1(k_3 + k_4)}{s^2 + (k_2 + k_3 + k_4)s + k_2 k_4} \end{cases} \quad (\text{Eqn. 5.2.21})$$

To relate IRF parameters $\{\alpha_1, \beta_1, \alpha_2, \beta_2\}$ to the state-space parameters $\{K_1, k_2, k_3, k_4\}$, we again set the transfer function of the I/O equation, $\hat{H}(s)$, equal to the transfer function of the state-space representation, $\hat{G}(s)$; yielding the system of 4 equations in (Eqn. 5.2.22). The system of equations can be solved uniquely to obtain the transformation equations (Eqn. 5.2.23) relating the two linear system descriptions.

$$\begin{cases} K_1 = (\alpha_1 + \alpha_2) \\ K_1(k_3 + k_4) = (\alpha_1\beta_2 + \alpha_2\beta_1) \\ (k_2 + k_3 + k_4) = (\beta_1 + \beta_2) \\ k_2k_4 = \beta_1\beta_2 \end{cases} \quad (\text{Eqn. 5.2. 22})$$

$$\begin{pmatrix} K_1 \\ k_2 \\ k_3 \\ k_4 \end{pmatrix} \rightarrow \begin{pmatrix} (\alpha_1 + \alpha_2) \\ \frac{(\alpha_1\beta_1 + \alpha_2\beta_2)}{\alpha_1 + \alpha_2} \\ \frac{\alpha_1\alpha_2(\beta_1 - \beta_2)^2}{(\alpha_1 + \alpha_2)(\alpha_1\beta_1 + \alpha_2\beta_2)} \\ \frac{(\alpha_1 + \alpha_2)\beta_1\beta_2}{\alpha_1\beta_1 + \alpha_2\beta_2} \end{pmatrix} \quad (\text{Eqn. 5.2.23})$$

Derivation of 3-Tissue Model Parameter Transformation

Figure 5-8 (above) shows the connectivity diagram for an open, reversible 3-tissue compartmental model with central compartment. (Eqn. 5.2.24) and (Eqn. 5.2.25) give the appropriate impulse response function $h(t)$ (where $u(t)$ denotes the step-function) and state-space

equations, respectively, appropriate for the 3-tissue compartment model. The corresponding transfer functions $\hat{H}(s)$ and $\hat{G}(s)$ are given in (Eqn. 5.2.26) and (Eqn. 5.2.27), respectively, where $\hat{G}(s)$ was obtained using (Eqn. 5.2.14) above.

$$\mathbf{h}(t) = \alpha_1 e^{-\beta_1 t} \mathbf{u}(t) + \alpha_2 e^{-\beta_2 t} \mathbf{u}(t) + \alpha_3 e^{-\beta_3 t} \mathbf{u}(t) \quad (\text{Eqn. 5.2.24})$$

$$\left\{ \begin{array}{l} \begin{bmatrix} \dot{x}_1 \\ \dot{x}_2 \\ \dot{x}_3 \end{bmatrix} = \begin{bmatrix} -(k_2 + k_3 + k_5) & k_4 & k_6 \\ k_3 & -k_4 & 0 \\ k_5 & 0 & -k_6 \end{bmatrix} \begin{bmatrix} x_1 \\ x_2 \\ x_3 \end{bmatrix} + K_1 \begin{bmatrix} i(t) \\ 0 \\ 0 \end{bmatrix} \\ \mathbf{y}(t) = [\mathbf{1} \quad \mathbf{1} \quad \mathbf{1}] \begin{bmatrix} x_1 \\ x_2 \\ x_3 \end{bmatrix} \end{array} \right. \quad (\text{Eqn. 5.2.25})$$

$$\hat{H}(s) = \left\{ \begin{array}{l} \frac{(\alpha_1 + \alpha_2 + \alpha_3)s^2 + [\alpha_1(\beta_2 + \beta_3) + \alpha_2(\beta_1 + \beta_3) + \alpha_3(\beta_1 + \beta_2)]s}{s^3 + (\beta_1 + \beta_2 + \beta_3)s^2 + (\beta_1\beta_2 + \beta_1\beta_3 + \beta_2\beta_3)s + \beta_1\beta_2\beta_3} + \\ + \frac{(\alpha_1\beta_2\beta_3 + \alpha_2\beta_1\beta_3 + \alpha_3\beta_1\beta_2)}{s^3 + (\beta_1 + \beta_2 + \beta_3)s^2 + (\beta_1\beta_2 + \beta_1\beta_3 + \beta_2\beta_3)s + \beta_1\beta_2\beta_3} \end{array} \right. \quad (\text{Eqn. 5.2.26})$$

$$\hat{G}(s) = \frac{K_1 s^2 + K_1(k_3 + k_4 + k_5 + k_6)s + K_1[k_4(k_5 + k_6) + k_3 k_6]}{s^3 + (\sum_{i=2}^6 k_i)s^2 + [k_2(k_4 + k_6) + k_4(k_5 + k_6) + k_3 k_6]s + k_2 k_4 k_6} \quad (\text{Eqn. 5.2.27})$$

In order to obtain the appropriate transformation equations relating IRF parameters $\{\alpha_1, \beta_1, \alpha_2, \beta_2, \alpha_3, \beta_3\}$ to the state-space parameters $\{K_1, k_2, k_3, k_4, k_5, k_6\}$, set the transfer function of the I/O equation, $\hat{H}(s)$, equal to the transfer function of the state-space representation, $\hat{G}(s)$; yielding the system of 6 equations in (Eqn. 5.2.28).

$$\left\{ \begin{array}{l}
K_1 = (\alpha_1 + \alpha_2 + \alpha_3) \\
K_1(k_3 + k_4 + k_5 + k_6) = \alpha_1(\beta_2 + \beta_3) + \alpha_2(\beta_1 + \beta_3) + \alpha_3(\beta_2 + \beta_1) \\
K_1k_4(k_5 + k_6) + K_1k_3k_6 = \alpha_1\beta_2\beta_3 + \alpha_2\beta_1\beta_3 + \alpha_3\beta_1\beta_2 \\
(k_2 + k_3 + k_4 + k_5 + k_6) = (\beta_1 + \beta_2 + \beta_3) \\
k_2(k_4 + k_6) + k_4(k_5 + k_6) + k_3k_6 = \beta_1\beta_2 + \beta_1\beta_3 + \beta_2\beta_3 \\
k_2k_4k_6 = \beta_1\beta_2\beta_3
\end{array} \right. \quad (\text{Eqn. 5.2.28})$$

A unique solution to the system of equations in (Eqn. 5.2.28) can be obtained by assuming $k_4 \leq k_6$ (i.e. by defining compartment 2 to be the specific binding compartment). In order to calculate this solution, it is helpful to make the definitions in (Eqn. 5.2.29).

$$\left\{ \begin{array}{l}
\Delta \triangleq \alpha_1(\beta_2 + \beta_3) + \alpha_2(\beta_1 + \beta_3) + \alpha_3(\beta_2 + \beta_1) \\
\Omega \triangleq \alpha_1\beta_2\beta_3 + \alpha_2\beta_1\beta_3 + \alpha_3\beta_1\beta_2 \\
\Gamma \triangleq (\beta_1 + \beta_2 + \beta_3) \\
\tilde{\beta} \triangleq \beta_1\beta_2 + \beta_1\beta_3 + \beta_2\beta_3 \\
\eta \triangleq \beta_1\beta_2\beta_3
\end{array} \right. \quad (\text{Eqn. 5.2.29})$$

From (Eqn. 5.2.29), the nonlinear system of equations in (Eqn. 5.2.28) can be re-written as in (Eqn. 5.2.30); where each equation has been labeled with a number.

$$\left\{ \begin{array}{l}
(1) \quad K_1 = (\alpha_1 + \alpha_2 + \alpha_3) \\
(2) \quad K_1(k_3 + k_4 + k_5 + k_6) = \Delta \\
(3) \quad K_1[k_4(k_5 + k_6) + k_3k_6] = \Omega \\
(4) \quad (k_2 + k_3 + k_4 + k_5 + k_6) = \Gamma \\
(5) \quad k_2(k_4 + k_6) + k_4(k_5 + k_6) + k_3k_6 = \tilde{\beta} \\
(6) \quad k_2k_4k_6 = \eta
\end{array} \right. \quad (\text{Eqn. 5.2.30})$$

From (Eqn. 5.2.30), k_2 can be calculated by inserting (2) into (4) to give (Eqn. 5.2.31).

$$k_2 = \Gamma - \left(\frac{\Delta}{K_1} \right) \quad (\text{Eqn. 5.2.31})$$

With a form for k_2 , k_4 can be calculated by inserting (3) into (5) to obtain (Eqn. 5.2.32), which can be written in terms of the unknown k_4 using (6) to obtain (Eqn. 5.2.33).

$$k_2(k_4 + k_6) + \frac{\Omega}{K_1} = \tilde{\beta} \quad (\text{Eqn. 5.2.32})$$

$$k_4^2 - \frac{(K_1\tilde{\beta} - \Omega)}{K_1k_2} k_4 + \frac{\eta}{k_2} = 0 \quad (\text{Eqn. 5.2.33})$$

(Eqn. 5.2.33) will have 2 real solutions, r_1 and r_2 , under the assumption that: $\alpha_1, \alpha_2, \alpha_3, \beta_1, \beta_2, \beta_3 > 0$ given in (Eqn. 5.2.34). The existence of two solutions for k_4 is a due to the

symmetry in the 3-tissue compartmental model between the two peripheral compartments x_2 and x_3 . This symmetry can be broken, as suggested above, by assuming $k_4 \leq k_6$ (i.e. that x_2 is the specific compartment) yielding (Eqn. 5.2.35).

$$r_1, r_2 = \frac{(K_1\tilde{\beta}-\Omega)}{2K_1k_2} \pm \frac{1}{2} \sqrt{\left[\frac{(K_1\tilde{\beta}-\Omega)}{K_1k_2}\right]^2 - \frac{4\eta}{k_2}} \quad (\text{Eqn. 5.2.34})$$

$$\begin{cases} k_4 = r_1; k_6 = \frac{4\eta}{k_2r_1}, & \text{if } k_4 \leq k_6 \\ \text{otherwise,} \\ k_4 = r_2; k_6 = \frac{4\eta}{k_2r_2}; \end{cases} \quad (\text{Eqn. 5.2.35})$$

With relations for K_1, k_2, k_4 , and k_6 the two remaining equations in (Eqn. 5.2.30) are (2) and (3). These equations can be re-arranged so that the dependence of k_3 and k_5 on the solved parameters is explicit as in (Eqn. 5.2.36).

$$\begin{cases} (\square) & (k_3 + k_5) = \kappa \\ (\star) & [k_4k_5 + k_3k_6] = \frac{\Omega}{K_1} - k_4k_6 \end{cases} \quad (\text{Eqn. 5.2.36})$$

where, $\kappa \triangleq \left[\frac{\Delta}{K_1} - (k_4 + k_6)\right]$

Solving (\square) for k_3 and inserting into (\star) gives (Eqn. 5.2.37) for k_5 , from which k_3 can be obtained from (Eqn. 5.2.38).

$$k_5 = \left[\frac{\Omega - K_1 k_4 k_6 - K_1 k_6 \kappa}{K_1 (k_4 - \kappa)} \right] \quad (\text{Eqn. 5.2.37})$$

$$k_3 = (\kappa - k_5) \quad (\text{Eqn. 5.2.38})$$

5.2.2 Background: Spectral Analysis of Tracer Uptake in PET

Spectral analysis (SA) provides non-compartmental method that can be used to study the IRF of a tumor tissue time-activity curve (TAC) [171]. The measured tissue response function, $C_T(t)$ is assumed to be described by the convolution of an IRF $h(t)$ of the form in (Eqn. 5.2.39) and the input tracer concentration from the blood $i(t)$; that is SA assumes the measured tissue concentration can be modeled as: $C_T(t) = h(t) \otimes i(t)$.

$$h(t) = \left[\alpha_{-1} \delta(t) + \alpha_0 u(t) + \sum_{j=1}^N \alpha_j e^{-\beta_j t} u(t) \right] \quad (\text{Eqn. 5.2.39})$$

The β_j in $h(t)$ represent fixed candidate poles/eigenvalues of the system IRF. Usually a set of logarithmically spaced candidate β_j are pre-specified by the user [171], but other approaches have been suggested [172]. The goal of SA is to determine the vector with the fewest non-zero coefficients $\bar{\alpha} = [\alpha_{-1} \quad \alpha_0 \quad \dots \quad \alpha_N]^T$ that explains the measured tissue response based on minimization of a specified cost-function.

From the estimated impulse response function, several parameters of interest can be estimated including: i.) the blood volume fraction, $V_B = \alpha_{-1}$, ii.) the transport rate of tracer from blood to tissue, $K_1 = \sum_{j=1}^N \alpha_j$, iii.) the total volume of tracer distribution, $V_T = \sum_{j=1}^N \frac{\alpha_j}{\beta_j}$, and iv.) the overall flux of tracer from blood into the tissue $K_i = \alpha_0$. By focusing on parameters that can be derived directly from the IRF of the system, SA does not require specification of a specific compartmental model structure.

For the majority of SA implementations, the search for the optimal set of spectral coefficients is formulated in the framework of a matrix regression problem for which the matrix of regression vectors Φ is defined as:

$$\Phi = \begin{bmatrix} \phi_{1,-1} & \phi_{1,0} & \cdots & \phi_{1,N} \\ \vdots & \vdots & \ddots & \vdots \\ \phi_{M,-1} & \phi_{M,0} & \cdots & \phi_{M,N} \end{bmatrix} \quad (\text{Eqn. 5.2.40})$$

with,

$$\phi_{ij} = \begin{cases} \frac{1}{(t_{end}^i - t_{start}^i)} \int_{t_{start}^i}^{t_{end}^i} \mathbf{i}(t) dt & ; j = -1 \\ \frac{1}{(t_{end}^i - t_{start}^i)} \int_{t_{start}^i}^{t_{end}^i} \mathbf{i}(t) \otimes \mathbf{u}(t) dt & ; j = 0 \\ \frac{1}{(t_{end}^i - t_{start}^i)} \int_{t_{start}^i}^{t_{end}^i} [\mathbf{i}(t) \otimes e^{-\beta_j t} \mathbf{u}(t)] dt & ; j \geq 1 \end{cases} \quad (\text{Eqn. 5.2.41})$$

where t_{start}^i and t_{end}^i are the start and stop times of the i^{th} PET frame, respectively, and $u(t)$ represents a step-function; thus Φ has size $M \times (N+2)$, where M is the number of PET frames and N is the number of rates, β_j , being tested. As mentioned in Chapter 2 each tissue time activity curve sample represents the time-averaged radioactivity concentration over the corresponding PET acquisition frame; that is, each measured tumor tissue response curve sample is given by $\tilde{C}_T^i = \frac{1}{(t_{end}^i - t_{start}^i)} \int_{t_{start}^i}^{t_{end}^i} C_T(t) dt$. Therefore, to account for this time-averaging, each component in (Eqn. 5.2.41) is shown time-averaged for the actual implementation of spectral analysis. Appendices A.2.1 and A.2.2 describe how, for a given probing rate, the corresponding time-averaged spectral basis vector can be calculated using either the Feng model (Appendix A.2.1) or the generalized Feng model (Appendix A.2.2).

In classical SA the spectral coefficients vector $\bar{\alpha}$ is obtained via constrained minimization of the L_1 or L_2 norm of the residuals; that is by solving the optimization problem:

$$\begin{cases} \min_{\bar{\alpha}}: \left\| \Sigma^{-\frac{1}{2}} (\bar{C}_T - \Phi \bar{\alpha}) \right\|_{L_1, L_2} \\ \text{subject to: } \bar{\alpha} \geq \mathbf{0} \end{cases} \quad (\text{Eqn. 5.2.42})$$

where $\bar{C}_T = [\tilde{C}_T^1 \quad \dots \quad \tilde{C}_T^M]^T$, and Σ represents a matrix of weights. Minimization under either the L_1 or L_2 norms implies different assumptions regarding the probability distribution of measurement noise and are carried out using different optimization algorithms. Specifically, minimization under the L_1 norm, $\min_{\bar{\alpha} \geq 0} \left| \Sigma^{-\frac{1}{2}} (C_T(t) - \Phi \bar{\alpha}) \right|$, allows to recast the optimization

problem as a linear program, and implies that the independent measurement errors each follow a Laplace distribution. Minimization under the L_2 norm results in the well-known non-negative least squares (NNLS) problem $\min_{\bar{\alpha} \geq 0} \left\| \Sigma^{-\frac{1}{2}}(C_T(t) - \Phi \bar{\alpha}) \right\|^2$, implying independent Gaussian distributed measurement errors. However, the results of the two methods are generally consistent [171].

The constraint $\bar{\alpha} \geq 0$ imposes a sparsity requirement on the solution to (Eqn. 5.2.42), which is required since the spectral basis matrix Φ is generally overcomplete (i.e. $N > M$). While SA does not require *a priori* knowledge of the size or connectivity of the underlying compartmental model system, the constraint $\bar{\alpha} \geq 0$ does imply that SA can only be applied to tumor TACs that can be written as a positive weighted sum of convolution integrals between the input concentration and a causal exponential [173]. One class of compartmental model systems that are guaranteed to produce IRFs with all non-negative coefficients are compartmental systems that are strongly connected, contain no cycles, and contain only a single compartment through which tracer can be excreted into the environment [173]. Moreover, any compartmental system containing a trap that can be created by setting a single transfer rate of a noncyclic, strongly connected compartmental system with only one compartment capable of tracer excretion to the environment equal to 0 can also be shown to produce IRFs that have all non-negative coefficients [173]. Essentially all practical compartmental models used in PET pharmacokinetic modeling are members of one of these classes of systems [173].

An important aspect of utilizing SA is the requirement to specify a fixed set of candidate washout rates β_j . If too few β_j are chosen, then the user risks not identifying all of the spectral

components in the signal. On the other hand, if too many β_j are chosen such that the interval between neighboring test β_j is very small, then the analysis will produce spurious spectral components centering around each true decay rate. Moreover, for sufficiently small β_j , spectral components will be indistinguishable from integrated blood activity and, conversely, for sufficiently fast β_j , spectral components will be indistinguishable from the tumor blood pool. That is in the limit $\beta_j \rightarrow 0$, $C_T \approx \int_0^t f(\tau) d\tau$.

Several studies using spectral analysis in PET have proposed and analyzed different methods for generating distributions of β_j , which include linear and logarithmically spaced methods [172] and data adaptive methods have also been proposed [174, 175]. However, in most cases, a simple logarithmic spacing scheme has produced adequate results.

Spectral Analysis using Linear Programming

Using the L_1 norm, (Eq. 5.2.42) becomes (Eq. 5.2.43), which can be written in component form as (Eq. 5.2.44); where Σ is assumed to be a diagonal matrix with non-zero diagonal components denoted σ_i^2 .

$$\min_{\bar{\alpha} \geq \mathbf{0}}: \left| \Sigma^{-\frac{1}{2}} (C_T(t) - \Phi \bar{\alpha}) \right| \quad (\text{Eqn. 5.2.43})$$

$$\min_{\bar{\alpha} \geq \mathbf{0}}: \sum_{i=1}^M \left| \frac{(C_T(t) - \Phi \bar{\alpha})_i}{\sigma_i} \right| \quad (\text{Eqn. 5.2.44})$$

Since the minimization problem in (Eq. 5.2.44) is composed of the summation of absolute value terms all with positive coefficients (i.e. this problem is convex) the solution to (Eq. 5.2.44) can be obtained by solving the equivalent minimization problem in (Eq. 5.2.45) below [176].

$$\begin{aligned}
 & \mathbf{min}: \sum_{i=1}^M s_i \\
 & \mathbf{subject\ to}: \begin{cases} -\bar{\alpha} \leq \mathbf{0} \\ -s_i \leq \mathbf{0}; \forall i \\ \frac{([C_T(t)]_i - [\Phi\bar{\alpha}]_i)}{\sigma_i} \leq s_i; \forall i \\ -\frac{([C_T(t)]_i - [\Phi\bar{\alpha}]_i)}{\sigma_i} \leq s_i; \forall i \end{cases} \quad (\text{Eqn. 5.2.45})
 \end{aligned}$$

(Eqn. 5.2.45) can be re-cast into standard form [177] by defining the $(N+2+M) \times 1$ cost vector $c = [0_{(N+2) \times 1} \mid 1_{M \times 1}]^T$ and the $(N+2+M) \times 1$ parameter vector $\theta = [\alpha_1 \ \dots \ \alpha_N \mid s_1 \ \dots \ s_M]^T$. Moreover, define \mathbf{b}_j to denote the j^{th} column of the spectral dictionary matrix Φ , so that the matrix product $\Phi\bar{\alpha}$ can be written as: $\Phi\bar{\alpha} = \sum_{j=1}^N \alpha_j \mathbf{b}_j$; where \mathbf{b}_j has elements $\mathbf{b}_j = [b_j^1 \ \dots \ b_j^M]^T$. Furthermore, let \mathbf{y} be a $1 \times M$ column vector such that: $\mathbf{y} = [[C_T(t)]_1 \ \dots \ [C_T(t)]_M]^T$.

Now consider the last two constraints in (Eqn. 5.2.45). For a given index i , the second to last constraint can be re-written as in (Eqn. 5.2.46). Re-arranging terms and substituting in: the vectors \mathbf{b}_j and \mathbf{y}_j gives (Eqn. 5.2.47).

$$([\mathbf{C}_T(\mathbf{t})]_i - [\Phi\bar{\alpha}]_i) \leq s_i \sigma_i \quad (\text{Eqn. 5.2.46})$$

$$-[\sum_{j=-1}^N \alpha_j \mathbf{b}_j]_i - s_i \sigma_i \leq -\mathbf{y}_i \quad (\text{Eqn. 5.2.47})$$

By defining the $M \times (N+2+M)$ matrix D_1 as in (Eqn. 5.2.48), (Eqn. 5.2.47) can be re-written in vector notation as in (Eqn. 5.2.49).

$$D_1 = (-\mathbf{1})x \left[\begin{array}{cccc|cccc} \mathbf{b}_{-1}^1 & \mathbf{b}_0^1 & \cdots & \mathbf{b}_N^1 & \sigma_1 & \mathbf{0} & \mathbf{0} & \mathbf{0} \\ \mathbf{b}_{-1}^2 & \mathbf{b}_0^2 & \cdots & \mathbf{b}_N^2 & \mathbf{0} & \sigma_2 & \vdots & \vdots \\ \vdots & \vdots & \vdots & \vdots & \vdots & \mathbf{0} & \ddots & \mathbf{0} \\ \mathbf{b}_{-1}^M & \mathbf{b}_0^M & \cdots & \mathbf{b}_N^M & \mathbf{0} & \cdots & \mathbf{0} & \sigma_M \end{array} \right] \quad (\text{Eqn. 5.2.48})$$

$$D_1 \theta \leq -\mathbf{y} \quad (\text{Eqn. 5.2.49})$$

Similarly, for a given index i , the last constraint in (Eqn. 5.2.45) can be re-written as in (Eqn. 5.2.50). Re-arranging terms and substituting in: the vectors \mathbf{b}_j and \mathbf{y}_j gives (Eqn. 5.2.51).

$$[\Phi\bar{\alpha}]_i - s_i \sigma_i \leq [\mathbf{C}_T(\mathbf{t})]_i \quad (\text{Eqn. 5.2.50})$$

$$[\sum_{j=1}^N \alpha_j \mathbf{b}_j]_i - s_i \sigma_i \leq \mathbf{y}_i \quad (\text{Eqn. 5.2.51})$$

By defining the $M \times (N+2+M)$ matrix D_2 as in (Eqn. 5.2.52), (Eqn. 5.2.51) can be written in vector notation as in (Eqn. 5.2.53).

$$D_2 = \left[\begin{array}{cccc|cccc} b_{-1}^1 & b_0^1 & \cdots & b_N^1 & -\sigma_1 & \mathbf{0} & \mathbf{0} & \mathbf{0} \\ b_{-1}^2 & b_0^2 & \cdots & b_N^2 & \mathbf{0} & -\sigma_2 & \vdots & \vdots \\ \vdots & \vdots & \vdots & \vdots & \vdots & \mathbf{0} & \ddots & \mathbf{0} \\ b_{-1}^M & b_0^M & \cdots & b_N^M & \mathbf{0} & \cdots & \mathbf{0} & -\sigma_M \end{array} \right] \quad (\text{Eqn. 5.2.52})$$

$$D_2 \boldsymbol{\theta} \leq \mathbf{y} \quad (\text{Eqn. 5.2.53})$$

Next, (Eqn. 5.2.49) and (Eqn. 5.2.52) can be used to combine the constraint equations in (Eqn. 5.2.45) into a single set of constraint equations given in (Eqn. 5.2.54), where the $(2 \times M) \times (N+2+M)$ matrix A and the $(2 \times M) \times 1$ column vector \mathbf{d} are defined in (Eqn. 5.2.55).

$$\left[\begin{array}{ccc} D_1 \boldsymbol{\theta} & \leq & -\mathbf{y} \\ - & - & - \\ D_2 \boldsymbol{\theta} & \leq & \mathbf{y} \end{array} \right] = A \boldsymbol{\theta} \leq \mathbf{d} \quad (\text{Eqn. 5.2.54})$$

$$\left\{ \begin{array}{l} A \triangleq \begin{bmatrix} D_1 \\ - \\ D_2 \end{bmatrix} \\ \mathbf{d} \triangleq [-\mathbf{y}_1 \quad \cdots \quad -\mathbf{y}_M \quad | \quad \mathbf{y}_1 \quad \cdots \quad \mathbf{y}_M]^T \end{array} \right. \quad (\text{Eqn. 5.2.55})$$

Finally, using (Eqn. 5.2.54) the linear program in (Eqn. 5.2.45) can be written in standard form [177] as in (Eqn. 5.2.56) below. The linprog.m function available in the optimization toolbox

of MATLAB (R2014a, The MathWorks, Natick, MA., USA) can then be used to solve (Eqn. 5.2.56) for the spectral coefficients contained in θ .

$$\begin{aligned} & \min: c^T \theta \\ & \text{subject to: } \begin{cases} A\theta \leq d \\ \theta \geq 0 \end{cases} \end{aligned} \quad (\text{Eqn. 5.2.56})$$

5.2.2.1 Limitations of Spectral Analysis

SA has several advantages for modeling PET tracer pharmacokinetics. Compared to conventional tracer compartmental modeling, in which the kinetic rate parameters are desired, SA makes few assumptions with respect to the connectivity of the tissue compartments and makes no a priori assumptions regarding the number of compartments. However, SA has limitations as well, which primarily arise from the sensitivity of the method to noise [178]. Indeed, measurement noise in the tissue TAC has been shown to result in the detection of spurious components as well as cause components to shift in location away from their true values [178]. Appreciable time-delays between the driving input function and the tissue TAC have also been observed to give rise to spurious components and shifts in component locations [178]. To address this shortcoming Turkheimer et al [178] have proposed an approach using bootstrap resampling of the SA fit residuals (described below) to evaluate the uncertainty in the component spectrum estimate (as well as the derived macroparameters) and provide a method for bias estimation and removal [178].

Additional challenges result from the finite number of probing rates used to generate the spectral dictionary. Specifically, in experimental conditions 2 or more neighboring components

are often detected (usually with different values for their coefficients), suggesting that the true-value of the spectral component falls somewhere in between [171, 172]. To date, there are no completely satisfactory methods for combining adjacent spectral components to obtain an accurate estimate of the true value; though approaches have been suggested [171, 172].

Due in part to the aforementioned challenges, SA is most often used as an exploratory method in tracer pharmacokinetic modeling. In this context the results of SA are used as a guide to support traditional compartmental modeling, especially for the purposes of model selection.

Bootstrap Method for Variance & Bias Estimation of the Component Spectrum

The goal of SA is to determine the coefficient vector $\bar{\alpha} = [\alpha_0 \quad \dots \quad \alpha_N]^T$ and compute the compartmental macroparameters (eg. V_T , K_1 , K_i) that can be derived from these coefficients; though, due to measurement noise, only an estimate of the spectral coefficient vector, denoted $\hat{\alpha}$, is obtainable. As a result of the high sensitivity of SA to measurement noise, knowledge of the probability distribution of the components would be highly desirable for uncertainty analysis. Moreover, since the macroparameters K_1 , V_T , and K_i are themselves a function of the corresponding estimate $\hat{\alpha}$, their individual sampling distributions will depend on the multivariate sampling distribution for $\hat{\alpha}$. However, even with the simplifying assumptions of zero mean Gaussian errors (NNLS method) or Laplace Distributed errors (L_1 norm case), it is difficult to determine the joint-distribution of the spectral coefficients directly from the underlying error distributions.

Bootstrap resampling provides a simple method for assessing uncertainty in an estimator when the sampling distribution for that estimator is unknown or difficult to determine [179]. Initially introduced by Efron et al [180], the bootstrap method has the advantage of requiring very few assumptions regarding the estimator sampling distribution, and can be used to obtain percentile confidence intervals for the estimator [178, 179]. The application of the bootstrap to SA was first described by Turkheimer et al [178], who used the bootstrap to assess uncertainty in the location of the detected spectral components as well as investigate bias in the estimates.

Following Turkheimer et al [178], SA is first performed using the measured tissue TAC from which the estimate for the spectrum ($\hat{\alpha}$) and a corresponding set of residuals $R = \{r_1, r_1, \dots, r_M\}$ is obtained. If SA is performed as described in (Eqn. 5.2.42) above, the residuals will all have the same variance. To see this consider that in the case of PET data, the errors are assumed to be normally distributed and independent between independent PET frames, with individual variances proportional to the measured signal (*see Section 2.4.1*), such that $\sigma_i^2 = \alpha_0^2 \left[\frac{x_i e^{\lambda t_i^*}}{(t_i^{end} - t_i^{start})} \right]$, where x_i is the measure activity at the i^{th} frame, t_i^{start} and t_i^{end} denote the start and end times of the i^{th} PET frame, λ is the ^{18}F -decay rate, t_i^* denotes the average time of decay over the i^{th} frame, and α_0^2 is a constant. Hence, the noise covariance matrix of the measured tumor TAC, Σ , is diagonal with the σ_i^2 along the diagonal. Therefore, in order to homogenize the variance a whitening transformation can applied to the data using a Cholesky factorization of Σ^{-1} where $\Sigma^{-1} = DD^T$; however, since Σ^{-1} is diagonal, $D = \Sigma^{-\frac{1}{2}}$.

Note that the outcome of this transformation will cause the data to all have the same variance equal to α_0^2 . The value of α_0^2 is generally unknown but typically ranges between [0.01, 0.1].

Using the estimated spectrum as the ‘true spectrum’, simulated noise can be added to the computed spectrum from the set of fit residuals to generate a set of bootstrap tissue TACs that are then treated as repeated measurements of the generating component spectrum. That is, using bootstrap resampling, B bootstrap tissue TACs, $y^{(b)}$, can be simulated based on the estimated spectrum and the estimated fit residuals such that $y^{(b)} = DA\hat{\alpha} + r^{(b)}$, where the bootstrapped residuals are sampled with replacement from the set of residuals $\{r_1, r_1, \dots, r_M\}$. Typically, the number of bootstrap samples, B, is equal to 1000 or more. With this simulated set of repeated tissue TAC measurements, the bias and uncertainty of the estimated component spectrum ($\hat{\alpha}$) can be estimated.

Specifically, the bias of an estimate is defined as: $b(\alpha) = (\hat{\alpha} - \alpha^{true})$, where α^{true} is the true spectra. To use bootstrap resampling to estimate the bias, denote as the estimate for the bias: $\hat{b}(\alpha^{true}) = (\bar{\alpha}_{boot} - \hat{\alpha})$, where $\bar{\alpha}_{boot}$ is the average of all of the bootstrapped spectra. That is, let the estimate $\hat{\alpha}$ serve as the ‘true’ spectra and let the average of the bootstrap samples serve as the ‘estimate’. Hence the difference between $\bar{\alpha}_{boot}$ and $\hat{\alpha}$ provides an estimate of the true bias, from which the bias corrected spectra can then be obtained: $\hat{\alpha}^* = \hat{\alpha} - \hat{b}(\alpha^{true})$.

Bootstrap resampling can also be used to estimate the probability distribution for the biased estimator $\hat{\alpha}$. To this end, consider the j^{th} spectral component $\hat{\alpha}_j$ and the corresponding set of bootstrap estimates: $\{\hat{\alpha}_j^{(1)}, \dots, \hat{\alpha}_j^{(B)}\}$. By ordering the $\hat{\alpha}_j^{(b)}$ from smallest to largest, p-percentiles can be computed, thereby giving an estimate of the cumulative distribution function of $\hat{\alpha}_j$. Now define $\hat{\alpha}_j^{(p)} = \left\{ \alpha \mid \Pr_{\mathcal{F}}(\hat{\alpha}_j \leq \alpha) = p \right\}$, where $\Pr_{\mathcal{F}}(\hat{\alpha}_j \leq \alpha)$ is the probability that the estimate $\hat{\alpha}_j$ takes a value less than or equal to α under the unknown distribution \mathcal{F} ; thus $\hat{\alpha}_j^{(p)}$ denotes the p^{th} bootstrap percentile of the probability distribution for $\hat{\alpha}_j$.

However, since each bootstrapped estimate $\hat{\alpha}_j^{(b)}$ may be a biased estimate for the j^{th} spectral component $\hat{\alpha}_j$, the $\hat{\alpha}_j^{(p)}$ bootstrap percentiles must also be corrected for this bias to get the correct CDF for the estimator $\hat{\alpha}_j$. Thus, the bias corrected bootstrap percentiles for $\hat{\alpha}_j$ are: $\rho(\hat{\alpha}_j, p) = \max\{0, \hat{\alpha}_j^{(p)} - ([\bar{\alpha}_{boot}]_j - \hat{\alpha}_j)\}$. If the estimate $\hat{\alpha}_j$ is itself bias corrected to obtain the bias corrected estimator $\hat{\alpha}_j^* = \hat{\alpha}_j - \hat{b}_j(\alpha_j^{true})$, then the bootstrap percentiles need to be corrected for this additional bias, such that the bootstrap percentiles for the bias corrected estimate $\hat{\alpha}_j^*$ are given by: $\rho(\hat{\alpha}_j^{*(p)}, p) = \max\{0, (\hat{\alpha}_j^{*(p)} - ([\bar{\alpha}_{boot}]_j - \hat{\alpha}_j))\} = \max\{0, \hat{\alpha}_j^{(p)} - 2([\bar{\alpha}_{boot}]_j - \hat{\alpha}_j)\}$.

Using either $\rho(\hat{\alpha}_j, p)$ or $\rho(\hat{\alpha}_j^*, p)$, a 100p% one-sided confidence interval (CI) can be constructed for $\hat{\alpha}_j$ or $\hat{\alpha}_j^*$, respectively, by determining the minimum value of $\hat{\alpha}_j$ or $\hat{\alpha}_j^*$, below which 100p% of the corresponding bootstrap percentiles fall; where $p \in [0,1]$.

Note that the method of bias estimation and generating CIs presented above is general, and, as a result the exact same arguments apply to evaluating estimation bias and generating CIs for estimates of the macroparameteres. That is, let θ denote the true value of one of the macroparameteres and let $\hat{\theta}$ denote its estimate. Then, the approximate bias for the estimate is given by $\hat{b}(\theta) = (\bar{\theta}_{boot} - \hat{\theta})$, where $\bar{\theta}_{boot}$ is the average of all of the bootstrapped estimates of $\hat{\theta}$, such that the bias corrected estimate for θ is $\hat{\theta}^* = \hat{\theta} - \hat{b}(\theta)$. Using either $\rho(\hat{\theta}, p)$ or $\rho(\hat{\theta}^*, p)$, a 100p% two-sided confidence interval (CI) can be constructed for $\hat{\theta}$ or $\hat{\theta}^*$, respectively, by determining the upper and lower bounds within which 100p% of the bootstrap samples reside. That is, if a_L and a_U are the lower and upper bounds within which 100p% of the bootstrap samples reside, then $a_L = \rho\left(\hat{\theta}, \frac{(1-p)}{2}\right)$ and $a_U = \rho\left(\hat{\theta}, \frac{(1+p)}{2}\right)$ for the non-bias corrected case or $a_L = \rho\left(\hat{\theta}^*, \frac{(1-p)}{2}\right)$ and $a_U = \rho\left(\hat{\theta}^*, \frac{(1+p)}{2}\right)$ for the bias corrected case.

5.2.3 Methods

5.2.3.1 PET Image Processing

All PET acquisitions were inspected for inter-frame motion, which, if necessary, was corrected for on a frame-by-frame basis using the motion correction tool available in PMOD 3.6 (PMOD Technologies LLC; Zürich, Switzerland). Because each PET imaging time-point consisted of two PET acquisitions, in which the subject got off the scanner between the two acquisitions, the 120-150 min scan was co-registered to the 0-45 min scan. To this end, the entire (motion corrected if necessary) 0-45 min acquisition was summed to produce a single static image. Next each frame of the 120-150 min acquisition was individually co-registered to the summed

static image derived from the 0-45 min scan using the normalized mutual information method available in PMOD 3.6. The resulting transformation was then applied to each individual frame of the 120-150 min scan, which was then combined with the 0-45 min acquisition to form a single dynamic acquisition volume.

5.2.3.2 Whole Tumor Tissue Time Activity Curve Extraction

Tumor VOI were defined for each acquisition by first summing together the entire 51 frame PET image to create a single static image. Tumor VOI were defined by drawing an initial VOI around the tumor on the summed PET image and then applying a 30%-to-60% of the difference between the maximum and minimum voxel value threshold to the initial VOI, thereby creating the final VOI from which tumor tissue activity curves could be extracted. For the reasons described above in the IBIF VOI sub-section, no metabolite correction was applied to the measured tumor tissue TAC.

5.2.3.3 Healthy Tissue Time Activity Curve Extraction

Healthy tissue VOI were defined for each acquisition by first summing together the entire 51 frame PET image to create a single static image. Next a 1.5 cm (radius) sphere was drawn in an uninvolved region of the brain, generally located in the lobe opposite to that containing the brain tumor, using the sphere VOI tool available in PMOD 3.6. For the reasons described above in the IBIF VOI sub-section, no metabolite correction was applied to the measured healthy tissue TAC.

5.2.3.4 Joint IBIF & Tumor IRF Model Order Selection

Throughout this dissertation, the measured [^{18}F]ML-10 uptake in each tumor, $C_T(t)$ is assumed to be a superposition of the [^{18}F]ML-10 activity in the tumor vasculature with the activity in the tumor tissue. Mathematically, $C_T(t)$ is modeled as in (Eqn. 5.2.57) where $V_B \in [0, 1]$ quantifies the fraction of the measured tumor tissue TAC that comes from the tumor vasculature, $h(t)$ denotes the particular impulse response function (IRF) model, and \otimes represents the convolution operation.

$$C_T(t) = V_B C_B(t) + (1 - V_B)[h(t) \otimes C_B(t)] \quad (\text{Eqn. 5.2.57})$$

Initial IBIF model selection analysis was performed in *Section 5.1*, where the IBIF was measured from each subject's internal carotid arteries. However, because the tumor tissue TAC is being modeled as a sum of the tracer concentration in the blood (i.e. attenuated IBIF) plus the tumor response to the IBIF, model order selection was carried out using a joint IBIF-IRF modeling approach.

Table 5-6 contains the list of candidate tumor IRF models evaluated for each [^{18}F]ML-10 PET scan. For each IRF Model mathematical form, $C_B(t)$ represents a general IBIF model. IRF Model $1\alpha-0\beta$ describes a tumor uptake profile that is attenuated blood activity only. IRF Model $1\alpha-1\beta$, IRF Model $2\alpha-2\beta$, and IRF Model $3\alpha-3\beta$ describe tracer uptake profiles that are composed of a superposition of 1, 2, and 3 causal exponentials, respectively, that all have non-zero exponential decay rates. That is, these models describe reversible tracer PK. IRF Model $2\alpha-1\beta$ and

IRF Model $3\alpha-2\beta$ each describe a radiotracer uptake profile that is composed of a trapping component, modeled as a scalar times a step-function, in addition to 1 or 2 reversible components, expressed by a single causal exponential, respectively.

Table 5-6. Candidate Impulse Response Models.

IRF Model	Candidate IRF Model Mathematical Form.
1α-0β	$R^{(0)}(t) = [\alpha_0 \delta(t - \tau)] \otimes C_B(t)$
1α-1β	$R^{(1)}(t) = [\alpha_1 e^{-\beta_1(t-\tau)}u(t - \tau)] \otimes C_B(t)$
2α-2β	$R^{(2)}(t) = \left[\sum_{i=1}^2 \alpha_i e^{-\beta_i(t-\tau)}u(t - \tau) \right] \otimes C_B(t)$
3α-3β	$R^{(3)}(t) = \left[\sum_{i=1}^3 \alpha_i e^{-\beta_i(t-\tau)}u(t - \tau) \right] \otimes C_B(t)$
2α-1β	$T^{(1)}(t) = [\alpha_1 e^{-\beta_1(t-\tau)}u(t - \tau) + \alpha_2 u(t - \tau)] \otimes C_B(t)$
3α-2β	$T^{(2)}(t) = \left[\sum_{i=1}^2 \alpha_i e^{-\beta_i(t-\tau)}u(t - \tau) + \alpha_3 u(t - \tau) \right] \otimes C_B(t)$
\otimes denotes the convolution operation. $C_B(t)$ represents a general image-based input function model.	

In *Section 5.1.4*, it was found that either IBIF Model 1b, IBIF Model 1c, or IBIF Model 2b was selected as the best candidate IBIF model (based on minimum AIC_c and model parameter estimability) to describe the measured [^{18}F]ML-10 uptake profile in the internal carotid arteries for 28 of 29 PET scans analyzed. The mathematical forms of these IBIF models are repeated in table 5-7 below. Each model in table 5-7 was used as the $C_B(t)$ in the table of tissue response models. That is, a total of 18 candidate models (6 IRF models and 3 IBIF models) were tested per subject per time-point.

Table 5-7. List of Candidate IBIF Models.

IBIF Model	Candidate IBIF Model Mathematical Form.
Model 1b	$f^{(2)}(t) = \left\{ \left[\theta_0(t - \tau) - \sum_{i=1}^2 \theta_i \right] e^{-p_0(t-\tau)} + \sum_{i=1}^2 \theta_i e^{-p_i(t-\tau)} \right\} u(t - \tau);$
Model 1c	$f^{(3)}(t) = \left\{ \left[\theta_0(t - \tau) - \sum_{i=1}^3 \theta_i \right] e^{-p_0(t-\tau)} + \sum_{i=1}^3 \theta_i e^{-p_i(t-\tau)} \right\} u(t - \tau);$
Model 2b	$g^{(2)}(t) = \{ \alpha_0(t - (\tau + \tau_\alpha)) e^{-\alpha_1(t - (\tau + \tau_\alpha))} \} u(t - (\tau + \tau_\alpha)) + f^{(2)}(t);$

Derivation of the Joint Log-Likelihood Function

As part of the derivation of the joint IBIF-IRF likelihood function, it was assumed that the measurement noise between independent PET frames is independent and that the measurement errors between the IBIF TAC obtained from the internal carotid arteries and the tumor TAC are not correlated. Moreover, it was assumed that the measured IBIF and tumor TAC values follow a multivariate Gaussian distribution. Under these assumptions, it can be shown that the cross-correlation between the input measurements and the tissue response measurements is equal to 0 such that the covariance matrix for each PET frame is diagonal. Hence, the uncertainties in the IBIF and IRF model parameters are related solely through the gradient of (Eqn. 5.2.57) in the associated Fisher information matrix (Eqn. 5.1.3) in Section 5.1.2.

(Eqn. 5.2.58) contains the general form of the joint Gaussian probability distribution for the i^{th} PET frame. Specifically, $M(\theta, \delta; \bar{t}_i) \triangleq [f(\theta; \bar{t}_i) \quad g(\theta, \delta; \bar{t}_i)]^T$ is a 2x1 column vector, where $f(\theta; \bar{t}_i)$ and $g(\theta, \delta; \bar{t}_i)$ denote the time-averaged values of the IBIF and tissue response models during the i^{th} frame, respectively. θ and δ represent the corresponding IBIF and tissue

model parameter vectors, respectively. Furthermore, x_i denotes the 2x1 column vector containing the i^{th} input, u_i , and tumor tissue, v_i , sample pairs (i.e. $x_i \triangleq [u_i, v_i]^T$).

$$p(x_i; \theta, \delta, \bar{t}_i) = (2\pi)^{-1} |\Sigma_i|^{-\frac{1}{2}} e^{-\frac{1}{2} [x_i - M(\theta, \delta; \bar{t}_i)]^T \Sigma_i^{-1} [x_i - M(\theta, \delta; \bar{t}_i)]} \quad (\text{Eqn. 5.2.58})$$

(Eqn. 5.2.59) gives the form of the joint-covariance matrix for the i^{th} PET frame, where $\sigma_{1,i}^2$ and $\sigma_{2,i}^2$ are the input and tissue sample variances for the i^{th} PET frame, respectively. For the i^{th} PET frame, the measured IBIF and tissue response noise variances were assumed to have the form: $\sigma_{1,i}^2 = \alpha_{0,u}^2 \left[\frac{u_i e^{\lambda t_i^*}}{(t_i^{\text{end}} - t_i^{\text{start}})} \right]$ and $\sigma_{2,i}^2 = \alpha_{0,v}^2 \left[\frac{v_i e^{\lambda t_i^*}}{(t_i^{\text{end}} - t_i^{\text{start}})} \right]$, respectively, where t_i^{start} and t_i^{end} are the start and end times of the i^{th} PET frame, λ is the ^{18}F -decay rate ($\lambda = 0.00631 \text{ min}^{-1}$), t_i^* denotes the average time of decay over the i^{th} frame, and $\alpha_{0,v}^2$ and $\alpha_{0,u}^2$ are constants of proportionality not necessarily equal to each other.

$$\Sigma_i = \begin{bmatrix} \sigma_{1,i}^2 & \mathbf{0} \\ \mathbf{0} & \sigma_{2,i}^2 \end{bmatrix} \quad (\text{Eqn. 5.2.59})$$

Treating the measurement noise in each PET frame as statistically independent, the likelihood function for the simultaneous system is given by the product of the individual probability densities (Eqn. 5.2.60), which has log-likelihood function given by (Eqn. 5.2.61).

$$\begin{cases} \mathcal{L}(\boldsymbol{\theta}, \boldsymbol{\delta}) = \prod_{i=1}^N p(\mathbf{x}_i; \boldsymbol{\theta}, \boldsymbol{\delta}, \bar{t}_i) \\ \mathcal{L}(\boldsymbol{\theta}, \boldsymbol{\delta}) = \frac{1}{(2\pi)^N} \prod_{i=1}^N |\boldsymbol{\Sigma}_i|^{-\frac{1}{2}} \mathbf{e}^{-\frac{1}{2}[\mathbf{x}_i - \mathbf{M}(\boldsymbol{\theta}, \boldsymbol{\delta}; \bar{t}_i)]^T \boldsymbol{\Sigma}_i^{-1} [\mathbf{x}_i - \mathbf{M}(\boldsymbol{\theta}, \boldsymbol{\delta}; \bar{t}_i)]} \end{cases} \quad (\text{Eqn. 5.2.60})$$

$$\ell(\boldsymbol{\theta}, \boldsymbol{\delta}) \triangleq \ln\{\mathcal{L}(\boldsymbol{\theta}, \boldsymbol{\delta})\} = \begin{cases} -N \ln\{2\pi\} - \frac{1}{2} \sum_{i=1}^N \ln\{|\boldsymbol{\Sigma}_i|\} - \\ -\frac{1}{2} \sum_{i=1}^N \left[[\mathbf{x}_i - \mathbf{M}(\boldsymbol{\theta}, \boldsymbol{\delta}; \bar{t}_i)]^T \boldsymbol{\Sigma}_i^{-1} [\mathbf{x}_i - \mathbf{M}(\boldsymbol{\theta}, \boldsymbol{\delta}; \bar{t}_i)] \right] \end{cases} \quad (\text{Eqn. 5.2.61})$$

Joint IBIF/IRF Parameter Estimation

The basic strategy of estimating both the IBIF and IRF model parameters will be to use a coordinate decent approach to maximize the log-likelihood function in (Eqn. 5.2.61).

As stated in the previous section, \mathbf{x}_i denotes the 2x1 column vector containing the input, \mathbf{u}_i , and tumor tissue, \mathbf{v}_i , sample pairs (i.e. $\mathbf{x}_i \triangleq [\mathbf{u}_i, \mathbf{v}_i]^T$) for the i^{th} PET frame. To see how both IBIF and IRF model parameters can be estimated, let $h(t)$ denote a particular impulse response model from table 5-6, and $f(t; \theta)$ represent a particular IBIF model from table 5-7. Then, from (Eqn. 5.2.57) above, the general tissue response model will be given by $C_T(t; \theta, \delta) = V_B f(t; \theta) + (1 - V_B)[h(t; \delta) \odot f(t; \theta)]$. Thus, with functional forms for the IBIF (i.e. $f(\theta; t)$) and the tissue response model (i.e. $C_T(\theta, \delta; t)$) the 2x1 model vector: $M(t_i; \theta, \delta) \triangleq [f(\theta; t_i) \quad C_T(\theta, \delta; t_i)]^T$ can be formed for each PET frame and used for maximization of the log-likelihood function in (Eqn. 5.2.61).

However, it is important to point out that in PET the measured IBIF and tissue response samples represent the time-averages of their true concentrations over corresponding frame dwell

times. As a result, it is the time-averaged versions of $f(\theta; t_i)$ and $C_T(\theta, \delta; t_i)$ that are actually used during the weighted least squares fitting. The use of the time-averaged versions of the input and tissue models is emphasized in (Eqn. 5.2.61) by writing the 2x1 model vector as $M(\bar{t}_i; \theta, \delta)$ where \bar{t}_i denotes time-averaging over the i^{th} PET frame.

In terms of the actual optimization a multi-stage approach was used, which consisted of a.) determining an initial guess, δ^0 , for the candidate IRF model, given the corresponding vector of initial guess parameters for the IBIF model θ_0 , followed by b.) a coordinate descent procedure to determine to obtain initial guess parameters for c.) a constrained nonlinear weighted maximization that allowed all IBIF and IRF model parameters to float. All constrained optimization was carried out using the `fmincon.m` function available in the optimization toolbox of MATLAB (R2014a, The MathWorks, Natick, MA., USA).

Figure 5-9 shows the workflow for generating the IRF initial guess parameter vector δ^0 . 500 random initial guesses were generated using the `MultiStart.m` function in the MATLAB optimization toolbox (R2014a, The MathWorks, Natick, MA., USA). Each of these random initial guesses were used as starting points for un-weighted OLS constrained maximization of (Eqn. 5.2.61) using only the first 0-45 min worth of measured tissue data. The solution to the OLS maximization from the 0-45 min data was then used as a starting point for un-weighted constrained OLS maximization using the complete set (0-150 min data) of measured tumor tissue concentration samples. The resulting solution obtained from the constrained, un-weighted OLS maximization of (Eqn 5.2.61) yielded the desired initial guess δ_0 , for the final weighted, unconstrained maximization of the likelihood function in (Eqn. 5.2.61.). Throughout the entire process used to

obtain δ_0 , the candidate IBIF model parameters, θ^0 , were held fixed to equal the estimated IBIF model parameters obtained during the IBIF model selection analysis in *Section 5.1*.

Figure 5-9 shows the workflow for the 3-stage coordinate descent procedure used to maximize (Eqn. 5.2.61) and obtain IBIF and tissue model parameter estimates, denoted as $\bar{\theta}$ and $\bar{\delta}$ respectively, to be used as initial guesses for the final constrained nonlinear weighted optimization of (Eqn. 5.2.61), in which all parameters were allowed to float simultaneously. The initial parameter guesses for the candidate IBIF model (θ^0) and candidate tissue model (δ^0) were used as initial starting points for the constrained nonlinear optimization. The first stage of the coordinate descent held the IBIF model parameters fixed while performing a weighted-constrained optimization of (Eqn. 5.2.61) allowing only the tissue model parameters to float. Next, a weighted-constrained maximization of (Eqn. 5.2.61) was performed allowing only the IBIF model parameters to float while keeping the tissue model parameter estimates fixed to their previously estimated values. Finally, the new value of the log-likelihood was calculated using the updated tissue and IBIF model parameters and compared to the previous value. If the relative change between the new value of the log-likelihood function and the previous value increased by less than 10^{-10} , the algorithm was said to converge.

Finally, the IBIF and IRF model estimates from the coordinate descent procedure were then used as initial guesses for constrained nonlinear weighted optimization of (Eqn. 5.2.61), in which all parameters were allowed to float simultaneously. The IBIF and IRF model estimates obtained from this final optimization step were used as the final estimates $\hat{\theta}$ and $\hat{\delta}$. For both the coordinate descent and the final simultaneous weighted optimization procedures, the frame-by-

frame weights matrices used during maximization were obtained from the inverses of the joint covariance matrices (Σ_i^{-1} ; (Eqn. 5.2.59)).

All constraints for IBIF and IRF model fitting consisted of set constraints only. The set constraints used for IBIF model fitting were the same set constraints described previously in *Section 5.1.3.5*. For the case of IRF model fitting, the linear coefficients (i.e. α_i) were restricted to be in the range $\alpha_i \in [0, \infty) \text{ min}^{-1}$ while exponential washout rates β_j were restricted to the range $\beta_j \in [0, 10] \text{ min}^{-1}$. The IRF time delay parameter was constrained to be $\tau \in [0, 2] \text{ min}$.

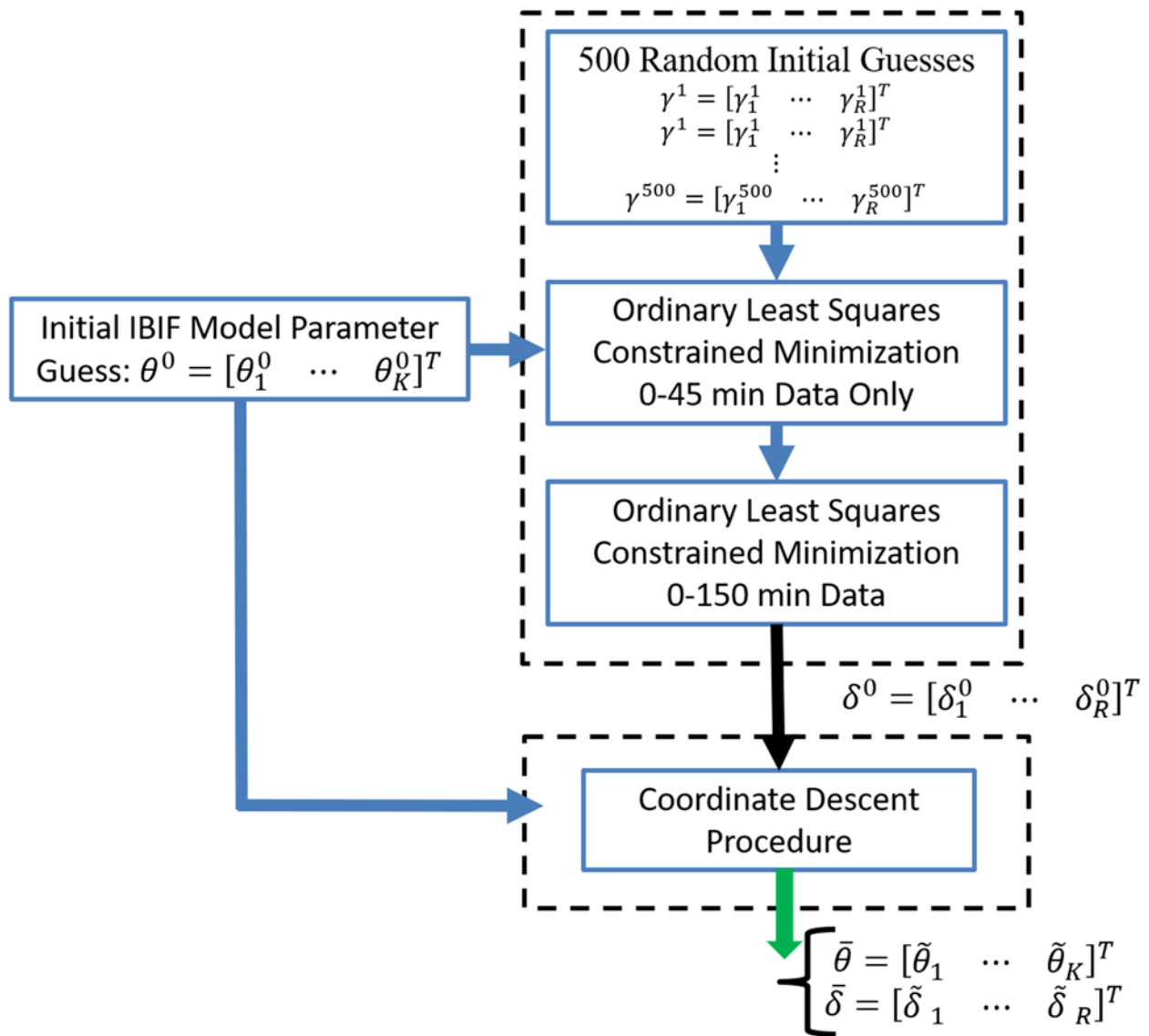


Figure 5-10. Procedure for Generating Initial Tissue Model Parameter Guesses for Maximization of the Joint IBIF and Tissue Model Log-Likelihood Function.

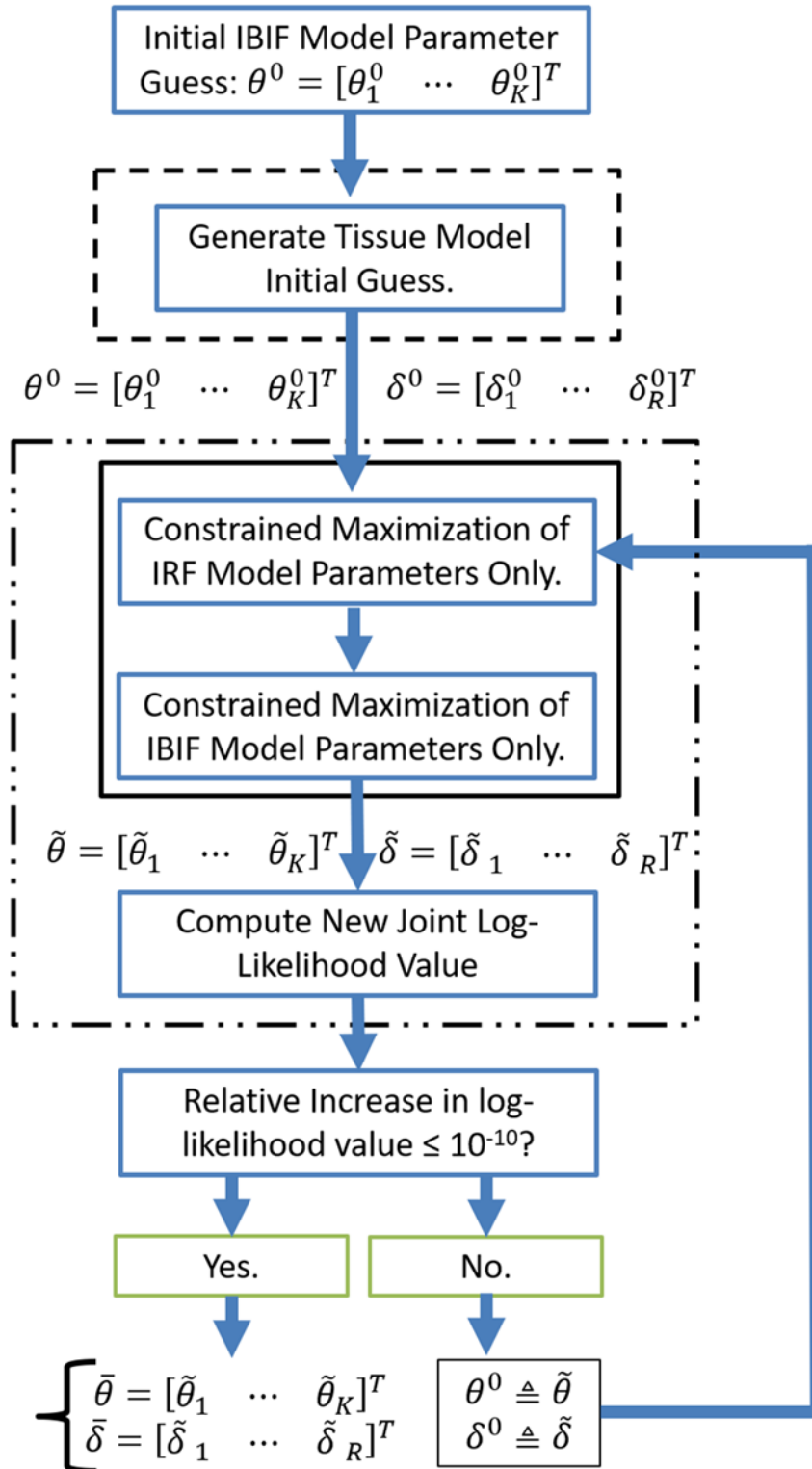


Figure 5-11. Coordinate Descent Procedure for Maximizing Joint IBIF and Tissue Model Log-Likelihood Function.

Statistical Evaluation of Joint IBIF/IRF Model Fit & Parameter Estimates

The residuals from each IBIF and IRF model fit were evaluated for normality via the Kolmogorov-Smirnov test, as well as correlation using the runs test [181], which counts the number of sign changes in the residuals.

Estimates for parameter variances were obtained by calculating the inverse of the Fisher information matrix for each joint IBIF/IRF model. Specifically, because the measurement errors are assumed to follow a Gaussian distribution, (Eqn. 5.1.3) can be used to compute the form of the Fisher Information matrix for the parameters of each candidate joint IBIF/IRF model, the inverse of which provides an estimate for the model parameter covariance matrix, (Eqn. 5.1.4).

Based on the obtained estimates of candidate joint IBIF/IRF model covariance matrices, the COV for each model parameter was computed, where the COV of a particular model parameter γ is given by the ratio of the standard deviation of the estimate, $\hat{\sigma}_\gamma$, divided by the estimated value of that parameter, $\hat{\gamma}$, that is $\widehat{COV}_\gamma = \frac{\hat{\sigma}_\gamma}{\hat{\gamma}}$. For the purposes of model fitting, a small COV for each model parameter is desired, as a large COV value for a model parameter suggests poor parameter estimability and can be indicative of model over-fitting and/or high correlation among model parameters [154].

Joint IBIF/IRF Model Selection

Candidate joint IBIF/IRF models were compared based on minimum AIC_c as well as model parameter estimability considerations. The AIC_c was previously described in Section 5.1.1. Briefly,

the standard Akaike Information Criteria (AIC) is given by: $AIC = -2 * \log(L(\hat{\theta})) + 2K$; where $L(\hat{\theta})$ denotes the maximum-likelihood value of the model being fitted and K is equal to the total number of estimated parameters. The noise model (Eqn. 5.2.58) (also see paragraph below (Eqn. 5.2.58)) included 2 additional parameters ($\alpha_{0,v}^2$ and $\alpha_{0,u}^2$) that were estimated in addition to the parameters specific to the IBIF and IRF models being fitted. The AICc compensates for small sample sizes relative to the number of parameters in the model being fitted, and can be obtained from the AIC as: $AIC_c = AIC + \frac{2K(K+1)}{N-K-1}$ [161]. In cases where the ratio of the number of samples (here, $N = 102$) to number of parameters of the largest model is small (i.e. $\frac{N}{K} < 40$), the AICc is generally recommended over the AIC [161].

Candidate joint IBIF/IRF models were first ranked based on relative differences in the small sample AICc, where the joint IBIF/IRF model with the minimum AICc score was taken to be the preliminary best model supported by the data. Next, the %COV (where %COV is the COV expressed as a percentage) of each parameter in the minimum AICc joint IBIF/IRF model was estimated. If the minimum AICc IRF model yielded one or more parameter estimates with %COV > 50%, then the IRF model was deemed not estimable, then the complexity of the IRF model (but not the IBIF model) was reduced by 1 parameter. If the reduced IRF model also yielded one or more parameter estimates with %COV > 50% the IRF model was again reduced by 1 parameter until an estimable IRF model was obtained. The same model reduction technique was implemented if the minimum AICc IBIF model yielded one or more parameter estimates with %COV > 50%, with the only difference being that the IBIF model (but not the IRF model) was reduced in complexity until an estimable IBIF model was obtained.

5.2.3.5 Estimating the Compartmental Rate Constants

All compartmental rate constants were calculated using the corresponding IRF model parameters (i.e. $\alpha_1, \alpha_2, \dots, \beta_1, \beta_2, \dots$) and the systems of equations in (Eqn. 5.2.17), (Eqn. 5.2.22), and (Eqn. 5.2.28) appropriate for a 1-tissue, 2-tissue and 3-tissue compartmental model, respectively. In the specific cases of the 2-tissue (Eqn. 5.2.22) and 3-tissue (Eqn. 5.2.28) compartmental models, the solve.m function available in the MATLAB symbolic toolbox (R2018a, The MathWorks, Natick, MA., USA) was used to obtain the associated transformation equations relating the IRF and compartmental rate constants. In order to obtain a unique solution for the 3-tissue compartment system, (Eqn. 5.2.28), it was assumed $k_4 \leq k_6$.

Estimating the Covariance Matrix of the Compartmental Rate Constants

All compartmental rate constants were calculated from algebraic transformations applied to the corresponding IRF model estimates (see above paragraph). Define the $r \times 1$ column vector $\boldsymbol{\theta} = [\alpha_1, \alpha_2, \dots, \alpha_K, \beta_1, \beta_2, \dots, \beta_K]^T$, where K equals the number of tissue compartments in the compartmental model. Next, let $\mathbf{g}(\boldsymbol{\theta})$ be an $r \times 1$ column vector containing as its elements the algebraic transformation equations relating the compartmental rate constants (K_1, k_2, \dots, k_r) to the IRF parameters in $\boldsymbol{\theta}$. That is, define $g(\boldsymbol{\theta})$ as in (Eqn. 5.2.62) below.

$$\mathbf{g}(\boldsymbol{\theta}) = \begin{bmatrix} K_1(\boldsymbol{\theta}) \\ k_2(\boldsymbol{\theta}) \\ k_3(\boldsymbol{\theta}) \\ \vdots \\ k_r(\boldsymbol{\theta}) \end{bmatrix} \quad (\text{Eqn. 5.2.62})$$

Because the measurement errors are assumed to follow a Gaussian distribution, (Eqn. 5.1.3) can be used to compute the form of the Fisher information matrix $I(\boldsymbol{\theta})$ for the parameters of each candidate joint IBIF/IRF model. Moreover, because the IRF model estimates in $\boldsymbol{\theta}$ are maximum likelihood estimates (MLEs), the rate constant estimates in (Eqn. 5.2.62) are all MLEs as well, with estimated covariance matrix given by (Eqn. 5.2.63) where $\frac{\partial g(\boldsymbol{\theta})}{\partial \boldsymbol{\theta}}$ is defined as in (Eqn. 5.2.64) [153, 155].

$$\boldsymbol{\Sigma}_{g(\boldsymbol{\theta})} = \left(\frac{\partial g(\boldsymbol{\theta})}{\partial \boldsymbol{\theta}} \right) [I(\boldsymbol{\theta})]^{-1} \left(\frac{\partial g(\boldsymbol{\theta})}{\partial \boldsymbol{\theta}} \right)^T \quad (\text{Eqn. 5.2.63})$$

$$\frac{\partial g(\boldsymbol{\theta})}{\partial \boldsymbol{\theta}} = \begin{bmatrix} \frac{\partial g_1(\boldsymbol{\theta})}{\partial \theta_1} & \dots & \frac{\partial g_1(\boldsymbol{\theta})}{\partial \theta_p} \\ \vdots & \vdots & \vdots \\ \frac{\partial g_r(\boldsymbol{\theta})}{\partial \theta_1} & \dots & \frac{\partial g_r(\boldsymbol{\theta})}{\partial \theta_p} \end{bmatrix} \quad (\text{Eqn. 5.2.64})$$

Therefore, when required, the covariance matrix of the associated compartmental rate constants for a particular IRF model was estimated using (Eqn. 5.2.63). The required gradients in (Eqn. 5.2.64) were computed using the `diff.m` function in the symbolic toolbox of MATLAB (R2018a, The MathWorks, Natick, MA., USA).

Sensitivity Analysis.

Sensitivity analysis can be used to evaluate the influence of the compartmental rate constants on the corresponding tissue model, $C_T(t)$, independent of measurement noise

considerations [182, 183]. For this analysis, a sensitivity function $S_{k_i}(t)$ is calculated for each compartmental rate constant that quantifies the influence of a small change in value of the k_i^{th} rate constant (with the others held fixed) on $C_T(t)$ [182, 183]. Based on these functions, the portion of the measured tumor TAC data that most heavily influences the estimated value of each rate constant can be determined. Ideally, different portions of the measured tumor TAC will relate to different compartmental rate constants [183]. In the case that two or more rate constants are primarily influenced by the same portion of the measured tumor TAC, these parameters will be strongly correlated and, in the extreme case, it may not be possible to uniquely separate estimates for these parameters [183].

(Eqn. 5.2.65) gives the general form of the tissue model fit to each [^{18}F]ML-10 tumor TAC for a general input function model $f(t)$ and a general IRF model composed of K causal exponentials, $h(t; \delta)$, where δ denotes the $rx1$ column vector of IRF parameters. The parameter V_B represents the blood volume fraction in the tumor, while \otimes denotes the convolution operation. The transformation equations relating the general tumor IRF model to the 1-tissue, 2-tissue, and 3-tissue compartmental models appropriate for PET were derived in *Section 5.2.1*.

$$\begin{cases} C_T(\mathbf{t}; \delta) = V_B f(t) + (1 - V_B)[h(\mathbf{t}; \delta) \otimes f(t)] \\ \text{where,} \\ \delta = [\alpha_1, \alpha_2, \dots, \alpha_K, \beta_1, \beta_2, \dots, \beta_K]^T \end{cases} \quad (\text{Eqn. 5.2.65})$$

The sensitivity function $S_{k_i}(t)$, characterizing the influence of a $\gamma\%$ increase in value of the k_i^{th} rate constant is given by (Eqn. 5.2.66); where $\theta^{(i)}$, (Eqn. 5.2.67), denotes the $(r-1) \times 1$ column vector of rate constants that are held constant.

$$S_{k_i}(t) = \frac{[C_T(t, k_i + \gamma k_i; \theta^{(i)}) - C_T(t, k_i; \theta^{(i)})]}{C_T(t, k_i; \theta^{(i)})} \quad (\text{Eqn. 5.2.66})$$

$$\theta^{(i)} = [k_1, k_2, \dots, k_{i-1}, k_{i+1}, \dots, k_r]^T \quad (\text{Eqn. 5.2.67})$$

Because the compartmental rate constants are calculated from estimates of the IRF model parameters in δ , the sensitivity functions $S_{k_i}(t)$ cannot be directly obtained from model fitting. However, they can be approximated using a first order Taylor expansion of $C_T(t, k_i; \theta^{(i)})$ in the neighborhood of the k_i^{th} rate constant. (Eqn. 5.2.68) gives the first order Taylor approximation to $C_T(t, k_i; \theta^{(i)})$ in the neighborhood of the estimate k_i for a γ increase in the value of k_i . Rearranging terms in (Eqn. 5.2.68) and dividing both sides by $C_T(t, k_i; \theta^{(i)})$ produces (Eqn. 5.2.69). Thus, for small γ (Eqn. 5.2.65) can be approximated using (Eqn. 5.2.70). For the present analysis $\gamma = 0.01$.

$$C_T(t, k_i + \gamma k_i; \theta^{(i)}) \approx C_T(t, k_i; \theta^{(i)}) + \frac{\partial C_T}{\partial k_i} ([k_i + \gamma k_i] - k_i) \quad (\text{Eqn. 5.2.68})$$

$$\frac{[C_T(t, k_i + \gamma k_i; \theta^{(i)}) - C_T(t, k_i; \theta^{(i)})]}{C_T(t, k_i; \theta^{(i)})} \approx \left[\frac{\gamma k_i}{C_T(t, k_i; \theta^{(i)})} \right] \left(\frac{\partial C_T}{\partial k_i} \right) \quad (\text{Eqn. 5.2.69})$$

$$\mathbf{S}_{k_i}(\mathbf{t}) \approx \left[\frac{\gamma \mathbf{k}_i}{C_T(t, k_i; \theta^{(l)})} \right] \left(\frac{\partial C_T(t, k_i; \theta^{(l)})}{\partial k_i} \right) \quad (\text{Eqn. 5.2.70})$$

The values of the partial derivatives $\frac{\partial C_T(t, k_i; \theta^{(l)})}{\partial k_i}$ can be obtained using the chain rule for differentiation and solving the resulting linear system in (Eqn. 5.2.71). The elements of the matrix of partial derivatives of the rate constants with respect to the IRF model parameters were computed using the diff.m function in the symbolic toolbox of MATLAB (R2018a, The MathWorks, Natick, MA., USA).

$$\begin{bmatrix} \frac{\partial C_T}{\partial \alpha_1} \\ \vdots \\ \frac{\partial C_T}{\partial \alpha_K} \\ \frac{\partial C_T}{\partial \beta_1} \\ \vdots \\ \frac{\partial C_T}{\partial \beta_K} \end{bmatrix} = \begin{bmatrix} \frac{\partial K_1}{\partial \alpha_1} & \frac{\partial k_2}{\partial \alpha_1} & \dots & \frac{\partial k_r}{\partial \alpha_1} \\ \vdots & \vdots & \dots & \vdots \\ \frac{\partial K_1}{\partial \alpha_K} & \frac{\partial k_2}{\partial \alpha_K} & \dots & \frac{\partial k_r}{\partial \alpha_K} \\ \frac{\partial K_1}{\partial \beta_1} & \frac{\partial k_2}{\partial \beta_1} & \dots & \frac{\partial k_r}{\partial \beta_1} \\ \vdots & \vdots & \vdots & \vdots \\ \frac{\partial k_r}{\partial \alpha_1} & \frac{\partial k_r}{\partial \alpha_1} & \frac{\partial k_r}{\partial \alpha_1} & \frac{\partial k_r}{\partial \alpha_1} \end{bmatrix} \begin{bmatrix} \frac{\partial C_T}{\partial K_1} \\ \frac{\partial C_T}{\partial k_2} \\ \frac{\partial C_T}{\partial k_3} \\ \vdots \\ \frac{\partial C_T}{\partial k_r} \end{bmatrix} \quad (\text{Eqn. 5.2.71})$$

5.2.3.6 Exploratory Spectral Analysis

SA was performed using both NNLS and L_1 norm minimization methods following the approaches described in Section 5.2.2. For both methods, SA was performed on tumor TACs that were corrected for radioactive decay. 151 logarithmically spaced rates, β_j , in the interval $[10^{-4} \text{ min}^{-1}, 200 \text{ min}^{-1}]$ were chosen for the basis vectors. The IBIF model selected as part of the joint IBIF/IRF model selection analysis (see Section 5.2.3.4) for each $[^{18}\text{F}]\text{ML-10}$ acquisition served as the 'true' (assumed noiseless) input function driving each corresponding measured tissue response.

All spectra were corrected for estimation bias using the bootstrap resampling approach described in *Section 5.2.2* with $B = 1000$ bootstrap samples. Furthermore, bias corrected one-sided 95% bootstrap confidence intervals were generated for each spectral component as described in *Section 5.2.2* in order to evaluate the veracity of detected spectral components.

Both the NNLS and L_1 norm minimization methods were carried out using MATLAB (2014a, The MathWorks, Natick, MA., USA) built-in functions. Specifically, NNLS was performed using the default settings of the `nonneglsq.m` function available in the optimization toolbox of MATLAB (2014a, The MathWorks, Natick, MA., USA). Solution to the minimum L_1 norm method was obtained by first re-writing the SA problem into standard form [177] for a linear program (see *Section 5.2.2*). The actual optimization was performed using the using the simplex algorithm and default settings of the `linprog.m` function available in the optimization toolbox of MATLAB (2014a, The MathWorks, Natick, MA., USA).

Estimating a Fast-Rate Threshold: A Data Adaptive Approach

For sufficiently fast β_j , spectral components will be indistinguishable from the tumor blood pool. That is in the limit $\beta_j \rightarrow \infty$, then $C_T \approx \frac{1}{\beta_j} f(t)$. Here we describe a data-adaptive approach that can be used to determine a fast-rate threshold, such that any spectral components detected at β_j larger than the threshold can be interpreted as noise components from blood pool.

The approach utilizes a Neyman-Pearson detector [156, 184] to determine the maximum possible spectral component that when convolved with the input function (i.e. $f(t) \otimes e^{-\beta_j t} u(t)$),

is still distinguishable from the scaled input function (i.e. $\frac{1}{\beta_j} f(t)$) given the noise level in the measured data. Following standard convention [156, 184], define the null (H_0) and alternative hypotheses (H_1) as in (Eqn. 5.2.72), where $\varepsilon \sim N(0_{Tx1}, \Sigma)$ and the $T \times 1$ vector μ_0 and μ_1 are as defined in (Eqn. 5.2.73) and (Eqn. 5.2.74), respectively, where T is the total number of PET frames. In (Eqn. 5.2.73) and (Eqn. 5.2.74) t_i^s and t_i^e denote the start and stop times of the i^{th} PET frame.

$$\begin{cases} H_0: \mathbf{x} = \boldsymbol{\mu}_0 + \boldsymbol{\varepsilon} \\ H_1: \mathbf{x} = \boldsymbol{\mu}_1 + \boldsymbol{\varepsilon} \end{cases} \quad (\text{Eqn. 5.2.72})$$

$$\begin{cases} \boldsymbol{\mu}_0 = [\mathbf{s}_0(\bar{t}_1) \quad \mathbf{s}_0(\bar{t}_2) \quad \cdots \quad \mathbf{s}_0(\bar{t}_T)]^T \\ \text{where, } \mathbf{s}_0(\bar{t}_i) = \frac{1}{\beta} \left[\frac{1}{(t_i^e - t_i^s)} \int_{t_i^s}^{t_i^e} \mathbf{f}(t) dt \right] \end{cases} \quad (\text{Eqn. 5.2.73})$$

$$\begin{cases} \boldsymbol{\mu}_1 = [\mathbf{s}_1(\bar{t}_1) \quad \mathbf{s}_1(\bar{t}_2) \quad \cdots \quad \mathbf{s}_1(\bar{t}_T)]^T \\ \text{where, } \mathbf{s}_1(\bar{t}_i) = \frac{1}{(t_i^e - t_i^s)} \int_{t_i^s}^{t_i^e} [\mathbf{f}(t) \otimes e^{-\beta t} \mathbf{u}(t)] dt \end{cases} \quad (\text{Eqn. 5.2.74})$$

Following the normally distributed, independent, heteroscedastic errors assumptions appropriate for PET tissue TAC data described in *Chapter 2*, the likelihood functions for the scaled input function (H_0) and the j^{th} probing function (H_1) are given by (Eqn. 5.2.75) and (Eqn. 5.2.76), respectively; where the covariance matrix, Σ , is diagonal and the same under both H_0 and H_1 .

$$p(x; H_0) = (2\pi)^{\frac{-N}{2}} \left(\prod_{i=1}^N \sigma_i^2 \right)^{-\frac{1}{2}} e^{-\frac{1}{2}(x-\mu_0)^T \Sigma^{-1}(x-\mu_0)} \quad (\text{Eqn. 5.2.75})$$

$$p(x; H_1) = (2\pi)^{\frac{-N}{2}} \left(\prod_{i=1}^N \sigma_i^2 \right)^{-\frac{1}{2}} e^{-\frac{1}{2}(x-\mu_1)^T \Sigma^{-1}(x-\mu_1)} \quad (\text{Eqn. 5.2.76})$$

The Neyman-Pearson detector chooses H_1 if the ratio of the likelihood functions is greater than a fixed threshold, γ , for a fixed probability of false alarm [156, 184]. The ratio of the likelihood functions under H_1 and H_0 is given below by (Eqn. 5.2.77) with corresponding Neyman-Pearson decision rule given in (Eqn. 5.2.78)

$$\mathcal{L}(x) = \frac{p(x; H_1)}{p(x; H_0)} = \frac{e^{-\frac{1}{2}(x-\mu_1)^T \Sigma^{-1}(x-\mu_1)}}{e^{-\frac{1}{2}(x-\mu_0)^T \Sigma^{-1}(x-\mu_0)}} \quad (\text{Eqn. 5.2.77})$$

$$\frac{e^{-\frac{1}{2}(x-\mu_1)^T \Sigma^{-1}(x-\mu_1)}}{e^{-\frac{1}{2}(x-\mu_0)^T \Sigma^{-1}(x-\mu_0)}} > \gamma \quad (\text{Eqn. 5.2.78})$$

Taking the logarithm of both sides of (Eqn. 5.2.78) and re-arranging terms leads to (Eqn. 5.2.79) below.

$$(\mu_1 - \mu_0)^T \Sigma^{-1} x > \ln(\gamma) + \frac{[\mu_1^T \Sigma^{-1} \mu_1 - \mu_0^T \Sigma^{-1} \mu_0]}{2} \quad (\text{Eqn. 5.2.79})$$

With the definitions given in (Eqn.5.2.80), the Neyman-Pearson decision rule of (Eqn.5.2.72) reduces to (Eqn.5.2.81).

$$\begin{cases} T(\mathbf{x}; \boldsymbol{\beta}) \triangleq (\boldsymbol{\mu}_1 - \boldsymbol{\mu}_0)^T \boldsymbol{\Sigma}^{-1} \mathbf{x}; \\ \gamma' \triangleq \ln(\gamma) + \frac{[\boldsymbol{\mu}_1^T \boldsymbol{\Sigma}^{-1} \boldsymbol{\mu}_1 - \boldsymbol{\mu}_0^T \boldsymbol{\Sigma}^{-1} \boldsymbol{\mu}_0]}{2} \end{cases} \quad (\text{Eqn. 5.2.80})$$

$$T(\mathbf{x}; \boldsymbol{\beta}) > \gamma' \quad (\text{Eqn. 5.2.81})$$

(Eqn.5.2.82) gives the equations for the probability of false alarm (P_F) and probability of detection (P_D) for a specified threshold γ' and the test statistic $T(\mathbf{x}; \boldsymbol{\beta})$ given in (Eqn.5.2.80); where $p(T(\mathbf{x}; \boldsymbol{\beta}); H_0)$ denotes the probability distribution of $T(\mathbf{x}; \boldsymbol{\beta})$ assuming H_0 is true and $p(T(\mathbf{x}; \boldsymbol{\beta}); H_1)$ denotes the probability distribution of $T(\mathbf{x}; \boldsymbol{\beta})$ assuming H_1 is true.

$$\begin{cases} P_F = \int_{\gamma'}^{\infty} p(T(\mathbf{x}; \boldsymbol{\beta}); H_0) dT \\ P_D = \int_{\gamma'}^{\infty} p(T(\mathbf{x}; \boldsymbol{\beta}); H_1) dT \end{cases} \quad (\text{Eqn. 5.2.82})$$

Since the measured tumor TAC data are assumed to be corrupted by independent, additive, heteroscedastic, Gaussian noise, $p(T(\mathbf{x}; \boldsymbol{\beta}); H_0)$ and $p(T(\mathbf{x}; \boldsymbol{\beta}); H_1)$ will both be Gaussian distributions. Therefore, in order to calculate P_F and P_D in (Eqn.5.2.82), only the first two moments of $T(\mathbf{x}; \boldsymbol{\beta})$ are needed under H_0 and H_1 . (Eqn.5.2.83) gives the expected value of $T(\mathbf{x}; \boldsymbol{\beta})$ under H_0 (\bar{T}_{H_0}) and H_1 (\bar{T}_{H_1}), while (Eqn. 5.2.84) gives the variance, σ_T^2 , when either H_0 or H_1 is true (i.e. σ_T^2 is the same regardless if H_0 or H_1 is true).

$$\begin{cases} \bar{T}_{H_0} = [\boldsymbol{\mu}_1^T(t; \boldsymbol{\beta}_i) - \boldsymbol{\mu}_0^T(t)] \boldsymbol{\Sigma}^{-1} \boldsymbol{\mu}_0(t) \\ \bar{T}_{H_1} = [\boldsymbol{\mu}_1^T(t; \boldsymbol{\beta}_i) - \boldsymbol{\mu}_0^T(t)] \boldsymbol{\Sigma}^{-1} \boldsymbol{\mu}_1(t; \boldsymbol{\beta}_i) \end{cases} \quad (\text{Eqn. 5.2.83})$$

$$\sigma_T^2 = (\boldsymbol{\mu}_1 - \boldsymbol{\mu}_0)^T \boldsymbol{\Sigma}^{-1} (\boldsymbol{\mu}_1 - \boldsymbol{\mu}_0) \quad (\text{Eqn. 5.2.84})$$

The final challenge to using the Neyman-Pearson detector to compute a data-adaptive fast-rate threshold for SA is to use γ' to write P_D as a function of P_F . To this end, define the function:

$Q(x) \triangleq \frac{1}{\sqrt{2\pi}} \int_x^\infty e^{-\frac{z^2}{2}} dz$, then P_F and P_D can be re-written as in (Eqn. 5.2.85).

$$\begin{cases} P_F = Q\left(\frac{\gamma' - \bar{T}_{H_0}}{\sigma_T}\right) \\ P_D = Q\left(\frac{\gamma' - \bar{T}_{H_1}}{\sigma_T}\right) \end{cases} \quad (\text{Eqn. 5.2.85})$$

Moreover, since $Q(x)$ is monotonically decreasing the inverse of $Q(x)$, denoted $Q^{-1}(x)$, is guaranteed to exist [156, 184]. Hence the threshold γ' can be written in terms of P_F as in (Eqn. 5.2.86) below.

$$\gamma' = \sigma_T Q^{-1}(P_F) + \bar{T}_{H_0} \quad (\text{Eqn. 5.2.86})$$

Inserting (Eqn. 5.2.86) into the equation for P_D in (Eqn. 5.2.85) gives (Eqn. 5.2.87), which reduces to (Eqn. 5.2.88).

$$P_D = Q\left(\frac{y' - \bar{T}_{H_1}}{\sigma_T}\right) = Q\left(\frac{\sigma_T Q^{-1}(P_F) - [\bar{T}_{H_1} - \bar{T}_{H_0}]}{\sigma_T}\right) \quad (\text{Eqn. 5.2.87})$$

$$P_D = Q\left(Q^{-1}(P_F) - \sqrt{(\mu_1 - \mu_0)^T \Sigma^{-1} (\mu_1 - \mu_0)}\right) \quad (\text{Eqn. 5.2.88})$$

(Eqn. 5.2.88) describes is the receiver operating characteristics (ROC) curve of the test statistic $T(x; \beta)$. A perfect test would be one where $\int_0^1 P_D dP_F = 1$; that is, H_1 (i.e. $f(t) \otimes e^{-\beta_j t} u(t)$) is perfectly distinguishable from H_0 (i.e. $\frac{1}{\beta_j} f(t)$) given the noise. This result can be used to define an optimization problem (Eqn. 5.2.89) for which the maximum β can be obtained under the constraint that $\int_0^1 P_D dP_F \geq \delta$, where $\delta \in [0.5, 1]$ controls degree of misidentification of H_1 as H_0 that is allowed.

$$\begin{aligned} & \mathbf{max:} \beta \\ \mathbf{subject\ to:} & \begin{cases} \beta \geq 0 \\ \int_0^1 P_D dP_F \geq \delta \end{cases} \end{aligned} \quad (\text{Eqn. 5.2.89})$$

Finally, one parameter is still to be defined, which is the constant of proportionality α_0^2 in the covariance matrix Σ . As described in *Chapter 2*, Σ is a diagonal matrix with elements of the form: $\sigma_i^2 = \alpha_0^2 \left[\frac{x_i e^{\lambda_i^*}}{(t_i^{end} - t_i^{start})} \right]$ along its diagonal. The terms inside the brackets are known (see *Chapter 2*); however, α_0^2 needs to be estimated based on the data. The approach used in this dissertation is to estimate α_0^2 from the normalized residuals obtained after SA. That is, let $\hat{\alpha}$ denote

the estimated spectrum after performing SA using either the NNLS or simplex methods. Then a method dependent estimate for α_0^2 is given by (Eqn. 5.2.90), where W is a diagonal matrix with elements of the form $w_i = \frac{x_i e^{\lambda t_i^*}}{(t_i^{end} - t_i^{start})}$ along its diagonal and T denotes the total number of PET frames.

$$\widehat{\alpha_0^2} = \frac{1}{T} [x - A\hat{\alpha}]^T W^{-1} [x - A\hat{\alpha}] \quad (\text{Eqn. 5.2.90})$$

In this dissertation $\delta = 0.99$, and a unique estimate for α_0^2 was computed for each of the NNLS and simplex methods.

Obtaining Macroparameter Estimates using Spectral Analysis

Estimates for tumor tissue compartmental macroparameteres: K_1 , K_i and V_T , were obtained for every PET imaging time-point (see *Section 5.2.2* for more detail). Following the suggestion of Cunningham and Jones [171], the blood volume fraction term V_B was treated as a high-frequency component and not specifically estimated. That is, IBIF model was not included as a basis vector in the SA basis matrix for either SA method used.

Following the definitions given in *Section 5.2.2*, (Eqn. 5.2.91) gives the estimators used for K_1 , K_i and V_T . Spectral components corresponding to probing rates β_j faster than 80% of the fast-rate threshold, β_{fast} , (defined above) were not allowed to contribute to the estimation of either K_1 and V_T . Moreover, $\beta = 10^{-4} \text{ min}^{-1}$ was the slowest spectral probing rate tested. Hence, a non-

zero spectral component observed at $\beta = 10^{-4} \text{ min}^{-1}$ was taken to indicate tracer trapping. Therefore, if a component was detected at the probing rate $\beta = 10^{-4} \text{ min}^{-1}$, this component was not allowed to contribute to the estimate for V_T . All detected components in the interval $\beta_j \in [10^{-4}, 0.8(\beta_{fast})]$ were allowed to contribute to the value of K_1 .

$$\begin{cases} \widehat{K}_t = \alpha_0; \beta_j = 10^{-4} \text{ min}^{-1} \\ \widehat{K}_1 = \sum_{j=1}^N \alpha_j; \beta_j \in [10^{-4}, 0.8(\beta_{fast})] \\ \widehat{V}_T = \sum_{j=1}^N \frac{\alpha_j}{\beta_j}; \beta_j \in (10^{-4}, 0.8(\beta_{fast})) \end{cases} \quad (\text{Eqn. 5.2.91})$$

While performing SA, it is common to observe 2 non-zero spectral components neighboring each other on the grid of β_j ; an effect that has been referred to as “line doubling” [172]. If 2 or more adjacent spectral components were observed, then to compute \widehat{K}_1 the approach of Cunningham and Jones [171] was followed where all spectral components were summed to produce the K_1 estimate; essentially ignoring the ‘line-doubling’ effect. For the case of the estimator \widehat{V}_T , where a specific β_j must be assigned to the adjacent peaks, the neighboring spectral components were summed and then divided by the spectral rate that corresponded to the component with the largest α_j . That is, suppose after performing SA only 2 non-zero, adjacent spectral components are detected α_k and α_{k+1} with corresponding spectral rates β_k and β_{k+1} such that $\beta_k, \beta_{k+1} \in (10^{-4}, 0.8(\beta_{fast}))$. To compute the corresponding \widehat{V}_T , define $\alpha^* \triangleq (\alpha_k + \alpha_{k+1})$ and $\beta^* \triangleq \{\beta_k, \beta_{k+1}\} \cap \{\beta_j | \alpha_j = \max(\alpha_k, \alpha_{k+1})\}$, such that the estimate for V_T becomes: $\widehat{V}_T = \frac{\alpha^*}{\beta^*}$.

Estimates obtained using (Eqn. 5.2.91) were not corrected for bias. One-sided, 95% bootstrap confidence intervals were generated for each estimator in (Eqn. 5.2.91) using the bootstrap resampling approach described in Section 5.2.2 with $B = 1000$ bootstrap samples.

5.2.3.7 Voxelwise Impulse Response Function Modeling

Voxelwise IRF modeling was performed for the purpose of generating voxelwise maps of tumor K_i and V_T . To this end, a maximum likelihood approach is used to fit the $2\alpha-1\beta$ and $2\alpha-2\beta$ IRF models on a voxel-by-voxel basis for a subset of GBM subjects exhibiting a tumor of sufficient size for voxelwise analysis. The VOI used to define the tumor for whole tumor uptake modeling (Section 5.2.3.2) is the same VOI used for voxelwise modeling. For each [^{18}F]ML-10 PET scan, tumor voxels are assumed to have the same input [^{18}F]ML-10 concentration, which is described by the corresponding IBIF model that was determined during joint IBIF/IRF model selection. Moreover, for each voxelwise fit the blood volume fraction, V_B , is constrained to equal the corresponding value of V_B estimated during whole tumor joint IBIF/IRF modeling. Therefore, only the exponential coefficients and exponential rates corresponding to the $2\alpha-1\beta$ and $2\alpha-2\beta$ IRF models are estimated for each tumor voxel.

The Voxelwise Log-Likelihood Function

In this dissertation, tumor voxels are modeled as statistically independent. Measurement noise for each tumor voxel is assumed to follow a Gaussian distribution with zero mean and homogeneous variance.

Let $x^{(j)}$ represent the $T \times 1$ column vector of measured tumor concentration samples for the j^{th} tumor voxel, where T is equal to the number of PET frames ($T=51$ for this dissertation). Additionally, let $C_T(t; \delta^{(j)})$ denote the tissue response model to be fit to the j^{th} tumor voxel, where $\delta^{(j)}$ is the vector of IRF model parameters to be estimated for that voxel. For voxelwise modeling, $C_T(t; \delta^{(j)})$ is assumed to have the general form given by (Eqn. 5.2.92). For a particular [^{18}F]ML-10 PET scan to which voxelwise modeling was applied, $f(t; \theta)$ represented the corresponding selected best candidate IBIF model obtained from the results of joint IBIF/IRF modeling, where θ denotes the vector of IBIF model parameters. $h(t; \delta^{(j)})$ represents the IRF model being fit during the voxelwise analysis, and \otimes denotes the convolution operation. In this dissertation, only the $2\alpha-1\beta$ and $2\alpha-2\beta$ tumor IRF models are considered for voxelwise modeling. V_B denotes the blood volume fraction, which is constrained to equal the corresponding value of V_B that was estimated during whole tumor IBIF/IRF model selection. For example, when voxelwise analysis using the $2\alpha-1\beta$ IRF model was applied to ML-10 #6 at ETA, the value of V_B at every voxel was fixed to equal the value of V_B that was obtained when IBIF Model 1b (i.e. the selected IBIF model for this subject and time-point) and IRF model $2\alpha-1\beta$ were fit to the subject's average tumor TAC during joint IBIF/IRF model selection. Similarly, non-zero tissue delays estimated during joint IBIF/IRF modeling were applied to every voxel during voxelwise modeling.

$$C_T^{(j)}(t; \delta^{(j)}) = V_B f(t; \theta) + (1 - V_B) [h(t; \delta^{(j)}) \otimes f(t; \theta)] \quad (\text{Eqn. 5.2.92})$$

Equation (Eqn. 5.2.93) gives the Gaussian likelihood function for the j^{th} tumor voxel, assuming constant variance σ_j^2 and statistical independence between PET frames. The log-

likelihood function $\ell^{(j)}(\boldsymbol{\delta}^{(j)}; \mathbf{x}^{(j)})$ for the j^{th} tumor voxel can be obtained by taking the natural log of both sides of (Eqn. 5.2.93) and is given in (Eqn. 5.2.94).

$$\mathbf{p}(\mathbf{x}^{(j)}; \boldsymbol{\delta}^{(j)}) = (2\pi\sigma_j^2)^{-\frac{T}{2}} \mathbf{e}^{-\frac{1}{2\sigma_j^2}[\mathbf{x}_i - \mathbf{M}^{(j)}(\boldsymbol{\delta}^{(j)}; \bar{\mathbf{t}}_i)]^T [\mathbf{x}_i - \mathbf{M}^{(j)}(\boldsymbol{\delta}^{(j)}; \bar{\mathbf{t}}_i)]} \quad (\text{Eqn. 5.2.93})$$

$$\ell^{(j)}(\boldsymbol{\delta}^{(j)}; \mathbf{x}^{(j)}) = -\frac{T}{2} \ln(2\pi\sigma_j^2) - \frac{1}{2\sigma_j^2} [\mathbf{x}_i - \mathbf{C}_T^{(j)}(\mathbf{t}; \boldsymbol{\delta}^{(j)})]^T [\mathbf{x}_i - \mathbf{C}_T^{(j)}(\mathbf{t}; \boldsymbol{\delta}^{(j)})] \quad (\text{Eqn. 5.2.94})$$

From (Eqn. 5.2.94), the maximum likelihood estimate for the noise variance σ_j^2 is given by (Eqn. 5.2.95). From the standpoint of voxelwise fitting, it is convenient to substitute this expression for the estimate $\widehat{\sigma_j^2}$ into the log-likelihood in (Eqn. 5.2.94) to obtain the corresponding concentrated log-likelihood function (Eqn. 5.2.96).

$$\widehat{\sigma_j^2} = \frac{1}{T} [\mathbf{x}^{(j)} - \mathbf{C}_T^{(j)}(\mathbf{t}; \boldsymbol{\delta}^{(j)})]^T [\mathbf{x}^{(j)} - \mathbf{C}_T^{(j)}(\mathbf{t}; \boldsymbol{\delta}^{(j)})] \quad (\text{Eqn. 5.2.95})$$

$$\ell_c^{(j)}(\boldsymbol{\delta}^{(j)}; \mathbf{x}^{(j)}) = -\frac{NT}{2} \ln\left(\frac{2\pi}{NT}\right) - \frac{NT}{2} + -\frac{NT}{2} \ln\left(\sum_{t=1}^T (\mathbf{Y}_t - \boldsymbol{\mu}_t(\boldsymbol{\beta}))^T (\mathbf{Y}_t - \boldsymbol{\mu}_t(\boldsymbol{\beta}))\right) \quad (\text{Eqn. 5.2.96})$$

Maximizing the Voxelwise Log-Likelihood Function

For each voxel, a constrained maximization of the concentrated log-likelihood function in (Eqn. 5.2.96) was performed using the `fmincon.m` function available in the MATLAB

optimization toolbox (R2014a, The MathWorks, Natick, MA., USA). The same constraints for joint IBIF/IRF modeling (*Section 5.2.3.4*) were applied during voxelwise fitting. Specifically, the linear coefficients for each voxel IRF model were restricted to be in the range $[0, \infty) \text{ min}^{-1}$ while IRF exponential washout rates were restricted to the range $[0, 10] \text{ min}^{-1}$. The corresponding IRF model parameters estimated during joint IBIF/IRF modeling of the average tumor TAC were used as the initial parameter guess for nonlinear maximization of (*Eqn. 5.2.96*) at each tumor voxel.

Generation of Standard Uptake Value PET Images

The last 6 frames of dynamic [^{18}F]ML-10 PET data (120-150 min post-injection) were averaged together to create a single “static” image. Static images were then converted to units of standard uptake values (SUVs) over the entire field of view using the commercially available software PMOD 3.6 (University Hospital Zurich, Zurich, Switzerland). The formula for calculating an SUV value for a particular voxel is given by (*Eqn. 5.2.97*), where the injected tracer dose and voxel activity are each decay-corrected to the start time of the PET scan.

$$SUV = \frac{\text{Voxel Activity}}{\left(\frac{\text{Injected Tracer Dose}}{\text{Subject Weight}} \right)} \quad (\text{Eqn. 5.2.97})$$

5.2.4 Results

5.2.4.1 Time Activity Curve Analysis

Figure 5-12 shows representative IBIF, tumor tissue, and healthy tissue activity data measured for two representative subjects, ML10 #9 at BL (left) and ML-10 #12 at BL (right). Across all figure panes, adjacent data points are shown connected by a solid line as a visual aid, no model fitting has been performed. Figure 5-12A shows measured IBIF data for subjects ML10 #9 at BL (left) and ML-10 #12 at BL (right). The illustrated IBIF uptake profiles are typical of all measured [^{18}F]ML-10 IBIFs.

Across [^{18}F]ML-10 PET scans, a distribution of tumor tissue TACs was observed, for which each measured tumor TAC could be visually placed into one of two categories: ‘blood-like’ or ‘accumulation-like’. ML-10 #9 illustrates a ‘blood-like’ example (figure 5-12B left), reflecting a relatively strong contribution from the vasculature to the tumor TAC, compared to the ‘accumulation-like’ quality demonstrated by ML-10 #12 (figure 5-12B right). Also shown in figure 5-12B are average TACs from healthy tissue (asterisks) for subjects ML10 #9 at BL (left) and ML-10 #12 at BL (right). For both subjects, the healthy tissue TACs are characterized by low-uptake and fast-clearance. Measured healthy tissue TACS were similar across subjects and imaging time-points.

Tumor-to-IBIF (Tumor:IBIF) ratios were also calculated for each imaging time-point. Figure 1C shows representative Tumor:IBIF ratios for subjects ML-10 #9 at BL (figure 5-12C, left) and ML-10 #12 BL (figure 5-12C, right). Tumor:IBIF ratios are observed to increase over the

entire 150 min acquisition time for both cases. Visual comparison between scans reveals that Tumor:IBIFs for ML-10 #12 at BL increase at a faster rate compared to those of ML-10 #9 at BL. Measured Tumor:IBIFs were similar across subjects and imaging time-points; however, the rate of increase in Tumor:IBIF ratios varied across [^{18}F]ML-10 PET scans.

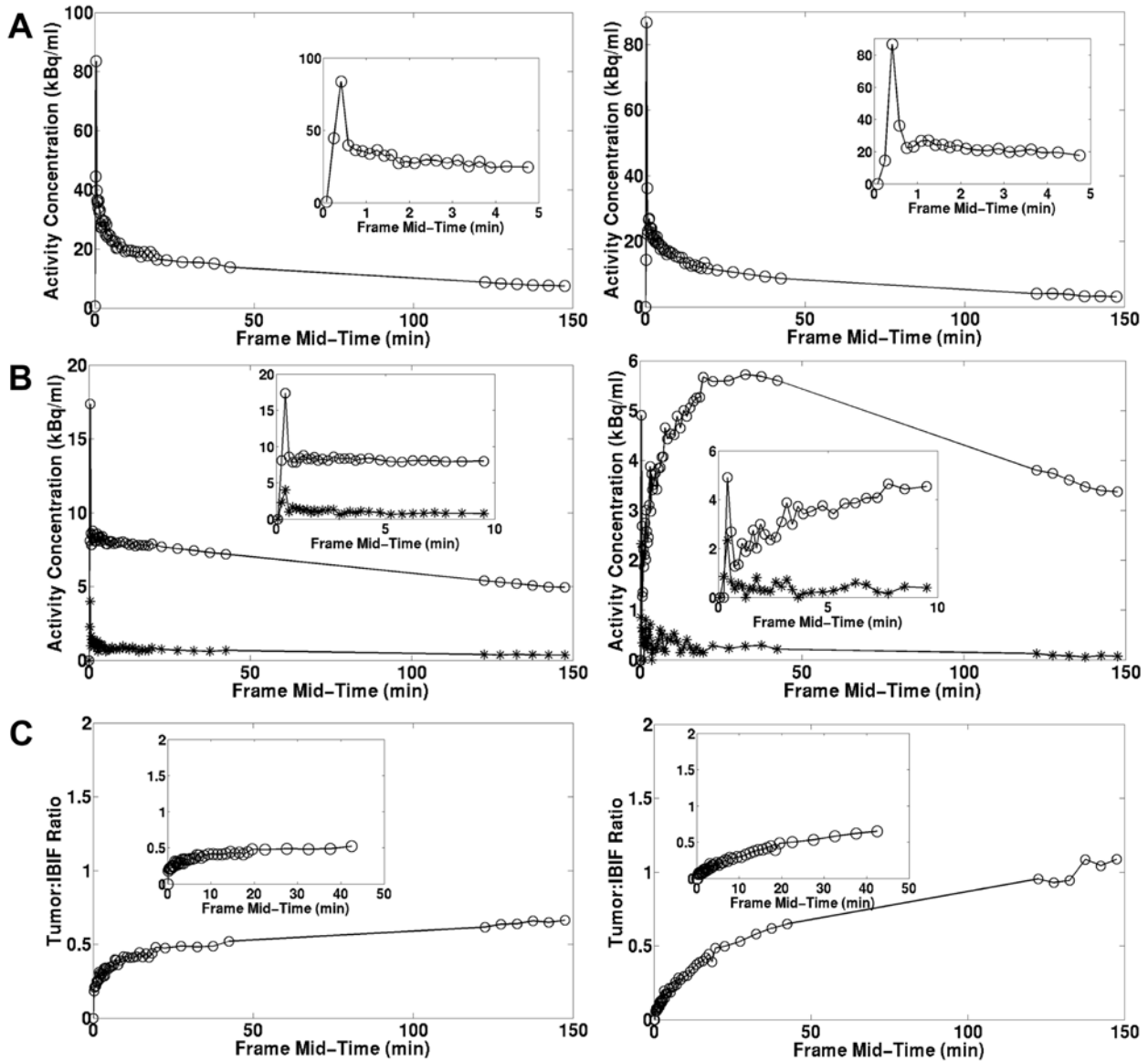


Figure 5-12. Representative IBIF, Tumor, and Healthy Tissue PET Time-Activity Curves. Across all figure panes, adjacent data points are shown connected by a solid line as a visual aid, no model fitting has been performed.

(A) Representative [^{18}F]ML-10 IBIFs for subjects ML-10 #9 at BL (left) and ML-10 #12 at BL (right). Insets show the first 0-5 min of IBIF data post-injection of [^{18}F]ML-10. The measured IBIFs were similar across subjects and imaging time-points. (B) Average PET time-activity data measured from tumor (circles) and healthy (asterisks) tissue regions for subjects ML-10 #9 BL (left) and ML-10 #12 at BL (right). Across [^{18}F]ML-10 PET scans, measured tumor data could be visually placed into one of two categories exhibiting either a 'blood-like' or an 'accumulation-like' quality. ML-10 #9 illustrates a 'blood-like' example (B, left), reflecting a relatively strong contribution from the vasculature to the tumor TAC, compared to the 'accumulation-like' quality demonstrated by ML-10 #12 (B, right). For all [^{18}F]ML-10 PET scans, the healthy brain tissue data visually appeared as an attenuated version of the corresponding IBIF. (C) Average Tumor:IBIF ratios (circles) for tumor tissue of subjects ML-10 #9 (left) and ML-10 #12 (right) at BL. Tumor:IBIF ratios are observed to increase over the over the entire 150 min acquisition time for both cases. Visually, Tumor:IBIFs for ML-10 #12 at BL increase at a faster rate compared to those of ML-10 #9 at BL. Measured Tumor:IBIFs were similar across subjects and imaging time-points; however, the rate of increase in Tumor:IBIF ratios varied across [^{18}F]ML-10 PET scans.

5.2.4.2 Model Selection via Simultaneous Estimation of IBIF and Tumor Tissue IRF Model Parameters

IBIF and tumor IRF model selection were performed as part of a simultaneous maximum likelihood fitting approach for each dynamic [^{18}F]ML-10 acquisition (a total of 29). For this analysis the measured tumor TAC was modeled as a convolution between the blood input concentration, modeled using a candidate IBIF model, and an IRF composed of a variable number of causal exponentials.

Figure 5-13 and figure 5-14 illustrate an example joint IBIF-IRF model selection analysis using measured IBIF and tumor TACs obtained from ML-10 #6 at ETA, who demonstrates an

‘accumulation-like’ [^{18}F]ML-10 uptake profile. For ML-10 #6 at ETA, the joint minimum AIC_c IBIF and IRF models were IBIF Model 1b and IRF model $3\alpha-2\beta$, respectively. Figure 5-13 shows a comparison of the candidate IBIF model fits to the measured IBIF data (black circles) for the $3\alpha-2\beta$ tumor IRF model. The inset plot shows the corresponding fits to the first 0-5min of data. Visually, IBIF Model 2b (black dashed line) fits the measured input [^{18}F]ML-10 concentration peak well but demonstrates overfitting between 2-3 min post tracer injection (blue circle). IBIF Model 1c (red dot-dash line) fits the IBIF peak well but, as a result, underestimates the IBIF concentration just after the peak tracer concentration (arrow). Visually, IBIF Model 1b (blue solid line) fits the overall trend of the measured IBIF data well.

Figure 5-14A-F shows representative IRF tissue model fits using IBIF Model 1b with maximum log-likelihood value (logLikeVal) and AIC_c values shown as insets for each IRF model fit. The simplest IRF model fit to the subject’s tumor TAC data was a scaled version of the IBIF model (Figure 5-14A). From left-to right, the fitted IRF models increase in complexity: (B) single exponential IRF model $1\alpha-1\beta$, (C) single exponential IRF model with a trap $2\alpha-1\beta$, (D) two-exponential reversible IRF model $2\alpha-2\beta$, (E) two-exponential IRF model with a trap $3\alpha-2\beta$, and (F) three-exponential reversible IRF model $3\alpha-3\beta$. For IRF model fitting, the exponential coefficients, α , were constrained to be positive while the exponential rates were constrained to be greater than or equal to zero as described in the methods. Across figure panes, increasing the number of simple causal exponentials in the IRF produced visually better fits to the measured tumor TAC data. However, little overall difference in fit quality is visually apparent between the selected $3\alpha-2\beta$ IRF model and the more complex $3\alpha-3\beta$ IRF model.

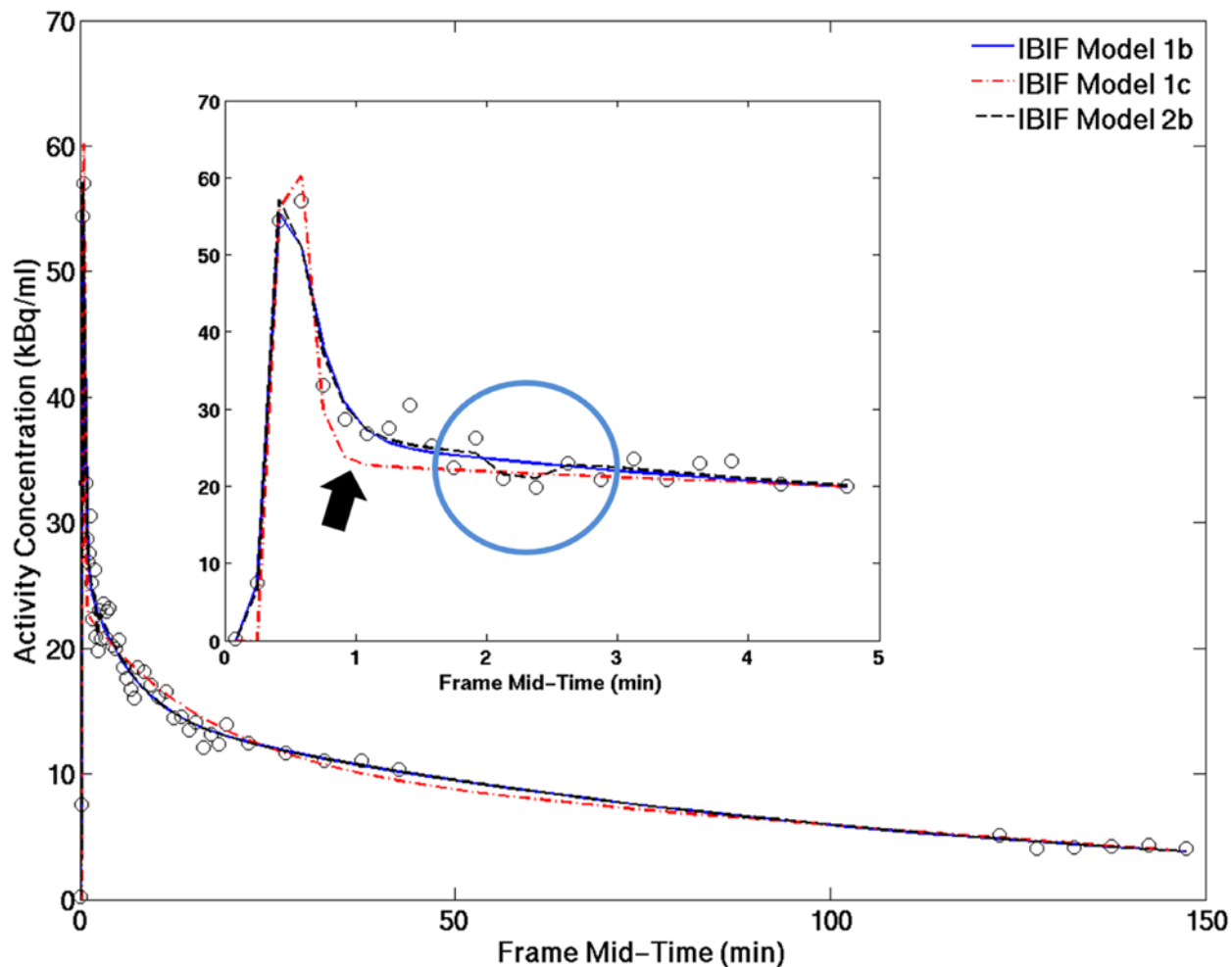


Figure 5-13. Representative IBIF Model Fits for ML-10 #6 at ETA Assuming a 3α - 2β Tumor IRF Model. Figure shows a comparison of the candidate IBIF model fits to the measured IBIF data (black circles) for ML-10 #6 at ETA assuming simultaneous maximum likelihood fit of a 3α - 2β tumor IRF model. Inset shows the IBIF and model fit for the first 0-5 min following injection of [^{18}F]ML-10. The selected IBIF model based on minimum AIC_c was IBIF Model 1b. Visually, IBIF Model 2b (black dashed line) fits the measured input [^{18}F]ML-10 concentration peak well but demonstrates overfitting between 2-3 min post tracer injection (blue circle). IBIF Model 1c (red dot-dash line) fits the IBIF peak well but, as a result, underestimates the IBIF concentration just after the peak tracer concentration (arrow). Visually, IBIF Model 1b (blue solid line) fits the overall trend of the measured IBIF data well.

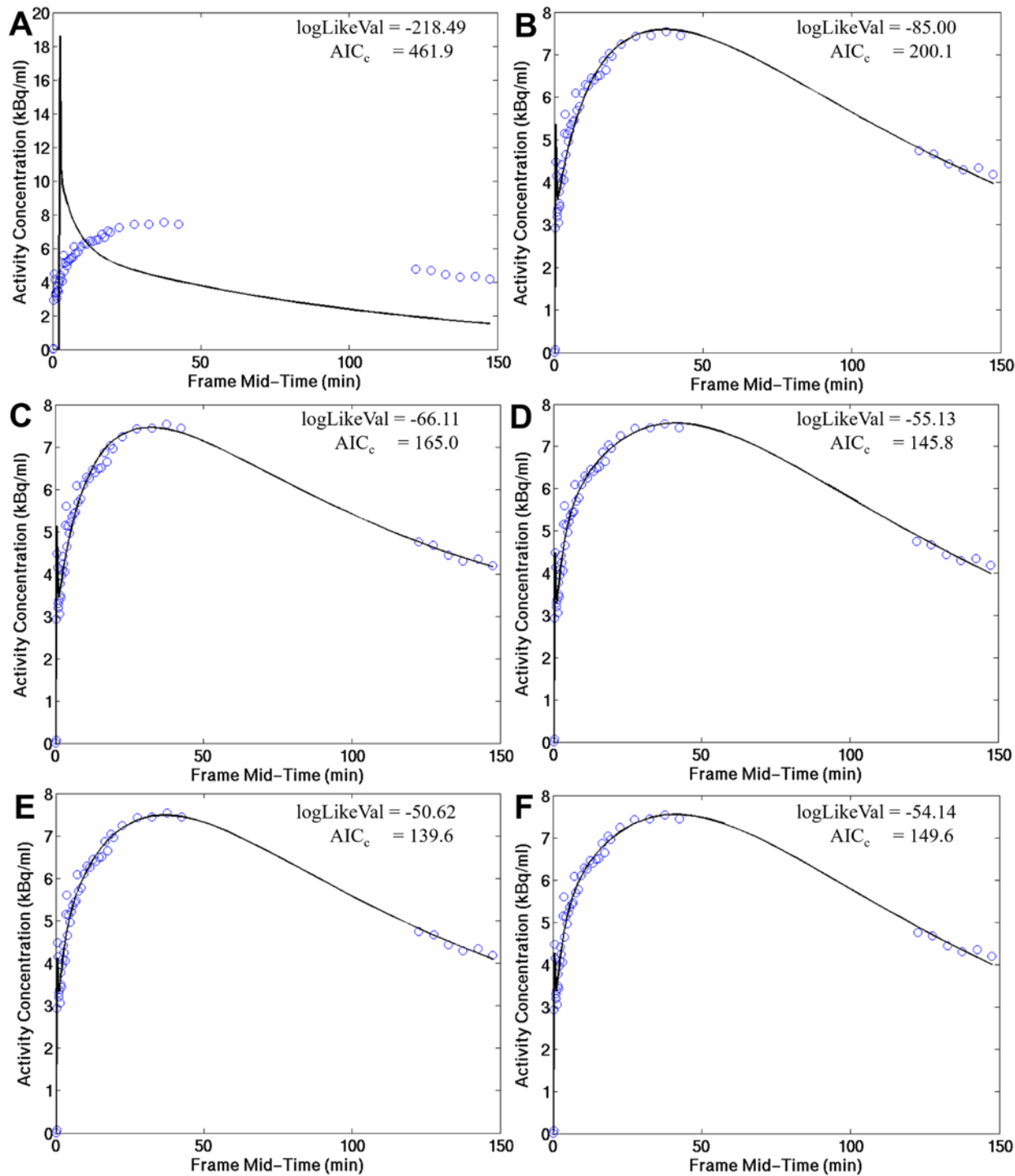


Figure 5-14. Representative Candidate IRF Model Fits for ML-10 #6 at ETA Assuming IBIF Model 1b as the Selected Input Model. Figure shows representative IRF tissue model fits assuming joint maximum likelihood fitting using IBIF Model 1b as input model. Estimated maximum log-likelihood value (logLikeVal) and AIC_c values shown

as insets for each IRF model fit. The simplest IRF model fit to the subject's tumor TAC data was a scaled version of the IBIF model (A). From left-to right, the fitted IRF models increase in complexity: (B) single exponential IRF model $1\alpha-1\beta$, (C) single exponential IRF model with a trap $2\alpha-1\beta$, (D) two-exponential reversible IRF model $2\alpha-2\beta$, (E) two-exponential IRF model with a trap $3\alpha-2\beta$, and (F) three-exponential reversible IRF model $3\alpha-3\beta$. For IRF model fitting, the exponential coefficients, α , were constrained to be positive while the exponential rates were constrained to be greater than or equal to zero as described in the methods. Across figure panes, increasing the number of simple causal exponentials in the IRF produced visually better fits to the measured tumor TAC data. However, little overall difference in fit quality is visually apparent between the $3\alpha-2\beta$ IRF model and the more complex $3\alpha-3\beta$ IRF model. Based on minimum AICc criteria, IRF model $3\alpha-2\beta$ was selected as the best IRF model among the tested candidates.

Table 5-8 contains the joint IBIF/IRF model selection results for subject ML-10 #6 at ETA. From left to right, the table contains: the candidate IBIF model, candidate IRF model, the total number of model parameters, K , to be estimated during the joint IBIF-IRF fitting (including IBIF and IRF noise variance parameters), and the sum of the squared weighted residuals (WRSS) for the IBIF and IRF models separately. Also tabulated are the values of the log-likelihood function for the model estimates ($\log(\mathcal{L}(\hat{\theta}, \hat{\sigma}^2 | data))$), the AIC, and the AICc. Also shown is the differences between each AICc value and the overall minimum AICc value (i.e. $\Delta AIC_c = AIC_c - (\text{minimum } AIC_c)$). The table row containing the joint IBIF/IRF model with minimum AICc values among the tested models is highlighted in bold.

Table 5-8. Joint IBIF-Tumor IRF Model Selection Results for ML-10 #6 at Early Therapy Response Assessment.

IBIF Model	IRF Model	^aK	^bWRSS	$\log(\mathcal{L}(\hat{\theta}, \hat{\sigma}^2 data))$	AIC	AIC_c	ΔAIC_c
IBIF Model 1b	(1 α -0 β)	11	3.177 (83.648)	-218.487	458.974	461.907	322.271
IBIF Model 1b	(1 α -1 β)	13	3.769 (0.376)	-84.000	195.999	200.135	60.499
IBIF Model 1b	(2 α -1 β)	14	2.323 (0.291)	-66.110	160.221	165.049	25.412
IBIF Model 1b	(2 α -2 β)	15	2.093 (0.210)	-55.126	140.253	145.834	6.198
IBIF Model 1b	(3α-2β)	16	2.089 (0.176)	-50.618	133.236	139.636	0
IBIF Model 1b	(3 α -3 β)	17	2.094 (0.202)	-54.140	142.280	149.565	9.929
IBIF Model 1c	(1 α -0 β)	13	3.435 (84.921)	-220.863	467.727	471.863	332.227
IBIF Model 1c	(1 α -1 β)	15	4.661 (0.473)	-96.290	222.579	228.160	88.524
IBIF Model 1c	(2 α -1 β)	16	5.090 (0.914)	-115.332	262.663	269.063	129.427
IBIF Model 1c	(2 α -2 β)	17	5.088 (0.234)	-80.574	195.148	202.434	62.798
IBIF Model 1c	(3 α -2 β)	18	5.088 (0.232)	-80.385	196.769	205.010	65.374
IBIF Model 1c	(3 α -3 β)	19	5.090 (0.218)	-78.789	195.577	204.846	65.210
IBIF Model 2b	(1 α -0 β)	14	2.845 (97.227)	-219.505	467.009	471.837	332.201
IBIF Model 2b	(1 α -1 β)	16	3.429 (0.466)	-88.0918	208.184	214.584	74.948
IBIF Model 2b	(2 α -1 β)	17	3.495 (0.286)	-76.157	186.314	193.599	53.963
IBIF Model 2b	(2 α -2 β)	18	1.882 (0.222)	-53.861	143.722	151.963	12.327
IBIF Model 2b	(3 α -2 β)	19	1.847 (0.186)	-48.822	135.644	144.912	5.276
IBIF Model 2b	(3 α -3 β)	20	1.871 (0.213)	-52.659	145.319	155.689	16.053

^aK = Total number of model parameters to be estimated (including IBIF and IRF noise variance parameters).
^bWRSS (weighted sum of squared residuals) are given in the form: IBIF Model WRSS (IRF Model WRSS).

Figure 5-15 and figure 5-16 show a second example model selection analysis for a subject exhibiting a ‘blood-like’ tumor TAC (subject ML-10 #13 at BL). For ML-10 #13 at BL, the joint minimum AIC_c IBIF and IRF models were IBIF Model 1b and IRF model 2 α -1 β , respectively. Figure 5-15 shows a comparison of the candidate IBIF model fits to the measured IBIF data (black circles) for the 2 α -1 β tumor IRF model. The inset plot shows the corresponding fits to the first 0-5min of data. Visually, little difference is observed between IBIF Model 1b (blue solid line) and IBIF Model 1c (red dot-dash line). IBIF Model 2b (black dashed line) shows signs of overfitting to the IBIF data (circle).

Figure 5-16A-F shows representative IRF tissue model fits using IBIF Model 1b with maximum log-likelihood value (logLikeVal) and AIC_c values shown as insets for each IRF model fit. The simplest IRF model fit to the subject’s tumor TAC data was a scaled version of the IBIF model (Figure 5-16A). As can be observed, the attenuated input concentration model over estimates both the peak tumor tissue [¹⁸F]ML-10 concentration and the tumor tracer uptake concentration early after the peak concentration. From left-to right, the fitted IRF models increase in complexity: (B) single exponential IRF model 1 α -1 β , (C) single exponential IRF model with a trap 2 α -1 β , (D) two-exponential reversible IRF model 2 α -2 β , (E) two-exponential IRF model with a trap 3 α -2 β , and (F) three-exponential reversible IRF model 3 α -3 β . For IRF model fitting, the exponential coefficients, α , were constrained to be positive while the exponential rates were constrained to be greater than or equal to zero as described in the methods. An increase in the visual quality of the IRF model fit is observed as the IRF model complexity increases from attenuated IBIF (figure 5-16A), to 1 α -1 β IRF model (figure 5-16B), to 2 α -1 β IRF model (figure 5-

16C). However, little overall difference between the fits of IRF model $2\alpha-1\beta$ and the higher complexity IRF models (figure 5-16D-F) is apparent.

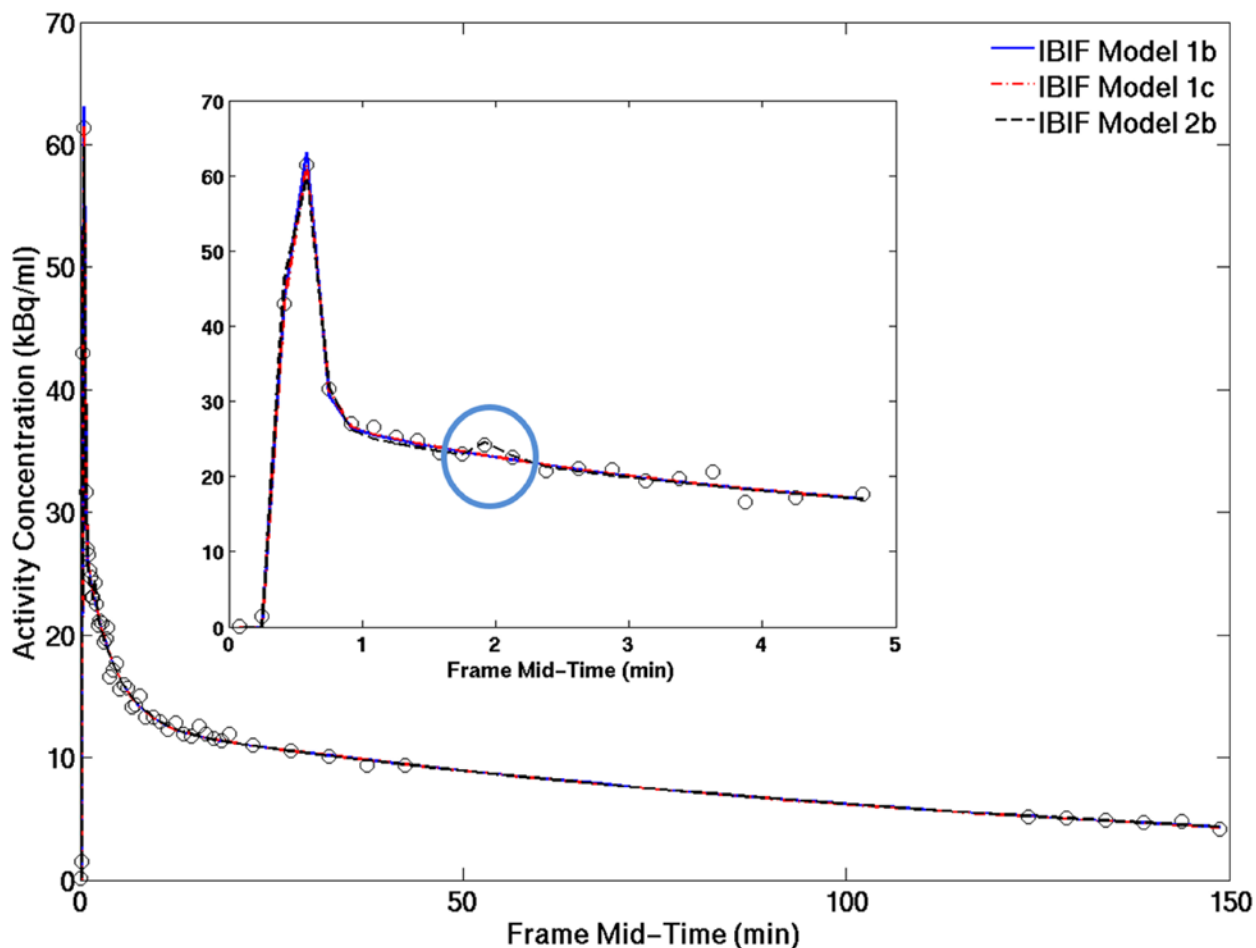


Figure 5-15. Representative IBIF Model Fits for ML-10 #13 at BL Assuming a $2\alpha-1\beta$ Tumor IRF Model. Figure shows a comparison of the candidate IBIF model fits to the measured IBIF data (black circles) for ML-10 #13 at BL assuming simultaneous maximum likelihood fit of a $2\alpha-1\beta$ tumor IRF model. Inset shows the IBIF and model fit for the first 0-5min following injection of [^{18}F]ML-10. The selected IBIF model based on minimum AIC_c was IBIF Model 1b. Visually, little difference is observed between IBIF Model 1b (blue solid line) and IBIF Model 1c (red dot-dash line). IBIF Model 2b (black dashed line) shows signs of overfitting to the IBIF data (circle).

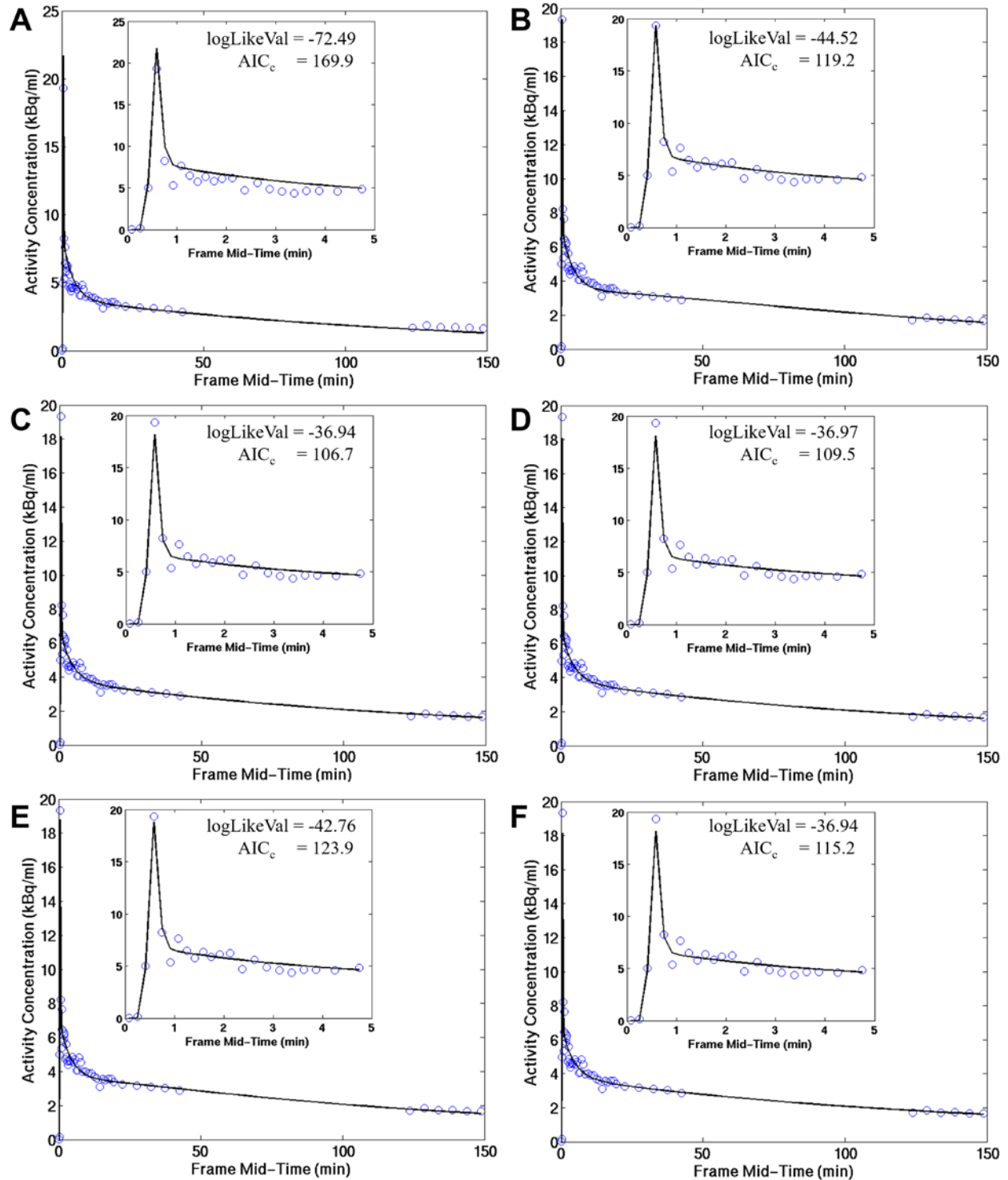


Figure 5-16. Representative Candidate IRF Model Fits for ML-10 #13 at BL Assuming IBIF Model 1b as the Selected Input Model. Figure shows representative IRF tissue model fits assuming joint maximum likelihood fitting using IBIF Model 1b as input model. Estimated maximum log-likelihood value (logLikeVal) and AIC_c values shown

as insets for each IRF model fit. The simplest IRF model fit to the subject's tumor TAC data was a scaled version of the IBIF model (A). From left-to right, the fitted IRF models increase in complexity: (B) single exponential IRF model $1\alpha-1\beta$, (C) single exponential IRF model with a trap $2\alpha-1\beta$, (D) two-exponential reversible IRF model $2\alpha-2\beta$, (E) two-exponential IRF model with a trap $3\alpha-2\beta$, and (F) three-exponential reversible IRF model $3\alpha-3\beta$. For IRF model fitting, the exponential coefficients, α , were constrained to be positive while the exponential rates were constrained to be greater than or equal to zero as described in the methods. An increase in the visual quality of the IRF model fit is observed as the IRF model complexity increases from attenuated IBIF (A), to $1\alpha-1\beta$ IRF model (B), to $2\alpha-1\beta$ IRF model (C). However, little overall difference between the fits of IRF model $2\alpha-1\beta$ and the higher complexity IRF models (D-F) is apparent. Based on minimum AICc criteria, IRF model $2\alpha-1\beta$ was selected as the best IRF model among the tested candidates.

Table 5-9 contains the joint IBIF/IRF model selection results for subject ML-10 #13 at BL. From left to right, the table contains: the candidate IBIF model, candidate IRF model, the total number of model parameters, K , to be estimated during the joint IBIF-IRF fitting (including IBIF and IRF noise variance parameters), and the sum of the squared weighted residuals (WRSS) for the IBIF and IRF models separately. Also tabulated are the values of the log-likelihood function for the model estimates ($\log(\mathcal{L}(\hat{\theta}, \hat{\sigma}^2 | data))$), the AIC, and the AICc. Also shown is the differences between each AICc value and the overall minimum AICc value (i.e. $\Delta AIC_c = AIC_c - (\text{minimum } AIC_c)$). The table row containing the joint IBIF/IRF model with minimum AICc value among the tested models is highlighted in bold.

Table 5-9. Joint IBIF tumor IRF Model Selection Results for ML-10 #13 at Baseline.

IBIF Model	IRF Model	^aK	^bWRSS	$\log(\mathcal{L}(\hat{\theta}, \hat{\sigma}^2 data))$	AIC	AIC_c	ΔAIC_c
IBIF Model 1b	(1 α -0 β)	11	0.853 (1.744)	-72.492	166.983	169.916	63.211
IBIF Model 1b	(1 α -1 β)	13	0.814 (0.610)	-44.516	115.032	119.168	12.463
IBIF Model 1b	(2α-1β)	14	0.778 (0.474)	-36.939	101.878	106.705	0
IBIF Model 1b	(2 α -2 β)	15	0.776 (0.476)	-36.973	103.945	109.527	2.82147
IBIF Model 1b	(3 α -2 β)	16	0.811 (0.571)	-42.757	117.514	123.914	17.209
IBIF Model 1b	(3 α -3 β)	17	0.778 (0.474)	-36.939	107.878	115.163	8.4582
IBIF Model 1c	(1 α -0 β)	13	0.851 (1.749)	-72.498	170.996	175.132	68.427
IBIF Model 1c	(1 α -1 β)	15	0.814 (0.611)	-44.550	119.099	124.681	17.976
IBIF Model 1c	(2 α -1 β)	16	0.767 (0.497)	-37.761	107.521	113.921	7.216
IBIF Model 1c	(2 α -2 β)	17	0.767 (0.497)	-37.761	109.521	116.807	10.102
IBIF Model 1c	(3 α -2 β)	18	0.767 (0.497)	-37.761	111.521	119.762	13.057
IBIF Model 1c	(3 α -3 β)	19	0.767 (0.497)	-37.761	113.521	122.790	16.084
IBIF Model 2b	(1 α -0 β)	14	0.843 (1.795)	-72.919	173.838	178.665	71.960
IBIF Model 2b	(1 α -1 β)	16	0.817 (0.612)	-44.664	121.329	127.729	21.023
IBIF Model 2b	(2 α -1 β)	17	0.811 (0.544)	-41.534	117.068	124.354	17.649
IBIF Model 2b	(2 α -2 β)	18	0.810 (0.595)	-43.768	123.537	131.778	25.073
IBIF Model 2b	(3 α -2 β)	19	0.770 (0.464)	-36.143	110.285	119.553	12.848
IBIF Model 2b	(3 α -3 β)	20	0.810 (0.589)	-43.483	126.965	137.336	30.630

^aK = Total number of model parameters to be estimated (including IBIF and IRF noise variance parameters).
^bWRSS (weighted sum of squared residuals) are given in the form: IBIF Model WRSS (IRF Model WRSS).

Table 5-10 summarizes the joint IBIF/IRF model selection results based on minimum AIC_c alone for each subject at each imaging time-point. For each scan, the selected IBIF model is written in parenthesis below the selected IRF model. In 10 of the 29 cases the 2α - 1β irreversible tissue model was selected as the best candidate IRF model, independent of which IBIF model was being fitted simultaneously. In 6 of the remaining 19 cases a 2α - 2β reversible IRF model was selected to be the best candidate tumor IRF model. Tumor TACs for subject ML-10 #13 were best fitted using a 2α - 1β model at all time-points. A 3α - 2β or a 3α - 3β IRF model was selected as the best candidate IRF model for 8 scans based on minimum AIC_c value alone. For one acquisition, ML-10 #7 at BL, the candidate tissue models failed to fit the measured data using the joint-estimation approach. As a result, the tumor uptake profile of ML-10 #7 at BL was also analyzed using the kinetic modeling tool in the commercially available image analysis software PMOD 3.6 (PMOD Technologies LLC; Zürich, Switzerland). However, PMOD also failed to fit the average tumor activity curve for ML-10 #7 at BL.

Table 5-10. Joint IBIF-Tissue Model Selected using AICc Alone.

Subject ID	BL	ETA	FUA
ML-10 #1	2 α -2 β (IBIF Model 1b)	†N/A	N/A
ML-10 #2	N/A	3 α -2 β (IBIF Model 1b)	N/A
ML-10 #4	2 α -1 β (IBIF Model 1b)	2 α -2 β (IBIF Model 1b)	1 α -1 β (IBIF Model 2b)
ML-10 #5	3 α -2 β (IBIF Model 2b)	2 α -2 β (IBIF Model 1c)	2 α -1 β (IBIF Model 2b)
ML-10 #6	2 α -1 β (IBIF Model 1b)	3 α -2 β (IBIF Model 1b)	3 α -2 β (IBIF Model 1b)
ML-10 #7	Failed fit	1 α -1 β (IBIF Model 1c)	(2 α -1 β) (IBIF Model 1b)
ML-10 #9	3 α -3 β (IBIF Model 2b)	2 α -1 β (IBIF Model 2b)	3 α -2 β (IBIF Model 1c)
ML-10 #10	2 α -2 β (IBIF Model 1c)	€2 α -1 β (IBIF Model 2b)	1 α -1 β (IBIF Model 1c)
ML-10 #11	1 α -1 β (IBIF Model 2b)	2 α -1 β (IBIF Model 2b)	2 α -1 β (IBIF Model 2b)
ML-10 #12	2 α -2 β (IBIF Model 2b)	N/A	N/A
ML-10 #13	2 α -1 β (IBIF Model 1b)	2 α -1 β (IBIF Model 1c)	N/A
ML-10 #14	3 α -2 β (IBIF Model 2b)	3 α -3 β (IBIF Model 1c)	2 α -2 β (IBIF Model 1c)
† N/A = Not available.			
€ Only first acquisition considered for IRF model fitting.			

Figure 5-17 shows an example case, ML10 #14 at ETA, for which the selected joint IBIF/IRF models were IBIF Model 1c and IRF model 3 α -3 β based on minimum AIC_c value alone. For each IRF model fit the IBIF model was IBIF Model-1c. Figure 5-17A shows the selected 3 α -3 β IRF model fit to the measured tumor [¹⁸F]ML-10 uptake profile over the entire 150min acquisition time (left) as well as a zoomed in version of the fit over the first 5 min post racer injection (right). Model estimates are shown as insets with %COV in parentheses. From the inset, the coefficient and exponential rate corresponding to the third IRF exponential are not estimable ((%COV) _{α_3} = 201% and (%COV) _{β_3} = 117%). This poor estimability in IRF model parameters

is likely to produce equally poor estimates of compartmental rate constants. Moreover, the estimated value for β_3 is equal to the maximum value of the constraint (i.e. $\beta_3=10 \text{ min}^{-1}$).

Figure 5-17B and figure 5-17C show IRF model fits using the $3\alpha-2\beta$ and $2\alpha-2\beta$ models, respectively. For IRF model $3\alpha-2\beta$ the accumulation coefficient (α_3) is nearly zero, contributing to its poor estimability. Similarly, β_1 is poorly estimated with $(\%COV)_{\beta_1} = 152\%$. For IRF model $2\alpha-2\beta$, all IBIF and IRF model parameter estimates exhibit a %COV of less than 50%. Visually, little difference between the IRF model selected via information criteria, IRF model $3\alpha-3\beta$, and the simplified IRF model, model $2\alpha-2\beta$, is observed.

Figure 5-18 shows a comparison of the IBIF Model 1c fits obtained through simultaneous estimation with the selected IRF model based on information theoretic considerations, $3\alpha-3\beta$ IRF model (black dashed line), and with the reduced IRF models: $2\alpha-2\beta$ (blue solid line) and $3\alpha-2\beta$ red dot-dash line). For all 3 three IRF models, the fit of IBIF Model 1c to the measured IBIF data is visually similar.

Table 5-11 contains the joint IBIF/IRF model selection results for subject ML-10 #14 at ETA. The table row containing the joint IBIF/IRF model with minimum AIC_c value among the tested models is highlighted in bold. For IBIF Model 1c, the WRSS of the IBIF and candidate IRF models are observed to decrease as estimated IRF model increases in complexity. The WRSS for the fit of IBIF Model 1c are essentially unchanged across IRF models starting with the $2\alpha-2\beta$ IRF model and increasing in complexity. Moreover, the associated IRF model WRSS shows marginal decrease in value starting with the $2\alpha-2\beta$ IRF and increasing in complexity to the $3\alpha-3\beta$ IRF model.

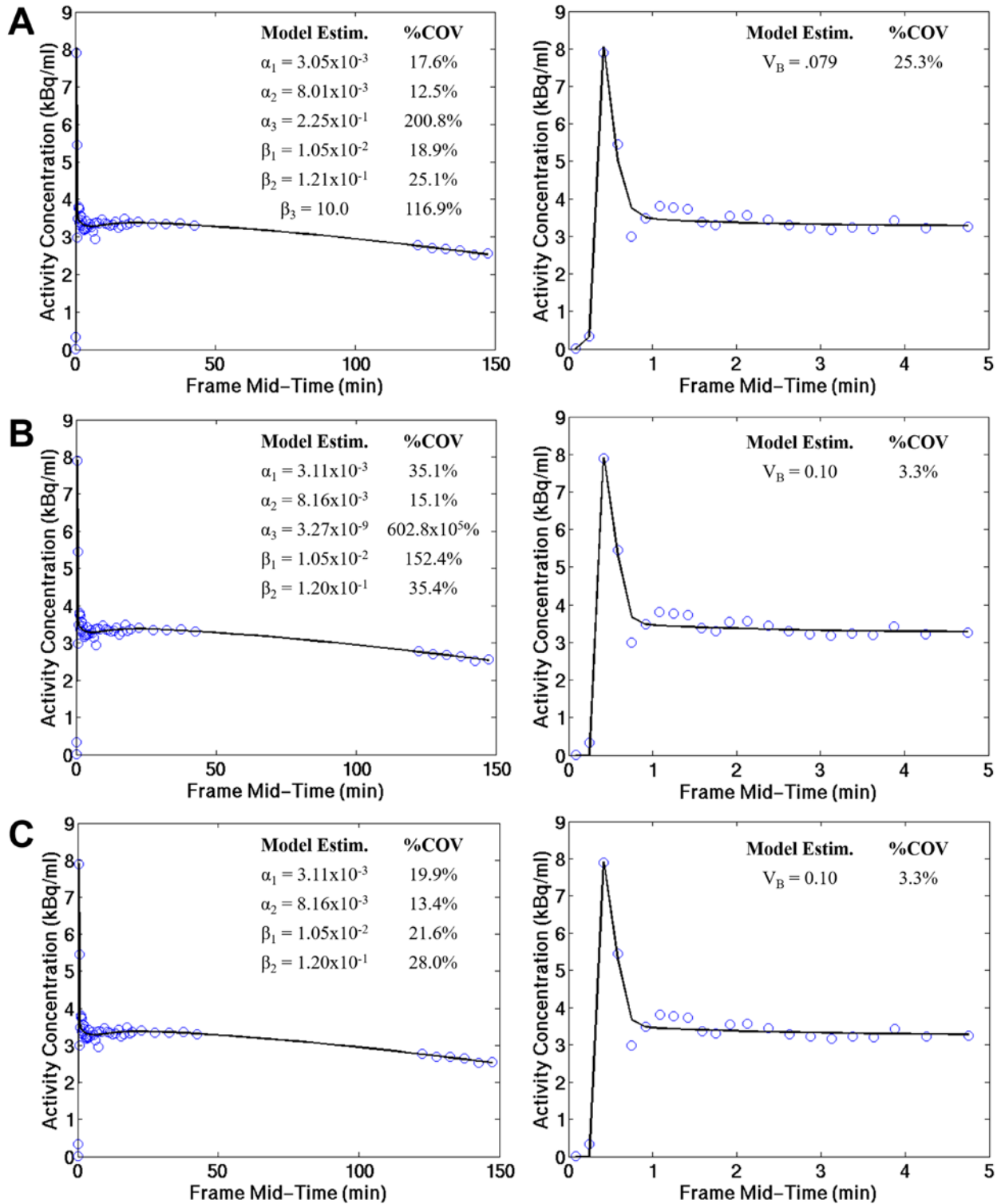


Figure 5-17. Comparison of IRF Model Parameter Fits for ML-10 #14 at ETA Assuming Joint Estimation using IBIF Model 1c. Figure shows a comparison of IRF Model fits in decreasing order of model complexity for ML10 #14

at ETA. IBIF Model 1c was used for simultaneous fitting of each IRF model fit. (A) shows the selected 3 α -3 β IRF model fit to the measured tumor [^{18}F]ML-10 uptake profile over the entire 150 min acquisition time (left) as well as a zoomed in version of the fit over the first 5 min post tracer injection (right). Model estimates are shown as insets with %COV in parentheses. From the inset, the coefficient and exponential rate corresponding to the third IRF exponential are not estimable ($(\%COV)_{\alpha_3} = 201\%$ and $(\%COV)_{\beta_3} = 117\%$). Moreover, the estimated value for β_3 is equal to the maximum value of the constraint (i.e. $\beta_3 = 10 \text{ min}^{-1}$). For model 3 α -2 β (B) the accumulation coefficient α_3 is nearly zero, contributing to its poor estimability. Similarly, β_1 is poorly estimated with $(\%COV)_{\beta_1} = 152\%$. For IRF model 2 α -2 β (C), all IRF model parameter estimates exhibit a %COV of less than 50%. Visually, little difference is apparent between the selected 3 α -3 β IRF model and the simplified 2 α -2 β IRF model.

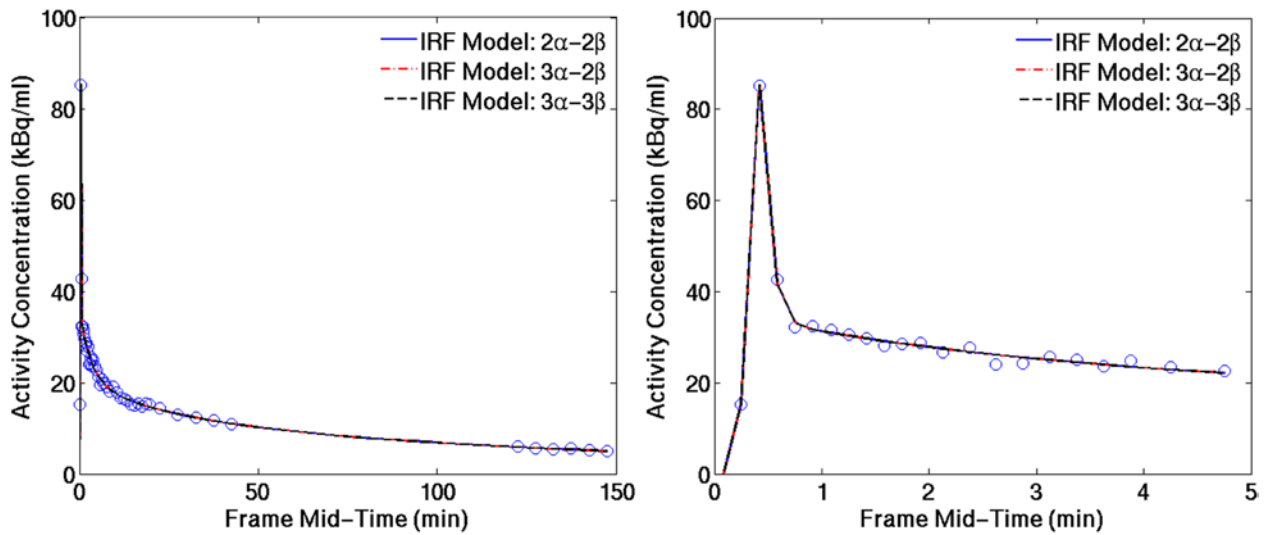


Figure 5-18. Comparison of the IBIF Model 1c Fits Obtained through Simultaneous Estimation with the 3 α -3 β , 3 α -2 β , and 2 α -2 β tumor IRF Models for ML-10 #14 at ETA. Figure shows a comparison of the IBIF Model 1c fits obtained through simultaneous estimation with the selected IRF model based on information theoretic considerations, 3 α -3 β IRF model (black dashed line), and with the reduced IRF models: 2 α -2 β (blue solid line) and 3 α -2 β red dot-dash line). For all 3 three IRF models, the fit of IBIF Model 1c to the measured IBIF data is visually similar.

Table 5-11. Joint IBIF tumor IRF Model Selection Results for ML-10 #14 at Early Therapy Assessment.

IBIF Model	IRF Model	^aK	^bWRSS	$\log(\mathcal{L}(\hat{\theta}, \hat{\sigma}^2 data))$	AIC	AIC_c	ΔAIC_c
IBIF Model 1b	(1 α -0 β)	11	0.761 (24.105)	-131.869	285.739	288.672	275.403
IBIF Model 1b	(1 α -1 β)	13	0.856 (0.391)	-29.782	85.564	89.7000	76.431
IBIF Model 1b	(2 α -1 β)	14	0.768 (0.173)	-6.148	40.295	45.123	31.854
IBIF Model 1b	(2 α -2 β)	15	0.790 (0.125)	1.266	27.469	33.050	19.781
IBIF Model 1b	(3 α -2 β)	16	0.760 (0.124)	2.492	27.016	33.416	20.147
IBIF Model 1b	(3 α -3 β)	17	0.761 (0.121)	3.170	27.6603	34.946	21.677
IBIF Model 1c	(1 α -0 β)	13	0.462 (24.280)	-119.320	264.640	268.776	255.507
IBIF Model 1c	(1 α -1 β)	15	0.495 (0.402)	-16.502	63.004	68.585	55.316
IBIF Model 1c	(2 α -1 β)	16	0.472 (0.181)	5.063	21.873	28.273	15.003
IBIF Model 1c	(2 α -2 β)	17	0.462 (0.160)	8.698	16.604	23.889	10.620
IBIF Model 1c	(3 α -2 β)	18	0.462 (0.160)	8.698	18.604	26.844	13.575
IBIF Model 1c	(3α-3β)	19	0.461 (0.116)	17.000	4.001	13.269	0
IBIF Model 2b	(1 α -0 β)	14	0.450 (24.288)	-118.661	265.323	270.150	256.881
IBIF Model 2b	(1 α -1 β)	16	0.481 (0.408)	-16.162	64.324	70.724	57.455
IBIF Model 2b	(2 α -1 β)	17	0.480 (0.184)	4.197	25.606	32.892	19.623
IBIF Model 2b	(2 α -2 β)	18	0.497 (0.129)	12.391	11.219	19.460	6.191
IBIF Model 2b	(3 α -2 β)	19	0.465 (0.180)	5.639	26.722	35.991	22.722
IBIF Model 2b	(3 α -3 β)	20	0.463 (0.163)	8.194	23.612	33.982	20.713

^aK = Total number of model parameters to be estimated (including IBIF and IRF noise variance parameters).
^bWRSS (weighted sum of squared residuals) are given in the form: IBIF Model WRSS (IRF Model WRSS).

Table 5-12 summarizes the joint IBIF/IRF model selection results for each subject at each imaging time-point based on minimum AIC_c and with the requirement that all model parameters be estimable (i.e. $\%COV \leq 50\%$ for IBIF and IRF model parameters). For each scan, the selected IBIF model is written in parenthesis below the selected IRF model. IRF models that were replaced by less complex models are indicated with an asterisk. 5 of the original 8 three-exponential IRF models in table 5-10 were replaced with a less complex IRF model. When IRF model parameter estimability was considered, the number of times the 2α - 1β irreversible tissue model was selected as the best candidate IRF model remained unchanged at 10, while the number of times the 2α - 2β reversible IRF model was selected increased from 6 to 9 times. The 1α - 1β IRF model was selected as the best candidate IRF model in 4 cases. For 2 subjects, ML-10 #4 and ML-10 #10, the selected IRF model changed from the 2α - 1β model at BL and ETA to a 1α - 1β model at FUA.

In 2 cases, both the IBIF model and tissue IRF model were decreased in complexity for ML-10 #5 at BL and ML-10 #9 at FUA. For the case of ML-10 #5 at BL, the IBIF model coefficient describing the second peak was not estimable ($(\%COV)_{\theta_1} = 58.8\%$). As a result, the IBIF model was reduced in complexity from IBIF Model 2b to IBIF Model 1c. However, the joint IBIF Model 1c and 3α - 2β IRF model returned a non-positive definite parameter co-variance matrix, indicating that this combination of IBIF and IRF model was also not estimable. Similarly, the joint IBIF Model 1c and 2α - 2β IRF model was not estimable. Reducing the complexity of the IBIF model further to IBIF Model 1b yielded estimable IBIF and IRF model parameters.

For the case of ML-10 #9 at FUA the K-L best joint IBIF/IRF model pair were IBIF Model 1c and 3α - 2β IRF model. When model parameter estimability were considered in conjunction with

AIC_c, the best candidate IBIF-IRF model pair was determined to be IBIF Model 1b and IRF model 2 α -1 β . Specifically, the fast washout rate after the peak IBIF concentration contributed to the poor estimability of the IBIF model parameters when IBIF Model 1c was used. To increase identifiability of IBIF parameter estimates, the complexity of the IBIF model was reduced from IBIF Model 1c to IBIF Model 1b. However, the joint estimation of IBIF Model 1b with either IRF models 3 α -2 β or 2 α -2 β resulted in IBIF model parameters that were again not estimable.

Table 5-12. Joint IBIF-Tissue Model Selected using AIC_c and Parameter Estimability Considerations.

Subject ID	BL	ETA	FUA
ML-10 #1	2 α -2 β (IBIF Model 1b)	†N/A	N/A
ML-10 #2	N/A	3 α -2 β (IBIF Model 1b)	N/A
ML-10 #4	2 α -1 β (IBIF Model 1b)	*2 α -1 β (IBIF Model 1b)	1 α -1 β (IBIF Model 2b)
ML-10 #5	*2 α -2 β *(IBIF Model 1b)	2 α -2 β (IBIF Model 1c)	2 α -1 β (IBIF Model 2b)
ML-10 #6	2 α -1 β (IBIF Model 1b)	3 α -2 β (IBIF Model 1b)	3 α -2 β (IBIF Model 1b)
ML-10 #7	Failed fit	1 α -1 β (IBIF Model 1c)	2 α -1 β (IBIF Model 1b)
ML-10 #9	*2 α -2 β (IBIF Model 2b)	2 α -1 β (IBIF Model 2b)	*2 α -1 β *(IBIF Model 1b)
ML-10 #10	2 α -2 β (IBIF Model 1c)	€2 α -1 β (IBIF Model 2b)	1 α -1 β (IBIF Model 1c)
ML-10 #11	1 α -1 β (IBIF Model 2b)	*1 α -0 β (IBIF Model 2b)	*1 α -0 β *(IBIF Model 1b)
ML-10 #12	2 α -2 β (IBIF Model 2b)	N/A	N/A
ML-10 #13	2 α -1 β (IBIF Model 1b)	2 α -1 β (IBIF Model 1c)	N/A
ML-10 #14	*2 α -2 β (IBIF Model 2b)	*2 α -2 β (IBIF Model 1c)	2 α -2 β (IBIF Model 1c)
† N/A = Not available. € Only first acquisition considered for IRF model fitting. * Less complex IRF model replacing the minimum AIC _c IRF model.			

In the case of ML-10 #11, who exhibited the shortest PFS of less than 1 month, a scaled version of the corresponding IBIF model was selected as the best model describing the [^{18}F]ML-10 time-course in the tumor for both the ETA and FUA time-points, consistent with poor therapeutic effect. Figure 5-19 shows a comparison of IRF model fits for ML-10 #11 at ETA assuming IBIF Model 2b as the IBIF model for each. IRF model parameters and associated %COV are shown as insets. The IBIF and IRF models selected based on minimum AIC_c for ML-10 #11 at ETA were IBIF Model 2b and the $2\alpha-1\beta$ IRF model. Figure 5-18A shows the fit of IRF model $2\alpha-1\beta$ to the entire tumor TAC (left) and the first 5 min of data (right). Similarly, Figure 5-19B and Figure 5-19C contain the IBIF model fits simultaneously estimated with the $1\alpha-1\beta$ and $1\alpha-0\beta$ IRF models. Thus, by visually moving from figure 5-19A thru figure 5-19C the effect of reducing the complexity of the IRF model on the estimates for the IRF model parameters can be observed. The IRF model coefficients and exponential rates for IRF models $2\alpha-1\beta$ and $1\alpha-1\beta$ are not estimable. The $1\alpha-0\beta$ IRF model (figure 5-19C) results in a blood volume fraction of $V_B = 0.307$ with %COV = 1.4% Visually, the $1\alpha-0\beta$ IRF model describes the overall trend of the tumor TAC.

Figure 5-20 shows fits of IBIF Model 2b to the measure blood TAC data assuming the (A) $2\alpha-1\beta$, (B) $1\alpha-1\beta$, and (C) $1\alpha-0\beta$ tumor IRF models. For each case, IBIF model fits are shown for the entire blood TAC (left) and the first 5min of data (right). Comparison across figure panes reveals a slight bias is incurred in fitting IBIF Model 2b to the measured IBIF data, in exchange for better parameter estimability gained by simultaneous estimation using the $1\alpha-0\beta$ IRF model in place of the more complex $2\alpha-1\beta$ and $1\alpha-1\beta$ IRF models.

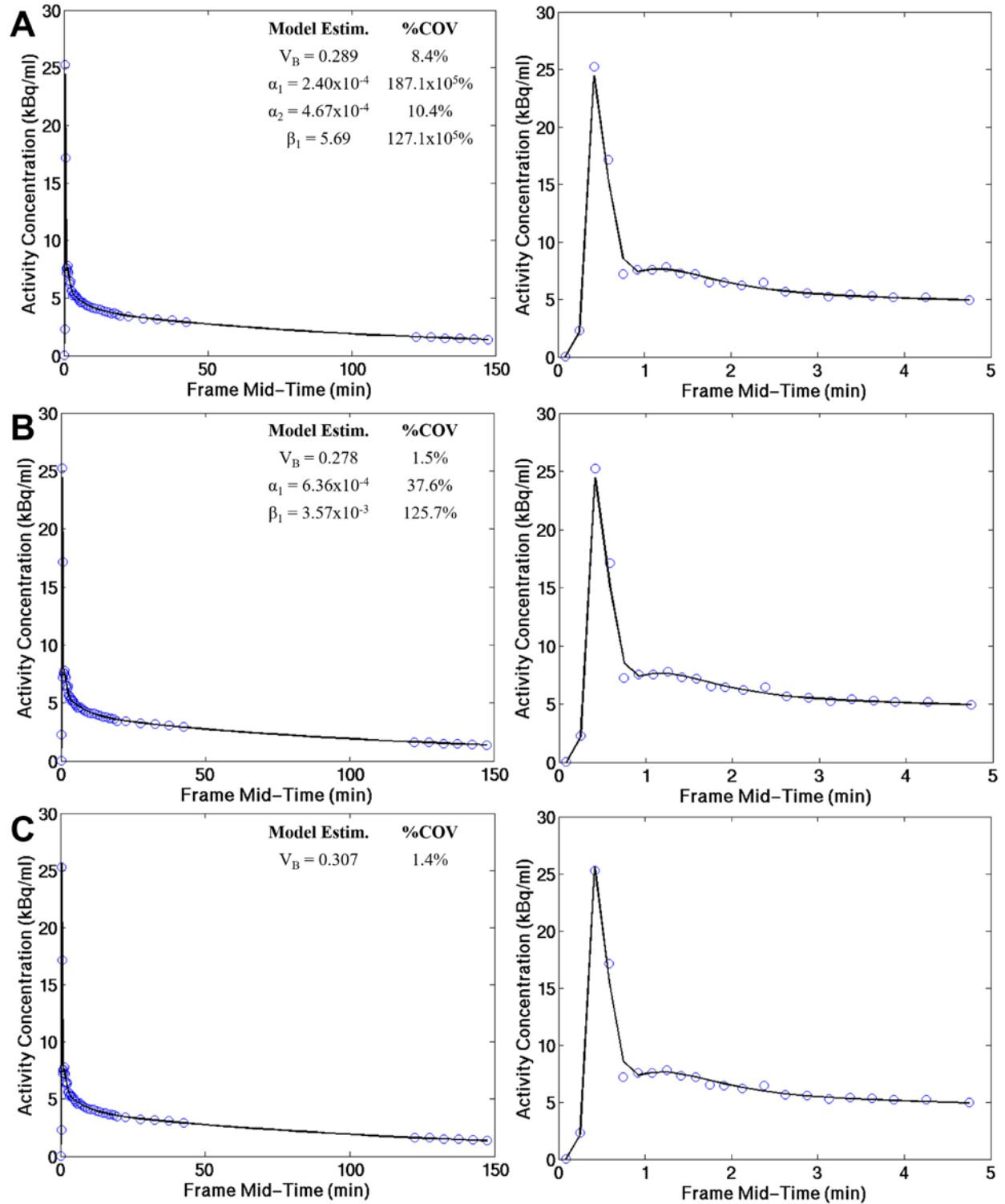


Figure 5-19. IRF model fits for ML-10 #11 at ETA Assuming Joint Maximum Likelihood Estimation with IBIF

Model 2b. For ML-10 #11 at ETA, the selected IBIF and IRF models based on minimum AICc alone were IBIF

Model 2b and the $2\alpha-1\beta$ IRF model, respectively. Figure shows resulting fits using the (A) $2\alpha-1\beta$, (B) $1\alpha-1\beta$, and (C) $1\alpha-0\beta$ models, assuming IBIF Model 2b for each fit. IRF model fits are shown for the entire 150 min tumor TAC (left) and the first 5 min of data (right), with parameter estimates and %COV shown as insets to the 150 min data fits. The IRF model coefficients and exponential rates for IRF models $2\alpha-1\beta$ and $1\alpha-1\beta$ are not estimable. The $1\alpha-0\beta$ IRF model (C) results in a blood volume fraction of $V_B = 0.307$ with %COV = 1.4%. Visually, the $1\alpha-0\beta$ IRF model describes the overall trend of the tumor TAC.

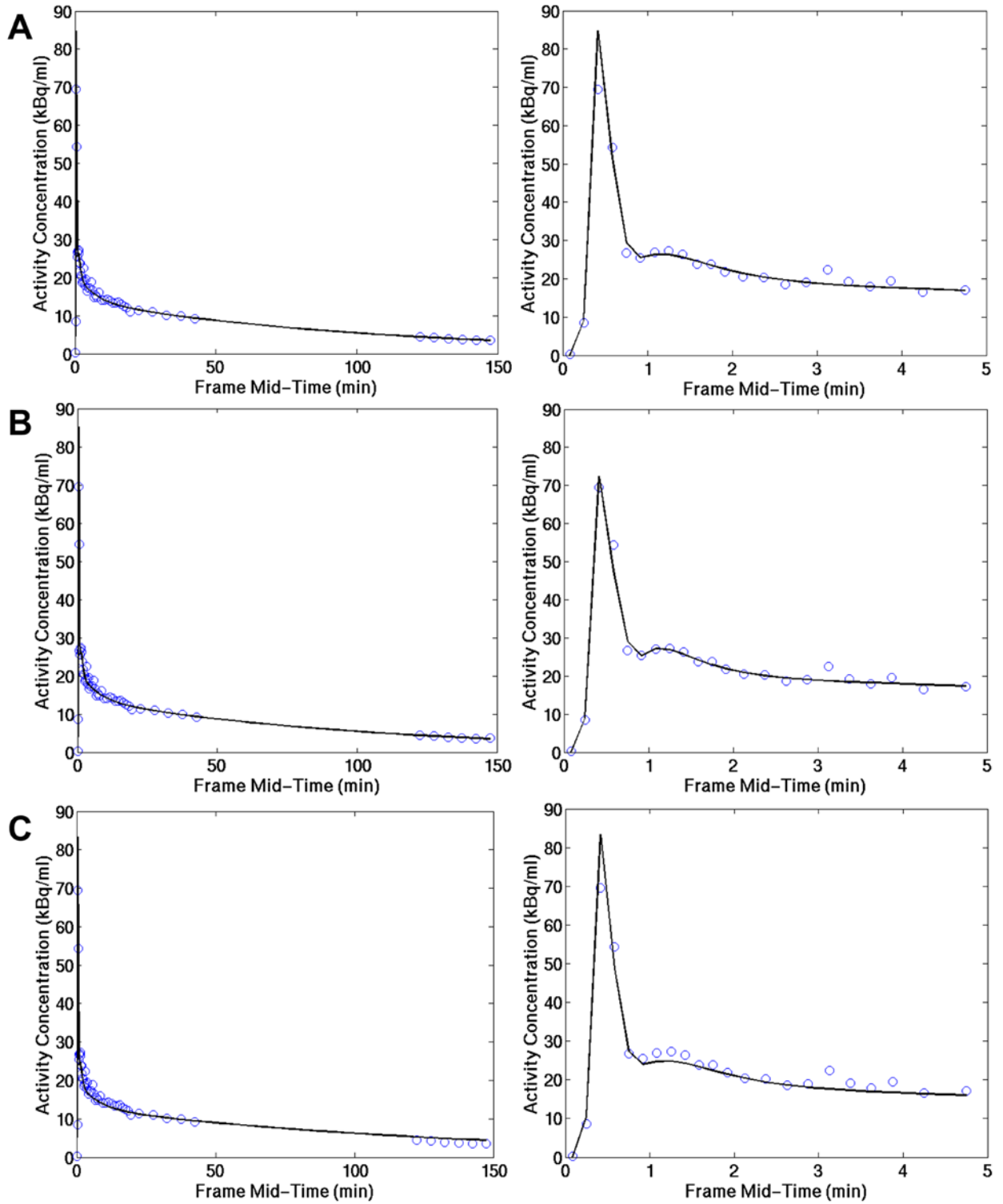


Figure 5-20. Comparison of fits for IBIF Model 2b to Measured Blood TAC Data for ML-10 #11 at ETA Assuming Joint Estimation with Different IRF Models. For ML-10 #11 at ETA, the selected IBIF and IRF models

based on minimum AIC_c alone were IBIF Model 2b and the $2\alpha-1\beta$ IRF model, respectively. Figure shows resulting fits of the IBIF model IBIF Model 2b and simultaneous estimation with IRF models (A) $2\alpha-1\beta$, (B) $1\alpha-1\beta$, and (C) $1\alpha-0\beta$ models. IBIF Model 2b fits are shown for the entire 150 min tumor TAC (left) and the first 5 min of data (right). Comparison across figure panes reveals a slight bias is incurred in fitting IBIF Model 2b to the measured IBIF data, in exchange for better parameter estimability gained by simultaneous estimation with the $1\alpha-0\beta$ IRF model in place of the more complex $2\alpha-1\beta$ and $1\alpha-1\beta$ IRF models.

Table 5-13 contains macroparameter estimates obtained from each IRF model fit in table 5-12 above with coefficient of variation expressed as a percentage given in parentheses. For reversible models the corresponding macroparameter is V_T , while for irreversible models the macroparameter is K_i . Across all acquisitions, estimates for the blood volume fraction (V_B) ranged from 0.025 to 0.391 (mean = 0.148 and median = 0.123). For tumor TACs for which the selected best model was a $2\alpha-1\beta$ IRF model, V_B ranged from 0.036 to 0.276 (mean = 0.132, median = 0.116), K_1 ranged from 0.006 ml/cm³/min to 0.030 ml/cm³/min (mean = 0.015 ml/cm³/min, median = 0.012 ml/cm³/min), and associated K_i values ranged from 4.787×10^{-4} ml/cm³/min to 1.829×10^{-3} ml/cm³/min (mean = 1.225×10^{-3} ml/cm³/min, median = 1.145×10^{-3} ml/cm³/min). For tumor TACs for which the selected best model was a $2\alpha-2\beta$ IRF model, V_B ranged from 0.0469 to 0.2111 (mean = 0.1194, median = 0.1154), K_1 ranged from 0.0113 ml/cm³/min to 0.0658 ml/cm³/min (mean = 0.0216 ml/cm³/min, median = 0.0266 ml/cm³/min), and associated V_T values ranged from 0.0275 ml/cm³ to 0.7157 ml/cm³ (mean = 0.5318 ml/cm³, median = 0.4554 ml/cm³).

Table 5-13. Estimated Macroparameter Values for Each Subject and Time-point using the Corresponding Selected IBIF and IRF Models in Table 5-12.

Subject ID	V_B			K_1 (ml/cm ³ /min)			K_i (ml/cm ³ /min)			V_T (ml/cm ³)		
	[†] BL	*ETA	[‡] FUA	BL	ETA	FUA	BL	ETA	FUA	BL	ETA	FUA
ML-10 #1	^a 0.1460 (8.90%)	N/A	N/A	0.0658 (32.26%)	N/A	N/A	---	N/A	N/A	0.4558 (3.53%)	N/A	N/A
ML-10 #2	N/A	0.1529 (6.29%)	N/A	N/A	0.0802 (24.14%)	N/A	N/A	4.105x10 ⁻⁴ (14.45%)	N/A	N/A	---	N/A
ML-10 #4	0.0683 (11.42%)	0.0254 (23.12%)	^b 0.0452 (14.17%)	0.0201 (10.63%)	0.0276 (7.13%)	^b 0.0069 (7.37)	1.002x10 ⁻³ (11.87%)	9.887x10 ⁻⁴ (15.19%)	---	---	---	^b 0.3041 (4.49%)
ML-10 #5	0.1374 (3.90%)	0.1407 (3.27%)	0.1390 (2.78%)	0.0181 (10.92%)	0.0157 (14.58%)	0.0152 (4.02%)	---	---	1.190x10 ⁻³ (7.88%)	0.6159 (4.16%)	0.6174 (2.75%)	---
ML-10 #6	0.0705 (6.66%)	0.0635 (8.99%)	0.0599 (11.12%)	0.0304 (3.81%)	0.0588 (12.16%)	0.1004 (18.15%)	1.143x10 ⁻³ (12.43%)	8.013x10 ⁻⁴ (25.60%)	8.262x10 ⁻⁴ (22.46%)	---	---	---
ML-10 #7	N/A	^b 0.1231 (3.28%)	0.1314 (5.63%)	N/A	^b 0.0051 (5.2%)	0.0170 (15.20%)	N/A	---	1.778x10 ⁻³ (4.14%)	N/A	^b 0.4085 (4.27%)	---
ML-10 #9	0.2111 (6.75%)	0.2692 (2.53%)	0.1080 (5.53%)	0.0349 (8.03%)	0.0211 (9.12%)	0.0278 (7.87%)	---	8.365x10 ⁻⁴ (10.01%)	1.086x10 ⁻³ (6.38%)	0.6078 (13.16%)	---	---
ML-10 #10	0.0811 (3.67%)	[‡] 0.0428 (6.85%)	^b 0.0407 (7.24%)	0.0265 (5.21%)	[‡] 0.0191 (3.61%)	^b 0.0074 (3.21%)	---	5.483x10 ⁻³ (3.41%)	---	0.7014 (2.13%)	---	^b 0.5214 (3.19%)
ML-10 #11	0.2871 (14.53%)	0.3074 (1.42%)	0.3910 (0.08%)	6.363x10 ⁻⁴ (37.57%)	---	---	---	---	---	0.1781 (89.89%)	---	---
ML-10 #12	0.0469 (23.28%)	N/A	N/A	0.0305 (7.15%)	N/A	N/A	---	N/A	N/A	0.7157 (1.57%)	N/A	N/A
ML-10 #13	0.2343 (3.95%)	0.2977 (2.68%)	N/A	0.0119 (37.85%)	0.0168 (13.18%)	N/A	3.675x10 ⁻⁴ (16.55%)	3.783x10 ⁻⁴ (28.56%)	N/A	---	---	N/A
ML-10 #14	0.1194 (3.01%)	0.0997 (3.29%)	0.0563 (4.67%)	0.0150 (9.32%)	0.0113 (12.36%)	0.0216 (8.36%)	---	---	---	0.3896 (3.95%)	0.3642 (5.89%)	0.3675 (1.85%)

^a Parameter estimates are reported as: estimated value (percent coefficient of variation).

[†] BL = Baseline.

*ETA = Early therapy assessment.

[‡] FUA = Follow-up assessment.

5.2.4.3 Spectral Analysis of Tumor Tissue TACs

Spectral Analysis (SA) can be used to obtain additional evidence to support joint IBIF-IRF model selection results as well as provide an alternative method for estimation of [¹⁸F]ML-10 uptake macroparameters. However, a principal difference between SA and the joint IBIF-IRF model fitting approach of the previous section is that SA requires *a priori* knowledge of the input concentration into the linear system. That is, SA requires knowledge of the IBIF model to estimate the spectrum of the measured [¹⁸F]ML-10 uptake profile of the tumor. Therefore, for each [¹⁸F]ML-10 PET scan, the selected IBIF model from the joint IBIF/IRF tumor model selection contained in table 5-12 will be used as the selected IBIF model.

Figure 5-21 shows the results from applying SA to the 0-150 min PET data of ML-10 #6 at ETA. The NNLS spectra is shown in the top pane while the spectra obtained by minimizing the L₁ norm is shown in the bottom pane. For each pane, spectral coefficients (blue circles) are plotted versus spectral probing rates (on log₁₀-scale). The thick vertical red dot-dashed line denotes the data-adaptive fast rate cut-off. Also plotted are one-sided 95% bootstrap confidence intervals (dashed-curves) to aid in assessing variability in peak locations. SA was performed on [¹⁸F]ML-10 tumor time activity curves corrected for radioactive decay in all cases.

Visual analysis of figure 5-21 reveals 2 strong components between the slow and fast rate thresholds for both spectral solutions, supporting an IRF model contain at least 2 causal exponentials. A weak trapping component (i.e. a spectral peak at $\beta_{\min} = 10^{-4} \text{ min}^{-1}$) is also observed for both SA methods. The appearance of a weak trapping component in addition to the 2 strong

reversible components is suggestive for 3α - 2β IRF tumor model for this subject and time-point, consistent with the nonlinear joint IBIF-IRF modeling results in table 5-12. Both SA methods also detect a strong component above their respective data-adaptive fast-rate cutoff values resulting from a strong blood component in the measured [^{18}F]ML-10 tumor TAC.

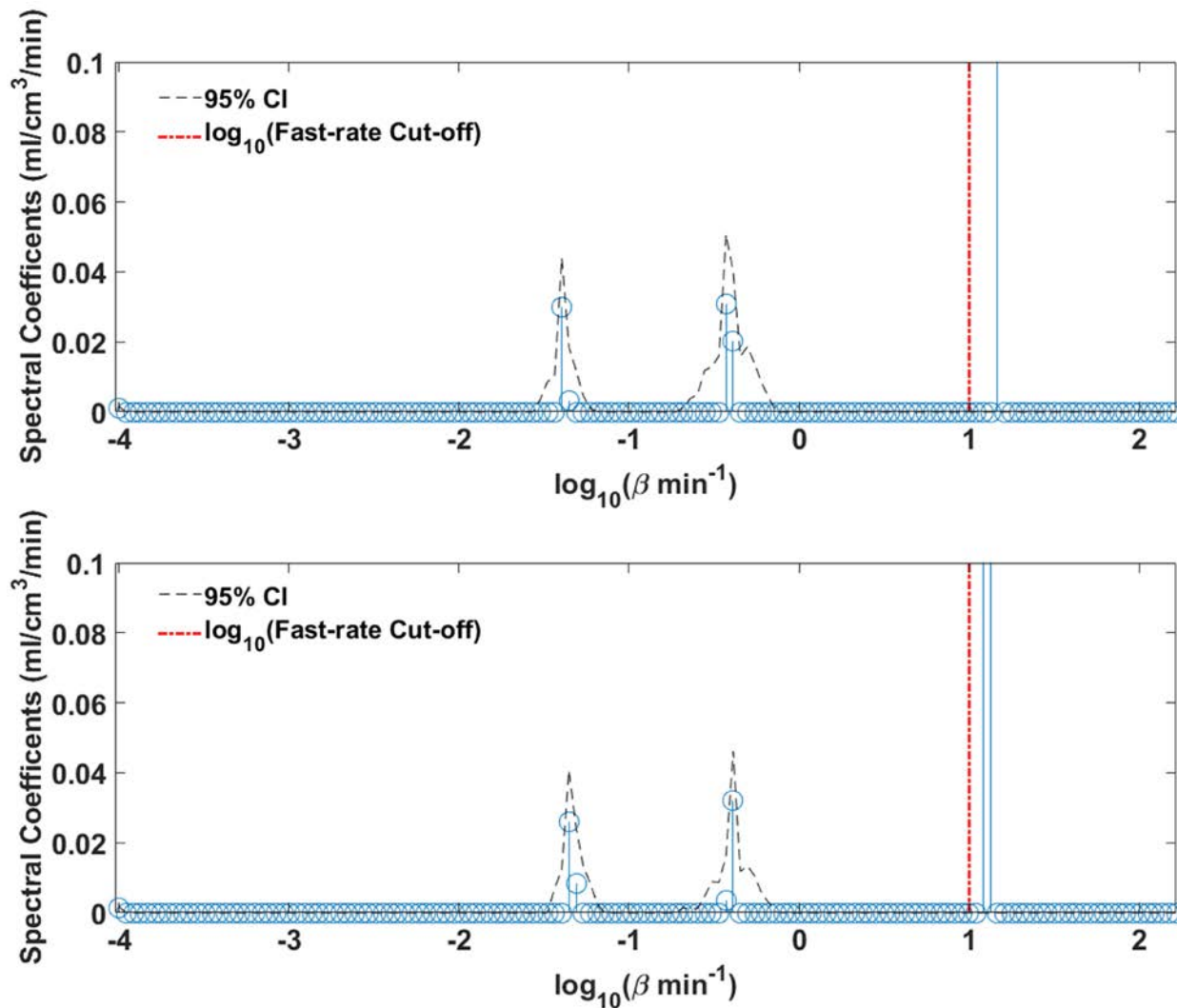


Figure 5-21. Tumor TAC Spectra for ML-10 # 6 at ETA using IBIF Model 1b. Spectral coefficients (blue circles) plotted versus spectral rates (on \log_{10} -scale) for ML-10 #6 at ETA assuming IBIF Model 1b. (Top) shows NNLS, while (bottom) shows and L_1 norm solution. SA is performed on PET data corrected for radioactive decay. 151 logarithmically spaced rates in the interval $[10^{-4} \text{ min}^{-1}, 200 \text{ min}^{-1}]$ were used for the basis vectors. Spectral coefficients are shown corrected for estimation bias via bootstrap resampling using 1000 bootstrap samples. One-sided bootstrap 95% confidence intervals (95% CIs) for each spectral probing rate are plotted as a dashed-curve for both methods. The estimated fast-rate thresholds are shown as vertical red dot-dash lines. Both methods detect 2 reversible components below the fast rate threshold. A comparatively weak trapping component at the smallest probing rate β_{\min}

$= 10^{-4} \text{ min}^{-1}$, suggestive for a $3\alpha\text{-}2\beta$ tumor IRF model. A spurious component is detected above the fast-rate threshold for both methods resulting from a strong blood signal in the measured tumor time activity curve.

A similar spectral profile to that of ML-10 #6 at ETA is observed for ML-10 #12 at BL as shown in figure 5-22. That is, 2 strong reversible components are observed between 10^{-4} min^{-1} and fast rate thresholds for both the NNLS (top) and L_1 norm (bottom) spectral solutions, along with a weak component observed at 10^{-4} min^{-1} . The strengths of the trapping components are considerably smaller in comparison with the detected reversible components. The appearance of a weak trapping component in addition to the 2 strong reversible components is suggestive for $3\alpha\text{-}2\beta$ IRF tumor model for this subject and time-point, in contrast to nonlinear joint IBIF-IRF modeling results, which support a $3\alpha\text{-}2\beta$ IRF tumor model (table 5-12).

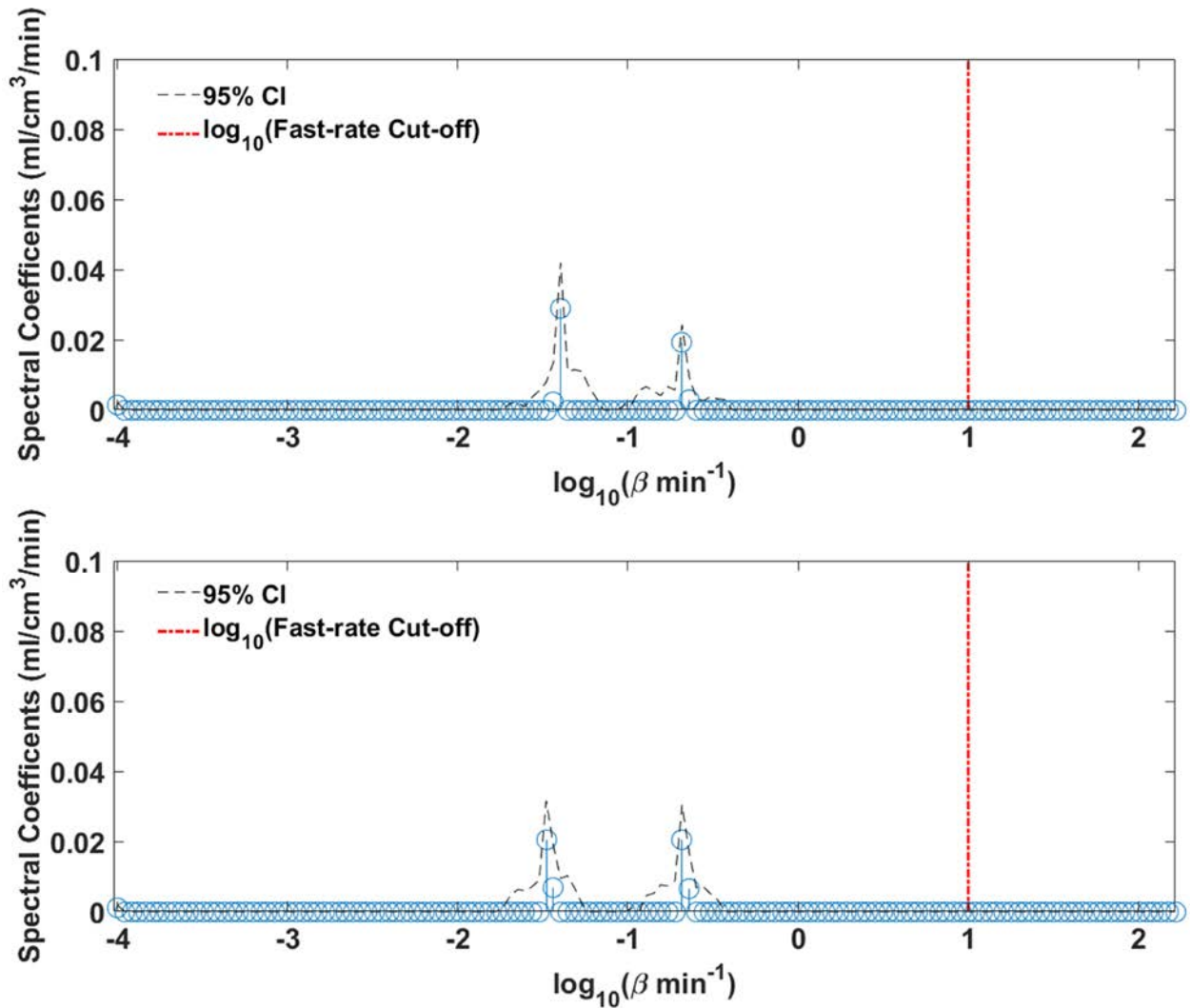


Figure 5-22. Tumor TAC Spectra for ML-10 # 12 at BL using IBIF Model 2b. Spectral coefficients (blue circles) plotted versus spectral rates (on \log_{10} -scale) for ML-10 #12 at BL assuming IBIF Model 2b. (Top) shows NNLS, while (bottom) shows and L_1 norm solution. SA is performed on PET data corrected for radioactive decay. 151 logarithmically spaced rates in the interval $[10^{-4} \text{ min}^{-1}, 200 \text{ min}^{-1}]$ were used for the basis vectors. Spectral coefficients are shown corrected for estimation bias via bootstrap resampling using 1000 bootstrap samples. One-sided bootstrap 95% confidence intervals (95% CIs) for each spectral probing rate are plotted as a dashed-curve for both methods. The estimated fast-rate thresholds are shown as vertical red dot-dash lines. Both methods detect 2 reversible components below the fast rate threshold. A comparatively weak trapping component at the smallest probing rate $\beta_{\min} = 10^{-4} \text{ min}^{-1}$, suggestive for a $3\alpha\text{-}2\beta$ tumor IRF model.

Figure 5-23 shows the SA results for ML-10 #14 at FUA assuming IBIF Model 1c as input $[^{18}\text{F}]\text{ML-10}$ concentration model. For this subject and time-point no spectral peak is observed at the slowest tested rate $\beta_{\min} = 10^{-4} \text{ min}^{-1}$. The NNLS solution (top) detects 3 reversible components as part of the tumor tissue IRF (suggesting a $3\alpha\text{-}3\beta$ IRF model), while the L_1 norm solution (bottom) detects only 2 components supporting a $2\alpha\text{-}2\beta$ tumor tissue IRF. The selected IRF model from joint IBIF/IRF modeling was a $2\alpha\text{-}2\beta$ model (table 5-12). Both SA methods are in agreement over the location of the slowest detected component. However, the NNLS method detects 2 additional components in the same spectral range that the L_1 norm solution detects only a single component. Interestingly, the bootstrap one-sided 95% CI of the NNLS solution covers the location of the single peak in the L_1 solution. This suggests that the 2 components observed from the NNLS solution may be due to an inability of the NNLS method to resolve a single component within this spectral range. Both SA methods also detect a strong component above their respective data-adaptive fast-rate cutoff values resulting from a strong blood component in the measured $[^{18}\text{F}]\text{ML-10}$ tumor TAC.

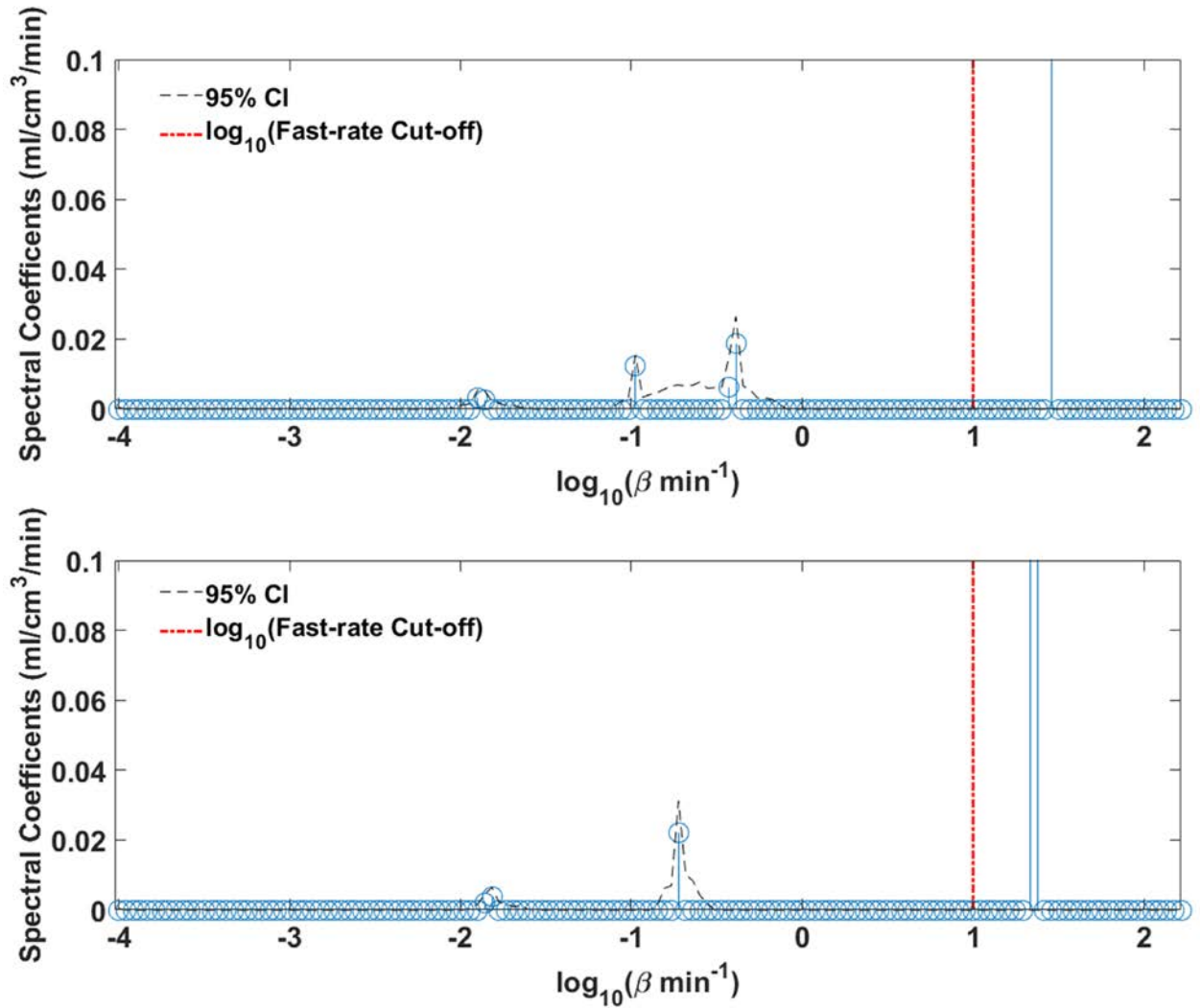


Figure 5-23. Tumor TAC Spectra for ML-10 # 14 at FUA using IBIF Model 1c. Spectral coefficients (blue circles) plotted versus spectral rates (on \log_{10} -scale) for ML-10 #14 at FUA assuming IBIF Model 1c. (Top) shows NNLS, while (bottom) shows and L_1 norm solution. SA is performed on PET data corrected for radioactive decay. 151 logarithmically spaced rates in the interval $[10^{-4} \text{ min}^{-1}, 200 \text{ min}^{-1}]$ were used for the basis vectors. Spectral coefficients are shown corrected for estimation bias via bootstrap resampling using 1000 bootstrap samples. One-sided bootstrap 95% confidence intervals (95% CIs) for each spectral probing rate are plotted as a dashed-curve for both methods. The estimated fast-rate thresholds are shown as vertical red dot-dash lines. No spectral peak is observed at the slowest tested rate $\beta_{\min} = 10^{-4} \text{ min}^{-1}$ for either method. Both SA methods are in agreement over the location of the slowest detected component. However, the NNLS method detects 2 additional components in the same spectral range that the

L_1 norm solution detects a single component. The bootstrap one-sided 95% CI of the NNLS solution covers the location of the single peak in the L_1 solution, suggesting that the 2 components observed from the NNLS solution may be due to an inability of the NNLS method to resolve a single component within this spectral range. A spurious component is detected above the fast-rate threshold for both methods resulting from a strong blood signal in the measured tumor time activity curve.

SA can provide additional support for reducing IRF model complexity in nonlinear joint IBIF/IRF modeling in addition to parameter estimability arguments. For example, based on minimum AIC_c value alone a $2\alpha-1\beta$ IRF model was determined to be the best IRF model to describe the measured Tumor TAC of ML-10 #11 at ETA (see table 5-10). However, the parameters of the $2\alpha-1\beta$ IRF model were observed to be poorly estimated (figure 5-19). Figure 5-24 shows the corresponding NNLS (top) and L_1 norm (bottom) SA solutions for ML-10 #11 at ETA assuming IBIF Model 2b. Both methods detect a strong component above their respective fast-rate cutoff values resulting from a strong contribution from blood pool to the measured tumor TAC, as well as a single weak component near $\log_{10}(\beta) \approx -2$ below their fast-rate cutoffs. These spectra are suggestive for a tumor TAC that is primarily composed of [^{18}F]ML-10 concentration in the blood, consistent with the reduced IRF model in table 5-12.

Similarly, joint IBIF/IRF model selection applied to ML-10 #14 at ETA minimum AIC_c alone supported a reversible $3\alpha-3\beta$ tumor IRF model. However, both the $3\alpha-3\beta$ and $3\alpha-2\beta$ IRF models produced parameter estimates that were not statistically estimable (figure 5-17). Reducing the IRF model complexity further to the $2\alpha-2\beta$ IRF model produced statistically reliable parameter estimates (figure 5-17). Figure 5-25 shows the corresponding NNLS (top) and L_1 norm (bottom)

SA solutions for ML-10 #14 at ETA assuming IBIF Model 1c. For both solutions, 2 strong components are observed between the minimum probing rate $\beta_{\min} = 10^{-4} \text{ min}^{-1}$ and the fast-rate cut-offs with no component trapping component observed. The NNLS solution detects an additional weak component ($\alpha = 2.032 \times 10^{-3}$) with spectral rate greater than 1 min^{-1} that lies outside its bootstrap one-sided 95%CI (95%CI upper-bound = 1.915×10^{-3}), suggesting this additional peak maybe a result of noise. Taken together, these SA results provide additional support for a 2α - 2β IRF model.

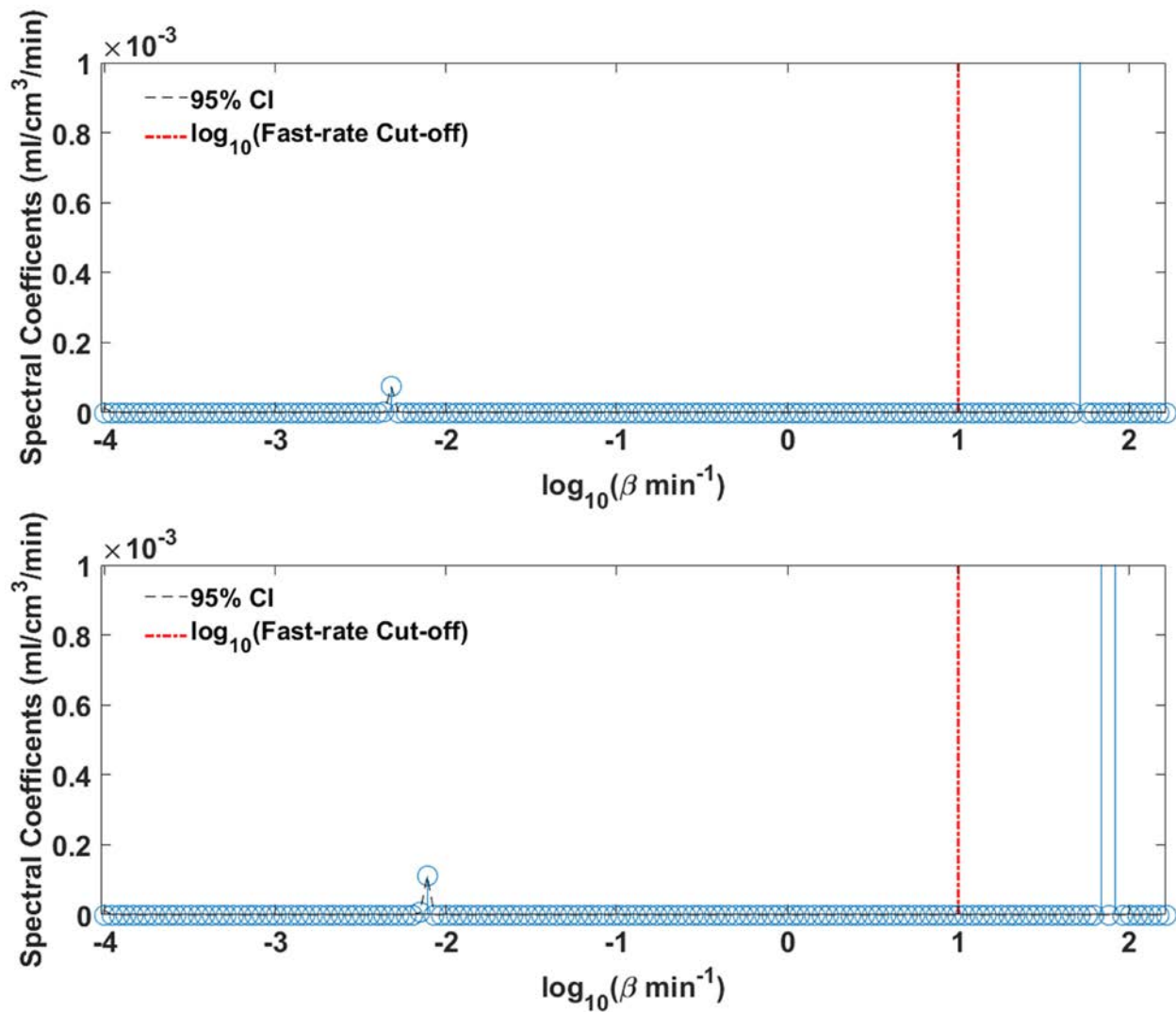


Figure 5-24. Tumor TAC Spectra for ML-10 # 11 at ETA using IBIF Model 2b. Spectral coefficients (blue circles) plotted versus spectral rates (on \log_{10} -scale) for ML-10 #11 at ETA assuming IBIF Model 2b. (Top) shows NNLS, while (bottom) shows and L_1 norm solution. SA is performed on PET data corrected for radioactive decay. 151 logarithmically spaced rates in the interval $[10^{-4} \text{ min}^{-1}, 200 \text{ min}^{-1}]$ were used for the basis vectors. Spectral coefficients are shown corrected for estimation bias via bootstrap resampling using 1000 bootstrap samples. One-sided bootstrap 95% confidence intervals (95% CIs) for each spectral probing rate are plotted as a dashed-curve for both methods. T The estimated fast-rate thresholds are shown as vertical red dot-dash lines. No spectral peak is observed at the slowest tested rate $\beta_{\min} = 10^{-4} \text{ min}^{-1}$ for either method. Both methods detect a strong component above their respective fast-rate cutoff values resulting from a strong blood contribution to the tumor TAC, as well as a single weak component

near $\log_{10}(\beta) \approx -2$ below their fast-rate cutoffs. These spectra are suggestive for a tumor TAC that is primarily composed of [^{18}F]ML-10 concentration in the blood, consistent with a $1\alpha-0\beta$ IRF model.

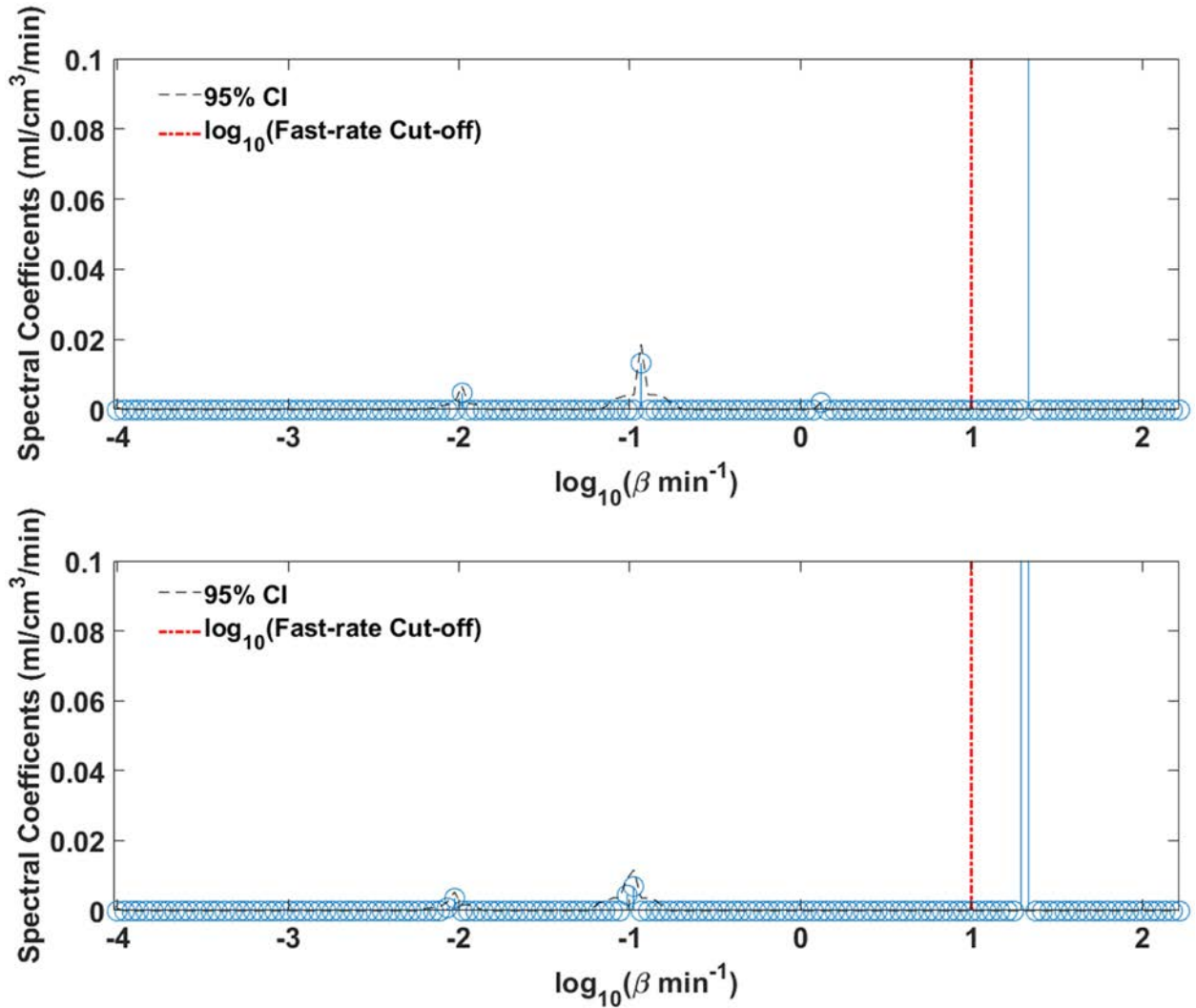


Figure 5-25. Tumor TAC Spectra for ML-10 # 14 at ETA using IBIF Model 1c. Spectral coefficients (blue circles) plotted versus spectral rates (on \log_{10} -scale) for ML-10 #14 at ETA assuming IBIF Model 1c. (Top) shows NNLS, while (bottom) shows and L_1 norm solution. SA is performed on PET data corrected for radioactive decay. 151 logarithmically spaced rates in the interval $[10^{-4} \text{ min}^{-1}, 200 \text{ min}^{-1}]$ were used for the basis vectors. Spectral coefficients are shown corrected for estimation bias via bootstrap resampling using 1000 bootstrap samples. One-sided bootstrap

95% confidence intervals (95% CIs) for each spectral probing rate are plotted as a dashed-curve for both methods. The estimated fast-rate thresholds are shown as vertical red dot-dash lines. No spectral peak is observed at the slowest tested rate $\beta_{\min} = 10^{-4} \text{ min}^{-1}$ for either method. For both solutions, 2 strong components are observed between the minimum probing rate $\beta_{\min} = 10^{-4} \text{ min}^{-1}$ and the fast-rate cut-offs with no component trapping component observed. The NNLS solution detects an additional weak component ($\alpha = 2.032 \times 10^{-3}$) with spectral rate greater than 1 min^{-1} that lies outside its bootstrap one-sided 95% CI (95% CI upper-bound = 1.915×10^{-3}), suggesting this additional peak maybe a result of noise. A spurious component is detected above the fast-rate thresholds for both methods resulting from a strong blood signal in the measured tumor time activity curve. Taken together, these SA results provide additional support for a 2α - 2β IRF model.

Table 5-14 summarizes the ranges in number of reversible components detected, estimated values of K_1 , K_i , and V_T across subjects and time-points for each SA method. SA results of ML-10 #10 at ETA are not included in the calculation of macroparameter ranges, because SA was applied to only the first acquisition (0-45 min PET data) for this time-point. The minimum number of detected reversible components was 0 and occurred for ML-10 #11 at FUA using both SA methods. This finding is consistent with joint IBIF/IRF model selection results above, in which the 1α - 0β (i.e. scaled blood concentration) IRF model determined to be the best candidate IRF model (table 5-12).

Table 5-14. Summary of Macroparameter Estimates for NNLS and L₁ Norm Spectral Analysis Methods.

	NNLS SA Method	L₁ Norm SA Method
Num. Reversible Components	[0, 3]	[0, 4]
$\overset{\text{r}}{K}_1$ (ml/cm³/min)	[2.062x10 ⁻⁵ , 0.1033]	[2.574x10 ⁻⁵ , 0.1003]
$\overset{\text{r}}{K}_i$ (ml/cm³/min)	[0, 1.489x10 ⁻³]	[0, 1.466x10 ⁻³]
$\overset{\text{r}}{V}_T$ (ml/cm³)	[0, 0.7929]	[0, 0.7234]
[‡] SA results of ML-10 #10 at ETA are not included in calculation of macroparameter range.		

Table 5-15 and table 5-16 contain the number of reversible components detected for each subject and time-point along with whether a trapping component was detected using the NNLS and L₁ norm methods, respectively. For the 29 total tumor TACs analyzed using SA, trapping component was detected using the NNLS method 13 times and using the L₁ norm method 15 times. However, the strength of the trapping component for each of these cases was small compared to the strengths of the reversible spectral components (as in figure 5-20 and figure 5-21).

ML-10 #5 at BL is found to have 4 spectral components detected using both SA methods. Figure 5-25 shows the corresponding spectra for this subject. A spectral peak is observed at the slowest tested rate $\beta_{\min} = 10^{-4} \text{ min}^{-1}$ for the NNLS solution but not the L₁ norm solution. Both SA methods detect a strong component near $\log_{10}(\beta) = 0$. Further comparison between the NNLS and L₁ norm methods suggest that the 2 detected components centering around $\log_{10}(\beta) = -2$ for the L₁ norm method may be due to an inability of the L₁ norm method to resolve a single component within this spectral range. Both SA methods also detect a strong component above their respective data-adaptive fast-rate cutoff values resulting from a strong blood component in the measured [¹⁸F]ML-10 tumor TAC.

Table 5-17 and table 5-18 contain the macroparameter estimates with associated one-sided 95% bootstrap confidence intervals using the NNLS (table 5-17) and L_1 norm (table 5-18) SA methods. Macroparameter estimates for K_1 , K_i , and V_T across subjects and time-points are consistent with corresponding estimates from simultaneous IBIF/IRF nonlinear fitting (table 5-13) above. Consistent with the joint IBIF/IRF modeling results, SA using both the NNLS and L_1 norm methods failed to fit the tumor TAC of ML-10 #7 at BL.

Table 5-15. Number of Detected Spectral Components using NNLS SA Method.

Subject ID	Total Number of Detected Reversible Components			Trapping Component Detected		
	[†] BL	*ETA	[‡] FUA	BL	ETA	FUA
ML-10 #1	3	N/A	N/A	No	N/A	N/A
ML-10 #2	N/A	3	N/A	N/A	No	N/A
ML-10 #4	3	3	2	No	Yes	No
ML-10 #5	3	2	3	Yes	Yes	No
ML-10 #6	2	2	3	Yes	Yes	Yes
ML-10 #7	N/A	2	2	N/A	No	Yes
ML-10 #9	3	2	3	No	Yes	Yes
ML-10 #10	2	[‡] 2	3	No	[‡] No	No
ML-10 #11	1	1	0	Yes	No	Yes
ML-10 #12	2	N/A	N/A	Yes	N/A	N/A
ML-10 #13	1	2	N/A	Yes	Yes	N/A
ML-10 #14	3	3	3	No	No	Yes

[†]BL = Baseline.
 *ETA = Early therapy assessment.
[‡]FUA = Follow-up assessment.
[‡] Only first acquisition (0-45 min PET data) was used for spectral analysis.

Table 5-16. Number of Detected Spectral Components using L₁ Norm SA Method.

Subject ID	Total Number of Reversible Spectral Components			Trapping Component Detected		
	[†] BL	*ETA	[‡] FUA	BL	ETA	FUA
ML-10 #1	3	N/A	N/A	No	N/A	N/A
ML-10 #2	N/A	3	N/A	N/A	No	N/A
ML-10 #4	3	3	2	No	Yes	No
ML-10 #5	4	2	3	No	Yes	No
ML-10 #6	3	2	2	Yes	Yes	Yes
ML-10 #7	N/A	2	2	N/A	No	Yes
ML-10 #9	3	2	3	No	Yes	Yes
ML-10 #10	3	[‡] 4	2	No	[‡] No	No
ML-10 #11	2	1	0	Yes	No	Yes
ML-10 #12	2	N/A	N/A	Yes	N/A	N/A
ML-10 #13	1	3	N/A	Yes	Yes	N/A
ML-10 #14	3	2	2	No	No	No

[†]BL = Baseline.
 *ETA = Early therapy assessment.
[‡]FUA = Follow-up assessment.
[‡] Only first acquisition (0-45 min PET data) was used for spectral analysis.

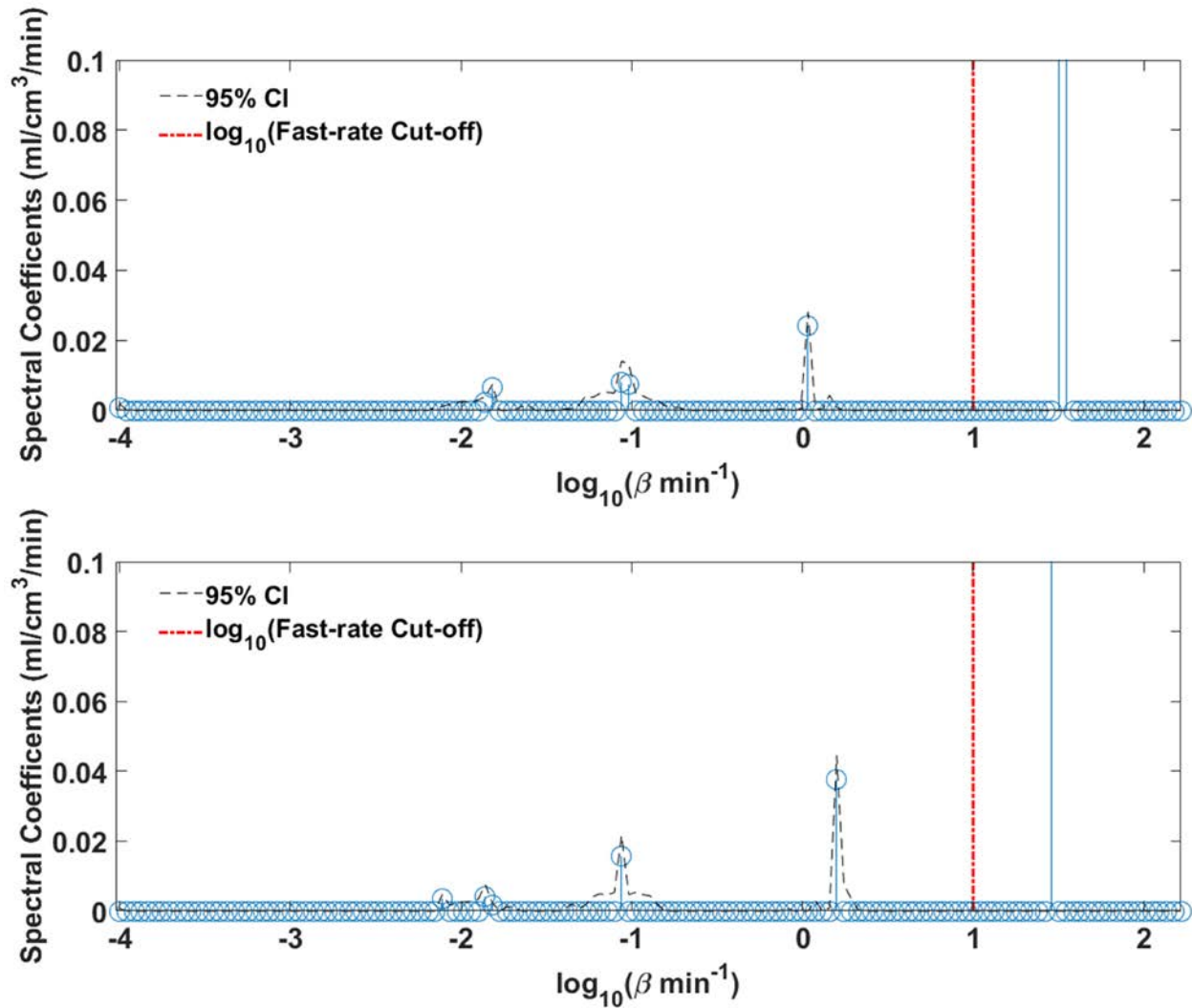


Figure 5-26. Tumor TAC Spectra for ML-10 # 5 at BL using IBIF Model 1b. Spectral coefficients (blue circles) plotted versus spectral rates (on \log_{10} -scale) for ML-10 #5 at BL assuming IBIF Model 1b. (Top) shows NNLS, while (bottom) shows and L_1 norm solution. SA is performed on PET data corrected for radioactive decay. 151 logarithmically spaced rates in the interval $[10^{-4} \text{ min}^{-1}, 200 \text{ min}^{-1}]$ were used for the basis vectors. Spectral coefficients are shown corrected for estimation bias via bootstrap resampling using 1000 bootstrap samples. One-sided bootstrap 95% confidence intervals (95% CIs) for each spectral probing rate are plotted as a dashed-curve for both methods. The estimated fast-rate thresholds are shown as vertical red dot-dash lines. A spectral peak is observed at the slowest tested rate $\beta_{\min} = 10^{-4} \text{ min}^{-1}$ for the NNLS solution but not the L_1 norm solution. Further comparison between the NLSS and L_1 norm methods suggest that the 2 detected components centering around $\log_{10}(\beta) = -2$ for the L_1 norm method

may be due to an inability of the L_1 norm method to resolve a single component within this spectral range. A spurious component is detected above the fast-rate threshold for both methods resulting from a strong blood signal in the measured tumor time activity curve.

Table 5-17. Macroparameter Estimates Obtained from Spectral Analysis using NNLS Method.

Subject ID	K ₁ (ml/cm ³ /min)			K _i (ml/cm ³ /min)			V _T (ml/cm ³)		
	[†] BL	[*] ETA	^e FUA	BL	ETA	FUA	BL	ETA	FUA
ML-10 #1	^a 0.0845 [0, 0.334]	N/A	N/A	0 [0, 1.04x10 ⁻³]	N/A	N/A	0.4261 [0, 0.719]	N/A	N/A
ML-10 #2	N/A	0.0718 [0, 0.126]	N/A	N/A	0 [0, 3.21x10 ⁻⁴]	N/A	N/A	0.3265 [0, 0.382]	N/A
ML-10 #4	0.0196 [0, 0.130]	0.0458 [0, 0.125]	0.0072 [0, 0.121]	0 [0, 1.05x10 ⁻³]	6.536x10 ⁻⁴ [0, 9.56x10 ⁻⁴]	0 [0, 6.45x10 ⁻⁴]	0.7929 [0, 0.879]	0.4054 [0, 0.638]	0.2903 [0, 0.348]
ML-10 #5	0.0264 [0, 0.102]	0.0141 [0, 0.059]	0.0154 [0, 0.052]	5.748 x10 ⁻⁴ [0, 1.37x10 ⁻³]	7.979x10 ⁻⁴ [0, 1.34x10 ⁻³]	0 [0, 9.54x10 ⁻⁴]	0.4071 [0, 0.900]	0.3510 [0, 0.766]	0.5291 [0, 0.822]
ML-10 #6	0.0316 [0, 0.121]	0.0513 [0, 0.141]	0.1033 [0, 0.222]	8.729x10 ⁻⁴ [0, 1.01x10 ⁻³]	7.386x10 ⁻⁴ [0, 9.07x10 ⁻⁴]	7.154x10 ⁻⁴ [0, 9.01x10 ⁻⁴]	0.5450 [0, 0.982]	0.6211 [0, 0.940]	0.7033 [0, 1.106]
ML-10 #7	N/A	0.0055 [0, 0.205]	0.0217 [0, 0.186]	N/A	0 [0, 1.22x10 ⁻³]	1.48910 ⁻³ [0, 1.61x10 ⁻³]	N/A	0.4034 [0, 0.560]	0.1319 [0, 1.403]
ML-10 #9	0.0346 [0, 0.066]	0.0246 [0, 0.086]	0.0436 [0, 0.114]	0 [0, 8.97x10 ⁻⁴]	5.391x10 ⁻⁴ [0, 6.38x10 ⁻⁴]	6.900x10 ⁻⁴ [0, 9.29x10 ⁻⁴]	0.5827 [0, 1.556]	0.2078 [0, 0.459]	0.2576 [0, 0.733]
ML-10 #10	0.0245 [0, 0.079]	[‡] 0.0186 [0, 0.044]	0.0455 [0, 0.121]	0 [0, 6.91x10 ⁻⁴]	[‡] 0 [0, 5.46x10 ⁻³]	0 [0, 1.48x10 ⁻³]	0.6490 [0, 0.687]	[‡] 2.4957 [0, 2.59]	0.5546 [0, 0.691]
ML-10 #11	0.0012 [0, 0.041]	3.74x10 ⁻⁵ [0, 0.034]	2.06x10 ⁻⁵ [0, 0.035]	2.739x10 ⁻⁴ [0, 3.25x10 ⁻⁴]	0 [0, 4.41x10 ⁻⁵]	2.062x10 ⁻⁵ [0, 3.85x10 ⁻⁵]	0.0224 [0, 0.167]	0.0078 [0, 0.021]	0 [0, 0.018]
ML-10 #12	0.0306 [0, 0.063]	N/A	N/A	1.039x10 ⁻³ [0, 1.31x10 ⁻³]	N/A	N/A	0.4975 [0, 0.968]	N/A	N/A
ML-10 #13	0.0090 [0, 0.127]	0.0179 [0, 0.273]	N/A	2.833x10 ⁻⁴ [0, 3.31x10 ⁻⁴]	2.319x10 ⁻⁴ [0, 3.18x10 ⁻⁴]	N/A	0.0561 [0, 0.237]	0.1649 [0, 0.304]	N/A
ML-10 #14	0.0224 [0, 0.214]	0.0110 [0, 0.054]	0.0232 [0, 0.064]	0 [0, 9.70x10 ⁻⁴]	0 [0, 7.73x10 ⁻⁴]	1.598x10 ⁻⁵ [0, 6.40x10 ⁻⁴]	0.4728 [0, 1.037]	0.3285 [0, 0.443]	0.3651 [0, 0.425]

^a Macroparameter estimates are reported as: estimated value [one-sided 95% confidence interval].
[†] BL = Baseline.
^{*} ETA = Early therapy assessment.
^e FUA = Follow-up assessment.
[‡] Only first acquisition (0-45 min PET data) was used for spectral analysis.

Table 5-18. Macroparameter Estimates Obtained from Spectral Analysis using L₁ Norm Method.

Subject ID	K ₁ (ml/cm ³ /min)			K _i (ml/cm ³ /min)			V _T (ml/cm ³)		
	[†] BL	[*] ETA	[‡] FUA	BL	ETA	FUA	BL	ETA	FUA
ML-10 #1	^a 0.0764 [0, 0.298]	N/A	N/A	0 [0, 8.75x10 ⁻⁴]	N/A	N/A	0.4181 [0, 0.481]	N/A	N/A
ML-10 #2	N/A	0.0925 [0, 0.172]	N/A	N/A	0 [0, 2.89x10 ⁻⁴]	N/A	N/A	0.3415 [0, 0.365]	N/A
ML-10 #4	0.0255 [0, 0.142]	0.0573 [0, 0.106]	0.0111 [0, 0.153]	0 [0, 1.01x10 ⁻³]	5.370x10 ⁻⁴ [0, 9.50x10 ⁻⁴]	0 [0, 8.57x10 ⁻⁴]	0.4929 [0, 0.560]	0.4304 [0, 0.609]	0.3045 [0, 0.368]
ML-10 #5	0.0327 [0, 0.118]	0.0149 [0, 0.049]	0.0158 [0, 0.043]	0 [0, 1.33x10 ⁻³]	9.771x10 ⁻⁴ [0, 1.43x10 ⁻³]	0 [0, 9.22x10 ⁻⁴]	0.5705 [0, 0.752]	0.3298 [0, 0.739]	0.5262 [0, 0.690]
ML-10 #6	0.0473 [0, 0.190]	0.0448 [0, 0.156]	0.1003 [0, 0.200]	1.008x10 ⁻³ [0, 1.13x10 ⁻³]	9.050x10 ⁻⁴ [0, 1.04x10 ⁻³]	8.316x10 ⁻⁴ [0, 1.01x10 ⁻³]	0.5053 [0, 1.230]	0.5915 [0, 1.109]	0.7234 [0, 1.121]
ML-10 #7	N/A	0.0060 [0, 0.280]	0.0248 [0, 0.258]	N/A	0 [0, 1.21x10 ⁻³]	1.466x10 ⁻³ [0, 1.58x10 ⁻³]	N/A	0.3798 [0, 0.549]	0.1243 [0, 1.833]
ML-10 #9	0.0360 [0, 0.060]	0.0328 [0, 0.124]	0.0404 [0, 0.078]	0 [0, 8.70x10 ⁻⁴]	6.094x10 ⁻⁴ [0, 6.72x10 ⁻⁴]	8.006x10 ⁻⁴ [0, 9.52x10 ⁻⁴]	0.5088 [0, 0.826]	0.2187 [0, 0.619]	0.2327 [0, 0.759]
ML-10 #10	0.0256 [0, 0.083]	[‡] 0.0221 [0, 0.047]	0.0099 [0, 0.089]	0 [0, 7.22x10 ⁻⁴]	[‡] 0 [0, 5.57x10 ⁻³]	0 [0, 1.68x10 ⁻³]	0.6430 [0, 0.699]	[‡] 1.1737 [0, 1.844]	0.5119 [0, 0.686]
ML-10 #11	0.0021 [0, 0.028]	6.110x10 ⁻⁵ [0, 0.024]	4.574x10 ⁻⁵ [0, 0.025]	3.296x10 ⁻⁴ [0, 3.51x10 ⁻⁴]	0 [0, 4.43x10 ⁻⁵]	2.574x10 ⁻⁵ [0, 5.11x10 ⁻⁵]	0.0194 [0, 0.339]	0.0079 [0, 0.027]	0 [0, 0.016]
ML-10 #12	0.0316 [0, 0.055]	N/A	N/A	8.030x10 ⁻⁴ [0, 1.16x10 ⁻³]	N/A	N/A	0.5527 [0, 0.842]	N/A	N/A
ML-10 #13	0.0121 [0, 0.122]	0.0840 [0, 0.343]	N/A	2.904x10 ⁻⁴ [0, 3.40x10 ⁻⁴]	2.224x10 ⁻⁴ [0, 2.80x10 ⁻⁴]	N/A	0.0691 [0, 0.309]	0.2007 [0, 0.325]	N/A
ML-10 #14	0.0142 [0, 0.134]	0.0091 [0, 0.058]	0.0183 [0, 0.049]	0 [0, 9.48x10 ⁻⁴]	0 [0, 8.84x10 ⁻⁴]	0 [0, 5.65x10 ⁻⁴]	0.4319 [0, 0.817]	0.3304 [0, 0.497]	0.3376 [0, 0.375]

^a Macroparameter estimates are reported as: estimated value [one-sided 95% confidence interval].
[†] BL = Baseline.
^{*} ETA = Early therapy assessment.
[‡] FUA = Follow-up assessment.
[‡] Only first acquisition (0-45 min PET data) was used for spectral analysis.

5.2.4.4 Compartmental Modeling

Compartmental modeling provides a means to understand and interpret macroparameter estimates. For example, radiotracer compartmental modeling can be used to determine what fraction of total distribution volume is related to the volume of the specific, or what proportion of tracer that enters the tissue gets irreversibly trapped in the tissue. IBIF Model 1b and IRF model $2\alpha-2\beta$ were selected as the best IBIF and tumor tissue IRF models among the tested candidates for ML-10 #5 at BL (table 5-12). Figure 5-27 shows the corresponding 2T-4K model fit results for ML-10 #5 at BL obtained via simultaneous modeling with IBIF Model 1b. The associated 2-tissue compartment model rate constants (K_1 , k_2 , k_3 , and k_4) are shown as an inset table of the tissue model fit along with V_B . Assuming radiotracer exchange is accurately described by a 2T-4K compartmental model, the ratio of V_S/V_T quantifies the proportion of radiotracer bound to the target tissue at steady-state if the radiotracer concentration in the blood were held constant. Interpreted this way, results suggest that approximately 63.48% of the [^{18}F]ML-10 uptake for this subject is by GBM tissue undergoing apoptosis.

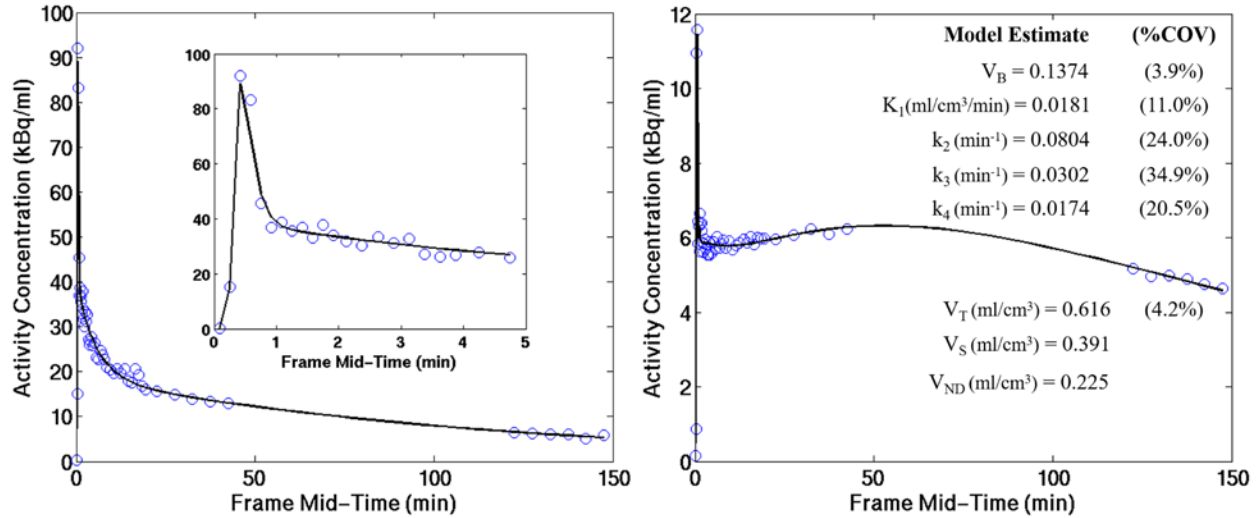


Figure 5-27. Example 2-Tissue Compartment Model Fit Obtained from Joint Maximum Likelihood Estimation with IBIF Model 1b for ML-10 #5 at BL. IBIF Model 1b (left) and 2T-4K tumor tissue model (right) fits obtained for subject ML-10 #5 at BL using the joint maximum likelihood estimation method. The associated 2-tissue compartment model rate constants are shown as an inset table of the tissue model fit. Normalized residuals from both the IBIF and 2T-4K model fits were consistent with following a standard Gaussian distribution based on the Kolmogorov-Smirnov test (IBIF Model 1b: $p \leq 0.7008$; 2T-4K model: $p \leq 0.5626$). Furthermore, both sets of residuals passed the runs test (IBIF Model 1b: $p \leq 0.6932$; 2T4K model: $p \leq 0.9551$).

Figure 5-28 shows example tissue compartmental modeling results for ML-10 #12 at BL. The selected best candidate IBIF and tumor IRF models for this subject were IBIF Model 2b and IRF model $2\alpha-2\beta$ (table 5-12). Figure 5-28A shows the resulting 2T-4K model fit consistent with a $2\alpha-2\beta$ IRF model (left) and corresponding compartmental rate constant sensitivity analysis (right). The estimated values of the 2T-4K rate constants are shown as inset to the tissue model fit with corresponding parameter %COV in parentheses. For this case, the estimated influx rate k_3 of [¹⁸F]ML-10 into the apoptotic tissue (i.e. the specific compartment) is larger than the efflux rate

of radiotracer returning from the compartment of the specific to the interstitial space (i.e. the non-displaceable compartment) quantified by k_4 .

Figure 5-28A (right) shows the corresponding sensitivity functions for each rate constants as well as V_B . The sensitivity functions for the influx rates K_1 , and k_3 are positive over the duration of the scan, indicating an increase in either one of these parameters results in an increase in the value of the tissue model C_T . Similarly, the sensitivity functions for the efflux parameters k_2 and k_4 are negative over the scan duration, indicating that an increase in either of these parameters corresponds to a decrease in C_T . Visually, the sensitivity functions for k_3 (green curve) and k_4 (magenta curve) are nearly scaled versions of each other and are primarily influenced by the same portion of the measured tumor TAC data. These results suggest that it is not possible to simultaneously separate the influence of k_3 from k_4 on the [^{18}F]ML-10 uptake profile for this scan using the measured tumor TAC alone.

Figure 5-28B shows the fit results when the reduced 2-tissue 3-rate constant (2T-3K) is fit to the same tumor TAC data for ML-10 #12 at BL. The estimated values of the 2T-3K rate constants are shown as inset to the tissue model fit with corresponding parameter %COV in parentheses. For this simplified case, the efflux parameter k_4 is constrained to equal 0, resulting in increased precision on the estimate for k_3 compared to the 2T-4K model. Figure 5-28B (right) shows corresponding sensitivity functions for the 2T-3K model. The individual sensitivity function profiles for each rate constant are visually different, suggesting it is possible to separate the influence of each rate constant on the measured tumor TAC assuming the 2T-3K model.

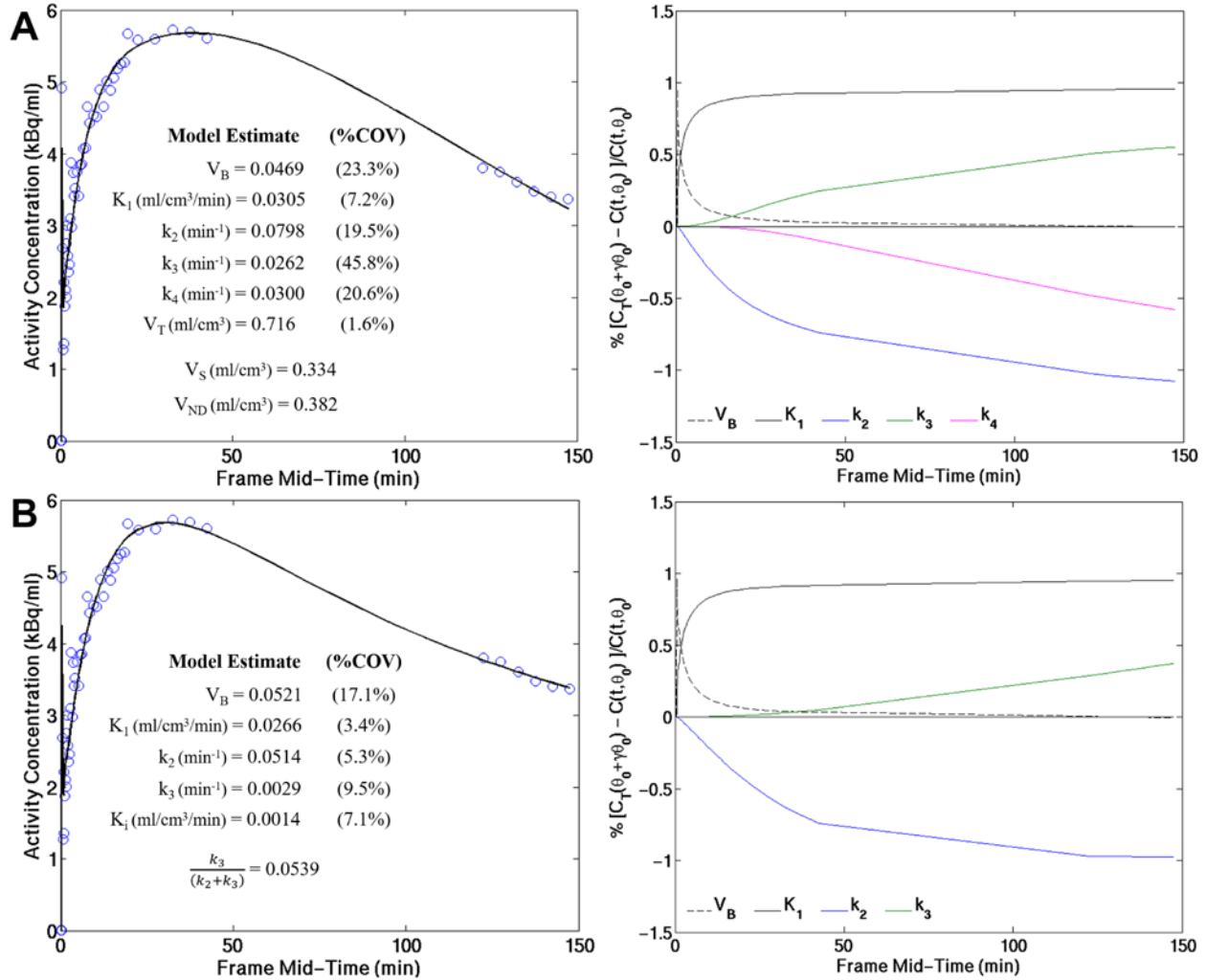


Figure 5-28. Comparison of 2T-4K and 2T-3K Compartmental Model Fit Results from Joint Maximum Likelihood Estimation with IBIF Model 2b for ML-10 #12 at BL. (A) 2T-4K compartmental model fit consistent with a 2α - 2β IRF model (left) with corresponding rate constant sensitivity functions (right). (B) 2T-3K compartmental model fit consistent with a 2α - 1β IRF model (left) with corresponding rate constant sensitivity functions (right). Compartmental rate constants for both tissue models are shown as insets. Normalized residuals from both the 2T-4K and 2T-3K model fits were consistent with following a standard Gaussian distribution based on the Kolmogorov-Smirnov test (2T-4K model: $p \leq 0.8516$; 2T-3K model: $p \leq 0.9441$). Furthermore, both sets of residuals passed the runs test (2T-4K model: $p \leq 0.9551$; 2T-3K model: $p \leq 0.9551$).

From table 5-12 the most complex tumor IRF model selected was a 3α - 2β model, consistent with a 3-tissue 5-rate constant (3T-5K) tissue compartmental model. Figure 5-29, figure 5-30, and figure 5-31 show comparisons of corresponding 3T-5K, 2T-4K, and 2T-3K tissue model fits for ML-10 #2 at ETA, ML-10 #6 at ETA and ML-10 #6 at FUA, respectively. IBIF Model 1b (table 5-12) was used for each tissue model fit. Inset for each plot are the estimates for the corresponding compartmental transfer rates with %COV in parentheses. Across these 3 cases, the %COV of the rate constant estimates decreased as the complexity of the compartmental model being fit was reduced from the 3T-5K model to the 2T-3K model. For each subject, sensitivity functions of k_2 , k_5 , and k_6 in the 3T-5K model plateau over nearly the same time range in measured tumor TAC samples. Moreover, compared to the 3T-5K tissue model, the less complex 2T-4K model yields estimate for corresponding compartmental transfer rates that have smaller %COV in exchange for a slight increase in bias of the overall model fit. For the cases of ML-10 #6 at ETA and ML-10 #6 at FUA, further reduction in complexity to the 2T-3K compartmental model produces visually worse fits to the respective tumor TAC data.

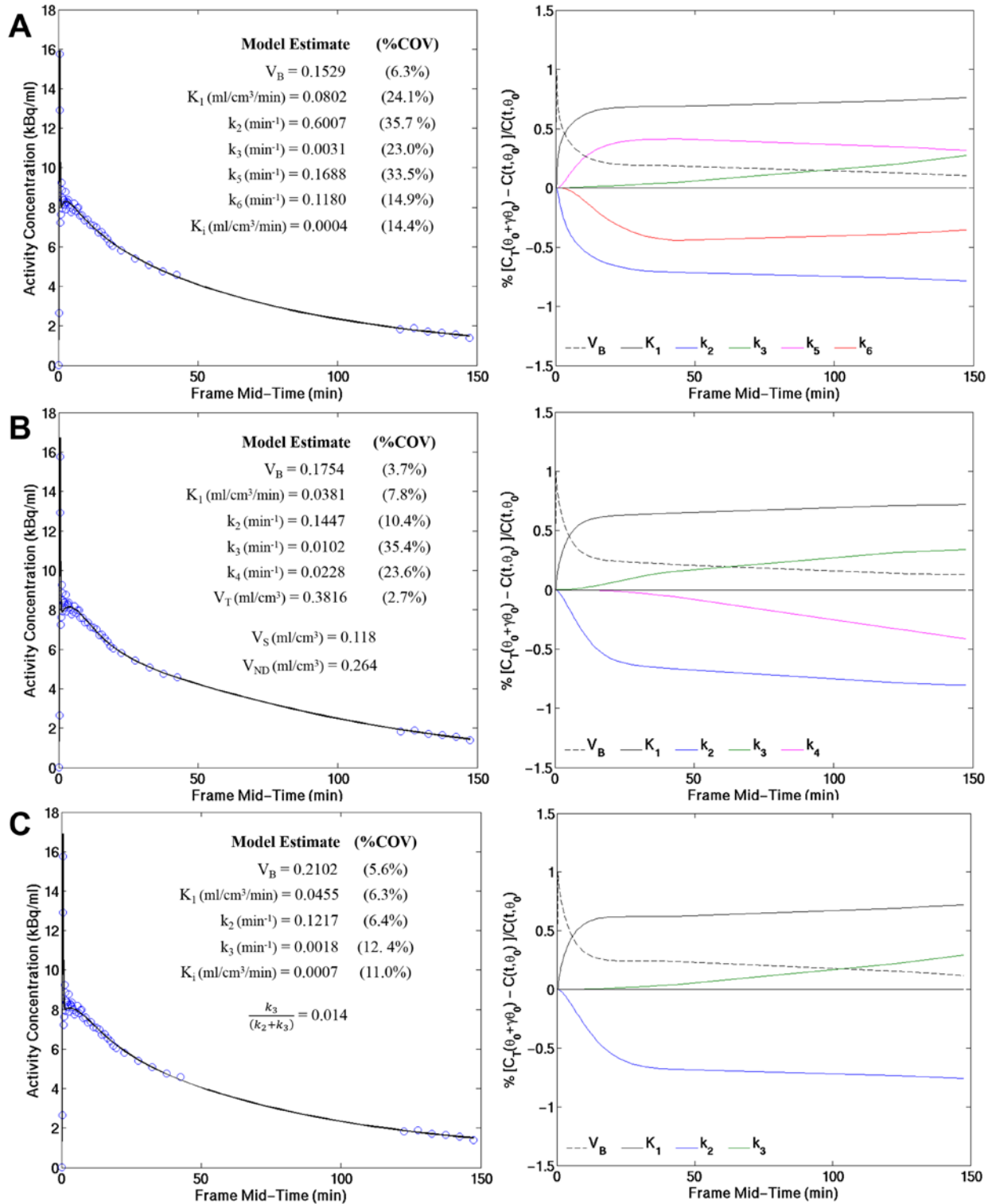


Figure 5-29. Comparison of 3T-5K, 2T-4K and 2T-3K Compartmental Model Fit Results from Joint Maximum Likelihood Estimation with IBIF Model 1b for ML-10 #2 at ETA. (A) 3T-5K compartmental model fit consistent

with a $3\alpha-2\beta$ IRF model (left) with corresponding rate constant sensitivity functions (right). (B) 2T-4K compartmental model fit consistent with a $2\alpha-2\beta$ IRF model (left) with corresponding rate constant sensitivity functions (right). (C) 2T-3K compartmental model fit consistent with a $2\alpha-1\beta$ IRF model (left) with corresponding rate constant sensitivity functions (right). Compartmental rate constants for all three tissue models are shown as insets. Normalized residuals from all three compartmental model fits were consistent with following a standard Gaussian distribution based on the Kolmogorov-Smirnov test (3T-5K model: $p \leq 0.9858$; 2T-4K model: $p \leq 0.7876$; 2T-3K model: $p \leq 0.9457$). Furthermore, all three sets of residuals passed the runs test (3T-5K model: $p \leq 0.9551$; 2T-4K model: $p \leq 0.6932$; 2T-3K model: $p \leq 0.6932$).

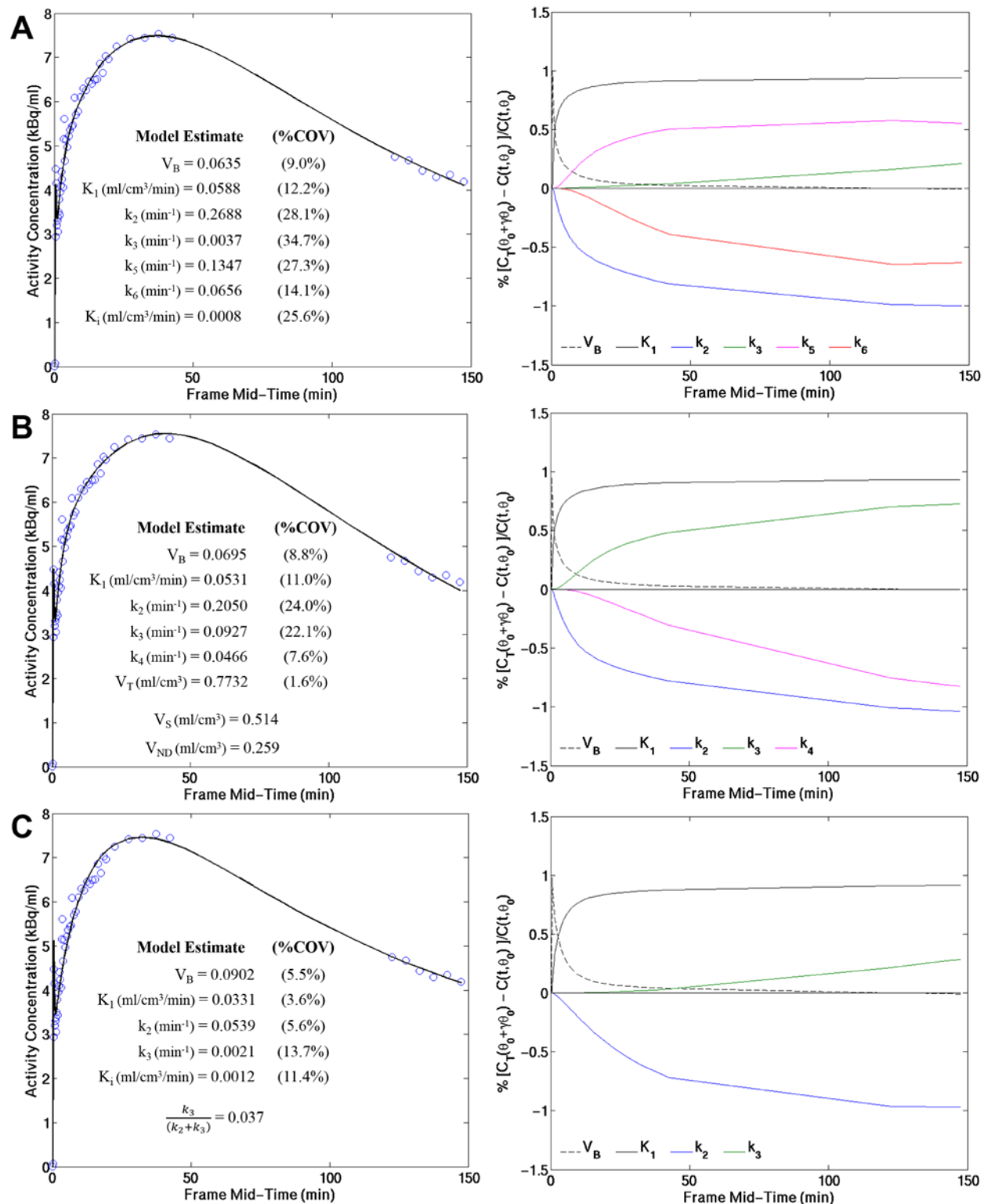


Figure 5-30. Comparison of 3T-5K, 2T-4K and 2T-3K Compartmental Model Fit Results from Joint Maximum Likelihood Estimation with IBIF Model 1b for ML-10 #6 at ETA. (A) 3T-5K compartmental model fit consistent

with a $3\alpha-2\beta$ IRF model (left) with corresponding rate constant sensitivity functions (right). (B) 2T-4K compartmental model fit consistent with a $2\alpha-2\beta$ IRF model (left) with corresponding rate constant sensitivity functions (right). (C) 2T-3K compartmental model fit consistent with a $2\alpha-1\beta$ IRF model (left) with corresponding rate constant sensitivity functions (right). Compartmental rate constants for all three tissue models are shown as insets. Normalized residuals from all three compartmental model fits were consistent with following a standard Gaussian distribution based on the Kolmogorov-Smirnov test (3T-5K model: $p \leq 0.7881$; 2T-4K model: $p \leq 0.3083$; 2T-3K model: $p \leq 0.5350$). Furthermore, all three sets of residuals passed the runs test (3T-5K model: $p \leq 0.5353$; 2T-4K model: $p \leq 0.3380$; 2T-3K model: $p \leq 0.9551$).

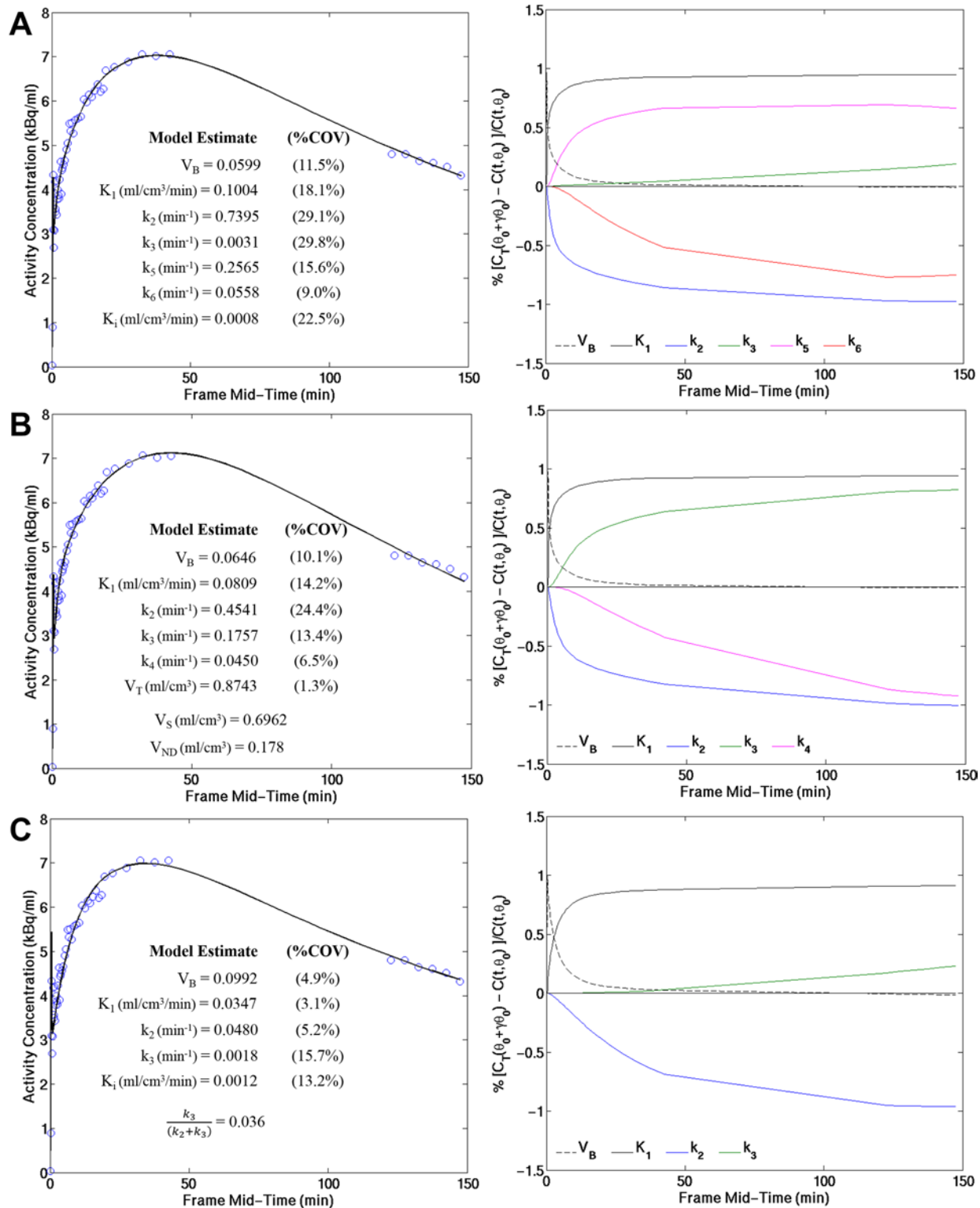


Figure 5-31. Comparison of 3T-5K, 2T-4K and 2T-3K Compartmental Model Fit Results from Joint Maximum Likelihood Estimation with IBIF Model 1b for ML-10 #6 at FUA. (A) 3T-5K compartmental model fit consistent

with a $3\alpha-2\beta$ IRF model (left) with corresponding rate constant sensitivity functions (right). (B) 2T-4K compartmental model fit consistent with a $2\alpha-2\beta$ IRF model (left) with corresponding rate constant sensitivity functions (right). (C) 2T-3K compartmental model fit consistent with a $2\alpha-1\beta$ IRF model (left) with corresponding rate constant sensitivity functions (right). Compartmental rate constants for all three tissue models are shown as insets. Normalized residuals from all three compartmental model fits were consistent with following a standard Gaussian distribution based on the Kolmogorov-Smirnov test (3T-5K model: $p \leq 0.6846$; 2T-4K model: $p \leq 0.8483$; 2T-3K model: $p \leq 0.8975$). Furthermore, all three sets of residuals passed the runs test (3T-5K model: $p \leq 0.7781$; 2T-4K model: $p \leq 0.4637$; 2T-3K model: $p \leq 0.7781$).

The two most commonly selected IRF models obtained as part of the joint IBIF/ IRF model order selection analysis (table 5-12) were the $2\alpha-2\beta$ (selected in 9 out of 29 cases) and $2\alpha-1\beta$ (selected in 10 out of 29 cases) IRF models, consistent with the 2T-4K and 2T-3K tissue compartment models, respectively. Moreover, in the 3 cases for which the $3\alpha-2\beta$ IRF model was selected (figures 5-29, 5-30, and 5-31), the corresponding compartmental transfer rates were not well estimated and showed evidence of strong correlation on sensitivity analysis. Model fitting using the reduced 2T-4K and 2T-3K compartmental models resulted in increased precision of rate constant estimates. Therefore, 26 of the 29 tumor TACS were evaluated using the 2T-4K and 2T-3K tissue compartment models. The exceptions being ML-10 #11 at ETA and ML-10 #11 at FUA, for which the selected tumor IRF model was attenuated blood concentration, and ML-10 #7 at BL whose tumor TAC did not support nonlinear modeling.

Table 5-19 and table 5-20 contain estimates for V_B and the associated compartmental rate constants, respectively, obtained by analyzing each measured [^{18}F]ML-10 tumor TAC using a 2T-

4K tissue compartmental model. The coefficient of variation on each model estimate is expressed as a percentage given in parentheses. From table 5-20, [¹⁸F]ML-10 PET scans for which the 1 α -1 β IRF model was selected as the best tumor IRF model produced estimates for the 2T-4K rate constants that were generally not estimable. Ignoring these cases, estimates for the blood volume fraction (V_B) ranged from 0.0162 to 0.2818 (mean = 0.1215 and median = 0.1096) and K_1 ranged from 0.0113 ml/cm³/min to 0.0809 ml/cm³/min (mean = 0.030513349 ml/cm³/min and median = 0.026836568 ml/cm³/min), respectively.

Table 5-21 contains estimates for the distribution volume V_T , as well as the volume of the specific (V_S) and volume of the non-displaceable (V_{ND}) compartments (ignoring the scans for which the 1 α -1 β IRF model was selected as the best tumor IRF model). From table 5-21, the ratio of V_S/V_T ranged from 0.3093 to 0.7997.

Table 5-22 contains estimates for V_B and the associated compartmental rate constants obtained from analyzing each measured [¹⁸F]ML-10 tumor TAC using a 2T-3K tissue compartmental model. The coefficient of variation on each model estimate is expressed as a percentage given in parentheses. As in the 2T-4K modeling case, scans for which the 1 α -1 β IRF model was selected as the best tumor IRF showed poor estimability when analyzed as a 2T-3K model. Ignoring these subject, estimates for V_B and K_1 ranged from 0.0254 to 0.2977 (mean = 0.1310 and median = 0.115) and from 0.0093 ml/cm³/min to 0.0347 ml/cm³/min (mean = 0.0211 ml/cm³/min and median = 0.0196 ml/cm³/min), respectively.

Table 5-23 contains the estimated value for the flux parameter K_i as well as the ratio of K_i to K_1 (denoted K_i/K_1). The uptake measure K_i/K_1 can be interpreted as the overall fraction of [^{18}F]ML-10 in the tumor tissue that is taken up by cells undergoing apoptosis. Ignoring the scans for which the 1α - 1β IRF model was selected as the best tumor IRF model, the associated K_i values ranged from 3.675×10^{-4} ml/cm³/min to 5.483×10^{-3} ml/cm³/min, with corresponding K_i/K_1 values ranging from 0.0142 to 0.2873.

Table 5-19. 2-Tissue Reversible Tracer Kinetics: Blood Volume Fraction V_B .

Subject ID	V_B		
	[†] BL	*ETA	[‡] FUA
ML-10 #1	^a 0.1460 (8.90%)	N/A	N/A
ML-10 #2	N/A	0.1754 (3.66%)	N/A
ML-10 #4	0.0679 (11.94%)	0.0162 (43.39%)	^b 0.0445 (114.14%)
ML-10 #5	0.1374 (3.90%)	0.1407 (3.27%)	0.1328 (3.84%)
ML-10 #6	0.0640 (8.75%)	0.0695 (8.85%)	0.0646 (10.14%)
ML-10 #7	N/A	^b 0.0426 (407.74%)	0.1260 (6.84%)
ML-10 #9	0.2111 (6.75%)	0.259 (7.55%)	0.0997 (6.31%)
ML-10 #10	0.0811 (3.67%)	[‡] 0.0427 (7.39%)	^b 0.0275 (38.05%)
ML-10 #11	^b 0.3247 (9.22%)	---	---
ML-10 #12	0.0469 (23.28%)	N/A	N/A
ML-10 #13	0.2343 (3.95%)	0.2818 (3.86%)	N/A
ML-10 #14	0.1194 (3.01%)	0.0997 (3.29%)	0.0563 (4.67%)

^a Parameter estimates are reported as: estimated value (percent coefficient of variation).
[†] BL = Baseline.
* ETA = Early therapy assessment.
[‡] FUA = Follow-up assessment.
^b Selected best tissue model is a 1-tissue compartmental model.
[‡] Rate constant estimates obtained from first acquisition only (i.e. only using 0-45 min PET data).

Table 5-20. 2-Tissue Reversible Tracer Kinetics: Compartmental Rate Constants.

Subject ID	K ₁ (ml/cm ³ /min)			k ₂ (min ⁻¹)			k ₃ (min ⁻¹)			k ₄ (min ⁻¹)		
	[†] BL	[*] ETA	[‡] FUA	BL	ETA	FUA	BL	ETA	FUA	BL	ETA	FUA
ML-10 #1	^a 0.0658 (32.26%)	N/A	N/A	0.5748 (29.14%)	N/A	N/A	0.0432 (16.72%)	N/A	N/A	0.0145 (9.09%)	N/A	N/A
ML-10 #2	N/A	0.0381 (7.77%)	N/A	N/A	0.1447 (10.40%)	N/A	N/A	0.0102 (35.44%)	N/A	N/A	0.0228 (23.61%)	N/A
ML-10 #4	0.0203 (13.04%)	0.0395 (17.89%)	^b 0.0109 (9.32x10 ³)	0.0768 (22.45%)	0.1804 (38.58%)	^b 3.3599 (3.07x10 ⁴ %)	0.0049 (127.54%)	0.0566 (50.08%)	^b 5.739 (6.84x10 ³ %)	0.0027 (575.73%)	0.0408 (17.35%)	^b 0.0616 (1.60x10 ⁴ %)
ML-10 #5	0.0181 (10.92%)	0.0157 (14.58%)	0.0191 (11.15%)	0.0804 (24.05%)	0.0858 (41.11%)	0.0858 (29.15%)	0.0302 (34.86%)	0.0542 (44.03%)	0.0418 (41.10%)	0.0174 (20.50%)	0.0229 (14.01%)	0.0301 (12.91%)
ML-10 #6	0.0359 (8.89%)	0.0531 (10.96%)	0.0809 (14.23%)	0.0956 (25.57%)	0.2050 (23.96%)	0.4541 (24.41%)	0.0392 (50.58%)	0.0927 (22.10%)	0.1757 (13.38%)	0.0435 (17.60%)	0.0466 (7.60%)	0.0450 (6.46%)
ML-10 #7	N/A	^b 0.8561 (321.54%)	0.0213 (22.29%)	N/A	^b 9.9462 (135.87%)	0.1542 (29.88%)	N/A	^b 0.0537 (209.92%)	0.0224 (33.72%)	N/A	^b 0.0124 (8.12%)	0.0060 (53.36%)
ML-10 #9	0.0349 (8.03%)	0.0272 (27.54%)	0.0358 (10.41%)	0.1203 (7.81%)	0.1128 (29.09%)	0.1805 (13.64%)	0.0062 (19.22%)	0.0086 (17.18%)	0.0184 (23.58%)	0.0056 (38.69%)	1.09x10 ⁻¹⁴ (176.68%)	0.0164 (18.83%)
ML-10 #10	0.0265 (5.21%)	[‡] 0.0194 (5.35%)	^b 0.0417 (126.77%)	0.0881 (12.76%)	[‡] 0.0829 (17.89%)	^b 1.8104 (133.07%)	0.0289 (22.54%)	[‡] 0.0401 (38.55%)	^b 0.3716 (48.89%)	0.0217 (11.49%)	[‡] 0.0100 (126.02%)	^b 0.0169 (26.25%)
ML-10 #11	^b 0.0013 (5.15x10 ⁴ %)	^c ---	^c ---	^b 0.0113 (5.1x10 ⁷ %)	^c ---	^c ---	^b 1.984 (1.43x10 ⁴ %)	^c ---	^c ---	^c ---	^b 3.0695 (2.22x10 ³ %)	^c ---
ML-10 #12	0.0305 (7.15%)	N/A	N/A	0.0798 (19.50%)	N/A	N/A	0.0262 (45.83%)	N/A	N/A	0.0300 (20.61%)	N/A	N/A
ML-10 #13	0.0118 (37.80%)	0.0295 (32.20%)	N/A	0.1532 (32.86%)	0.2007 (49.15%)	N/A	0.0050 (25.25%)	0.0432 (59.82%)	N/A	2.01x10 ⁻¹³ (8885.85%)	0.0427 (23.20%)	N/A
ML-10 #14	0.0150 (9.32%)	0.0113 (12.36%)	0.0216 (8.36%)	0.0998 (16.92%)	0.0901 (25.66%)	0.1791 (13.21%)	0.0227 (27.57%)	0.0268 (38.38%)	0.0391 (13.35%)	0.0143 (19.97%)	0.0140 (25.88%)	0.0191 (7.01%)

^a Parameter estimates are reported as: estimated value (percent coefficient of variation).

[†] BL = Baseline.

^{*} ETA = Early therapy assessment.

[‡] FUA = Follow-up assessment.

^b Selected best tissue model is a 1-tissue compartmental model.

[‡] Rate constant estimates obtained from first acquisition only (i.e. only using 0-45 min PET data).

^c Selected best tissue model is an attenuated blood concentration model.

Table 5-21. 2-Tissue Reversible Tracer Kinetics: Total Volume of Distribution V_T .

Subject ID	V_T (ml/cm ³)			V_S (ml/cm ³)			V_{ND} (ml/cm ³)			V_S/V_T		
	[†] BL	*ETA	[‡] FUA	BL	ETA	FUA	BL	ETA	FUA	BL	ETA	FUA
ML-10 #1	0.4558 (3.53%)	N/A	N/A	0.3412	N/A	N/A	0.1146	N/A	N/A	0.7486	N/A	N/A
ML-10 #2	N/A	0.3816 (2.68%)	N/A	N/A	0.1180	N/A	N/A	0.2636	N/A	N/A	0.3093	N/A
ML-10 #4	0.7359 (298.27%)	0.5226 (2.74%)	^b 0.3043 (12.81%)	0.4714	0.3037	0.3010	0.2645	0.2189	0.0032	0.6406	0.5811	^b 0.9894
ML-10 #5	0.6159 (4.16%)	0.6174 (2.75%)	0.5304 (1.88%)	0.3910	0.4341	0.3082	0.2250	0.1832	0.2222	0.6348	0.7032	0.5810
ML-10 #6	0.7150 (1.97%)	0.7732 (1.62%)	0.8743 (1.27%)	0.3393	0.5143	0.6962	0.3757	0.2589	0.1781	0.4745	0.6652	0.6962
ML-10 #7	N/A	^b 0.4599 (21.47%)	0.6537 (26.42%)	N/A	0.3739	0.5155	N/A	0.0861	0.1382	N/A	^b 0.8129	0.7885
ML-10 #9	0.6078 (13.16%)	#---	0.4214 (3.57%)	0.3174	#---	0.2229	0.2904	0.2409	0.1985	0.5222	#---	0.5290
ML-10 #10	0.7014 (2.13%)	[‡] 1.1673 (82.45%)	^b 0.5311 (21.47%)	0.4008	0.9335	0.5081	0.3006	0.2338	0.0230	0.5714	[‡] 0.7997	^b 0.9566
ML-10 #11	^b 0.1124 (38.07%)	^c ---	^c ---	0.0012	^c ---	^c ---	0.1112	^c ---	^c ---	^b 0.0105	^c ---	^c ---
ML-10 #12	0.7157 (1.57%)	N/A	N/A	0.3342	N/A	N/A	0.3815	N/A	N/A	0.4669	N/A	N/A
ML-10 #13	#---	0.2956 (4.84%)	N/A	#---	0.1486	N/A	0.0769	0.1470	N/A	#---	0.5028	N/A
ML-10 #14	0.3896 (3.95%)	0.3642 (5.89%)	0.3675 (1.85%)	0.2390	0.2391	0.2468	0.1506	0.1251	0.1207	0.6135	0.6564	0.6716

^a Macroparameter estimates are reported as: estimated value (percent coefficient of variation).

[†] BL = Baseline.

* ETA = Early therapy assessment.

[‡] FUA = Follow-up assessment.

[‡] Rate constant estimates obtained from first acquisition only (i.e. only using 0-45 min PET data).

^b Selected best tissue model is a 1-tissue compartmental model.

^c Selected best tissue Model is an attenuated blood concentration model.

V_T and V_S are undefined for $k_4 \approx 0$.

Table 5-22. 2-Tissue Irreversible Kinetics: Compartmental Rate Constants.

Subject ID	V_B			K_1 (ml/cm ³ /min)			k_2 (min ⁻¹)			k_3 (min ⁻¹)		
	[†] BL	*ETA	[‡] FUA	BL	ETA	FUA	BL	ETA	FUA	BL	ETA	FUA
ML-10 #1	^a 0.1883 (3.70%)	N/A	N/A	0.0135 (13.22%)	N/A	N/A	0.0705 (16.79%)	N/A	N/A	0.0083 (10.62%)	N/A	N/A
ML-10 #2	N/A	0.1807 (3.53%)	N/A	N/A	0.0336 (6.45%)	N/A	N/A	0.1130 (6.40%)	N/A	N/A	0.0016 (13.99%)	N/A
ML-10 #4	0.0683 (11.42%)	0.0254 (23.12%)	^b 0.0438 (17.67%)	0.0201 (10.63%)	0.0276 (7.13%)	^b 0.0073 (15.51%)	0.0747 (13.53%)	0.0709 (10.12%)	^b 0.0271 (37.4%)	0.0039 (15.95%)	0.0026 (18.86%)	^b 0.0014 (189.89%)
ML-10 #5	0.1454 (3.24%)	0.1472 (2.60%)	0.1390 (2.78%)	0.0142 (6.09%)	0.0121 (5.58%)	0.0152 (4.02%)	0.0419 (10.76%)	0.0340 (11.75%)	0.0414 (6.78%)	0.0059 (11.59%)	0.0066 (13.24%)	0.0035 (11.15%)
ML-10 #6	0.0705 (6.66%)	0.0902 (5.52%)	0.0992 (4.86%)	0.0304 (3.81%)	0.0331 (3.61%)	0.0347 (3.13%)	0.0536 (5.87%)	0.0539 (5.56%)	0.0480 (5.23%)	0.0021 (14.92%)	0.0021 (13.73%)	0.0018 (15.73%)
ML-10 #7	N/A	^b 0.0455 (564.64%)	0.1314 (5.63%)	N/A	^b 0.9927 (344.96%)	0.0170 (15.20%)	N/A	^b 8.3379 (154.45%)	0.1048 (17.38%)	N/A	^b 0.0164 (226%)	0.0122 (8.83%)
ML-10 #9	0.2124 (2.70%)	0.2692 (2.53%)	0.1080 (5.53%)	0.0329 (5.55%)	0.0211 (9.12%)	0.0278 (7.87%)	0.1083 (5.88%)	0.0773 (10.43%)	0.1159 (8.42%)	0.0038 (6.84%)	0.0032 (12.83%)	0.0047 (8.47%)
ML-10 #10	0.0874 (3.31%)	[‡] 0.0428 (6.85%)	^b 0.0376 (8.95%)	0.0221 (2.92%)	[‡] 0.0191 (3.61%)	^b 0.0083 (7.00%)	0.0513 (4.67%)	[‡] 0.0763 (8.34%)	^b 0.0223 (21.53%)	0.0043 (6.98%)	[‡] 0.0308 (8.62%)	^b 0.0042 (46.29%)
ML-10 #11	^b 0.3338 (10.11%)	c---	c---	^b 0.0005 (1.44x10 ⁵ %)	c---	c---	^b 0.0004 (4.5x10 ⁹)	c---	c---	^b 7.195 (1.71x10 ⁹)	c---	c---
ML-10 #12	0.0521 (17.10%)	N/A	N/A	0.0266 (3.38%)	N/A	N/A	0.0514 (5.31%)	N/A	N/A	0.0029 (9.52%)	N/A	N/A
ML-10 #13	0.2343 (3.95%)	0.2977 (2.68%)	N/A	0.0118 (37.85%)	0.0168 (13.18%)	N/A	0.1544 (32.84%)	0.0734 (14.62%)	N/A	0.0049 (25.26%)	0.0017 (32.39%)	N/A
ML-10 #14	0.1229 (2.25%)	0.1031 (2.68%)	0.0659 (3.99%)	0.0126 (4.76%)	0.0093 (6.47%)	0.0137 (4.98%)	0.0648 (6.17%)	0.0545 (9.64%)	0.0707 (6.52%)	0.0064 (5.03%)	0.0072 (8.00%)	0.0060 (6.00%)

^a Parameter estimates are reported as: estimated value (percent coefficient of variation).

[†] BL = Baseline.

* ETA = Early therapy assessment.

[‡] FUA = Follow-up assessment.

^b Selected best tissue model is a 1-tissue compartmental model.

[‡] Rate constant estimates obtained from first acquisition only (i.e. only using 0-45 min PET data).

^c Selected best tissue model is an attenuated blood concentration model.

Table 5-23. 2-Tissue Irreversible Kinetics: Influx Rate K_i .

Subject ID	K_i (ml/cm ³ /min)			K_i/K_1		
	[†] BL	[*] ETA	[‡] FUA	BL	ETA	FUA
ML-10 #1	^a 1.423x10 ⁻³ (5.78%)	N/A	N/A	0.1057	N/A	N/A
ML-10 #2	N/A	4.750x10 ⁻⁴ (12.74%)	N/A	N/A	0.0142	N/A
ML-10 #4	1.002x10 ⁻³ (11.87%)	9.887x10 ⁻⁴ (15.19%)	^b 3.677x10 ⁻⁴ (159.28%)	0.0499	0.0359	^b 0.0504
ML-10 #5	1.757x10 ⁻³ (6.58%)	1.955x10 ⁻³ (6.91%)	1.190x10 ⁻³ (7.88%)	0.1238	0.1616	0.0781
ML-10 #6	1.143x10 ⁻³ (12.43%)	1.228x10 ⁻³ (11.40%)	1.24x10 ⁻³ (13.19%)	0.0377	0.0371	0.0357
ML-10 #7	N/A	^b 1.947x10 ⁻³ (27.33%)	1.778x10 ⁻³ (4.14%)	N/A	^b 0.0020	0.1046
ML-10 #9	1.110x10 ⁻³ (5.29%)	8.365x10 ⁻⁴ (10.01%)	1.086x10 ⁻³ (6.38%)	0.0337	0.0396	0.0391
ML-10 #10	1.715x10 ⁻³ (5.03%)	[‡] 5.483x10 ⁻³ (3.41%)	^b 1.330x10 ⁻⁴ (27.57%)	0.0776	[‡] 0.2873	^b 0.1596
ML-10 #11	^b 5.146x10 ⁻⁴ (12.22%)	^c ---	^c ---	^b 0.9999	^c ---	^c ---
ML-10 #12	1.436x10 ⁻³ (7.11%)	N/A	N/A	0.0539	N/A	N/A
ML-10 #13	3.675x10 ⁻⁴ (16.55%)	3.783x10 ⁻⁴ (28.56%)	N/A	0.0310	0.0226	N/A
ML-10 #14	1.121x10 ⁻³ (3.10%)	1.089x10 ⁻³ (4.53%)	1.061x10 ⁻³ (3.95%)	0.0893	0.1174	0.0776

^a Macroparameter estimates are reported as: estimated value (percent coefficient of variation).
[†] BL = Baseline.
^{*} ETA = Early therapy assessment.
[‡] FUA = Follow-up assessment.
^b Selected best tissue model is a 1-tissue compartmental model.
[‡] Estimates obtained from first acquisition only (i.e. only using 0-45 min PET data).
^c Selected best tissue model is an attenuated blood concentration model.

5.2.4.5 Response Evaluation using Compartmental Modeling of [¹⁸F]ML-10.

In addition to radiotracer characterization, a principle motivation for the study of [¹⁸F]ML-10 uptake in GBM was to evaluate the radiotracer for potential use in early therapy response assessment. From the above analysis, the macroparameters V_T and K_i generally have better precision than their associated compartmental rate constants. Moreover, V_T and K_i do not rely on assuming specific compartmental structure to describe [¹⁸F]ML-10 exchange in the tumor.

Since a consistent tumor IRF model was not observed across [¹⁸F]ML-10 PET scans, both V_T and K_i are evaluated as measures for early therapy response assessment. Additionally, the ratio K_i -to- K_1 , denoted as K_i^* , was also evaluated for use as a quantitative measure of response. Under the assumptions of the 2T-3K model $K_i^* = \frac{k_3}{(k_2+k_3)}$ and quantifies the fraction of tracer entering the tissue that is irreversibly taken up by the GBM tissue, while $(1- K_i^*)$ quantifies the proportion of [¹⁸F]ML-10 that is transported from the blood to the tissue but ultimately escapes back into the tumor vasculature. While this measure assumes a particular compartmental model structure, it was investigated because it can be calculated directly from the macroparameters. Importantly, neither of the macroparameters V_T or K_i depended on the specific number or arrangement of compartments.

A total of 8 subjects (including ML-10 #11) had at least a BL and an ETA scan, allowing for analysis of V_T , K_i and K_i^* as response measures though, ML-10 #13 and ML-10 #14 do not have a true BL scan as they both started therapy prior to their first [¹⁸F]ML-10 PET scans (see *Section 4.2*, Table 4-3). However, because the tumor [¹⁸F]ML-10 uptake concentration for ML-10 #11 at both the ETA and FUA time-points was determined to be primarily composed of radiotracer concentration in the vasculature, ML-10 #11 was not included for response assessment evaluation. Therefore, the evaluation of V_T , K_i and K_i^* as measures of GBM response to therapy using [¹⁸F]ML-10 PET was limited to just 7 subjects.

Table 5-24 contains the percent change in V_T from: BL to ETA (denoted $\Delta V_T(\text{ETA}, \text{BL})$), BL to FUA ($\Delta V_T(\text{FUA}, \text{BL})$), and ETA to FUA (denoted $\Delta V_T(\text{FUA}, \text{ETA})$). Subjects are ordered in decreasing rank order according to their progression-free survival (PFS). For subject imaging

time-points that were best modeled using a 1α - 1β IRF model (i.e. a 1T-2K tissue compartment model), the associated 1α - 1β values for V_T were used in the percent change calculation.

The median PFS for a newly diagnosed GBM subject receiving standard of care concomitant radiotherapy plus temozolomide chemotherapy is 6.9 months [4]. This makes a PFS of 6.9 months a natural threshold for categorizing subjects as exhibiting a poor PFS (i.e. PFS < 6.9 months). For the limited number of subjects analyzed, no obvious association between $\Delta V_T(\text{ETA}, \text{BL})$ and subject PFS is apparent. For example, ML-10 #9 exhibited the longest PFS (25 months) but showed a 41.185% decrease in V_T between the pre-therapy BL and the post-therapy administration ETA time-points suggesting an overall decrease in apoptosis at ETA compared to BL. In contrast, subject ML-10 #13 demonstrated the shortest PFS (2 months) post-therapy initiation, consistent with a poor response to therapy, but exhibited the largest percent increase in V_T between BL and ETA.

Table 5-25 contains percent change in K_i from: BL to ETA ($\Delta K_i(\text{ETA}, \text{BL})$), BL to FUA ($\Delta K_i(\text{FUA}, \text{BL})$), and ETA to FUA ($\Delta K_i(\text{FUA}, \text{ETA})$), while table 5-26 contains percent change in K_i^* from BL to ETA ($\Delta K_i^*(\text{ETA}, \text{BL})$), BL to FUA ($\Delta K_i^*(\text{FUA}, \text{BL})$), and ETA to FUA ($\Delta K_i^*(\text{FUA}, \text{ETA})$). For the limited number of subjects analyzed, no obvious association between $\Delta K_i(\text{ETA}, \text{BL})$ and subject PFS is apparent. Overall percent change in K_i compared to PFS showed a similar pattern to percent change in V_T compared to PFS. For example, ML-10 #9 exhibited the longest PFS (25 months) but showed a 24.61% decrease in K_i between the BL and ETA time-points suggesting an overall decrease in apoptosis at ETA compared to BL. In contrast, subject ML-10 #13 demonstrated the shortest PFS (2 months) post-therapy initiation, consistent with a

poor response to therapy, but exhibited an increase in K_i (though the percent increase observed for K_i was not as large as the corresponding percent increase in V_T). Furthermore, percent change in K_i between BL and FUA and between ETA and FUA decreased for all subjects except ML-10 #6.

In contrast to $\Delta V_T(\text{ETA}, \text{BL})$ and $\Delta K_i(\text{ETA}, \text{BL})$, K_i^* showed an increased from BL to ETA for all subjects with PFS > 11 months. Moreover, a 1.42% decrease in K_i^* between BL and ETA time-points was observed for ML-10 #6 who exhibited a PFS of 11 months. Furthermore, 2 out of 3 subjects with a poor PFS (i.e. PFS < 6.9 months) did not increase in K_i^* between the BL and ETA time-points. The exception being ML-10 #14 (PFS = 2 months) who exhibited an increase in K_i^* from the BL to ETA; though, this result is confounded by the fact that ML-10 #14 does not have a true BL scan.

Table 5-24. Percent Change in V_T Compared to Subject Clinical End-points.

Subject ID	^a $\Delta V_T(\text{@ETA}, \text{†BL})$	$\Delta V_T(\text{²FUA}, \text{BL})$	$\Delta V_T(\text{FUA}, \text{ETA})$	^{&} PFS (months)	[#] OS (months)
ML-10 #9	^d -41.185%	-30.665%	^d 17.887%	25	35
^c ML-10 #10	66.425%	^b -25.660%	^b -55.331%	18	19
ML-10 #5	0.233%	-13.885%	-14.086%	15	25
ML-10 #6	8.133%	22.2706%	13.0739%	11	22
ML-10 #4	-28.979%	^b -58.670%	^b -41.805%	4	5
^f ML-10 #14	-6.506%	-5.674%	0.89%	3	9
^g ML-10 #13	^e 185.696%	N/A	N/A	2	13

$$^a \Delta V_T(x, y) = 100 * \left(\frac{V_T^{(x)} - V_T^{(y)}}{V_T^{(y)}} \right).$$

[†] BL = Baseline.

[@] ETA= Early therapy assessment.

^²FUA = Follow-up assessment.

[&]PFS = Progression-free survival.

[#]OS = Overall survival.

^b Indicates V_T for FUA time-point obtained from a 1-tissue model.

^c ML-10 #10 V_T estimate for ETA time-point used first acquisition only (i.e. only 0-45 min PET data).

^d Indicates V_T for ETA time-point obtained from a 1-tissue model.

^e Indicates V_T for BL time-point obtained from a 1-tissue model.

^f Subject does not have a true BL scan, since therapy was initiated 5 days prior to receiving first [¹⁸F]ML-10 PET scan.

^g Subject does not have a true BL scan, since therapy was initiated 6 days prior to receiving first [¹⁸F]ML-10 PET scan.

Table 5-25. Percent Change in K_i Compared to Subject Clinical End-points.

Subject ID	^a ΔK _i ([@] ETA, †BL)	ΔK _i (^² FUA, BL)	ΔK _i (FUA, ETA)	^{&} PFS (months)	[#] OS (months)
ML-10 #9	-24.61%	-2.07%	29.89%	25	35
^c ML-10 #10	219.61%	-22.49%	-75.75%	18	19
ML-10 #5	11.27%	-32.27%	-39.14%	15	25
ML-10 #6	7.42%	8.46%	0.97%	11	22
ML-10 #4	-1.31%	-63.30%	-62.81%	4	5
[†] ML-10 #14	-2.83%	-5.27%	-2.52%	3	9
[§] ML-10 #13	2.94%	---	---	2	13

^a $\Delta K_i(x, y) = 100 * \left(\frac{K_i^{(x)} - K_i^{(y)}}{K_i^{(y)}} \right)$.
[†] BL = Baseline.
[@] ETA= Early therapy assessment.
^²FUA = Follow-up assessment.
[&]PFS = Progression-free survival.
[#] OS = Overall survival.
^c ML-10 #10 K_i estimate for ETA time-point used first acquisition only (i.e. only 0-45 min PET data).
[†] Subject does not have a true BL scan, since therapy was initiated 5 days prior to receiving first [¹⁸F]ML-10 PET scan.
[§] Subject does not have a true BL scan, since therapy was initiated 6 days prior to receiving first [¹⁸F]ML-10 PET scan.

Table 5-26. Percent Change in K_i* Compared to Subject Clinical End-points.

Subject ID	^a ΔK _i *([@] ETA, †BL)	ΔK _i *(^² FUA, BL)	ΔK _i * (FUA, ETA)	^{&} PFS (months)	[#] OS (months)
ML-10 #9	17.45%	15.83%	-1.38%	25	35
^c ML-10 #10	270.40%	105.67%	-44.47%	18	19
ML-10 #5	30.50%	-36.92%	-51.66%	15	25
ML-10 #6	-1.42%	-5.19%	-3.81%	11	22
ML-10 #4	-28.14%	1.00%	40.56%	4	5
[†] ML-10 #14	31.57%	-13.03%	-33.90%	3	9
[§] ML-10 #13	-27.19%	---	---	2	13

^a $\Delta K_i^*(x, y) = 100 * \left(\frac{K_i^{*(x)} - K_i^{*(y)}}{K_i^{*(y)}} \right)$.
[†] BL = Baseline.
[@] ETA= Early therapy assessment.
^²FUA = Follow-up assessment.
[&]PFS = Progression-free survival.
[#] OS = Overall survival.
^c ML-10 #10 K_i* estimate for ETA time-point used first acquisition only (i.e. only 0-45 min PET data).
[†] Subject does not have a true BL scan, since therapy was initiated 5 days prior to receiving first [¹⁸F]ML-10 PET scan.
[§] Subject does not have a true BL scan, since therapy was initiated 6 days prior to receiving first [¹⁸F]ML-10 PET scan.

5.2.4.6 Voxelwise Compartmental Modeling

PK macroparameters were estimated on a voxelwise basis to investigate voxelwise change in response to treatment for 6 out of the 7 subjects in table 5-24. ML-10 #4 was not considered for voxelwise analysis due to the small size of their tumor. Figure 5-32 shows example voxelwise IRF model fits for (A) tumor voxel number 55 and (B) tumor voxel number 108 using the $2\alpha-2\beta$ IRF model (left) and $2\alpha-1\beta$ IRF model (right) for ML-10 #6 at ETA. IBIF Model 1b was used for each voxelwise fit. $V_B = 0.070$ for the $2\alpha-2\beta$ IRF model fits (left; A and B) and $V_B = 0.090$ for the $2\alpha-1\beta$ IRF model fits (right; A and B).

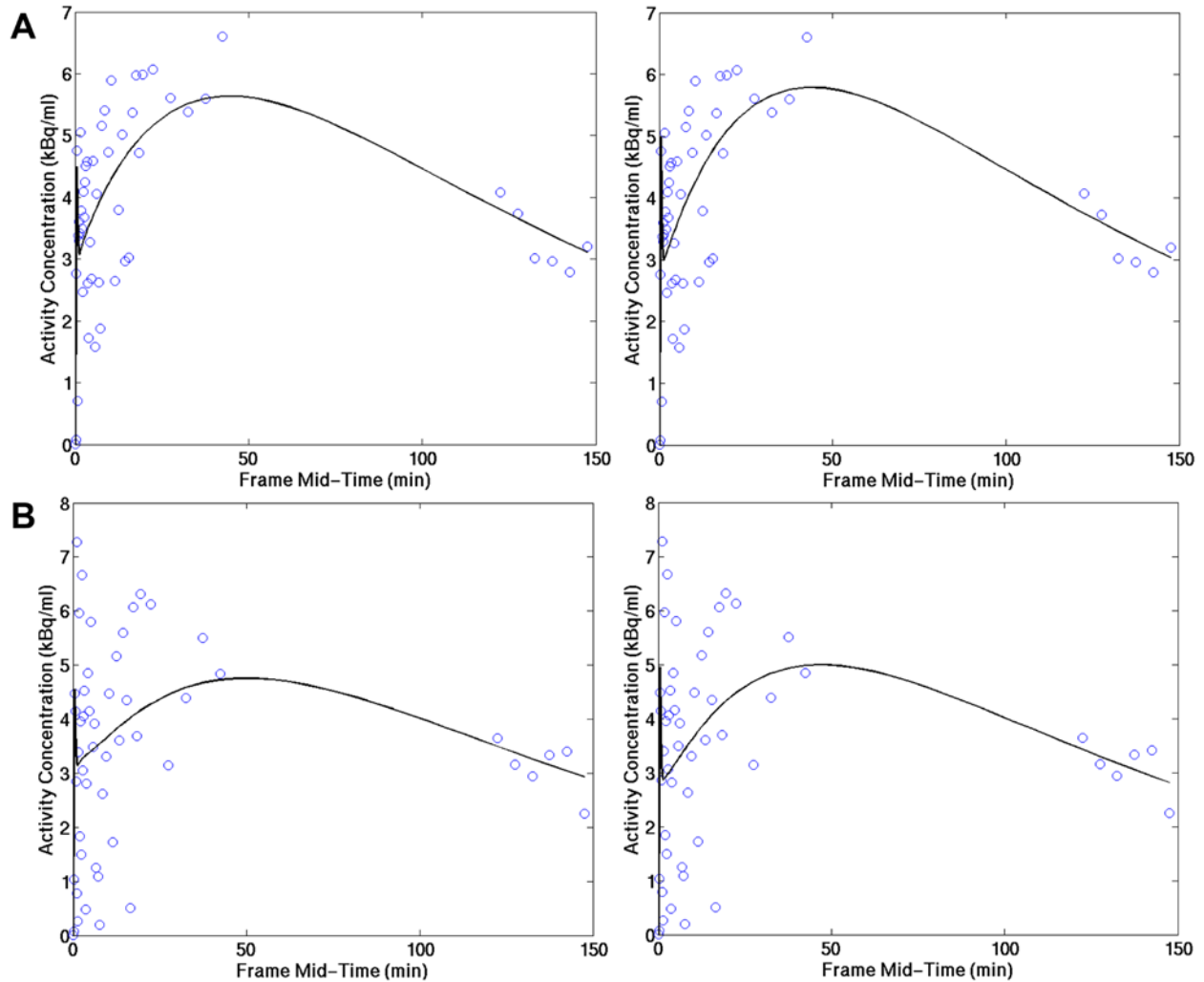


Figure 5-32. Example Voxelwise Fits for Subject ML-10 #6 at ETA using the $2\alpha-2\beta$ and $2\alpha-1\beta$ IRF models. (A) Representative fits using a $2\alpha-2\beta$ IRF model with V_B fixed to $V_B = 0.070$ (left) and a $2\alpha-1\beta$ IRF model with V_B fixed to $V_B = 0.090$ (right) for tumor voxel number 55 for ML-10 #6 at ETA estimated using IBIF Model 1b as IBIF model. (B) Representative fits using a $2\alpha-2\beta$ IRF model with V_B fixed to $V_B = 0.070$ (left) and a $2\alpha-1\beta$ IRF model with V_B fixed to $V_B = 0.090$ (right) for tumor voxel number 108 for ML-10 #6 at ETA estimated using IBIF Model 1b as IBIF model.

Figure 5-33 shows representative (A) SUV PET sections at BL (left), ETA (center), and FUA (right) time-points for ML-10 #6. Also shown are voxelwise maps of (B) V_T and (C) K_i overlaid on their corresponding PET time-point (e.g. the ETA V_T map is overlaid on the ETA SUV PET image). All images were co-registered to the BL PET scan. No MR imaging was acquired for ML-10 #6. Across imaging time-points [^{18}F]ML-10 uptake is observed to increase in SUV. Visually, V_T maps at BL, ETA, and FUA exhibit similar intensity distribution to their corresponding SUV PET counterparts. Similarly, a local increase in [^{18}F]ML-10 uptake rate is visually apparent between ETA and FUA K_i maps (arrows).

Figure 5-34 shows the corresponding voxelwise histograms of V_T and K_i for ML-10 #6. Specifically, figure 5-34A shows histograms of V_T at BL and ETA only and at BL, ETA, and FUA all together (right). Histograms of V_T were generated using 200 bins over the range of 0-2 ml/cm³ (V_T histogram binwidth = 0.01). Purple color indicates areas overlap between BL and ETA V_T histograms. Similarly, figure 5-34B shows histograms of voxelwise K_i at BL and ETA (left) and BL, ETA, and FUA (right). Purple color indicates areas overlap between BL and ETA K_i histograms. Histograms of K_i were generated using 200 bins over the range of 0-0.01ml/cm³/min (K_i histogram binwidth = 0.00005). The progression-free survival for this subject was 11 months.

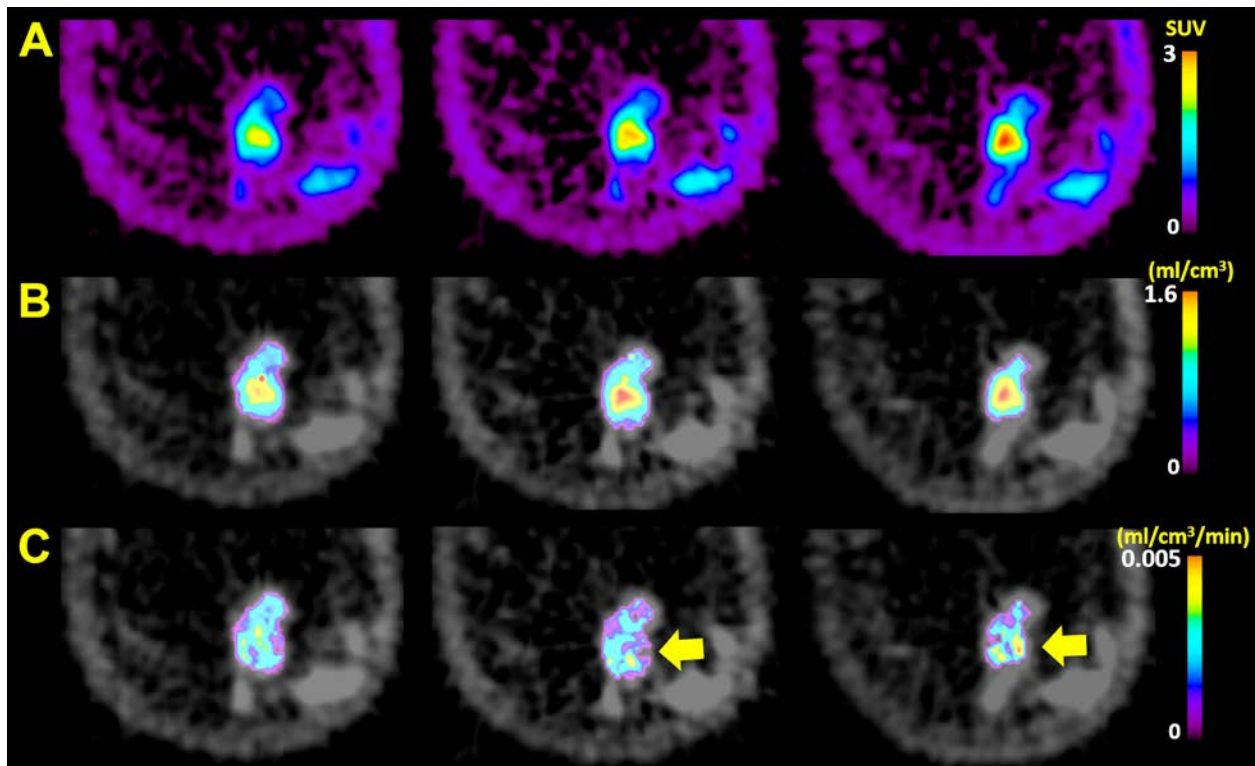


Figure 5-33. Example Voxelwise Analysis for ML-10 #6. Figure shows representative (A) SUV PET sections at BL (left), ETA (center), and FUA (right) time-points. Also shown are voxelwise maps of (B) V_T and (C) K_i overlaid on their corresponding PET time-point (e.g. the ETA V_T map is overlaid on the ETA SUV PET image). All images were co-registered to the BL PET scan. No MR imaging was acquired for this subject. Across imaging time-points [^{18}F]ML-10 uptake is observed to increase in SUV. Visually, V_T maps at BL, ETA, and FUA exhibit similar intensity distribution to their corresponding SUV PET counterparts. Similarly, a local increase in [^{18}F]ML-10 uptake rate is visually apparent between ETA and FUA K_i maps (arrows).

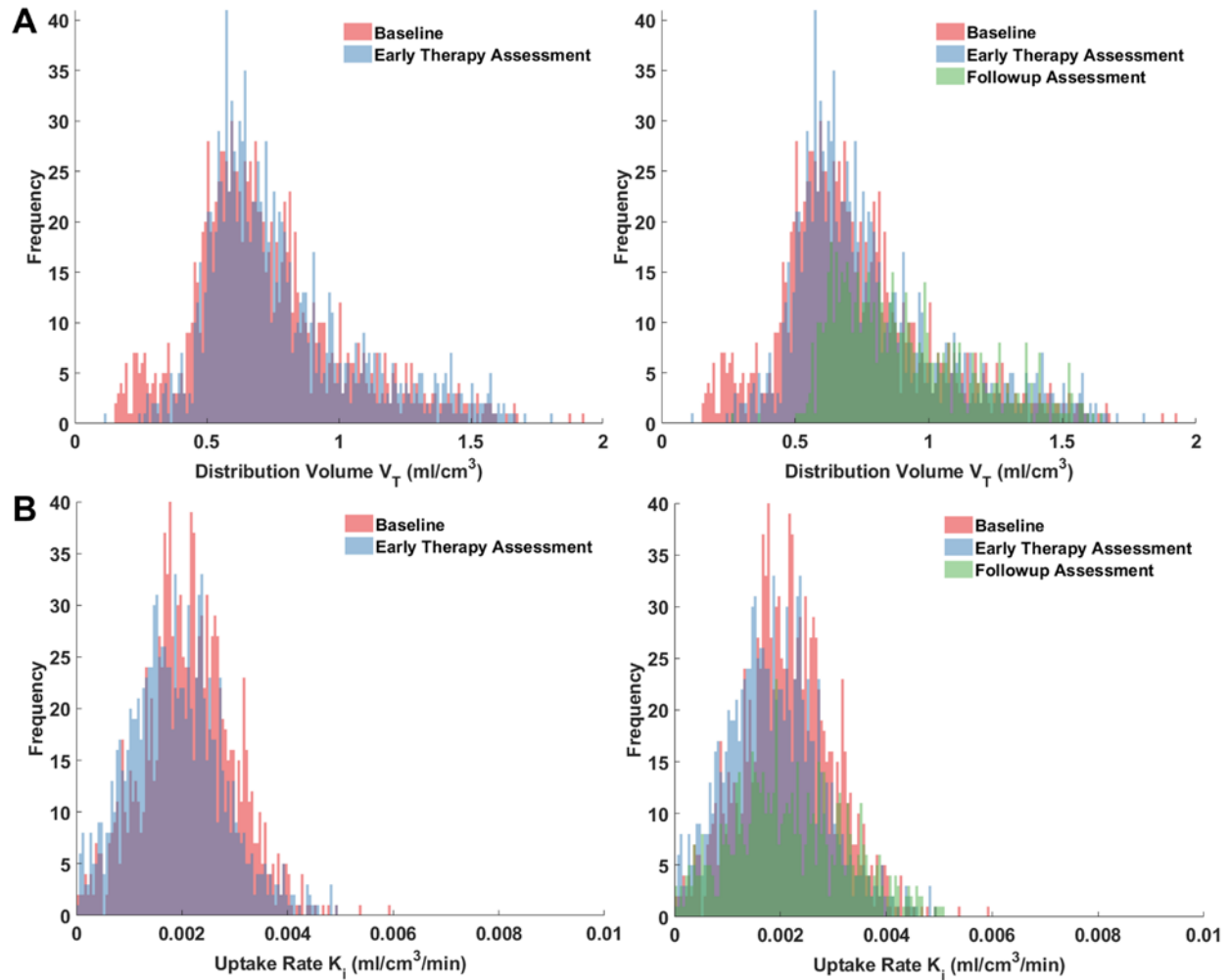


Figure 5-34. Histograms of Voxelwise V_T and K_i for ML-10 #6 Across Imaging Time-points. (A) Histogram of voxelwise V_T at baseline (BL) and early therapy assessment (ETA; left) and BL, ETA, and follow-up assessment (FUA; right). Purple color indicates areas overlap between BL and ETA V_T histograms. (B) Histogram of voxelwise K_i at BL and ETA (left) and BL, ETA, and FUA (right). Purple color indicates areas overlap between BL and ETA K_i histograms. The progression-free survival for this subject was 11 months. Histograms of V_T were generated using 200 histograms. The progression-free survival for this subject was 11 months. Histograms of V_T were generated using 200 bins over the range of 0-2 ml/cm³ (V_T histogram binwidth = 0.01). Histograms of K_i were generated using 200 bins over the range of 0-0.01 ml/cm³/min (K_i histogram binwidth = 0.00005).

Figure 5-35 shows representative (A) contrast enhanced (CE) MRI and (B) SUV PET sections at BL (left), ETA (center), and FUA (right) time-points for ML-10 #5. Also shown are voxelwise maps of (C) V_T and (D) K_i overlaid on their corresponding PET time-point (e.g. the ETA V_T map is overlaid on the ETA SUV PET image). All images were co-registered to the BL PET scan. Across imaging time-points the GBM increases in both size and extent of [^{18}F]ML-10 uptake on CE MRI and [^{18}F]ML-10 PET, respectively. The distribution in V_T intensity does not markedly change between BL and ETA time-points; however, an overall reduction in V_T intensity is visually apparent when comparing the FUA V_T map to either the BL or ETA maps. Similarly, the distribution in K_i values at FUA are visually lower in value compared to the BL and ETA time-points.

Figure 5-36 shows the corresponding voxelwise histograms of V_T and K_i for ML-10 #5. Specifically, figure 5-36A shows histograms of V_T at BL and ETA only and at BL, ETA, and FUA all together (right). Histograms of V_T were generated using 200 bins over the range of 0-2 ml/cm³ (V_T histogram binwidth = 0.01). Purple color indicates areas overlap between BL and ETA V_T histograms. Similarly, figure 5-36B shows histograms of voxelwise K_i at BL and ETA (left) and BL, ETA, and FUA (right). Purple color indicates areas overlap between BL and ETA K_i histograms. Histograms of K_i were generated using 200 bins over the range of 0-0.01ml/cm³/min (K_i histogram binwidth = 0.00005). The progression-free survival for this subject was 15 months.

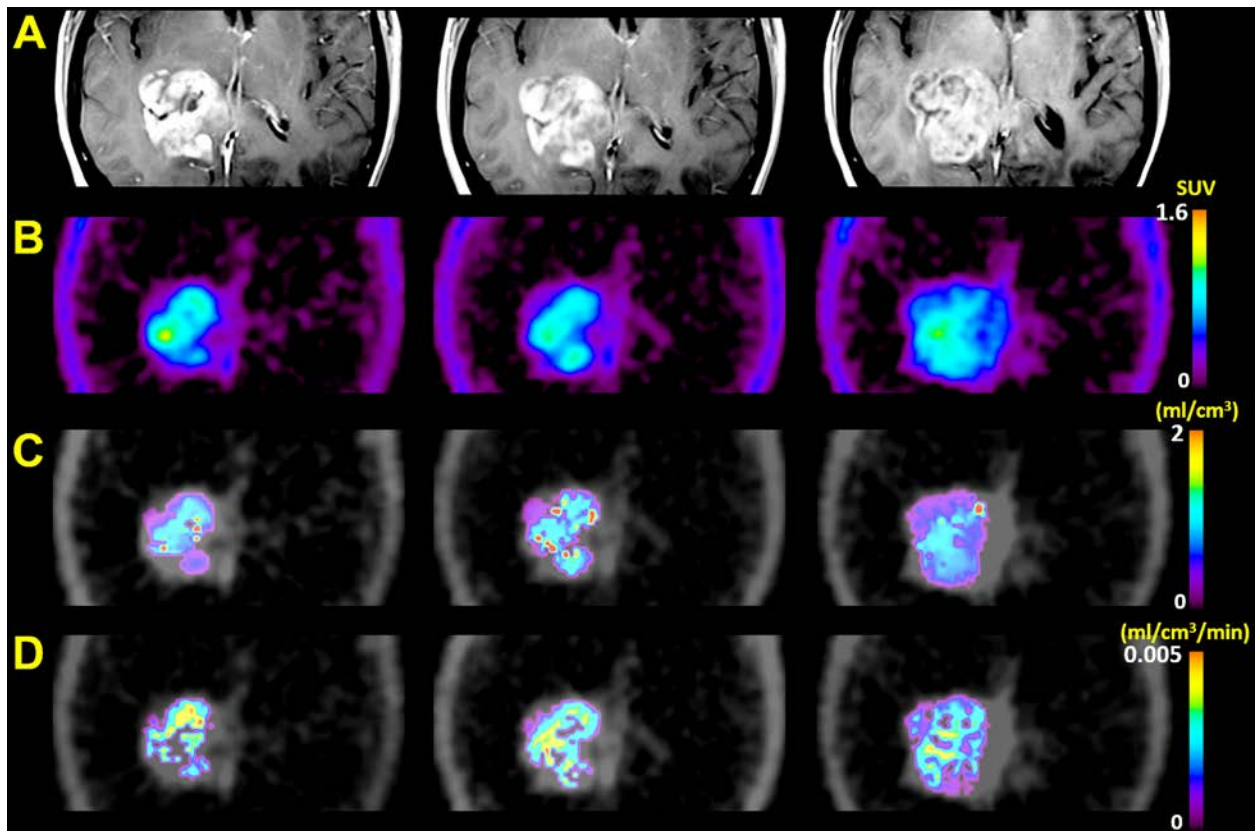


Figure 5-35. Example Voxelwise Analysis for ML-10 #5. Figure shows representative (A) contrast enhanced (CE) MRI and (B) SUV PET sections at BL (left), ETA (center), and FUA (right) time-points. Also shown are voxelwise maps of (C) V_T and (D) K_i overlaid on their corresponding PET time-point (e.g. the ETA V_T map is overlaid on the ETA SUV PET image). All images were co-registered to the BL PET scan. Across imaging time-points the GBM increases in both size and extent of [^{18}F]ML-10 uptake on CE MRI and [^{18}F]ML-10 PET, respectively. The distribution in V_T intensity does not markedly change between BL and ETA time-points; however, an overall reduction in V_T intensity is visually apparent when comparing the FUA V_T map to either the BL or ETA V_T maps. Similarly, the distribution in K_i values at FUA are visually lower in value compared to the BL and ETA time-points.

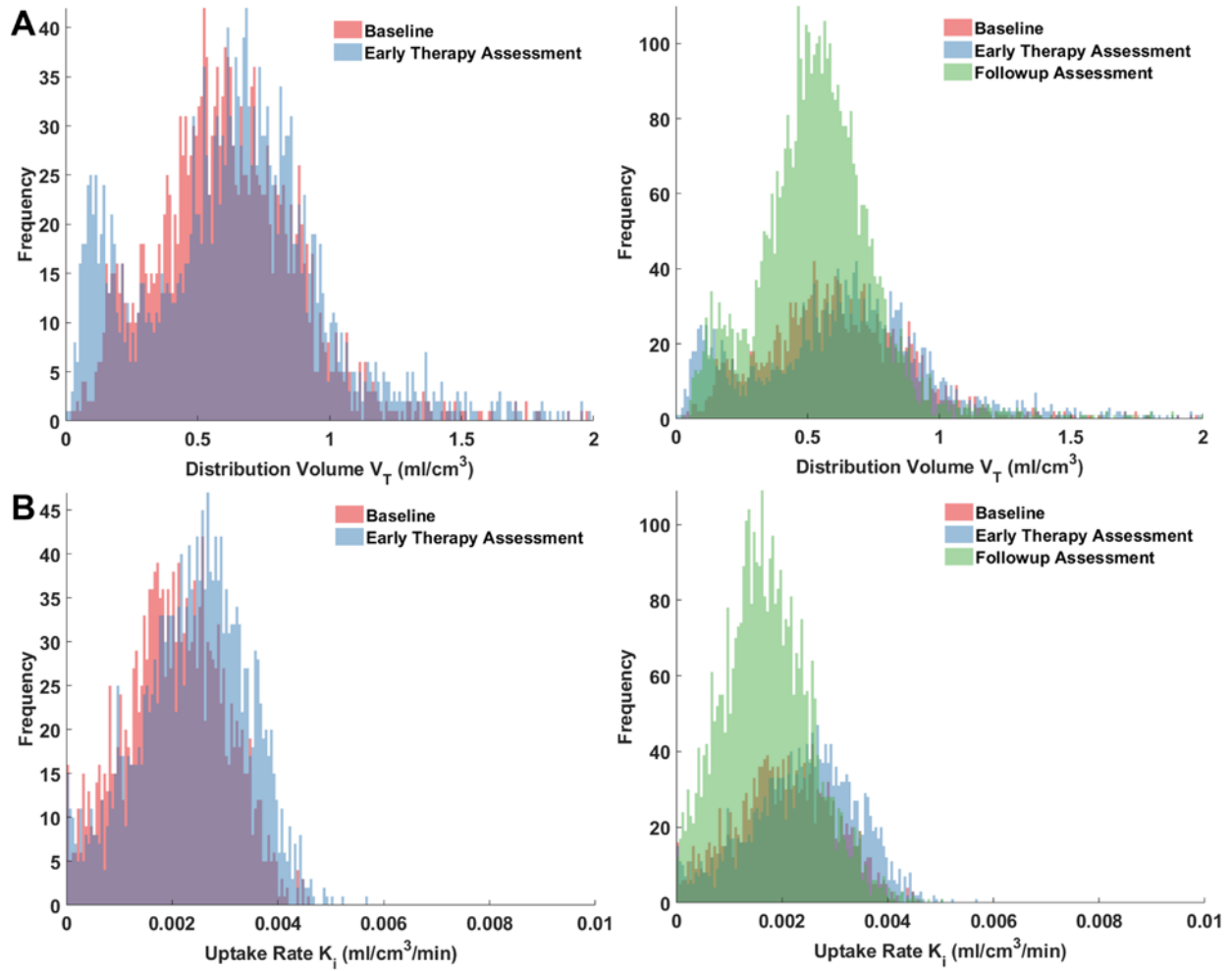


Figure 5-36. Histograms of Voxelwise V_T and K_i for ML-10 #5 Across Imaging Time-Points. (A) Histogram of voxelwise V_T at baseline (BL) and early therapy assessment (ETA; left) and BL, ETA, and follow-up assessment (FUA; right). Purple color indicates areas overlap between BL and ETA V_T histograms. (B) Histogram of voxelwise K_i at BL and ETA (left) and BL, ETA, and FUA (right). Purple color indicates areas overlap between BL and ETA K_i histograms. The progression-free survival for this subject was 15 months. Histograms of V_T were generated using 200 bins over the range of 0-2 ml/cm³ (V_T histogram binwidth = 0.01). Histograms of K_i were generated using 200 bins over the range of 0-0.01 ml/cm³/min (K_i histogram binwidth = 0.00005).

For 2 subjects (ML10 #10 and ML-10 #14) maps of apparent diffusion coefficients (ADCs), obtained from diffusion weighted imaging, were available at the ETA and FUA time-points. In brain tumors, increased diffusion of water molecules (measured on a voxelwise basis using maps of ADC) has been shown to correlate with the breakdown of cellular membranes and an overall decrease in cellular density after successful therapy [185]. Thus, the subject ADC images allow for comparison [¹⁸F]ML-10 uptake at ETA with later change in tumor cellularity at FUA.

Figure 5-37 shows representative (A) CE MRI and (B) SUV PET sections for ML-10 #10 (left) and ML-10 #14 (right) at ETA with (C) corresponding voxelwise V_T maps. (D) shows color coded histograms of V_T values for ML-10 #10 (left) and ML-10 #14 (right). Voxels are binned into 1 of 3 bins based on the total range of V_T values observed: voxels with V_T values in the lower-third of values (green), voxels with V_T values in the middle-third of values (yellow), and voxels with V_T values in the upper-third of values (red). Representative sections of ADC maps are shown at (E) ETA and (F) FUA for ML-10 #10 (left) and ML-10 #14 (right). Each set of images is co-registered to the corresponding subject's ETA SUV PET image.

Compared to ML-10 #14, ML-10 #10 shows overall higher values of V_T at ETA. Furthermore, visual comparison of the ADC maps for ML-10 #10 (figure 5-37E and F; left) and ML-10 #14 (figure 5-37E and F; right) reveals a marked increase in tumor ADC for ML-10 #10 compared to ML-10 #14. The region of marked increase on ML-10 #10's FUA map corresponds to the region of tumor exhibiting the upper third of V_T values. By comparison, ML-10 #14 exhibits overall lower V_T values at ETA.

Figure 5-38 shows representative (A) CE MRI and (B) SUV PET sections for ML-10 #10 (left) and ML-10 #14 (right) at ETA with (C) corresponding voxelwise maps K_i . (D) shows color coded histograms of K_i values for ML-10 #10 (left) and ML-10 #14 (right). Voxels are binned into 1 of 3 bins based on the total range of K_i values observed: voxels with K_i values in the lower-third of values (green), voxels with K_i values in the middle-third of values (yellow), and voxels with K_i values in the upper-third of values (red). Representative sections of ADC maps are shown at (E) ETA and (F) FUA for ML-10 #10 (left) and ML-10 #14 (right). Each set of images is co-registered to the corresponding subject's ETA SUV PET image. Comparatively higher K_i values for ML-10 #10 at ETA are observed to correspond to the region of marked increase in ADC values.

Figure 5-39 shows histograms of voxelwise V_T for (A) ML-10 #10 and (B) ML-10 #14 at BL and ETA alone (left) and BL, ETA, and FUA all together (right). Areas of overlap between BL and ETA V_T histograms are indicated by the purple color. In the case of ML-10 #10, the frequency of voxels with $V_T \leq 0.5 \text{ ml/cm}^3$ is increased at ETA compared to BL, indicating an overall decrease in tumor V_T values between time-points. Moreover, the total number tumor of voxels decreases steadily from BL to ETA to FUA time-points, consistent with subject response to therapy. By comparison, V_T histograms for ML-10 #14 are visually unchanged in extent and location of distribution across time-points. Moreover, a marked reduction in the total number tumor of voxels over time is not observed as in the case of ML-10 #10, consistent with poor response to treatment. PFS for ML-10 #10 and ML-10 #14 were 18 months and 3 months, respectively.

Figure 5-40 shows histograms of voxelwise K_i for (A) ML-10 #10 and (B) ML-10 #14 at BL and ETA alone (left) and BL, ETA, and FUA all together (right). Areas of overlap between BL and ETA K_i histograms are indicated by the purple color. In the case of ML-10 #10, the distribution of K_i at ETA exhibits a marked increase in frequency of K_i values above $K_i = 0.004$ ml/cm³/min compared to BL consistent with an overall increase in tumor apoptosis between time-points. In contrast, K_i histograms for ML-10 #14 are visually unchanged in extent and location of distribution across time-points. Moreover, a marked reduction in the total number tumor of voxels over time is not observed as in the case of ML-10 #10, consistent with poor response to treatment.

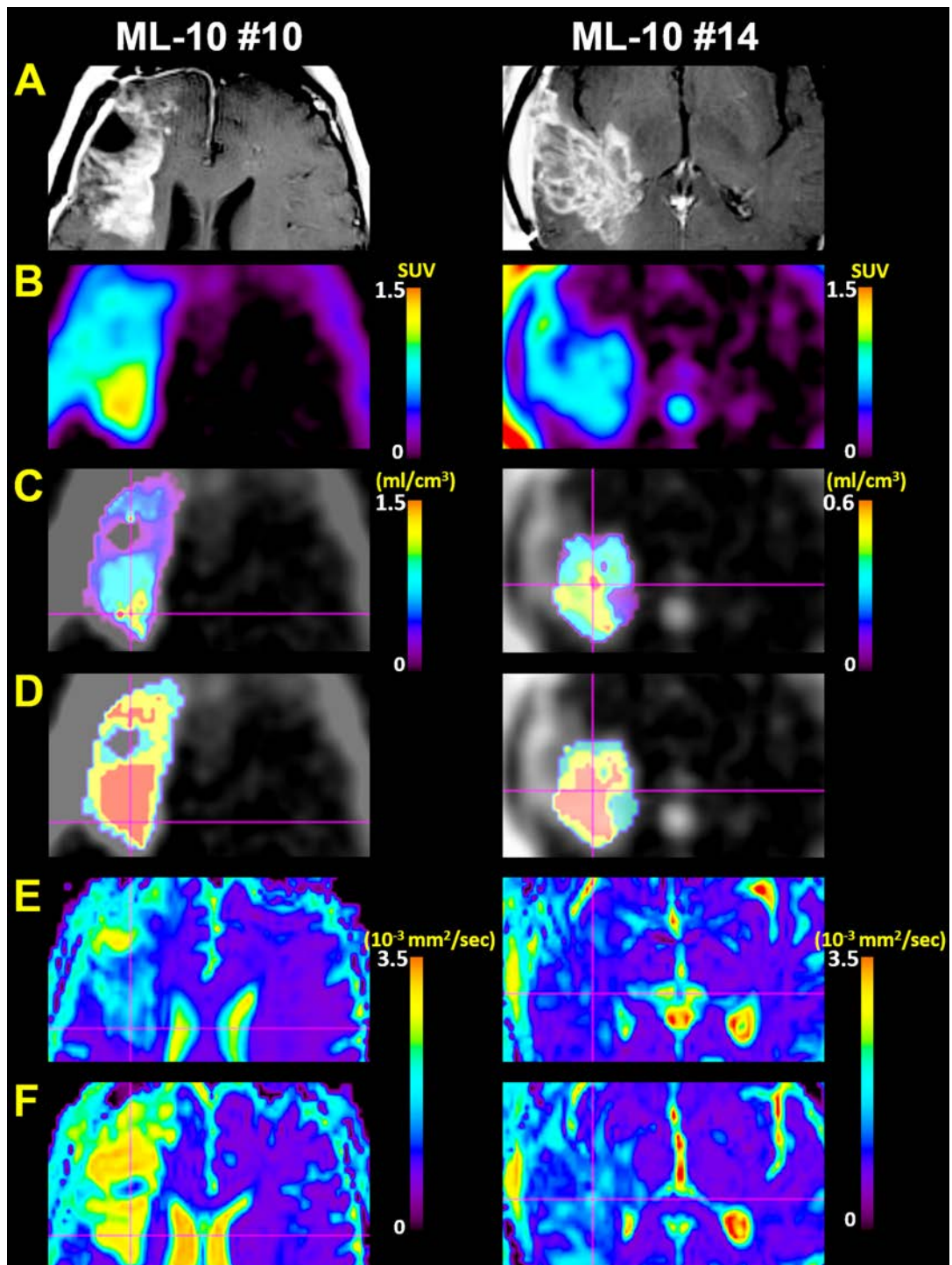


Figure 5-37. Example Voxelwise Maps of V_T at ETA Compared to ADC Change on Diffusion MRI for ML-10 #10 and ML-10 #14. Figure shows representative (A) contrast enhanced (CE) MRI and (B) SUV PET sections for ML-10 #10 (left) and ML-10 #14 (right) at ETA with (C) corresponding voxelwise maps V_T . (D) shows color coded histograms of V_T values for ML-10 #10 (left) and ML-10 #14 (right). Voxels are binned into 1 of 3 bins based on the

total range of V_T values observed: voxels with V_T values in the lower-third of values (green), voxels with V_T values in the middle-third of values (yellow), and voxels with V_T values in the upper-third of values (red). Representative sections of apparent diffusion coefficient (ADC) maps are shown at (E) ETA and (F) FUA for ML-10 #10 (left) and ML-10 #14 (right). Each set of images is co-registered to the corresponding subject's ETA SUV PET image.

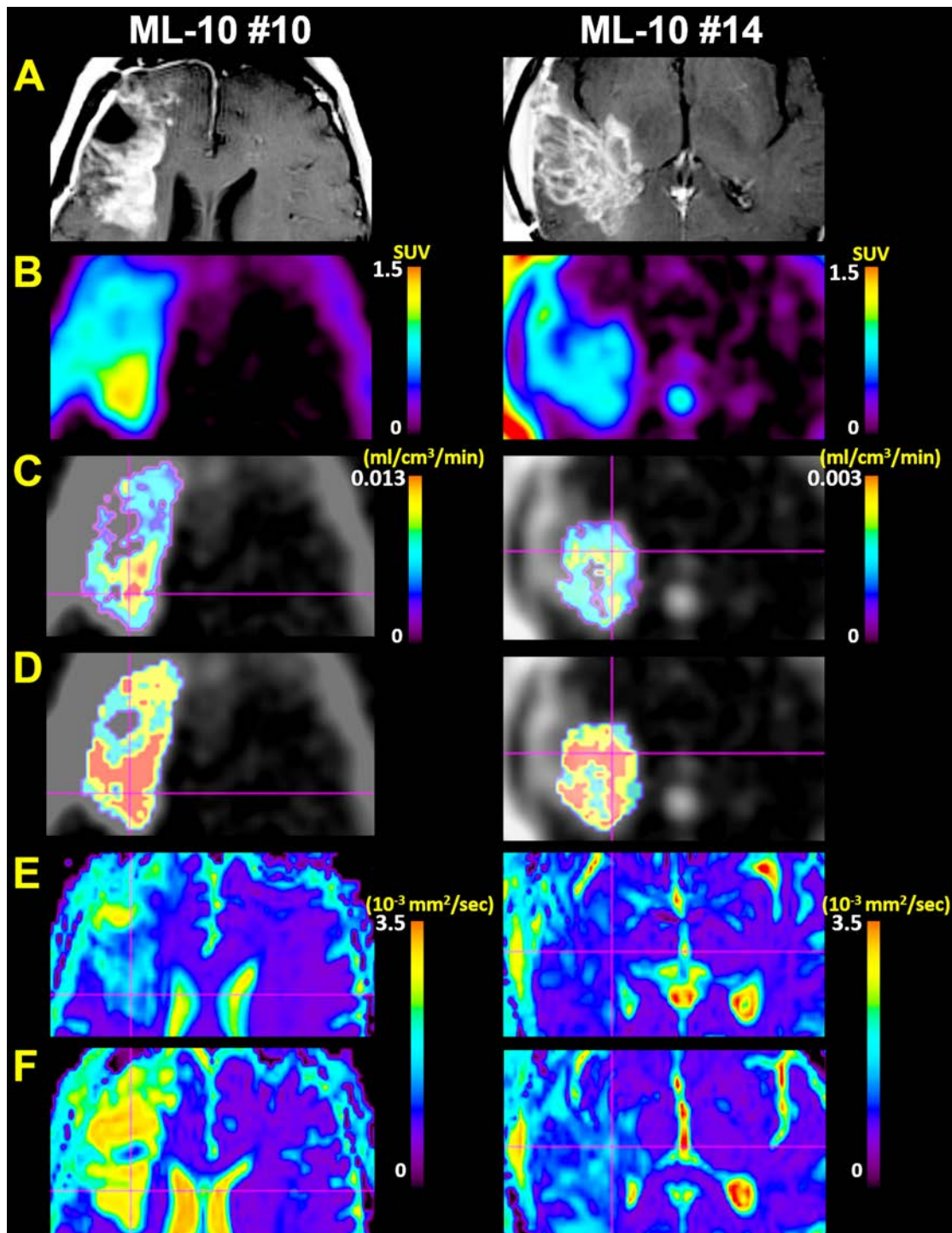


Figure 5-38. Example Voxelwise Maps of K_i at ETA Compared to ADC Change on Diffusion MRI for ML-10 #10 and ML-10 #14. Figure shows representative (A) contrast enhanced (CE) MRI and (B) SUV PET sections for ML-10 #10 (left) and ML-10 #14 (right) at ETA with (C) corresponding voxelwise maps K_i . (D) shows color coded histograms of K_i values for ML-10 #10 (left) and ML-10 #14 (right). Voxels are binned into 1 of 3 bins based on the

total range of K_i values observed: voxels with K_i values in the lower-third of values (green), voxels with K_i values in the middle-third of values (yellow), and voxels with K_i values in the upper-third of values (red). Representative sections of apparent diffusion coefficient (ADC) maps are shown at (E) ETA and (F) FUA for ML-10 #10 (left) and ML-10 #14 (right). Each set of images is co-registered to the corresponding subject's ETA SUV PET image.

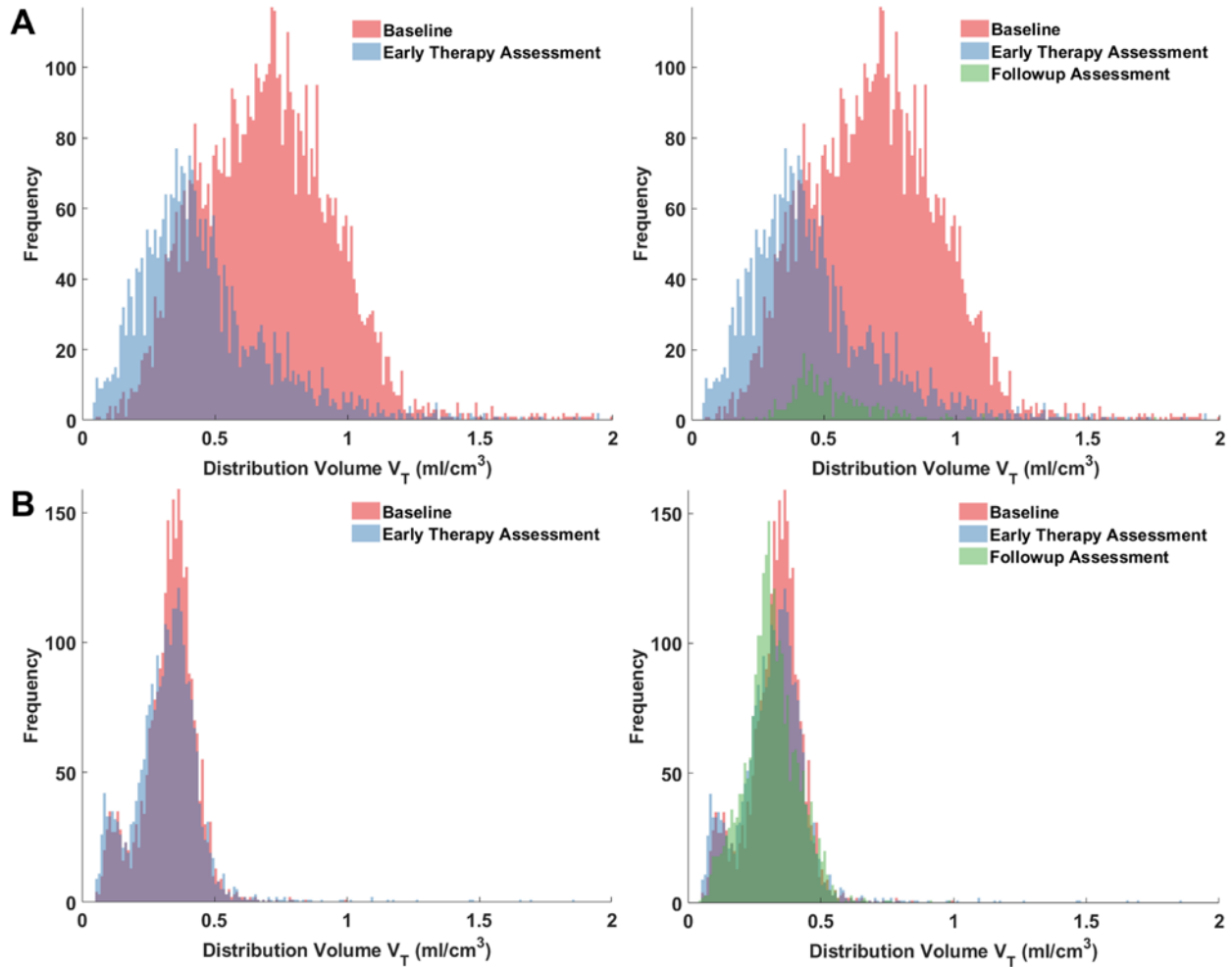


Figure 5-39. Histograms of Voxelwise V_T Over Time for ML-10 #10 and ML-10 #14. (A) Histogram of voxelwise V_T at baseline (BL) and early therapy assessment (ETA; left) and BL, ETA, and follow-up assessment (FUA; right) for ML-10 #10. Purple color indicates areas overlap between BL and ETA V_T histograms. The frequency of voxels with $V_T \leq 0.5 \text{ ml/cm}^3$ is increased at ETA compared to BL, indicating an overall decrease in tumor V_T values between time-points. Moreover, the total number tumor of voxels decreases steadily from BL to ETA to FUA time-points, consistent with subject response to therapy. (B) Histogram of voxelwise V_T at BL and ETA (left) and BL, ETA, and FUA (right) for ML-10 #14. Purple color indicates areas overlap between BL and ETA V_T histograms. V_T histograms for ML-10 #14 are visually unchanged in extent and location of distribution across time-points. Moreover, a marked reduction in the total number tumor of voxels over time is not observed as in the case of ML-10 #10, consistent with poor response to treatment. PFS for ML-10 #10 and ML-10 #14 were 18 months and 3 months, respectively. Histograms of V_T were generated using 200 bins over the range of 0-2 ml/cm^3 (V_T histogram binwidth = 0.01).

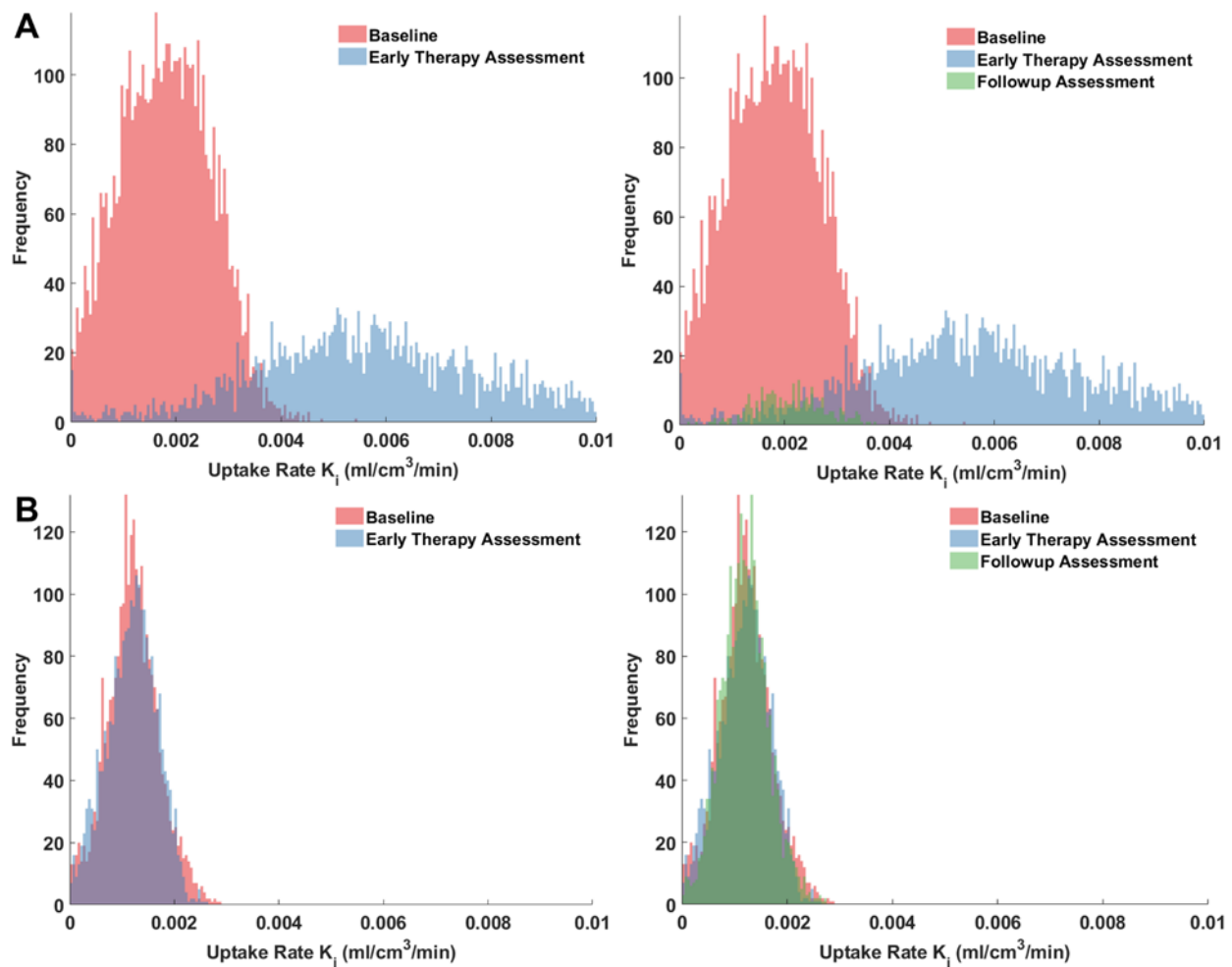


Figure 5-40. Histograms of Voxelwise K_i Over Time for ML-10 #10 and ML-10 #14. (A) Histogram of voxelwise K_i at baseline (BL) and early therapy assessment (ETA; left) and BL, ETA, and follow-up assessment (FUA; right) for ML-10 #10. Purple color indicates areas overlap between BL and ETA K_i histograms. The distribution of K_i at ETA exhibits a marked increase in frequency of K_i values above $K_i = 0.004$ ml/cm³/min compared to BL consistent with an overall increase in tumor apoptosis between time-points. (B) Histogram of voxelwise K_i at BL and ETA (left) and BL, ETA, and FUA (right) for ML-10 #14. Purple color indicates areas overlap between BL and ETA K_i histograms. K_i histograms for ML-10 #14 are visually unchanged in extent and location of distribution across time-points. Moreover, a marked reduction in the total number tumor of voxels over time is not observed as in the case of ML-10 #10, consistent with poor response to treatment. Progression-free survival for ML-10 #10 and ML-10 #14 were 18 months and 3 months, respectively. Histograms of K_i were generated using 200 bins over the range of 0-0.01 ml/cm³/min (K_i histogram binwidth = 0.00005).

5.2.5 Discussion and Conclusions: Tumor Tissue Modeling and Response Assessment

This dissertation presents a detailed study of [^{18}F]ML-10 pharmacokinetics in a cohort of 11 GBM subjects and 1 grade three astrocytoma (ML-10 #12). The results of this analysis are the first reported analysis of [^{18}F]ML-10 PK in humans for any indication. The unprecedented nature of this study meant that methodology for quantifying [^{18}F]ML-10 uptake in arterial blood and brain tissue needed to be developed and evaluated based on PK first principles. To this end, [^{18}F]ML-10 time-course in GBM was studied on a whole tumor and voxelwise level. In both cases, [^{18}F]ML-10 uptake was modeled as the response of a linear time-invariant system using the radiotracer concentration in blood as the input function.

In the whole tumor analysis, candidate models for the IBIF and GBM IRF were fit simultaneously using a maximum likelihood approach. The relative merits of the joint IBIF/IRF models were compared using the Akaike information criterion and model parameter estimability considerations. Spectral analysis was performed to support model selection and provide alternative estimates of standard PK uptake measures. The selected IBIF/IRF models were further interpreted through tissue compartmental modeling. Based on findings from linear and nonlinear model fitting, measures of whole tumor tracer uptake were derived and compared across subjects. For a limited number of subjects, the macroparameters V_T , K_i , and K_i/K_1 were evaluated for their utility in early therapy response assessment for a limited number of subjects using progression-free survival and overall survival as clinical endpoints.

Voxelwise compartmental modeling of [^{18}F]ML-10 uptake was also performed to investigate heterogeneity in apoptosis over the entire tumor volume, to identify regions of GBM

undergoing the highest and lowest rates of apoptosis. For 2 subjects, comparison of voxelwise maps of [¹⁸F]ML-10 uptake at ETA was made with change in tumor density (quantified via diffusion MRI) between ETA and FUA time-points.

5.2.5.1 [¹⁸F]ML-10 Uptake Profile in Healthy Brain Tissue

A central question to be answered for any radiotracer to be used for neuro-imaging applications is to determine how readily the tracer under study is transported across an intact blood-brain-barrier (BBB) [186, 187]. Generally, radiotracers that readily cross an intact BBB (allowing for homogeneous delivery of tracer in the target brain tissue) while simultaneously exhibiting a fast clearance from non-target tissue are highly desirable for good contrast between target and background tissue uptake.

Several factors can influence the ease that a radiotracer crosses the BBB, including: i) the lipophilicity of the radio-labeled compound, ii) its molecular weight, iii) the ability of the molecule to form hydrogen bonding, and iv) the existence of a formal charge on the radiotracer [186, 188]. Ideally, a radiotracer that is to be used for neuro-imaging will show moderate lipophilicity as molecules with high lipophilicity generally result in a low free fraction of tracer in the blood as well as high nonspecific binding to brain fats and proteins [186, 187, 189]. Moreover, an ideal radioligand will possess a low molecular weight (< 500 Da), low propensity for hydrogen bonding, and be electrostatically neutral [187].

[¹⁸F]ML-10 was rationally designed with a low molecular weight (206 Da) to aid in passage across an intact BBB [119, 124]. Pre-clinical fluorescence imaging in mouse stroke models using dansyl-ML-10 observed green fluorescence of dansyl-ML-10 in brain tissue sections

without concomitant BBB disruption, suggestive for passage of dansyl-ML-10 across an intact mouse BBB [124]. However, due to the attached malonic acid (composed of two carboxylic acid groups) in the chemical structure of [^{18}F]ML-10, the radiotracer molecules are generally negatively charged at physiologic pH [119].

To date, no results have been reported regarding passage of [^{18}F]ML-10 across an intact BBB into healthy human brain tissue. Figure 5-12B shows average tumor tissue time activity curves (circles) for two representative subjects, ML10 #2 at ETA (left) and ML-10 #12 at BL (right) measured from both tumor (circles) and healthy (asterisks) tissues. For both subjects, the healthy tissue TACs are characterized by overall low-uptake after the initial peak concentration and fast-clearance. Visually both curve shapes have the appearance of attenuated blood concentration, consistent with [^{18}F]ML-10 not being able to appreciably cross an intact BBB. The healthy tissue TACs for these subjects are representative of the measured healthy tissue TACs across all subjects and imaging time-points.

5.2.5.2 Tumor TAC Discussion

The primary goal of this dissertation was to investigate the pharmacokinetic properties of [^{18}F]ML-10 in GBMs and obtain preliminary evidence that supports [^{18}F]ML-10 imaging, in combination with appropriate quantitative methodology, as an imaging biomarker for early therapy response assessment of GBMs in humans. To date, cancer response assessment using [^{18}F]ML-10 in humans has been limited to so called static imaging studies, in which a series of PET image volumes are acquired over a 20-30 min period, initiating 20 min or more post tracer injection, and then averaged together to create a single 'static' PET image [91, 129, 134-136].

In the case of Allen et al [91] [¹⁸F]ML-10 static PET images were obtained from a cohort of 10 subjects suffering from brain metastases. PET images were quantified using tissue activity concentration normalized to blood pool activity concentration and compared to tumor size change on MRI [91]. Results revealed a strong correlation between the percentage of voxels that increased between PET imaging time-points with percent reduction in tumor size using either the WHO (R = .92) or the volumetric based (R = .91) methods [91].

The potential utility of [¹⁸F]ML-10 static PET imaging to predict early therapy response in GBM has also been reported for a limited number of subjects [134-136]. For each of these studies, either tumor-to-blood ratio (TBR) or SUV were the principal quantitative measures of tumor uptake [134-136]. Fractional change in SUV or TBR, either on a whole tumor or voxelwise basis, was compared to subject PFS or OS. However, the ability of these simplified measures to predict response to therapy in GBM was less obvious compared to the brain metastases study of Allen et al [91], as changes between BL and ETA [¹⁸F]ML-10 PET SUV images were not clearly associated with patient clinical outcome [135, 136].

The differences in findings between these studies may be due to several factors. First, Allen et al [91] used tumor size change on contrast enhanced MRI or CT between baseline and at 6-8 weeks post-therapy as their response measure, not subject PFS or OS as in Oborski et al [135, 136]. Second, brain metastases and GBM have very different etiology and physiology (e.g. brain metastases generally do not form behind the BBB). Finally, differences in findings may indicate limitations of SUV and TBR as measures of tumor [¹⁸F]ML-10 uptake in GBM.

The primary advantage of using simplified uptake measures such as SUV and TBR is their ease of measurement and clinical practicality. However, in the case of GBM SUV and TBR cannot distinguish between increased [^{18}F]ML-10 uptake that is due to increased tumor apoptosis and increased [^{18}F]ML-10 uptake due to increased radiotracer transport resulting from BBB breakdown. Moreover, SUV and TBR are measures of total radioactivity in the tumor at a specific instant post-tracer injection. Therefore, these measures can be biased by radioactivity in the tumor vasculature and, in the case of SUV, often depend on time-of-measurement post-injection. Generally, the use of SUV or TBR as measures of radiotracer uptake requires validation with radiotracer PK modeling.

Figure 5-12C shows plots of TBR for ML-10 #9 at BL and ML-10 #12 at BL. For both cases the TBR is observed to increase over time. More generally, a time dependent TBR was observed across subjects and imaging time-points; however, the rate of increase in TBRs varied across [^{18}F]ML-10 PET scans.

5.2.5.3 PK Modeling of the Tumor Tissue Impulse Response Function

Tracer compartmental modeling provides a principled approach to quantifying the time-course of [^{18}F]ML-10 concentration in tumor, and is a ubiquitous tool used in PET imaging to evaluate the *in vivo* PK of novel radiotracers. However, compartmental modeling makes specific assumptions regarding the state-space properties of the tumor tissue IRF (and thus assumptions regarding [^{18}F]ML-10 transport in the tumor) that should be supported by *in vitro* or pre-clinical data. However, limited published results are available on the specific mechanism of [^{18}F]ML-10 uptake by cells undergoing apoptosis. For this reason, a model selection approach was first used

to study the tumor system IRF without making any assumptions regarding underlying compartmental (or state-space) structure.

As part of the IRF model selection process, models for describing the [^{18}F]ML-10 concentration profile in the blood were also evaluated. Candidate IBIF and IRF models were fit to the measured [^{18}F]ML-10 concentration time-course data simultaneously and selected for by using the model order selection criterion AIC_c and with the requirement that the parameters of the selected IBIF and IRF models be estimable (that is % COV \leq 50% on all model parameters).

Figure 5-14 shows an example IRF model selection analysis for ML-10 #6 at ETA. Table 5-12 summarizes the model selection results using AIC_c and parameter estimability considerations. Of the 29 subjects analyzed, the 2α - 2β IRF model was chosen as the best fitting IRF model 9 times while the 2α - 1β IRF model was selected 10 times. In 2 cases an attenuated IBIF model was selected, suggesting for each case that the dominant component in the measure GBM uptake profile comes from the vascular component. Interestingly these 2 cases occurred for the same subject, ML-10 #11, at ETA and FUA who exhibited a PFS of less than 1 month.

The total distribution volume, V_T , can be interpreted as the ratio of [^{18}F]ML-10 concentration in tumor to [^{18}F]ML-10 concentration in blood at equilibrium, assuming the tracer concentration in blood was held constant. Table 5-13 contains V_T estimates for subject scans in which a reversible tumor IRF model was selected. For all cases the $V_T < 1$, indicating that for these cases there is a higher concentration of [^{18}F]ML-10 in the arterial blood than in tumor at equilibrium. For tumor TACs for which the selected best model was a 2α - 1β IRF model, V_B ranged

from 0.036 to 0.276 (mean = 0.132, median = 0.116) and associated K_i values ranged from 4.787×10^{-4} ml/cm³/min to 1.829×10^{-3} ml/cm³/min (mean = 1.225×10^{-3} ml/cm³/min, median = 1.145×10^{-3} ml/cm³/min). For tumor TACs for which the selected best model was a 2α - 2β IRF model, V_B ranged from 0.0469 to 0.2111 (mean = 0.1194, median = 0.1154) and associated V_T values ranged from 0.0275 ml/cm³ to 0.7157 ml/cm³ (mean = 0.5318 ml/cm³, median = 0.4554 ml/cm³).

As mentioned above, [¹⁸F]ML-10 is the first and only PET radiotracer designed for *in vivo* imaging of apoptosis to be evaluated in humans to date. Therefore, there are no other PET apoptosis radiotracer in human results with which findings of [¹⁸F]ML-10 macroparameters V_T or K_i can be directly compared. However, in the case of the blood-to-tissue transport rate parameter K_1 , comparison of K_1 estimates from [¹⁸F]ML-10 scans with published K_1 values of well understood radiotracers evaluated in GBM can reasonably be made.

For example, [¹⁸F]FDG is actively transported across an intact BBB [190]. Previous studies using [¹⁸F]FDG PET have observed average K_1 values of 0.064 ± 0.02 ml/g/min [166] and 0.072 ± 0.032 ml/g/min [167] in GBM subjects. In contrast, 3'-deoxy-3'-¹⁸F-fluorothymidine ([¹⁸F]FLT), is PET tracer of cell proliferation, that is known to require loss of BBB integrity for efficient transport from blood into GBM tissue [168]. Representative reported ranges in K_1 observed for [¹⁸F]FLT PET studies [0.06, 0.164] ml/g/min [191] and [0.013, 0.126] ml/g/min [192] in newly diagnosed and recurrent GBM subjects, respectively.

For tumor TACs for which the selected best model was a $2\alpha-1\beta$ IRF model, K_1 ranged from 0.006 ml/cm³/min to 0.030 ml/cm³/min (mean = 0.015 ml/cm³/min, median = 0.012 ml/cm³/min), while for tumor TACs for which the selected best model was a $2\alpha-2\beta$ IRF model, K_1 ranged from 0.0113 ml/cm³/min to 0.0658 ml/cm³/min (mean = 0.0216 ml/cm³/min, median = 0.0266 ml/cm³/min). Comparison with established neuro-oncology radiotracers in this narrow context, suggests [¹⁸F]ML-10 exhibits overall poor transport from blood to GBM tissue and is limited to brain tumors with significant BBB breakdown.

Another key finding was the range in estimates for the blood volume fraction, V_B , across scans. V_B controls the relative contribution of the vascular and tumor tissue components to the measured tumor TAC. The largest values for V_B were observed for ML-10 #11 at ETA ($V_B = 0.3074$) and FUA ($V_B = 0.3910$). For both cases, the selected best IRF model was an attenuated IBIF model, suggesting that the large vascular component renders the [¹⁸F]ML-10 signal component in the tumor essentially undetectable for these cases. The wide range in blood volume fraction estimates, suggests that V_B cannot be ignored as a model parameter.

Spectral Analysis Results

SA is particularly appropriate for analyzing the dynamics of [¹⁸F]ML-10 because, to date the kinetics of [¹⁸F]ML-10 have not been investigated in either pre-clinical or clinical models nor has any compartmental model structure been hypothesized.

In order to provide independent estimates of [¹⁸F]ML-10 uptake measures as well as provide additional guidance on IRF model selection, SA was performed on each measured tumor

tissue TAC. Because SA requires *a priori* knowledge of the input [^{18}F]ML-10 concentration into the tumor, the corresponding IBIF model selected during the joint IRF/IBIF modeling was used as input for each scan.

The number of detected reversible spectral components ranged from 0-4 components across subjects. The number of detected components generally supported model selection decisions made during joint IBIF/IRF model selection analysis. Moreover, as in the case of IBIF/IRF modeling both reversible and irreversible IRF models were detected. Table 5-17 and table 5-18 contain SA estimates for K_1 , V_T , and K_i for each scan using the NNLS and L_1 norm methods, respectively. Overall macroparameter estimates obtained using both the NNLS and L_1 norm methods were consistent in value with those obtained using the joint IBIF/IRF nonlinear modeling approach.

Tracer Compartmental Modeling

IRF modeling has the advantage of requiring few assumptions regarding radiotracer PK in GBM (aside from those required by a linear and time invariant system). This generality has advantages from the standpoint of initial study and quantification of the [^{18}F]ML-10 uptake profile in GBM but is limited with regard to interpretation of the macroparameters.

Tracer compartmental modeling provides a framework within which the macroparameters V_T and K_i , derived from IRF modeling, can be interpreted. Figure 5-27 shows an example $2\alpha-2\beta$ IRF model fit, for which the corresponding compartmental rate constants have been calculated. In

the context of compartmental modeling, figure 5-27 illustrates a 2-tissue 4 rate constant (2T-4K) fit to the subject's GBM time activity curve.

A challenge to obtaining reliable estimates of compartmental rate constants in tissue compartmental modeling is the high degree of co-linearity between the transfer rates. Figure 5-28A (left) shows an example scan for which the 2T-4K model was selected as the best candidate model that explains the data. Visually, the sensitivity functions for k_3 and k_4 (figure 5-28A, right) are nearly scaled versions of each other and are primarily influenced by the same portion of the measured tumor TAC data. These results suggest that it is not possible to simultaneously separate the influence of k_3 from k_4 on the [^{18}F]ML-10 uptake profile for this scan using the measured tumor TAC alone.

Constraining the efflux parameter k_4 to equal 0 (figure 5-28B) results in increased precision on the estimate for k_3 compared to the 2T-4K model. Figure 5-28B (right) shows corresponding sensitivity functions for the 2T-3K model. The individual sensitivity function profiles for each rate constant are visually different, suggesting it is possible to separate the influence of each rate constant on the measured tumor TAC assuming the 2T-3K model. For this case, the preponderance of findings provides support for K_i over V_T as the better measure of [^{18}F]ML-10 uptake.

For 3 of 29 scans analyzed, a $3\alpha-2\beta$ IRF model was selected during the joint IBIF/IRF model selection, which corresponds to a 3T-5K tissue compartment model. Figures 5-29, 5-30, and 5-31 illustrate the compartmental model fits for these cases (ML-10 #2 at ETA, ML-10 #6 at ETA, and ML-10 #6 at FUA). For all 3 cases, the sensitivity functions for k_2 , k_5 , and k_6 plateau

over nearly the same time range in measured tumor TAC samples, indicating strong correlation between these parameters and consistent with the overall lower precision on associated rate constant estimates compared to the corresponding 2T-4K and 2T-3K fit results.

For all 3 cases, the 2T-3K tissue model yielded compartmental rates with the best precision. Furthermore, individual sensitivity function profiles for each 2T-3K rate constant were visually different within each subject, suggesting the measured tumor data allow for identification of the individual influence of each rate constant (in contrast to the 2T-4K and 3T-5K models). However, this increase in model parameter estimability comes at the expense of increased bias in the model fitting (especially in the case of ML-10 #6 at ETA and FUA).

The two most commonly selected IRF models obtained as part of the joint IBIF-tumor IRF model order selection analysis (table 5-12) were the 2α - 2β (selected in 9 out of 29 cases) and 2α - 1β (selected in 10 out of 29 cases) IRF models, consistent with the 2T-4K and 2T-3K tissue compartment models, respectively. Moreover, in the 3 cases for which the 3α - 2β IRF model was selected (figures 5-29, 5-30, and 5-31), the corresponding compartmental transfer rates were not well estimated and showed evidence of strong correlation on sensitivity analysis. As a result, all [^{18}F]ML-10 acquisitions were analyzed using both a 2T-4K and a 2T-3K tissue compartmental model separately (with the exception of ML-10 #11 at ETA and ML-10 #11 at FUA). Additionally, analyzing each scan using a 2T-4K and a 2T-3K model allowed for comparison of model results across subjects.

Table 5-19 and table 5-20 contain estimates for V_B and the associated compartmental rate constants, respectively, obtained by analyzing each measured [^{18}F]ML-10 tumor TAC using a 2T-4K tissue compartmental model. The coefficient of variation on each model estimate is expressed as a percentage given in parentheses. From table 5-20, [^{18}F]ML-10 PET scans for which the $1\alpha-1\beta$ IRF model was selected as the best tumor IRF model produced estimates for the 2T-4K rate constants that were generally not estimable. Ignoring these cases, estimates for the blood volume fraction (V_B) ranged from 0.0162 to 0.2818 (mean = 0.1215 and median = 0.1096) and K_1 ranged from 0.0113 ml/cm³/min to 0.0809 ml/cm³/min (mean = 0.0305 ml/cm³/min and median = 0.0268 ml/cm³/min), respectively.

The large %COV (e.g. %COV \geq 100% in some cases) on some of the estimates for the transfer rate constants is consistent with model overfitting and suggests the specific tissue model being fit is important in these cases. For example, the IRF model for ML-10 #9 at ETA was selected to be the $2\alpha-1\beta$ model during joint IBIF/IRF modeling, consistent with a 2T-3K tissue compartmental model. The 2T-3K model can be obtained from the more complex 2T-4K tissue model by constraining the transfer rate from the specifically bound compartment, k_4 , to equal 0. As can be observed the estimate for k_4 using the 2T-4K model for this scan is $k_4 = 1.09 \times 10^{-14}$ (%COV = 176.68).

From estimates of the compartmental rate constants, the corresponding volumes of the specifically bound (V_S) and non-displaceable (V_{ND}) tracer can be computed. Table 5-21 contains estimates for the total distribution volume V_T , as well as V_S and V_{ND} . Table 5-21 also contains the ratio of V_S/V_T for each scan, which quantifies the proportion of total tracer in the GBM that is

bound to cells undergoing apoptosis at equilibrium. Ignoring the scans for which a 1α - 1β or attenuated IRF model was selected during joint IBIF/IRF modeling, the ratio of V_S/V_T ranged from 0.3093 to 0.7997. This wide range in observed V_S/V_T ratio suggests a wide range in apoptosis rates is being exhibited across [^{18}F]ML-10 scans.

Table 5-22 contains estimates for V_B and the associated compartmental rate constants obtained from analyzing each measured [^{18}F]ML-10 tumor TAC using a 2T-3K tissue compartmental model. The coefficient of variation on each model estimate is expressed as a percentage given in parentheses. As in the 2T-4K modeling case, scans for which the 1α - 1β IRF model was selected as the best tumor IRF showed poor estimability when analyzed as a 2T-3K model. Ignoring these subject, estimates for V_B and K_1 ranged from 0.0254 to 0.2977 (mean = 0.1310 and median = 0.115) and from 0.0093 ml/cm³/min to 0.0347 ml/cm³/min (mean = 0.0211 ml/cm³/min and median = 0.0196 ml/cm³/min), respectively.

Table 5-23 contains the estimated value for the flux parameter K_i as well as the ratio of K_i -to- K_1 (denoted K_i/K_1). Under the assumptions of the 2T-3K model, the ratio K_i/K_1 (also equal to $\frac{k_3}{(k_2+k_3)}$) quantifies the fraction of tracer entering the system that is irreversibly taken up by the GBM tissue, while $\left(1 - \frac{K_i}{K_1}\right)$ quantifies the proportion of [^{18}F]ML-10 that is transported from the blood to the tissue but ultimately escapes back into the tumor vasculature. Ignoring the scans for which the 1α - 1β IRF model was selected as the best tumor IRF model, the associated K_i values ranged from 3.675×10^{-4} ml/cm³/min to 5.483×10^{-3} ml/cm³/min, with corresponding K_i/K_1 values ranging from 0.0142 to 0.2873 (table 5-23). Assuming a 2T-3K model to be appropriate for all [^{18}F]ML-10 PET acquisitions, these findings indicate that the majority of [^{18}F]ML-10 that is

transported into the tissue is ultimately not irreversibly trapped in the tissue. As with the 2T-K analysis, the range in observed K_i/K_1 suggests a range of apoptosis rates is being observed across all acquired [^{18}F]ML-10 PET scans.

Early Therapy Response Assessment

Since both reversible and irreversible IRF models were selected during the joint IBIF/IRF model selection analysis, and further supported by SA and compartmental modeling, the macroparameters V_T , K_i , K_i/K_1 were evaluated for their utility in predicting response to therapy in a subset of GBM subjects that received at least a BL and ETA [^{18}F]ML-10 PET scan using both PFS and OS as clinical outcome measures. Compared to the individual compartmental rate constants, the macroparameters have better precision, do not rely on assuming a specific compartmental structure and, in some cases, can be approximated using simplified graphical methods (e.g. graphical analysis) [193-195]. Thus, it is natural to evaluate the macroparameters for their utility in predicting early response to therapy.

Table 5-24 contains the percent change in V_T from: BL to ETA (denoted $\Delta V_T(\text{ETA}, \text{BL})$), BL to FUA ($\Delta V_T(\text{FUA}, \text{BL})$), and ETA to FUA (denoted $\Delta V_T(\text{FUA}, \text{ETA})$). Subjects are ordered in decreasing rank order according to their PFS. For subject imaging time-points that were best modeled using a 1α - 1β IRF model (i.e. a 1T-2K tissue compartment model), the associated 1α - 1β values for V_T were used in the percent change calculation.

The median PFS for a newly diagnosed GBM subject receiving standard of care concomitant radiotherapy plus temozolomide chemotherapy is 6.9 months [4]. This makes a PFS

of 6.9 months a natural threshold for categorizing subjects as exhibiting a poor PFS (i.e. PFS < 6.9 months). For the limited number of subjects analyzed, no obvious association between ΔV_T (ETA, BL) and subject PFS is apparent. For example, ML-10 #9 exhibited the longest PFS (25 months) but showed a 41.185% decrease in V_T between the pre-therapy BL and the post-therapy administration ETA time-points suggesting an overall decrease in apoptosis at ETA compared to BL. In contrast, subject ML-10 #13 demonstrated the shortest PFS (2 months) post-therapy initiation, consistent with a poor response to therapy, but exhibited the largest percent increase in V_T between BL and ETA.

Table 5-25 contains percent change in K_i from: BL to ETA (ΔK_i (ETA, BL)), BL to FUA (ΔK_i (FUA, BL)), and ETA to FUA (ΔK_i (FUA, ETA)) , while table 5-26 contains percent change in the ratio K_i/K_1 , henceforth referred to as K_i^* , from BL to ETA (ΔK_i^* (ETA, BL)), BL to FUA (ΔK_i^* (FUA, BL)), and ETA to FUA (ΔK_i^* (FUA, ETA)). For the limited number of subjects analyzed, no obvious association between ΔK_i (ETA, BL) and subject PFS is apparent. Overall percent change in K_i compared to PFS showed a similar pattern to percent change in V_T compared to PFS. For example, ML-10 #9 exhibited the longest PFS (25 months) but showed a 24.61% decrease in K_i between the BL and ETA time-points suggesting an overall decrease in apoptosis at ETA compared to BL. In contrast, subject ML-10 #13 demonstrated the shortest PFS (2 months) post-therapy initiation, consistent with a poor response to therapy, but exhibited an increase in K_i (though the percent increase observed for K_i was not as large as the corresponding percent increase in V_T). Furthermore, percent change in K_i between BL and FUA and between ETA and FUA decreased for all subjects except ML-10 #6.

In contrast to $\Delta V_T(\text{ETA}, \text{BL})$ and $\Delta K_i(\text{ETA}, \text{BL})$, subjects with $\text{PFS} \geq 15$ months all showed an increase in K_i^* from the BL to ETA time-point, while 3 out of 4 subjects with $\text{PFS} \leq 11$ demonstrated a decrease in K_i^* from BL to ETA. K_i^* was observed to increase for ML-10 #14 (who had a $\text{PFS} = 2$ months) from the BL to ETA; though, this result is confounded by the fact that ML-10 #14 does not have a true BL scan. This finding suggests that percent change in K_i/K_1 may have utility in predicting response to therapy between the BL and ETA time-points.

For all tested uptake measures no clear association between percent change in V_T , K_i , or K_i^* from BL to the FUA time-point is apparent.

5.2.6 Evaluation of Local Heterogeneity in Apoptosis Rate via Voxelwise PK Modeling

Quantitative methodology for response assessment of GBM using apoptosis as a biomarker is under active development. Some studies have suggested the use of a voxelwise change approach [196, 197], which has been shown to be fruitful in diffusion-weighted MRI [198-200]. For example, studies have demonstrated an inverse relationship between apparent diffusion coefficient (ADC) measurements from diffusion-weighted MRI and cell density in both low and high-grade glioma [200]. Additionally, small volumetric increase in brain tumor ADC have been shown to correlate with overall poorer response to therapy compared with large volumetric increases [198], suggesting that regions of tumor exhibiting little to no increase in ADC may be demonstrating ineffective therapy.

In this study, all tumor voxels were treated as statistically independent. Moreover, the noise variance for each voxel was assumed constant over time and both the IBIF model and V_B were

assumed known. Figure 5-32 shows representative fits using a $2\alpha-2\beta$ IRF model and a $2\alpha-1\beta$ IRF model for 2 different tumor voxels for ML-10 #6 at ETA estimated using IBIF Model 1b as IBIF model.

For 2 subjects (ML10 #10 and ML-10 #14) ADC maps were available at the ETA and FUA time-points, which allowed to correlate GBM apoptosis at ETA with change in tumor density from ETA to FUA. Figure 5-37 shows representative (A) contrast enhanced (CE) MRI and (B) SUV PET sections for ML-10 #10 (left) and ML-10 #14 (right) at ETA with (C) corresponding voxelwise maps V_T . (D) shows color coded histograms of V_T values for ML-10 #10 (left) and ML-10 #14 (right). Voxels are binned into 1 of 3 bins based on the total range of V_T values observed: voxels with V_T values in the lower-third of values (green), voxels with V_T values in the middle-third of values (yellow), and voxels with V_T values in the upper-third of values (red). Representative sections of apparent diffusion coefficient (ADC) maps are shown at (E) ETA and (F) FUA for ML-10 #10 (left) and ML-10 #14 (right). Each set of images is co-registered to the corresponding subject's ETA SUV PET image.

Comparison of the scales of the individual V_T maps between subjects emphasizes that the range in observed V_T for ML-10 #10 at ETA was almost twice as large as ML-10 #14 at ETA, suggesting overall more apoptosis occurring in the GBM of ML-10 #10 at ETA. Visual comparison of the ADC maps for ML-10 #10 (figure 5-37E and F; left) and ML-10 #14 (figure 5-37E and F; right) reveals a marked increase in tumor ADC for ML-10 #10 compared to ML-10 #14. These findings are consistent with a larger decrease in tumor cellularity for ML-10 #10 than ML-10 #14

between ETA and FUA, as presaged by [¹⁸F]ML-10 imaging at ETA. A similar result is observed when voxelwise uptake of [¹⁸F]ML-10 is quantified using the flux parameter K_i (figure 5-38).

Figure 5-39 shows voxelwise V_T histograms for (A) ML-10 #10 and (B) ML-10 #14 at BL and ETA alone (left) and BL, ETA, and FUA all together (right). For ML-10 #10 the steady decrease in tumor size from BL to ETA to FUA time-points is apparent. In spite of patient response to treatment the number of voxels exhibiting a $V_T > 1$ is larger at BL compared to ETA. For the case of ML-10 #14 the distributions of V_T remain visually similar across time-points.

Figure 5-40 shows voxelwise K_i histograms for (A) ML-10 #10 and (B) ML-10 #14 at BL and ETA alone (left) and BL, ETA, and FUA all together (right). In contrast to V_T , the range in K_i shows marked increase at ETA compared to BL for ML-10 #10, consistent with an overall increase in the rate of apoptosis by the tumor after therapy administration. For the case of ML-10 #14 the histograms of K_i remain visually similar across time-points, and do not exhibit the range in K_i values observed for ML-10 #10 at ETA.

Taken together, these findings provide further support that an [¹⁸F]ML-10 uptake measure proportional to K_i (either K_i/K_1 or K_i itself) may have better utility than V_T in predicting early therapy response in GBM.

5.2.6.1 Study Limitations

This study presented a first-pass analysis of [¹⁸F]ML-10 uptake profiles in human GBM subjects before and after therapy initiation. The limitations with respect to using an IBIF instead of arterial blood sampling to measure the [¹⁸F]ML-10 concentration in blood were discussed in

Section 5.1 above. However, an additional limitation not discussed previously is the fact that no blood samples were obtained at all, which not only prevents correction of the IBIF for partial volume effects, but also means it is not possible to obtain the [^{18}F]ML-10 concentration in the plasma.

This is an important point because it is the radiotracer concentration in the plasma that is available for transport into the tissue, which we have approximated by using an IBIF. Given the available data it is not possible to determine the accuracy of this approximation, but a poor approximation will bias estimates of the transport parameter K_1 to some degree, and, as a result will bias estimates of V_T and K_i . In order to minimize the effect of potential inaccuracy of K_1 , fractional change in the V_T , K_i , and K_i/K_1 was used for evaluating response to therapy.

A second study limitation is the lack of a clear understanding of the mechanism for [^{18}F]ML-10 uptake by cells undergoing apoptosis. As described in detail in *Section 3.3*, the [^{18}F]ML-10 is hypothesized to be taken up by cells with a permanently depolarized cell membrane [119]. However, the exact substrate, if any, that [^{18}F]ML-10 binds to once inside a cell undergoing apoptosis has not been elucidated. The current limited knowledge of the [^{18}F]ML-10 uptake mechanism challenges interpretation of compartmental rate constants and limits certainty on the arrangement and connectivity of potential tissue compartment models consistent with the observed tumor tissue IRF models. For this reason, emphasis was placed on radiotracer macroparameters, which do not assume a particular arrangement of tissue compartments.

However, in the case of the macroparameter K_i some ambiguity still exists since unlabeled ML-10 is not an endogenous substance. Generally, the uptake flux macroparameter, K_i , of the tracer is multiplied by the steady-state concentration of the tracee to obtain an estimate for the overall uptake flux of the tracee. For example, in the case of [^{18}F]FDG multiplication of K_i by the plasma concentration of glucose (technically the plasma glucose concentration divided by the lumped constant) gives the net glucose accumulation rate in normal tissue [19, 20, 167], under the assumption that the body's glucose concentration is in steady state. Since [^{18}F]ML-10 has no tracee, it is difficult to interpret the physiologic meaning of K_i as a measure of [^{18}F]ML-10 uptake.

Voxelwise maps of V_T and K_i for [^{18}F]ML-10 were evaluated in with the goal of identifying heterogeneity in GBM response to therapy. While tumor functional heterogeneity has important implications, the ability to measure heterogeneity is limited by the resolution of PET. We note that there are a number of methods of resolution compensation that have been developed [76]. Many of these require a priori assumptions of tracer distribution in the brain or body. For example, in one popular procedure, the geometric transfer matrix method, it is assumed that the brain can be divided into regions of uniform uptake [79]. However, such an assumption is unwarranted for tumor imaging and would also mask heterogeneity.

Other methods do not require a priori knowledge. The most important of these are the point spread function recovery reconstruction methods being developed by PET scanner manufacturers [80]. In this method, painstaking measurements of the scanner point spread function, which varies as a function of position in the scanner, are made by the manufacturer and

incorporated directly into the reconstruction. However, this method has not been well evaluated for our purposes and was not available on the HR+ scanner used for this work.

Additionally, a more general study limitation is that of interpreting a change in GBM apoptosis rate in the context of overall tumor status. For example, a relative increase in apoptosis may or may not be indicative of effective therapy depending on the relative growth rate of the tumor. Regardless of tumor growth rate though, an increase in tumor [^{18}F]ML-10 uptake would likely be observed. In this sense apoptosis imaging as a stand-alone method may be limited to identifying GBM patients that are refractory to a particular anti-cancer therapy (i.e. cases where no increase in apoptosis is observed between BL and post therapy time-points) rather than identifying patients likely to exhibit a positive therapy response.

Finally, the initial study design aimed to image GBM subjects receiving the same treatment regimen at a fixed number of days post-therapy initiation. However, due to clinical realities we could not always be uniform about the therapy each subject received or the number of days between pre-therapy (baseline) and post-therapy administration (early therapy assessment or follow-up assessment) [^{18}F]ML-10 PET time-points. Though, all subjects were on continuous therapy which may mitigate the impact of differences in image timing between subjects on study response assessment results.

5.2.7 [^{18}F]ML-10 Pharmacokinetic Modeling Conclusions

[^{18}F]ML-10 demonstrates comparatively low tracer uptake in healthy brain tissue resulting in good contrast between tumor and healthy brain tissue signal. In tumor, [^{18}F]ML-10 exhibits

overall poor transport rate from blood pool into tumor tissue. A large range in fractional contribution of blood component (V_B) to tumor signal was observed across subjects. In some cases, the combination of a low K_1 with high tumor vascularity (i.e. high V_B) caused the tumor blood concentration signal to be the only detectable signal component in the tumor.

The distribution of selected tumor impulse response function models across subjects and, in some cases, within the same subject but across imaging time-points makes it difficult to quantify uptake across subjects with a unique macroparameter (e.g. V_T or K_i). However, the 2α - 1β IRF model (consistent with a 2T-3K compartment model) generally provided satisfactory fits to measured tumor TACs (based on parameter uncertainty and model sensitivity) for which the selected best IRF model was not a 1α - 1β or 1α -10 IRF model. A detailed investigation of both reversible and irreversible 2-tissue compartment rate constants revealed a wide range in values of the ratio of V_S/V_T ([0.3093, 0.7997]) and the ratio K_i/K_1 ([0.0142, 0.2873]).

The uptake measures V_T , K_i , and K_i/K_1 were evaluated for their utility in early therapy response assessment for a limited number of GBM subjects using PFS and OS as outcome measures. Of the three uptake measures evaluated, percent change in K_i/K_1 between the BL and ETA time-points showed promise as a predictor of GBM response to therapy in the sense that subjects with a PFS > 11 months showed an increase in K_i/K_1 . In an analysis of 2 subjects, relative differences in K_i values between the 2 subjects were consistent with comparative increase in tumor density evaluated on diffusion weighted MRI. Taken together, these findings suggest that an [^{18}F]ML-10 uptake measure proportional to K_i (either K_i/K_1 or K_i itself) may have utility in predicting early therapy response of GBM.

6.0 FUTURE DIRECTIONS

The ability to probe apoptosis by *in vivo* imaging would allow access to a key cellular function and, thereby, would offer a direct and potentially rapid measure of the efficacy of many types of cancer therapy. However, several challenges related to interpretation and quantification must be overcome before this technology can be utilized in the clinic. For example, the optimal time to image therapy induced cell death must be determined. Additional questions linger with regard to the establishment of appropriate quantitative methodology for response assessment as well as are whether a measure of the total amount of tumor apoptosis post-therapy initiation alone can provide enough information with respect to tumor status to support reliable therapy response prediction.

6.1 OPTIMAL IMAGE TIMING

Arguably, the single biggest impediment establishing robust and reliable quantitative response assessment methodology using apoptosis as a biomarker [201], assuming appropriate radio-compound biodistribution, is the difficulty of determining the optimal time to image post-therapy initiation, and is a fundamental step for timing of larger therapy-response clinical efficacy trials. Initial in human therapy response assessment imaging protocols using radio-labeled

Annexin-V were based on the observation that the peak 2-3 days post- single dose of FasL ligand and or in treated rodent xenograft models [202, 203]. Though, this phenomenon of observing a time of maximum apoptosis radiotracer uptake has been described in other pre-clinical studies using [^{18}F]ML-10 as well [122]. However, the degree to which the results from these pre-clinical studies translate to de novo in human neoplasms being treated with clinical doses of chemotherapy or concomitant chemotherapy and radiation or radiation alone, often over a period of several days to weeks, has yet to be demonstrated. Moreover, it's not obvious that in these cases only a single 'spike' in apoptosis should be expected.

From a practical standpoint the possibility of an optimal time or optimal window of time to assess response to therapy raises several questions [202]. For example, is the optimal imaging period cancer type dependent, therapy dependent or both? Given a particular cancer type and therapy regimen, is the optimal imaging time consistent between patients, or is this time patient specific? What happens if a patient is scanned at a sub-optimal time due to, for example, a scheduling issue in the clinic? Will their imaging results still be useful?

In order to answer some of these questions, some authors have suggested attaching a radio-label with a long physical half-life (eg. $^{99\text{m}}\text{Tc}$, ^{111}In) to apoptosis radiotracers, which, assuming appropriate uptake kinetics and biodistribution properties, may allow for repeated imaging following a single injection of radiotracer [92]. This approach may be particularly useful if included as part of a stereotactic radiosurgery (SRS) treatment protocol, as patients receiving SRS for primary or secondary brain tumors often receive only a single large "impulse" of radiation specifically targeted to the tumor. As a result, an SRS therapy trial may provide an opportunity to

determine the profile of tumor apoptosis (for which it would be reasonable to expect a single peak apoptosis rate) as a function of time by serially measuring changes in apoptosis after treatment administration.

6.2 STRATEGIES FOR NORMALIZATION OF MEASURES OF OVERALL APOPTOSIS

The primary mode of action of many cancer therapies is the induction of apoptosis. Quantifying the change in tumor apoptosis rate during therapy would therefore provide a direct measure of therapy effect, and as such, is crucial for a complete understanding of patient status and therapy efficacy. However, it may prove difficult to interpret response to therapy based on an absolute increase or decrease in apoptosis signal without knowledge of additional biomarkers of tumor status such as proliferation rate and tumor density.

In the context of neuroimaging, one way to form an image-based "apoptotic index" may be to normalize measures of overall apoptosis with other, complementary, biomarkers related to tumor density and oncologic status. For example, overall sodium concentration has been shown to be elevated in tumors compared healthy tissue due to membrane depolarization during mitosis and/or changes in cell morphology [204-206]. As a result, sodium MRI may be able to provide a measure of proliferative and/or cell volume fraction that occur in tumors and normal tissues after anticancer treatment complementary to that of apoptosis imaging. Additional biomarkers for normalization may be measured using magnetic resonance spectroscopic imaging (MRSI). For example, measures of choline (Ch, increased cellularity and membrane synthesis/turnover)

concentration, as well as the ratios of Ch/N-Acetyl Aspartate (NAA, synthesized only in neurons) and Choline/Creatine (Cr, metabolites in bioenergetic pathways[207]) have all been used extensively in the detection, grading, surgical planning, and predicting outcome in patients with brain tumors [208-211]. While the use of these biomarkers of tumor status for normalization of measures of therapy induced apoptosis would need to be explored and validated, the development of a fully integrated hybrid PET/MR system (mMR Biograph, Siemens) may make this approach clinically feasible for PET radio-pharmaceuticals.

6.3 FUTURE DIRECTIONS SPECIFIC TO [¹⁸F]ML-10 AND GBM

The results of this dissertation suggest that the 2α - 1β IRF model (consistent with a 2T-3K compartment model) can generally provide satisfactory fits to measured tumor TACs for which the selected best IRF model is not a 1α - 1β or 1α -10 IRF model. Moreover, results suggest that an [¹⁸F]ML-10 uptake measure proportional to K_i (either K_i/K_1 or K_i itself) may have utility in predicting early therapy response of GBM. However, both K_i and K_i/K_1 would need to be further validated as quantitative imaging biomarkers for tumor early therapy response. A component of this validation process would include pre-clinical studies to evaluate [¹⁸F]ML-10 kinetic properties in tumor tissue sections. For example, small animal studies could be used to provide additional evidence to decide between modeling [¹⁸F]ML-10 uptake kinetics as either irreversible or reversible in tumor tissue undergoing apoptosis as well as further elucidate appropriate compartmental model structure.

If one or both K_i and K_i/K_1 can be validated as a measure of treatment response, the next step would be to investigate simplified, clinically practical measures of [^{18}F]ML-10 uptake that correlate with K_i or K_i/K_1 . For example, one could investigate correlation between K_i (or K_i/K_1) and SUV or K_i and TBR and determine an optimal time post-injection when fractional change in SUV or TBR is maximally correlated with fractional change in K_i (or K_i/K_1). If, for example, it was found that SUV change was strongly correlated with change in K_i (or K_i/K_1) 30 min after [^{18}F]ML-10 injection, then a clinically practical GBM imaging protocol might be to acquire a 10 min [^{18}F]ML-10 PET scan initiating 25 min post radiotracer injection.

If a static measure of tracer uptake that correlates well with either K_i (or K_i/K_1) cannot be found, it may be possible to develop shortened imaging protocols that can be used to obtain estimates for K_i and K_1 . The feasibility of performing shortened imaging protocols has already been demonstrated using [^{18}F]FDG [212, 213]. Given our current data, it would be possible to compare estimates of K_i and K_i/K_1 obtained using only, for example, the first 0-15 min of the PET acquisition and compare fractional change in K_i (or K_i/K_1) estimated using the shortened protocol to fractional change in K_i (or K_i/K_1) using the entire acquired data-set. However, a practical hurdle to developing a shortened dynamic imaging protocol is that arterial blood sampling is not likely to become routine in the clinic; hence, approximating the radiotracer concentration in the plasma with the radiotracer concentration in the blood using an IBIF would have to be validated.

Analysis of K_i on a voxelwise level also showed promise as response measure. A future direction would be to investigate voxelwise change in K_i (or K_i/K_1) more closely. Incorporation of additional tumor status information from, for example, MRSI or diffusion weighted MRI would

likely be more feasible on a voxelwise level. In order to maintain clinical practicality, it is likely that a voxelwise approach to estimating K_i (or K_i/K_1) would have to be implemented using a direct reconstruction approach (i.e. an approach in which parameter maps of K_i or K_i/K_1 are generated as part of the image reconstruction) [33, 214, 215] in combination with using a shortened imaging protocol.

APPENDIX A

MATHEMATICAL DERIVATIONS

A.1 INPUT FUNCTION MODELS

In order to quantify the pharmacokinetics of a radiotracer within a tissue, knowledge of the input time-course is required. In this dissertation, the time-course of radioactivity concentration in the blood pool is sampled directly from each PET acquisition; referred to as an image-derived input function (IBIF). Therefore, each measured blood sample represents the average radioactivity concentration in the blood pool over the corresponding PET imaging time frame.

Let $\gamma(t)$ denote a candidate input function model. Then, the time-average radioactivity concentration over a particular time-interval $[t_i^s, t_i^e]$ is given by (Eqn. A.1.1), where t_i^s and t_i^e denote the start and end times of the i^{th} PET frame, respectively.

$$\langle \gamma(t) \rangle_i = \frac{1}{t_i^e - t_i^s} \int_{t_i^s}^{t_i^e} \gamma(t) dt \quad (\text{Eqn. A.1.1})$$

However, (Eqn. A.1.1) can be written in a more convenient form by re-writing (Eqn. A.1.1) in terms of (Eqn. A.1.2) to obtain (Eqn. A.1.3).

$$\mathbf{I}(\mathbf{t}) \triangleq \int_{-\infty}^{\mathbf{t}} \gamma(\mathbf{t}) d\mathbf{t} \quad (\text{Eqn. A.1.2})$$

$$\langle \gamma(\mathbf{t}) \rangle_i = \frac{1}{t_i^e - t_i^s} \int_{t_i^s}^{t_i^e} \gamma(\mathbf{t}) d\mathbf{t} = \frac{[I(t_i^e) - I(t_i^s)]}{t_i^e - t_i^s} \quad (\text{Eqn. A.1.3})$$

The approach used in (Eqn. A.1.3) to compute the time-average of an input function model will be used extensively in this appendix. Moreover, as (Eqn. A.1.3) is a general method for computing the time-average of a function over a time-interval, (Eqn. A.1.3) is also used throughout this appendix to compute the time-averages of various convolution integrals.

There are two general input model forms used throughout the main body of this dissertation: the Feng model and the generalized Feng model, which are contained in table 5-1 of *Section 5.1*. In table 5-1, these input model forms are called IBIF Model 1 and IBIF Model 2; however, for the purposes of this entire Appendix, these model forms will be referred to as the Feng Model and generalized Feng model, respectively. The following two subsections sections, *Section A.1.1* and *Section A.1.2*, derive the time-averaged versions of the Feng model (*Section A.1.1*) and the generalized Feng model (*Section A.1.2*), respectively.

A.1.1 Time-Averaged Feng Model

The goal of this section is to derive a time-averaged form of the Feng model that is appropriate for modeling a time-course of blood radioactivity concentration samples obtained from dynamic PET scanning. Moreover, the gradient of the time-averaged Feng model will be computed as will the time-average of the running integral of this model.

The Feng model presented in this dissertation is based on the input model (*Eqn. A. 1.4*) defined in Feng et al. [151], which was originally developed for the purpose of simulating ^{18}F -labeled fluorodeoxyglucose (^{18}F FDG) plasma concentration curves [151].

$$\mathbf{f}(t) = [(\mathbf{A}t - \mathbf{B} - \mathbf{C})e^{-p_1 t} + \mathbf{B}e^{-p_2 t} + \mathbf{C}e^{-p_3 t}]\mathbf{u}(t) \quad (\text{Eqn. A.1.4})$$

For the purposes of the analysis presented in this dissertation, the Feng model is expanded to allow for a variable number of first-order decaying exponentials as shown in (*Eq. A. 1.5*). In this dissertation, the "Feng model" refers to model defined by (*Eq. A. 1.5*), and can be shown to have Laplace transform given by (*Eqn. A. 1.6*).

$$\mathbf{f}(t) = [(\gamma_0 t - \sum_{i=2}^N \gamma_i) e^{-p_1 t} + \sum_{i=2}^N \gamma_i e^{-p_i t}]\mathbf{u}(t) \quad (\text{Eqn. A.1.5})$$

$$\hat{\mathbf{f}}(s) = \frac{\gamma_0}{(s+p_1)^2} + \frac{-\sum_{i=2}^N \gamma_i}{(s+p_1)} + \sum_{i=2}^N \frac{\gamma_i}{(s+p_i)} \quad (\text{Eqn. A.1.6})$$

As stated above, the blood radioactivity concentration samples used in this dissertation are obtained directly from the PET acquisition. Therefore, each blood concentration sample represents

the average radioactivity concentration in the blood pool over the corresponding imaging time interval. Hence, in order to account for the time averaging in the measure blood radioactivity concentration, the model fitted to the measure blood samples must also be time-averaged. To this end, following the procedure described by (Eqn. A.1.3) above, the running integral of (Eqn. A.1.6) can be written as (Eqn. A.1.7), which has Laplace representation given by (Eqn. A.1.8).

$$F(t) = \int_{-\infty}^t f(t) dt = f(t) \otimes u(t) \quad (\text{Eqn. A.1.7})$$

$$\widehat{F}(s) = \frac{1}{s} * \widehat{f}(s) \quad (\text{Eqn. A.1.8})$$

Inserting (Eqn. A.1.6) into (Eqn. A.1.8) gives (Eqn. A.1.9), which simplifies to (Eqn. A.1.10).

$$\widehat{F}(s) = \frac{1}{s} \left[\frac{\gamma_0}{(s+p_1)^2} + \frac{-\sum_{i=2}^N \gamma_i}{(s+p_1)} + \sum_{i=2}^N \frac{\gamma_i}{(s+p_i)} \right] \quad (\text{Eqn. A.1.9})$$

$$\widehat{F}(s) = \frac{\gamma_0}{s(s+p_1)^2} + \frac{-\sum_{i=2}^N \gamma_i}{s(s+p_1)} + \sum_{i=2}^N \frac{\gamma_i}{s(s+p_i)} \quad (\text{Eqn. A.1.10})$$

A form for (Eqn. A.1.5) useful for fitting to time-averaged data can then be obtained by performing a partial fraction expansion of (Eqn. A1.10) and implementing a transformation of variables defined in (Eqn. A.1.11) leading to (Eqn. A.1.12).

$$\begin{cases} \mathbf{b}_0 \triangleq -\frac{\gamma_0}{p_1} \\ \mathbf{b}_1 \triangleq \left(-\frac{\gamma_0}{p_1^2} + \frac{\sum_{i=2}^N \gamma_i}{p_1}\right) \\ \mathbf{b}_i \triangleq -\left(\frac{\gamma_i}{p_i}\right); \quad i = 2 \dots N \end{cases} \quad (\text{Eqn. A.1.11})$$

$$\widehat{\mathbf{F}}(s) = \frac{b_0}{(s+p_1)^2} + \frac{b_1}{(s+p_1)} + \sum_{i=2}^N \frac{b_i}{(s+p_i)} - \frac{[b_1 + \sum_{i=2}^N b_i]}{s} \quad (\text{Eqn. A.1.12})$$

However, from (Eqn. A.1.11), b_1 can be further simplified by writing it in terms of b_0 , b_i , and p_i . Specifically,

$$b_1 \triangleq \left(-\frac{\gamma_0}{p_1^2} + \frac{\sum_{i=2}^N \gamma_i}{p_1}\right)$$

$$\Leftrightarrow b_1 = \frac{b_0}{p_1} - \frac{\sum_{i=2}^N b_i p_i}{p_1} = \frac{b_0 - \sum_{i=2}^N b_i p_i}{p_1}$$

,which leads to

$$\boxed{\mathbf{b}_1 = \frac{b_0 - \sum_{i=2}^N b_i p_i}{p_1}} \quad (\text{Eqn. A.1.13})$$

Inserting the simplified expression for b_1 given by (Eqn. A.1.13) into (Eqn. A.1.12), and defining $b_{N+1} \triangleq -[b_1 + \sum_{i=2}^N b_i]$ leads to a further re-parameterization of (Eqn. A.1.12)

given by (Eqn. A.1.14) with coefficient definitions given by (Eqn. A.1.15). Thus the coefficients in (Eqn. A.1.15) relate the instantaneous representation of the input function to its running integral.

$$\widehat{F}(s) = \frac{b_0}{(s+p_1)^2} + \frac{b_1}{(s+p_1)} + \sum_{i=2}^N \frac{b_i}{(s+p_i)} + \frac{b_{N+1}}{s} \quad (\text{Eqn. A.1.14})$$

$$\left\{ \begin{array}{l} b_0 \triangleq -\frac{y_0}{p_1} \\ b_1 \triangleq \frac{b_0 - \sum_{i=2}^N b_i p_i}{p_1} \\ b_i \triangleq -\left(\frac{y_i}{p_i}\right); \quad i = 2 \dots N \\ b_{N+1} \triangleq -[b_1 + \sum_{i=2}^N b_i] \end{array} \right. \quad (\text{Eqn. A.1.15})$$

Taking the inverse Laplace transform of (Eqn. A.1.14) gives the time-domain representation for the running integral if the Feng input model (Eqn. A.1.16).

$$F(t) = [b_0 t e^{-p_1 t} + b_1 e^{-p_1 t} + \sum_{i=2}^N b_i e^{-p_i t} + b_{N+1}] u(t) \quad (\text{Eqn. A.1.16})$$

a. Calculating the Gradient of the Time-Averaged Feng Model

For the purposes of fitting the time-averaged Feng input model to the measured data, it is helpful to have an explicit expression for the gradient of (Eqn. A.1.16) with respect to the individual model parameters (including any time-delay parameter τ). (Eqn. A.1.17) gives the Laplace transform of (Eqn. A.1.16) with a time-delay, τ , included, while (Eqn. A.1.18)-thru-

(Eqn. A.1.23) give the partial derivatives of (Eqn. A.1.17) with respect to each model parameters in the Laplace domain.

$$\widehat{F}(s) = \left[\frac{b_0}{(s+p_1)^2} + \frac{b_1}{(s+p_1)} + \sum_{i=2}^N \frac{b_i}{(s+p_i)} + \frac{b_{N+1}}{s} \right] e^{-s\tau} \quad (\text{Eqn. A.1.17})$$

$$\frac{\partial \widehat{F}(s)}{\partial b_0} = \left[\frac{1}{(s+p_1)^2} + \frac{\frac{\partial b_1}{\partial b_0}}{(s+p_1)} + \frac{\frac{\partial b_{N+1}}{\partial b_0}}{s} \right] e^{-s\tau} \quad (\text{Eqn. A.1.18})$$

$$\frac{\partial \widehat{F}(s)}{\partial b_i} = \left[\frac{\frac{\partial b_1}{\partial b_i}}{(s+p_1)} + \frac{1}{(s+p_i)} + \frac{\frac{\partial b_{N+1}}{\partial b_i}}{s} \right] e^{-s\tau} \quad (\text{Eqn. A.1.19})$$

$$\frac{\partial \widehat{F}(s)}{\partial p_1} = \left[\frac{-2b_0}{(s+p_1)^3} - \frac{b_1}{(s+p_1)^2} + \frac{\frac{\partial b_1}{\partial p_1}}{(s+p_1)} + \frac{\frac{\partial b_{N+1}}{\partial p_1}}{s} \right] e^{-s\tau} \quad (\text{Eqn. A.1.20})$$

$$\frac{\partial \widehat{F}(s)}{\partial p_i} = \left[\frac{\frac{\partial b_1}{\partial p_i}}{(s+p_1)} - \frac{b_i}{(s+p_i)^2} + \frac{\frac{\partial b_{N+1}}{\partial p_i}}{s} \right] e^{-s\tau} \quad (\text{Eqn. A.1.21})$$

$$\frac{\delta \widehat{F}(s)}{\delta \tau} = - \left[\frac{b_0 s}{(s+p_1)^2} + \frac{b_1 s}{(s+p_1)} + \sum_{i=2}^N \frac{b_i s}{(s+p_i)} + b_{N+1} \right] e^{-s\tau} \quad (\text{Eqn. A.1.22})$$

$$\left\{ \begin{array}{l} \frac{\partial b_1}{\partial b_0} = \frac{1}{p_1}; \\ \frac{\partial b_1}{\partial b_i} = -\left(\frac{p_i}{p_1}\right); \quad i = 2, \dots, N \\ \frac{\partial b_1}{\partial p_1} = -\left(\frac{b_1}{p_1}\right); \\ \frac{\partial b_1}{\partial p_i} = -\left(\frac{b_i}{p_1}\right); \quad i = 2, \dots, N \\ \frac{\partial b_{N+1}}{\partial b_0} = -\left(\frac{1}{p_1}\right) \\ \frac{\partial b_{N+1}}{\partial b_i} = \left(\frac{p_i}{p_1} - 1\right); \quad i = 2, \dots, N \\ \frac{\partial b_{N+1}}{\partial p_1} = \frac{b_1}{p_1} \\ \frac{\partial b_{N+1}}{\partial p_i} = \frac{b_i}{p_1}; \quad i = 2, \dots, N \end{array} \right. \quad (\text{Eqn. A.1.23})$$

The partial derivatives in (Eqn. A.1.18)-thru-(Eqn. A.1.23) can be transformed to the time domain, (Eqn. A.1.25)-thru-(Eqn. A.1.29), to give partial derivatives of the running integral of the delayed generalized Feng model (Eqn. A.1.24).

$$F(t) = [b_0 t e^{-p_1 t} u(t) + b_1 e^{-p_1 t} u(t) + \sum_{i=2}^N b_i e^{-p_i t} u(t) + b_{N+1} u(t)] \otimes \delta(t - \tau) \quad (\text{Eqn. A.1.24})$$

$$\frac{\partial F}{\partial b_0} = [t e^{-p_1 t} u(t) + \left(\frac{1}{p_1}\right) e^{-p_1 t} u(t) - \left(\frac{1}{p_1}\right) u(t)] \otimes \delta(t - \tau) \quad (\text{Eqn. A.1.25})$$

$$\frac{\partial F}{\partial b_i} = \left[\left(-\frac{p_i}{p_1}\right) e^{-p_1 t} u(t) + e^{-p_i t} u(t) + \left(\frac{p_i}{p_1} - 1\right) u(t) \right] \otimes \delta(t - \tau); \quad i = 2, \dots, N \quad (\text{Eqn. A.1.26})$$

$$\frac{\partial F}{\partial p_1} = \left[-b_0 t^2 e^{-p_1 t} u(t) - b_1 t e^{-p_1 t} u(t) - \left(\frac{b_1}{p_1}\right) e^{-p_1 t} u(t) + \left(\frac{b_1}{p_1}\right) u(t) \right] \otimes \delta(t - \tau) \quad (\text{Eqn. A.1.27})$$

$$\frac{\partial F}{\partial p_i} = \left[-\left(\frac{b_i}{p_1}\right) e^{-p_1 t} u(t) - b_i t e^{-p_i t} u(t) + \left(\frac{b_i}{p_1}\right) u(t) \right] \otimes \delta(t - \tau); \quad i = 2, \dots, N \quad (\text{Eqn. A.1.28})$$

$$\frac{\partial F}{\partial \tau} = [\mathbf{b}_0 \mathbf{p}_1 t e^{-p_1 t} - (\mathbf{b}_0 - \mathbf{b}_1 \mathbf{p}_1) e^{-p_1 t} + \sum_{i=2}^N \mathbf{b}_i \mathbf{p}_i e^{-p_i t}] \otimes \delta(t - \tau) \quad (\text{Eqn. A.1.29})$$

Therefore, equations (Eqn. A.1.25)-thru-(Eqn. A.1.29) along with (Eqn. A.1.23) specify the gradient of the running integral of the input function (Eqn. A.1.24) with respect to the column vector of parameters $\theta = [b_0, b_2, \dots, b_N, p_1, p_2, \dots, p_N, \tau]^T$. That is, in vector form the gradient of (Eqn. A.1.24) at any time t is given by equation (Eqn. A.1.30).

$$\nabla_{\theta} \mathbf{F}(\mathbf{t}) = \left[\frac{\partial \mathbf{F}(\mathbf{t})}{\partial b_0}, \frac{\partial \mathbf{F}(\mathbf{t})}{\partial b_2}, \dots, \frac{\partial \mathbf{F}(\mathbf{t})}{\partial b_N}, \frac{\partial \mathbf{F}(\mathbf{t})}{\partial p_1}, \frac{\partial \mathbf{F}(\mathbf{t})}{\partial p_2}, \dots, \frac{\partial \mathbf{F}(\mathbf{t})}{\partial p_N}, \frac{\partial \mathbf{F}(\mathbf{t})}{\partial \tau} \right]^T \quad (\text{Eqn. A.1.30})$$

Therefore, in order to fit the Feng input model to a column vector of blood concentration samples, Y , measured directly from a set of M total PET frames, the least-squares minimization procedure can be written as:

$$\min_{\theta} \|Y - I\|^2$$

where $I = [I_1, I_2, \dots, I_M]^T$ is a column vector of time-averaged model activities for each PET frame, such that $I_i \triangleq \frac{[F(t_i^e) - F(t_i^s)]}{t_i^e - t_i^s} \quad \forall i = 1 \dots M$. Moreover, the $(M \times 2N)$ matrix of partial derivatives of the time-averaged input function model as a function of time (i.e. the sensitivity matrix, S) can be constructed from (Eqn. A.1.30) using the linearity of the derivative operation, and is given by (Eqn. A.1.31).

$$\mathbf{S} = \begin{pmatrix} \frac{[\nabla_{\theta} \mathbf{F}(t_1^e)]^T}{(t_1^e - t_1^s)} \\ \frac{[\nabla_{\theta} \mathbf{F}(t_2^e)]^T}{(t_2^e - t_2^s)} \\ \vdots \\ \frac{[\nabla_{\theta} \mathbf{F}(t_M^e)]^T}{(t_M^e - t_M^s)} \end{pmatrix} - \begin{pmatrix} \frac{[\nabla_{\theta} \mathbf{F}(t_1^s)]^T}{(t_1^e - t_1^s)} \\ \frac{[\nabla_{\theta} \mathbf{F}(t_2^s)]^T}{(t_2^e - t_2^s)} \\ \vdots \\ \frac{[\nabla_{\theta} \mathbf{F}(t_M^s)]^T}{(t_M^e - t_M^s)} \end{pmatrix} \quad (\text{Eqn. A.1.31})$$

b. Calculating the Time-Average of the Running Integral the Feng Model

For some spectral analysis implementations, it is required to have knowledge of the running integral of the input blood activity concentration. For the Feng model, (Eqn. A. 1.6), this means being able to compute the integral $\int_{-\infty}^t f(\omega) d\omega$ at arbitrary times, where $f(\omega)$ denotes the Feng model. However, in this dissertation, all blood radioactivity samples are obtained directly from the PET image, and, as such, correspond to the average radioactivity concentration in the blood over the corresponding dynamic PET frame length. Thus, in order to produce a running-integral basis vector for spectral analysis, a time-averaged version of the integral $\int_{-\infty}^t f(\omega) d\omega$ is required.

The process for computing a time-averaged version of $\int_{-\infty}^t f(\omega) d\omega$ will be carried out using the approach described by (Eqn. A. 1.3) above. To this end let $F(t) \triangleq \int_{-\infty}^t f(\omega) d\omega$, then the time-average of $F(t)$ over the i^{th} PET frame, with respective start and stop times t_i^s and t_i^e , can be obtained by calculating the normalized difference: $\frac{1}{(t_i^e - t_i^s)} \left[\int_{-\infty}^{t_i^e} F(t) dt - \int_{-\infty}^{t_i^s} F(t) dt \right]$.

For clarity in derivation let $K(t) \triangleq \int_{-\infty}^t F(z)dz$, such that $K(t) = F(t) \otimes u(t)$, which has Laplace transform given by: $\widehat{K}(s) = s^{-1}\widehat{F}(s)$. Inserting (Eqn. A.1.17) in for $\widehat{F}(s)$ gives (Eqn. A.1.32).

$$\widehat{K}(s) = \frac{1}{s} \left[\frac{b_0}{(s+p_1)^2} + \frac{b_1}{(s+p_1)} + \sum_{i=2}^N \frac{b_i}{(s+p_i)} + \frac{b_{N+1}}{s} \right] e^{-s\tau} \quad (\text{Eqn. A.1.32})$$

After partial fraction expansion and re-grouping of terms, (Eqn. A.1.33) is obtained from (Eqn. A.1.32). Transformation of (Eqn. A.1.33) to the time-domain then produces (Eqn. A.1.34).

$$\widehat{K}(s) = \left\{ \left[\frac{-b_0}{p_1} \right] \frac{1}{(s+p_1)^2} + \left[\frac{-b_0}{p_1^2} + \frac{-b_1}{p_1} \right] \frac{1}{(s+p_1)} + \sum_{i=2}^N \frac{-\left(\frac{b_i}{p_i}\right)}{(s+p_i)} + \left[\frac{b_0}{p_1^2} + \frac{b_1}{p_1} + \sum_{i=2}^N \left(\frac{b_i}{p_i}\right) \right] \frac{1}{s} + \frac{b_{N+1}}{s^2} \right\} e^{-s\tau} \quad (\text{Eqn. A.1.33})$$

$$K(t) = \left\{ \left[\frac{-b_0}{p_1} \right] t e^{-p_1 t} \mathbf{u}(t) + \left[\frac{-b_0}{p_1^2} + \frac{-b_1}{p_1} \right] e^{-p_1 t} \mathbf{u}(t) + \sum_{i=2}^N -\left(\frac{b_i}{p_i}\right) e^{-p_i t} \mathbf{u}(t) + \left[\frac{b_0}{p_1^2} + \frac{b_1}{p_1} + \sum_{i=2}^N \left(\frac{b_i}{p_i}\right) \right] \mathbf{u}(t) + b_{N+1} t \mathbf{u}(t) \right\} \otimes \delta(t - \tau) \quad (\text{Eqn. A.1.34})$$

Therefore, the time-averaged running integral of the Feng model over the i^{th} PET frame can be computed using (Eqn. A1.34) following the equation: $\frac{1}{(t_i^e - t_i^s)} [K(t_i^e) - K(t_i^s)]$.

A.1.2 Time-Averaged Generalized Feng Model

The form of the instantaneous generalized Feng model is given by (Eqn. A.1.35). Since the actual blood radioactivity concentration samples are obtained from a PET image, a time-averaged form of (Eqn. A.1.35) is required for data fitting.

$$\begin{aligned} \mathbf{g}(\mathbf{t}) = & \left[(\gamma_0 \mathbf{t} - \sum_{i=2}^N \gamma_i) e^{-p_1 \mathbf{t}} + \sum_{i=2}^N \gamma_i e^{-p_i \mathbf{t}} \right] \mathbf{u}(\mathbf{t}) + \\ & + r_0 (\mathbf{t} - \tau_{dblPk}) e^{-r_1 (\mathbf{t} - \tau_{dblPk})} \mathbf{u}(\mathbf{t} - \tau_{dblPk}) \end{aligned} \quad (\text{Eqn. A.1.35})$$

The approach followed for deducing the time-averaged form of (Eqn. A.1.35) is equivalent to that followed in obtaining the time-averaged form of the Feng model in the previous section (Appendix A.1.1). That is, by defining $G(t)$ such that $G(t) \triangleq \int_{-\infty}^t g(\omega) d\omega$, then the time-averaged uptake during the i^{th} PET acquisition frame is given by: $\frac{[G(t_i^e) - G(t_i^s)]}{(t_i^e - t_i^s)}$. In order to simplify the calculation of $G(t)$, define $f(t)$ such that: $f(t) \triangleq [(\gamma_0 t - \sum_{i=2}^N \gamma_i) e^{-p_1 t} + \sum_{i=2}^N \gamma_i e^{-p_i t}] u(t)$; that is $f(t)$ represents the Feng model defined in (Eqn. A.1.5) of Appendix A.1.1. Therefore, for the generalized Feng model, $G(t)$ takes the form in (Eqn. A.1.36).

$$\mathbf{G}(\mathbf{t}) = \int_{-\infty}^{\mathbf{t}} [\mathbf{f}(\boldsymbol{\omega}) + r_0 (\boldsymbol{\omega} - \tau_{dblPk}) e^{-r_1 (\boldsymbol{\omega} - \tau_{dblPk})} \mathbf{u}(\boldsymbol{\omega} - \tau_{dblPk})] d\boldsymbol{\omega} \quad (\text{Eqn. A.1.36})$$

The running integral of the Feng model (ie. $F(t) = \int_{-\infty}^t f(\omega) d\omega$) was calculated in Appendix A.1.1 and is given by (Eqn. A.1.14). Therefore, (Eqn. A.1.36) can be re-written as (Eqn. A.1.37).

$$\mathbf{G}(t) = \mathbf{F}(t) + \int_{-\infty}^t [\mathbf{r}_0(\omega - \tau_{dblPk})e^{-r_1(\omega - \tau_{dblPk})}\mathbf{u}(\omega - \tau_{dblPk})]d\omega \quad (\text{Eqn. A.1.37})$$

Thus, for the purposes of calculating $G(t)$, I will focus on a time-averaged parameterization of only the component originating from the added second-order pole [i.e. the second term on the right hand side of (Eqn. A.1.37)]. To this end define $M(t) \triangleq \int_{-\infty}^t [r_0(\omega - \tau_{dblPk})e^{-r_1(\omega - \tau_{dblPk})}\mathbf{u}(\omega - \tau_{dblPk})]d\omega$, which can be written in terms of convolution as in (Eqn. A.1.38) below. The Laplace transform of (Eqn. A.1.38) is given by (Eqn. A.1.39).

$$\mathbf{M}(t) = [\mathbf{r}_0 t e^{-r_1 t} \mathbf{u}(t)] \otimes \mathbf{u}(t) \otimes \delta(t - \tau_{dblPk}) \quad (\text{Eqn. A.1.38})$$

$$\widehat{\mathbf{M}}(s) = \left[\left(\frac{r_0}{r_1} \right) \frac{1}{(s+r_1)^2} + \frac{r_0}{r_1^2} \frac{1}{(s+r_1)} + \frac{r_0}{r_1^2} \frac{1}{s} \right] e^{-s\tau_{dblPk}} \quad (\text{Eqn. A.1.39})$$

An appropriate form of $\widehat{\mathbf{M}}(s)$ to be used for curve fitting of time-averaged data can be obtained by defining $a_0 \triangleq -\left(\frac{r_0}{r_1^2}\right)$, such that $\widehat{\mathbf{M}}(s)$ has the form:

$$\widehat{\mathbf{M}}(s) = \left[\frac{r_1 a_0}{(s+r_1)^2} + \frac{a_0}{(s+r_1)} - \frac{a_0}{s} \right] e^{-s\tau_{dblPk}}, \quad (\text{Eqn. A.1.40})$$

which has time domain representation given by (Eqn. A.1.41) below.

$$\mathbf{M}(t) = [\mathbf{r}_1 \mathbf{a}_0 t e^{-r_1 t} + \mathbf{a}_0 e^{-r_1 t} - \mathbf{a}_0 \mathbf{u}(t)] \otimes \delta(t - \tau_{dblPk}) \quad (\text{Eqn. A.1.41})$$

Therefore, for the purposes of fitting the time-averaged generalized Feng model, (Eqn. A.1.37) can be written as (Eqn. A.1.42), where $F(t)$ is given by (Eqn. A.1.14) and $M(t)$ is given by (Eqn. A.1.41).

$$\mathbf{G}(t) = \mathbf{F}(t) + \mathbf{M}(t) \quad (\text{Eqn. A.1.42})$$

a. Calculating the Gradient of the Time-Averaged Generalized Feng Model

For the purposes of speeding up model fitting as well as estimating the input model parameter covariance matrix, it is useful to calculate the gradient of (Eqn. A.1.41) with respect to each of the model parameters. Moreover, as (Eqn. A.1.41) will be combined with the Feng model, which itself is allowed an overall time delay term, denoted τ_{bd} , it is also useful to calculate the partial derivative of (Eqn. A.1.41) with respect to this overall 'bulk delay' term. Allowing for the overall time delay τ_{bd} , (Eqn. A.1.41) becomes (Eqn. A.1.43), which has partial derivatives given by (Eqn. A.1.44).

$$\mathbf{M}(t) = [\mathbf{r}_1 \mathbf{a}_0 t e^{-r_1 t} + \mathbf{a}_0 e^{-r_1 t} - \mathbf{a}_0 \mathbf{u}(t)] \otimes \delta(t - [\tau_{bd} + \tau_{dblPk}]) \quad (\text{Eqn. A.1.43})$$

$$\begin{cases}
\frac{\delta M(t)}{\delta a_0} = [\mathbf{r}_1 \mathbf{t} e^{-r_1 \mathbf{t}} \mathbf{u}(t) + \mathbf{e}^{-r_1 \mathbf{t}} \mathbf{u}(t) - \mathbf{u}(t)] \otimes \delta(\mathbf{t} - [\tau_{bd} + \tau_{dblPk}]) \\
\frac{\delta M(t)}{\delta r_1} = [-\mathbf{a}_0 \mathbf{r}_1 \mathbf{t}^2 \mathbf{e}^{-r_1 \mathbf{t}} \mathbf{u}(t)] \otimes \delta(\mathbf{t} - [\tau_{bd} + \tau_{dblPk}]) \\
\frac{\delta M(t)}{\delta \tau_{dblPk}} = \{\mathbf{a}_0 \mathbf{r}_1^2 \mathbf{t} \mathbf{e}^{-r_1 \mathbf{t}} \mathbf{u}(t)\} \otimes \delta(\mathbf{t} - [\tau_{bd} + \tau_{dblPk}]) \\
\frac{\delta M(t)}{\delta \tau_{bd}} = \{\mathbf{a}_0 \mathbf{r}_1^2 \mathbf{t} \mathbf{e}^{-r_1 \mathbf{t}} \mathbf{u}(t)\} \otimes \delta(\mathbf{t} - [\tau_{bd} + \tau_{dblPk}])
\end{cases} \quad (\text{Eqn. A.1.44})$$

b. Calculating the Time-Average of the Running Integral of the Generalized Feng Model

For some spectral analysis implementations, it is required to have knowledge of the running integral of the input blood activity concentration. For the generalized Feng model, (Eqn. A.1.35), this means being able to compute the integral $\int_{-\infty}^t g(\omega) d\omega$ at arbitrary times, where $g(\omega)$ denotes the generalized Feng model. However, in this dissertation, all blood radioactivity samples are obtained directly from the PET image, and, as such, correspond to the average radioactivity concentration in the blood over the corresponding dynamic PET frame length. Thus, in order to produce a running-integral basis vector for spectral analysis, a time-averaged version of the integral $\int_{-\infty}^t g(\omega) d\omega$ is required.

The process for computing a time-averaged version of $\int_{-\infty}^t g(\omega) d\omega$ will be carried out using the approach described by (Eqn. A.1.3) above. To this end let $G(t) \triangleq \int_{-\infty}^t g(\omega) d\omega$, then the time-average of $G(t)$ over the i^{th} PET frame, with respective start and stop times denoted by

t_i^s and t_i^e , can be obtained by calculating the normalized difference: $\frac{1}{(t_i^e - t_i^s)} \left[\int_{-\infty}^{t_i^e} G(t) dt - \int_{-\infty}^{t_i^s} G(t) dt \right]$.

For clarity in derivation let $H(t) \triangleq \int_{-\infty}^t G(z) dz$, such that $H(t) = G(t) \otimes u(t)$, which has Laplace transform given by: $\widehat{H}(s) = s^{-1} \widehat{G}(s)$. Recall from *Appendix A.1.2* that $G(t)$ can be written as $G(t) = F(t) + M(t)$, where $F(t)$ denotes the running integral of the Feng model, (*Eqn. A.1.14*), and $M(t)$ denotes the running integral of a second-order pole (*Eqn. A.1.41*). Therefore, the Laplace transform of $G(t)$ is given by $\widehat{G}(s) = \widehat{F}(s) + \widehat{M}(s)$. Hence $\widehat{H}(s) = s^{-1} \widehat{G}(s)$, can be written as (*Eqn. A.1.45*).

$$\widehat{H}(s) = \frac{\widehat{F}(s)}{s} + \frac{\widehat{M}(s)}{s} \quad (\text{Eqn. A.1.45})$$

However, the first term on the right-hand side of (*Eqn. A.1.45*) was evaluated in *Appendix A.1.1* and is given by (*Eqn. A.1.33*). Thus, for the purposes of the current subsection, I will focus only on the second-term on the right-hand side of (*Eqn. A.1.45*). Specifically, let $\widehat{W}(s) \triangleq s^{-1} \widehat{M}(s)$ to give (*Eqn. A.1.46*).

$$\widehat{W}(s) = \frac{1}{s} \left[\frac{r_1 a_0}{(s+r_1)^2} + \frac{a_0}{(s+r_1)} - \frac{a_0}{s} \right] e^{-s[\tau_{bd} + \tau_{dblPk}]} \quad (\text{Eqn. A.1.46})$$

After partial fraction expansion and re-grouping of terms, (Eqn. A. 1.47) is obtained from (Eqn. A1.46). Transformation of (Eqn. A1.47) to the time-domain then produces (Eqn. A. 1.48).

$$\widehat{W}(s) = \left\{ \frac{-a_0}{(s+r_1)^2} - \left[\frac{2a_0}{r_1} \right] \frac{1}{(s+r_1)} + \left[\frac{2a_0}{r_1} \right] \frac{1}{s} - \frac{a_0}{s^2} \right\} e^{-s[\tau_{bd} + \tau_{dblPk}]} \quad (\text{Eqn. A.1.47})$$

$$W(t) = \left\{ -a_0 t e^{-p_1 t} u(t) - \frac{2a_0}{r_1} e^{-p_1 t} u(t) + \frac{2a_0}{r_1} u(t) - a_0 t u(t) \right\} \otimes \delta(t - [\tau_{bd} + \tau_{dblPk}]) \quad (\text{Eqn. A.1.48})$$

From here, the time-averaged running integral of the generalized Feng model can be obtained by forming $H(t) = K(t) + W(t)$ and computing the required differences as in (Eqn. A. 1.3). Note that $K(t)$ is as defined in (Eqn. A. 1.34).

A.2 SPECTRAL ANALYSIS USING THE FENG MODEL CUMULATIVE INPUT FUNCTION

The spectral analysis (SA) method requires the user to pre-define a dictionary of potential spectral components that could compose a measured tissue response signal. Generally, each component vector is equal to the convolution of the input function model with a single-order pole with unit amplitude. This section shows explicitly the derivation of the general formula used to compute the spectral component vectors for the spectral analysis dictionary used throughout this

dissertation. The presented derivation takes advantage of the fact that the integral of a convolution is the convolution between the integral of one function and the remaining original function [152].

Specifically, consider a spectral rate β corresponding the causal spectral component $e^{-\beta t}u(t)$. Then the convolution of this spectral component with a general input function, $\gamma(t)$, is given by (Eqn. A.2.1).

$$\mathbf{g}(t) = [e^{-\beta t}u(t)] \otimes \gamma(t) \quad (\text{Eqn. A.2.1})$$

However, each tissue concentration sample measured from a particular PET dynamic frame represents the time-average of the instantaneous activity in the tissue over the duration of that frame. That is for the i^{th} PET frame with start and stop times t_i^s and t_i^e , respectively, what is actually measured is (Eqn. A.2.2).

$$\frac{1}{(t_i^e - t_i^s)} \int_{t_i^s}^{t_i^e} \mathbf{g}(t) dt = \frac{1}{(t_i^e - t_i^s)} \int_{t_i^s}^{t_i^e} ([e^{-\beta t}u(t)] \otimes \gamma(t)) dt \quad (\text{Eqn. A.2.2})$$

However, (Eqn. A.2.2) can be re-written in a form that is more consistent with the data collected by defining (Eqn. A.2.3):

$$\mathbf{G}(t) = [e^{-\beta t}u(t)] \otimes \left[\int_{-\infty}^t \gamma(\tau) d\tau \right] \quad (\text{Eqn. A.2.3})$$

such that,

$$\frac{1}{(t_i^e - t_i^s)} \int_{t_i^s}^{t_i^e} \mathbf{g}(t) dt = \frac{[G(t_i^e) - G(t_i^s)]}{(t_i^e - t_i^s)} \quad (\text{Eqn. A.2.4})$$

Thus, the time-dependence for each spectral component of the SA dictionary (in the case of time-averaged radioactivity concentration samples) can be calculated easily via (Eqn. A.2.4).

The following two subsections sections, *Section A.2.1* and *Section A.2.2*, derive the function $G(t)$ referred to in (Eqn. A.2.4) for the Feng Model (*Section A.2.1*) and the generalized Feng model (*Section A.2.2*), respectively.

A.2.1 Spectral Analysis using the Time-Averaged Feng Model

For the specific case that the input function model is the Feng input model, (Eqn. A.1.5), the running integral of the input function is given by (Eqn. A.1.16) in *Appendix Section A1.1*, but is repeated below as (Eqn. A.2.5) with an overall bulk time delay, τ_{bd} , included.

$$\mathbf{F}(t) = [\mathbf{b}_0 t e^{-p_1 t} \mathbf{u}(t) + \mathbf{b}_1 e^{-p_1 t} \mathbf{u}(t) + \sum_{i=2}^N \mathbf{b}_i e^{-p_i t} \mathbf{u}(t) + \mathbf{b}_{N+1} \mathbf{u}(t)] \otimes \delta(t - \tau_{bd}) \quad (\text{Eqn. A.2.5})$$

Inserting (Eqn. A.2.5) into (Eqn. A.2.3) gives (Eqn. A.2.6).

$$\mathbf{G}(t) = [e^{-\beta t} \mathbf{u}(t)] \otimes \mathbf{F}(t) \quad (\text{Eqn. A.2.6})$$

The Laplace transform of (Eqn. A.2.5) was calculated in the previous section and was given by (Eqn. A.1.14), but is repeated here as (Eqn. A.2.7) with a delay term τ_{bd} .

$$\widehat{F}(s) = \left[\frac{b_0}{(s+p_1)^2} + \frac{b_1}{(s+p_1)} + \sum_{i=2}^N \frac{b_i}{(s+p_i)} + \frac{b_{N+1}}{s} \right] e^{-s\tau_{bd}} \quad (\text{Eqn. A.2.7})$$

Therefore, (Eqn. A.2.6) has Laplace transform given by (Eqn. A.2.8).

$$\widehat{G}(s) = \frac{1}{(s+\beta)} [\widehat{F}(s)] \quad (\text{Eqn. A.2.8})$$

Multiplying the $\frac{1}{(s+\beta)}$ term through in (Eqn. A.2.8) gives (Eqn. A.2.9), which has partial fraction expansion given in (Eqn. A.2.10).

$$\widehat{G}(s) = \left[\frac{b_0}{(s+\beta)(s+p_1)^2} + \frac{b_1}{(s+\beta)(s+p_1)} + \sum_{i=2}^N \frac{b_i}{(s+\beta)(s+p_i)} + \frac{b_{N+1}}{(s+\beta)s} \right] e^{-s\tau_{bd}} \quad (\text{Eqn. A.2.9})$$

$$\begin{aligned} \widehat{G}(s) = & \left(b_0 \left[\frac{1}{(s+p_1)^2} + \frac{-1}{(s+p_1)} + \frac{1}{(s+\beta)} \right] + \right. \\ & + b_1 \left[\frac{1}{(s+p_1)} + \frac{-1}{(s+\beta)} \right] + \\ & \left. \sum_{i=2}^N b_i \left[\frac{1}{(s+p_i)} + \frac{-1}{(s+\beta)} \right] + b_{N+1} \left[\frac{1}{s} + \frac{-1}{(s+\beta)} \right] \right) e^{-s\tau_{bd}} \end{aligned} \quad (\text{Eqn. A.2.10})$$

Collecting terms and re-organizing (Eqn. A.2.10) yields (Eqn. A.2.11), which can be transformed from the Laplace domain to the time to obtain the desired result (Eqn. A.2.12).

$$\begin{aligned} \widehat{G}(s) = & \left\{ \left[\frac{b_0}{(-p_1+\beta)} \right] \frac{1}{(s+p_1)^2} + \left[\frac{-b_0}{(-p_1+\beta)^2} + \frac{b_1}{(-p_1+\beta)} \right] \frac{1}{(s+p_1)} + \right. \\ & + \sum_{i=2}^N \left[\frac{b_i}{(-p_i+\beta)} \right] \frac{1}{(s+p_i)} + \left. \left[\frac{b_{N+1}}{\beta} \right] \frac{1}{s} - \right. \\ & \left. - \left[\frac{-b_0}{(-p_1+\beta)^2} + \frac{b_1}{(-p_1+\beta)} + \sum_{i=2}^N \frac{b_i}{(-p_i+\beta)} + \frac{b_{N+1}}{\beta} \right] \frac{1}{(s+\beta)} \right\} e^{-s\tau_{bd}} \end{aligned} \quad (\text{Eqn. A.2.11})$$

$$\begin{aligned} G(t) = & \left\{ \left[\frac{b_0}{(-p_1+\beta)} \right] t e^{-p_1 t} \mathbf{u}(t) + \left[\frac{-b_0}{(-p_1+\beta)^2} + \frac{b_1}{(-p_1+\beta)} \right] e^{-p_1 t} \mathbf{u}(t) + \right. \\ & + \sum_{i=2}^N \left[\frac{b_i}{(-p_i+\beta)} \right] e^{-p_i t} \mathbf{u}(t) + \left. \left[\frac{b_{N+1}}{\beta} \right] \mathbf{u}(t) - \right. \\ & \left. - \left[\frac{-b_0}{(-p_1+\beta)^2} + \frac{b_1}{(-p_1+\beta)} + \sum_{i=2}^N \frac{b_i}{(-p_i+\beta)} + \frac{b_{N+1}}{\beta} \right] e^{-\beta t} \mathbf{u}(t) \right\} \otimes \delta(t - \tau_{bd}) \end{aligned} \quad (\text{Eqn. A.2.12})$$

A.2.2 Spectral Analysis using the Time-Averaged Generalized Feng Input Model

For the case that the input function model is the generalized Feng input model, the running integral of the input function is given by $G(t) = F(t) + M(t)$ [i.e. (Eqn. A.1.42) in *Appendix Section A1.1*], where $F(t)$ is defined in (Eqn. A.2.5) and $M(t)$ is defined below in (Eqn. A.2.13) with bulk time delay term, τ_{bd} , included.

$$M(t) = [\mathbf{r}_1 \mathbf{a}_0 t e^{-r_1 t} \mathbf{u}(t) + \mathbf{a}_0 e^{-r_1 t} \mathbf{u}(t) - \mathbf{a}_0 \mathbf{u}(t)] \otimes \delta(t - [\tau_{bd} + \tau_{dblPk}]) \quad (\text{Eqn. A.2.13})$$

Thus, inserting (Eqn. A.2.13) into (Eqn. A.1.42) gives running integral of the generalized Feng model (Eqn. A.2.14).

$$\mathbf{G}(\mathbf{t}) = + \int_{-\infty}^{\mathbf{t}} [\mathbf{r}_0(\boldsymbol{\omega} - [\boldsymbol{\tau}_{bd} + \boldsymbol{\tau}_{dblPk}]) \mathbf{e}^{-r_1(\boldsymbol{\omega} - [\boldsymbol{\tau}_{bd} + \boldsymbol{\tau}_{dblPk}])} \mathbf{u}(\boldsymbol{\omega} - [\boldsymbol{\tau}_{bd} + \boldsymbol{\tau}_{dblPk}])] d\boldsymbol{\omega} \quad (\text{Eqn. A.2.14})$$

Inserting (Eqn. A.2.14) into (Eqn. A.2.3) gives (Eqn. A.2.15), which simplifies to (Eqn. A.2.16).

$$\widehat{\mathbf{G}}(\mathbf{s}) = \frac{1}{(s+\beta)} [\widehat{\mathbf{F}}(\mathbf{s}) + \widehat{\mathbf{M}}(\mathbf{s})] \quad (\text{Eqn. A.2.15})$$

$$\widehat{\mathbf{G}}(\mathbf{s}) = \frac{\widehat{\mathbf{F}}(\mathbf{s})}{(s+\beta)} + \frac{\widehat{\mathbf{M}}(\mathbf{s})}{(s+\beta)} \quad (\text{Eqn. A.2.16})$$

(Eqn. A.2.11) gives the result for the first-term on the right-hand side of (Eqn. A.2.16), therefore, in this section I will only evaluate the $(s + \beta)^{-1} \widehat{\mathbf{M}}(\mathbf{s})$ term. Substituting the Laplace transform of (Eqn. A.2.13) for $\widehat{\mathbf{M}}(\mathbf{s})$ gives (Eqn. A.2.17), which has partial fraction expansion (Eqn. A.2.19) and time-domain representation (Eqn. A.2.20).

$$\frac{\widehat{\mathbf{M}}(\mathbf{s})}{(s+\beta)} = \frac{1}{(s+\beta)} \left[\frac{r_1 a_0}{(s+r_1)^2} + \frac{a_0}{(s+r_1)} - \frac{a_0}{s} \right] \mathbf{e}^{-s[\boldsymbol{\tau}_{bd} + \boldsymbol{\tau}_{dblPk}]} \quad (\text{Eqn. A.2.17})$$

$$\frac{\widehat{\mathbf{M}}(\mathbf{s})}{(s+\beta)} = \left[\frac{r_1 a_0}{(s+r_1)^2(s+\beta)} + \frac{a_0}{(s+r_1)(s+\beta)} - \frac{a_0}{s(s+\beta)} \right] \mathbf{e}^{-s[\boldsymbol{\tau}_{bd} + \boldsymbol{\tau}_{dblPk}]} \quad (\text{Eqn. A.2.18})$$

$$\frac{\widehat{\mathbf{M}}(\mathbf{s})}{(s+\beta)} = - \left[\frac{a_0}{\beta} \right] \frac{1}{s} - \left\{ \left[\frac{r_1 a_0}{(-r_1+\beta)} \right] \frac{1}{(s+r_1)^2} + \left[\frac{-r_1 a_0}{(-r_1+\beta)^2} + \frac{a_0}{(-r_1+\beta)} \right] \frac{1}{(s+r_1)} \right\} \mathbf{e}^{-s[\boldsymbol{\tau}_{bd} + \boldsymbol{\tau}_{dblPk}]} \quad (\text{Eqn. A.2.19})$$

$$\begin{aligned}
M(t) \otimes e^{-\beta t} = & \left\{ \left[\frac{r_1 a_0}{(-r_1 + \beta)} \right] t e^{-r_1 t} \mathbf{u}(t) + \right. \\
& \left[\frac{-r_1 a_0}{(-r_1 + \beta)^2} + \frac{a_0}{(-r_1 + \beta)} \right] e^{-r_1 t} \mathbf{u}(t) - \left[\frac{a_0}{\beta} \right] \mathbf{u}(t) - \\
& \left. - \left[\frac{-r_1 a_0}{(-r_1 + \beta)^2} + \frac{a_0}{(-r_1 + \beta)} - \frac{a_0}{\beta} \right] e^{-\beta t} \mathbf{u}(t) \right\} \otimes \delta(t - [\tau_{bd} + \tau_{dblPk}])
\end{aligned} \tag{Eqn. 2.20}$$

Therefore, using the generalized Feng model as the input model in (Eqn. A.2.3) gives $\left[\int_{-\infty}^t \gamma(\tau) d\tau \right] = F(t) + M(t)$, resulting in (Eqn. A.2.21); where $F(t) \otimes e^{-\beta t} \mathbf{u}(t)$ is given by (Eqn. A.2.12) and $M(t) \otimes e^{-\beta t} \mathbf{u}(t)$ is given by (Eqn. A.2.20).

In other words, for a fixed spectral rate β and a set of dynamic PET start and stop frame times, $[t_i^s, t_i^e] \ i = 1 \dots N$, the spectral component corresponding the that rate β can be calculated using (Eqn. A.2.4) where $G(t)$ is calculated by (Eqn. A.2.21).

$$G(t) = F(t) \otimes e^{-\beta t} \mathbf{u}(t) + M(t) \otimes e^{-\beta t} \mathbf{u}(t) \tag{Eqn. A.2.21}$$

A.3 MODELING THE TIME-AVERAGED TISSUE IMPULSE RESPONSE

Compartmental analysis is commonly used in PET imaging to evaluate the performance of a radiotracer *in vivo* as well as provide a foundation for the development of quantitative methodology with regard to response assessment. While an overview of compartmental modeling theory as applied to PET quantification was presented in *Section 5.2* of this dissertation, all of the presented results assumed knowledge of both the instantaneous input concentration and the instantaneous tissue response concentration. However, as discussed in Appendix A.1, the

instantaneous input function cannot be measured directly from an image-based input function. Similarly, since the tissue response is also measured directly from the PET image, it is the time-averaged tissue concentration that is measured from the PET and not the instantaneous tissue response. Fortunately, the time averaging does not affect the compartmental modeling theory or interpretations presented in Chapter 5; however, it does require some additional manipulations similar to those presented in *Appendix A.1 and Appendix A.2*.

Specifically, in *Appendix A.2* it was shown that for a given input function model, $\gamma(t)$, the time averaged value of the convolution of $\gamma(t)$ with a first order pole, $\alpha e^{-\beta t} u(t)$, could be calculated using (*Eqn. A.3.1*) and (*Eqn. A.3.2*), where $g(t) = [\alpha e^{-\beta t} u(t)] \otimes \gamma(t)$.

$$\frac{1}{(t_i^e - t_i^s)} \int_{t_i^s}^{t_i^e} g(t) dt = \frac{[G(t_i^e) - G(t_i^s)]}{(t_i^e - t_i^s)} \quad (\text{Eqn. A.3.1})$$

$$G(t) = [\alpha e^{-\beta t} u(t)] \otimes \left[\int_{-\infty}^t \gamma(\tau) d\tau \right] \quad (\text{Eqn. A.3.2})$$

(*Eqn. A.3.1*) and (*Eqn. A.3.2*) give the general approach that will be followed in deriving the time-averaged version of the tissue response given either the Feng model (*Section A.3.1*) or the generalized Feng model (*Section A.3.2*) as input. For either input model I will calculate the tissue response assuming only a single compartmental model since the responses from multiple compartments can be added by linearity of the compartmental model structures appropriate for PET quantification (*see Section 5.2*). Moreover, each section will include the time-averaged tissue response that would be produced by a trap (*see Section 5.2*).

A.3.1 Time-Averaged Tissue Response using the Feng Input Model

For a 1-tissue compartment model with reversible kinetics, the tissue impulse response function is given by (Eqn. A.3.3). Hence, the tissue response, $y(t)$, is given by (Eqn. A.3.4) where $f(t)$ denotes the Feng model (Eqn. A.1.5).

$$\mathbf{h}(t) = \alpha e^{-\beta t} \mathbf{u}(t) \quad (\text{Eqn. A.3.3})$$

$$\mathbf{y}(t) = \mathbf{h}(t) \otimes \mathbf{f}(t) \quad (\text{Eqn. A.3.4})$$

However, as the measurements of the tissue response are taken directly from the dynamic PET image the time-averaged version of (Eqn. A.3.4) is required. That is for each of the $i = 1 \dots N$ PET frames with corresponding start and end times t_i^s and t_i^e , respectively, the corresponding value of (Eqn. A.3.5) is required.

$$\langle \mathbf{y}(t) \rangle_i = \frac{1}{(t_i^e - t_i^s)} \int_{t_i^s}^{t_i^e} \left([\alpha e^{-\beta t} \mathbf{u}(t)] \otimes \mathbf{f}(t) \right) dt \quad (\text{Eqn. A.3.5})$$

However, as stated above, (Eqn. A.3.5) can be easily evaluated for any pair of t_i^s and t_i^e , by using (Eqn. A.3.1) and (Eqn. A.3.2). Therefore, in order to compute the time-averaged tissue response for a 1-tissue compartment, all that is necessary is to evaluate (Eqn. A.3.6).

$$\mathbf{Y}(t) = [\alpha e^{-\beta t} \mathbf{u}(t)] \otimes \left[\int_{-\infty}^t \mathbf{f}(\tau) d\tau \right] \quad (\text{Eqn. A.3.6})$$

(Eqn. A.3.6) was previously evaluated in *Appendix Section A.2.1* [(Eqn. A.2.12)], for the case $\alpha = 1$, but is easily modified to include arbitrary values for α as well as a time-delay, τ_{tis} , in addition to the bulk time delay of the Feng input model (Eqn. A.3.7).

$$Y(t) = \begin{cases} \alpha \left\{ \left[\frac{b_0}{(-p_1+\beta)} \right] t e^{-p_1 t} \mathbf{u}(t) + \left[\frac{-b_0}{(-p_1+\beta)^2} + \frac{b_1}{(-p_1+\beta)} \right] e^{-p_1 t} \mathbf{u}(t) + \right. \\ \quad \left. + \sum_{i=2}^N \left[\frac{b_i}{(-p_i+\beta)} \right] e^{-p_i t} \mathbf{u}(t) + \left[\frac{b_{N+1}}{\beta} \right] \mathbf{u}(t) - \right. \\ \left. - \left[\frac{-b_0}{(-p_1+\beta)^2} + \frac{b_1}{(-p_1+\beta)} + \sum_{i=2}^N \frac{b_i}{(-p_i+\beta)} + \frac{b_{N+1}}{\beta} \right] e^{-\beta t} \mathbf{u}(t) \right\} \otimes \delta(t - [\tau_{bd} + \tau_{tis}]) \end{cases} \quad (\text{Eqn. A.3.7})$$

a. Gradient of Model Parameters for Time-Averaged Tissue Response using the Feng Model as Input: Reversible Kinetics

For the purposes of speeding up model fitting as well as estimating the covariance matrix of the impulse response model being fitted, it is useful to calculate the gradient of (Eqn. A.3.7) with respect to each of the model parameters. (Eqn. A.3.8)-thru-(Eqn. A.3.10) give the gradients of (Eqn. A.3.7) with respect to the amplitude (α), decay-rate (β), and time-delay (τ_{tis}), respectively, of the 1-tissue impulse response function convolved with the Feng input model.

$$\frac{\delta Y(t)}{\delta \alpha} = \begin{cases} \left\{ \left[\frac{b_0}{(-p_1+\beta)} \right] t e^{-p_1 t} \mathbf{u}(t) + \left[\frac{-b_0}{(-p_1+\beta)^2} + \frac{b_1}{(-p_1+\beta)} \right] e^{-p_1 t} \mathbf{u}(t) + \right. \\ \quad \left. + \sum_{i=2}^N \left[\frac{b_i}{(-p_i+\beta)} \right] e^{-p_i t} \mathbf{u}(t) + \left[\frac{b_{N+1}}{\beta} \right] \mathbf{u}(t) - \right. \\ \left. - \left[\frac{-b_0}{(-p_1+\beta)^2} + \frac{b_1}{(-p_1+\beta)} + \sum_{i=2}^N \frac{b_i}{(-p_i+\beta)} + \frac{b_{N+1}}{\beta} \right] e^{-\beta t} \mathbf{u}(t) \right\} \otimes \delta(t - [\tau_{bd} + \tau_{tis}]) \end{cases} \quad (\text{Eqn. A.3.8})$$

$$\begin{aligned}
\frac{\delta Y(t)}{\delta \beta} = & \alpha \left\{ \left[\frac{-b_0}{(-p_1+\beta)^2} \right] t e^{-p_1 t} \mathbf{u}(t) + \left[\frac{2b_0}{(-p_1+\beta)^3} - \frac{b_1}{(-p_1+\beta)^2} \right] e^{-p_1 t} \mathbf{u}(t) - \right. \\
& - \sum_{i=2}^N \left[\frac{b_i}{(-p_i+\beta)^2} \right] e^{-p_i t} \mathbf{u}(t) - \left[\frac{b_{N+1}}{\beta^2} \right] \mathbf{u}(t) - \\
& - \left[\frac{2b_0}{(-p_1+\beta)^3} - \frac{b_1}{(-p_1+\beta)^2} - \sum_{i=2}^N \frac{b_i}{(-p_i+\beta)^2} - \frac{b_{N+1}}{\beta^2} \right] e^{-\beta t} \mathbf{u}(t) + \\
& \left. + \left[\frac{-b_0}{(-p_1+\beta)^2} + \frac{b_1}{(-p_1+\beta)} + \sum_{i=2}^N \frac{b_i}{(-p_i+\beta)} + \frac{b_{N+1}}{\beta} \right] t e^{-\beta t} \mathbf{u}(t) \right\} \otimes \delta(\mathbf{t} - [\boldsymbol{\tau}_{bd} + \boldsymbol{\tau}_{tis}])
\end{aligned} \tag{Eqn. A.3.9}$$

$$\frac{\delta Y(t)}{\delta \tau_{tis}} = \left[\boldsymbol{\beta} \left(F(t) \otimes \alpha e^{-\beta t} \mathbf{u}(t) \right) - \alpha F(t) \right] \otimes \delta(\mathbf{t} - [\boldsymbol{\tau}_{bd} + \boldsymbol{\tau}_{tis}]) \tag{Eqn. A.3.10}$$

b. Time-Averaged Tissue Response using the Feng Model as Input: A Trap

The impulse response function for a trap is given by (Eqn. A.3.11). Inserting (Eqn. A.3.11) into (Eqn. A.3.6) gives (Eqn. A.3.12), where $f(\tau)$ is again the Feng model (Eqn. A.1.5). Therefore, following the approach defined in (Eqn. A.3.1), the time-averaged response for a trap, assuming the Feng model as input, can be calculated via (Eqn. A.3.13) for a particular pair of PET frame $[t_i^s, t_i^e]$.

$$\mathbf{h}_{trap}(t) = \alpha \mathbf{u}(t) \tag{Eqn. A.3. 11}$$

$$\mathbf{Y}_{trap}(t) = [\alpha \mathbf{u}(t)] \otimes \left[\int_{-\infty}^t f(\tau) d\tau \right] \tag{Eqn. A.3. 12}$$

$$\frac{1}{(t_i^e - t_i^s)} \int_{t_i^s}^{t_i^e} \mathbf{y}_{trap}(t) dt = \frac{[\mathbf{Y}_{trap}(t_i^e) - \mathbf{Y}_{trap}(t_i^s)]}{(t_i^e - t_i^s)} \tag{Eqn. A.3. 13}$$

However, (Eqn. A.3.12) is simply the convolution of the running integral of the Feng model with a step-function scaled by α . This quantity was previously calculated in *Appendix A.1.1* [(Eqn. A.1.34)] for the case of $\alpha = 1$. Thus, allowing for arbitrary α as well as a time-delay, τ_{tis} , in addition to the bulk time delay of the Feng input model (Eqn. A.3.12) becomes (Eqn. A.3.14).

$$\begin{aligned}
Y_{trap}(\mathbf{t}) = & \alpha \left\{ \left[\frac{-b_0}{p_1} \right] t e^{-p_1 t} \mathbf{u}(t) + \left[\frac{-b_0}{p_1^2} + \frac{-b_1}{p_1} \right] e^{-p_1 t} \mathbf{u}(t) + \dots \right. \\
& \dots + \sum_{i=2}^N - \left(\frac{b_i}{p_i} \right) e^{-p_i t} \mathbf{u}(t) + \dots \\
& \left. \dots + \left[\frac{b_0}{p_1^2} + \frac{b_1}{p_1} + \sum_{i=2}^N \left(\frac{b_i}{p_i} \right) \right] \mathbf{u}(t) + \mathbf{b}_{N+1} t \mathbf{u}(t) \right\} \otimes \delta(\mathbf{t} - [\boldsymbol{\tau}_{bd} + \boldsymbol{\tau}_{tis}])
\end{aligned} \tag{Eqn. A.3.14}$$

c. Gradient of Model Parameters for Time-Averaged Tissue Response using the Feng Model as Input: A Trap

For the purposes of speeding up model fitting as well as estimating the covariance matrix of the impulse response model being fitted, it is useful to calculate the gradient of (Eqn. A.3.14) with respect to each of the model parameters. (Eqn. A.3.15) and (Eqn. A.3.16) give the gradients of (Eqn. A.3.14) with respect to the amplitude (α) and time-delay (τ_{tis}), respectively, of an impulse response function describing a trap convolved with the Feng input model.

$$\begin{aligned}
\frac{\delta Y_{trap}(\mathbf{t})}{\delta \alpha} = & \left\{ \left[\frac{-b_0}{p_1} \right] t e^{-p_1 t} \mathbf{u}(t) + \left[\frac{-b_0}{p_1^2} + \frac{-b_1}{p_1} \right] e^{-p_1 t} \mathbf{u}(t) + \sum_{i=2}^N - \left(\frac{b_i}{p_i} \right) e^{-p_i t} \mathbf{u}(t) + \right. \\
& \left. + \left[\frac{b_0}{p_1^2} + \frac{b_1}{p_1} + \sum_{i=2}^N \left(\frac{b_i}{p_i} \right) \right] \mathbf{u}(t) + \mathbf{b}_{N+1} t \mathbf{u}(t) \right\} \otimes \delta(\mathbf{t} - [\boldsymbol{\tau}_{bd} + \boldsymbol{\tau}_{tis}])
\end{aligned} \tag{Eqn. A.3.15}$$

$$\frac{\delta Y_{trap}(\mathbf{t})}{\delta \tau_{tis}} = [-\alpha \mathbf{F}(\mathbf{t})] \otimes \delta(\mathbf{t} - [\boldsymbol{\tau}_{bd} + \boldsymbol{\tau}_{tis}]) \tag{Eqn. A.3.16}$$

A.3.2 Time-Averaged Tissue Response using the Generalized Feng Input Model

This section derives the appropriate equations for fitting the time-averaged tissue response for both a 1-tissue compartment model and a trap assuming the generalized Feng model (Eqn. A.1.35) as the input model. The approach for deriving these equations parallels the approach used in the previous sections when the Feng model was assumed as input.

Specifically, for a 1-tissue compartment model with reversible kinetics, the tissue impulse response function is given by (Eqn. A.3.3). Therefore, following the same argument that lead to (Eqn. A.3.6), only calculation of (Eqn. A.3.17) is required, where $g(\tau)$ represents the generalized Feng model.

$$Y(t) = [\alpha e^{-\beta t} u(t)] \otimes \left[\int_{-\infty}^t g(\tau) d\tau \right] \quad (\text{Eqn. A.3.17})$$

(Eqn. A.3.17) was previously evaluated in *Appendix Section A.2.2* [(Eqn. A.2.21)] for the case $\alpha = 1$, but is easily modified to include arbitrary values for α as well as a time-delay, τ_{tis} , in addition to the bulk time delay of the generalized Feng input model (Eqn. A.3.18) below, where $F(t) \otimes e^{-\beta t} u(t)$ is given by (Eqn. A.2.12) and $M(t) \otimes e^{-\beta t} u(t)$ is given by (Eqn. A.2.20).

$$G(t) = \alpha [F(t) \otimes e^{-\beta t} u(t) + M(t) \otimes e^{-\beta t} u(t)] \otimes \delta(t - \tau_{tis}) \quad (\text{Eqn. A.3.18})$$

a. Gradient of Model Parameters for Time-Averaged Tissue Response using the Generalized Feng Model as Input: Reversible Kinetics

For the purposes of speeding up model fitting as well as estimating the covariance matrix of the impulse response model being fitted, it is useful to calculate the gradient of (Eqn. A3.18) with respect to each of the model parameters. To this end, note that $\frac{\delta G(t)}{\delta \alpha}$ is given by (Eqn. A3.19), which is a linear combination two partial derivatives with respect to the amplitude α . However, the top partial derivative was evaluated previously and is given by (Eqn. A3.8) above.

$$\begin{aligned} \frac{\delta G(t)}{\delta \alpha} = & \frac{\delta}{\delta \alpha} [F(t) \otimes \alpha e^{-\beta t} \mathbf{u}(t)] \otimes \delta(t - \tau_{tis}) + \\ & + \frac{\delta}{\delta \alpha} [\alpha M(t) \otimes \alpha e^{-\beta t} \mathbf{u}(t)] \otimes \delta(t - \tau_{tis}) \end{aligned} \quad (\text{Eqn. A.3.19})$$

The superposition of partial derivatives in (Eqn. A3.19) is due to the assumption of linearity in the response of the tissue to the injected tracer, and, as a result will also hold for the partial derivatives of (Eqn. A3.18) with respect to β and τ_{tis} . As a result, only the partial derivatives of (Eqn. A3.20) with respect to the impulse response model parameters will be derived in this section.

$$[M(t) \otimes \alpha e^{-\beta t} \mathbf{u}(t)] \otimes \delta(t - \tau_{tis}) \quad (\text{Eqn. A.3.20})$$

(Eqn. A.3.21)-thru-(Eqn. A.3.23) give the gradients of (Eqn. A.3.20) with respect to the amplitude (α), decay-rate (β), and time-delay (τ_{tis}) of the 1-tissue impulse response function,

respectively. To obtain the complete set of partial derivatives of (Eqn. A.3.18) with respect to the impulse response model parameters, (Eqn. A.3.21)-thru-(Eqn. A.3.23) must be linearly combined with the corresponding partial derivatives in (Eqn. A.3.8)-thru-(Eqn. A.3.10).

$$\frac{\delta[M(t) \otimes \alpha e^{-\beta t} \mathbf{u}(t)]}{\delta \alpha} = \left\{ \left[\frac{r_1 a_0}{(-r_1 + \beta)} \right] \mathbf{t} e^{-r_1 t} \mathbf{u}(t) + \left[\frac{-r_1 a_0}{(-r_1 + \beta)^2} + \frac{a_0}{(-r_1 + \beta)} \right] e^{-r_1 t} \mathbf{u}(t) - \left[\frac{a_0}{\beta} \right] \mathbf{u}(t) - \left[\frac{-r_1 a_0}{(-r_1 + \beta)^2} + \frac{a_0}{(-r_1 + \beta)} - \frac{a_0}{\beta} \right] e^{-\beta t} \mathbf{u}(t) \right\} \otimes \delta(t - \tau_{tis}) \quad (\text{Eqn. A.3.21})$$

$$\frac{\delta[M(t) \otimes \alpha e^{-\beta t}]}{\delta \beta} = \alpha \left\{ \left[\frac{-r_1 a_0}{(-r_1 + \beta)^2} \right] \mathbf{t} e^{-r_1 t} \mathbf{u}(t) + \left[\frac{2r_1 a_0}{(-r_1 + \beta)^3} - \frac{a_0}{(-r_1 + \beta)^2} \right] e^{-r_1 t} \mathbf{u}(t) + \left[\frac{a_0}{\beta^2} \right] \mathbf{u}(t) - \left[\frac{2r_1 a_0}{(-r_1 + \beta)^3} - \frac{a_0}{(-r_1 + \beta)^2} + \frac{a_0}{\beta^2} \right] e^{-\beta t} \mathbf{u}(t) + \left[\frac{-r_1 a_0}{(-r_1 + \beta)^2} + \frac{a_0}{(-r_1 + \beta)} - \frac{a_0}{\beta} \right] \mathbf{t} e^{-\beta t} \mathbf{u}(t) \right\} \otimes \delta(t - \tau_{tis}) \quad (\text{Eqn. A.3.22})$$

$$\frac{\delta[M(t) \otimes \alpha e^{-\beta t}]}{\delta \tau_{tis}} = \left\{ \beta \left(M(t) \otimes \alpha e^{-\beta t} \mathbf{u}(t) \right) - \alpha M(t) \right\} \otimes \delta(t - \tau_{tis}) \quad (\text{Eqn. A.3.23})$$

b. Time-Averaged Tissue Response using the Generalized Feng Model as Input: A Trap

The impulse response function for a trap is given by (Eqn. A.3.11) above. Inserting (Eqn. A.3.11) into (Eqn. A.3.6) gives (Eqn. A.3.24), where $g(\tau)$ is the generalized Feng model [(Eqn. A.1.35)]. Therefore, following the approach defined in (Eqn. A.3.1), the time-averaged response for a trap assuming the generalized Feng model as input can be calculated via (Eqn. A.3.25) for a particular pair of PET frame $[t_i^s, t_i^e]$.

$$\mathbf{Y}_{trap}(t) = [\alpha \mathbf{u}(t)] \otimes \left[\int_{-\infty}^t g(\tau) d\tau \right] \quad (\text{Eqn. A.3.24})$$

$$\frac{1}{(t_i^e - t_i^s)} \int_{t_i^s}^{t_i^e} y_{trap}(t) dt = \frac{[Y_{trap}(t_i^e) - Y_{trap}(t_i^s)]}{(t_i^e - t_i^s)} \quad (\text{Eqn. A.3.25})$$

However, (Eqn. A.3.24) is simply the running integral of the generalized Feng model convolved with a step-function and scaled by α . The convolution of the running integral of the generalized Feng model with a step-function has previously been calculated *Appendix A.1.2* for the case of $\alpha = 1$. This quantity can thus be written for arbitrary α as well as a non-zero delay, τ_{tis} , in addition to the bulk delay, τ_{bd} , and second peak delay, τ_{dblPk} , of the generalized Feng model as in (Eqn. A.3.26); where $K(t)$ is as defined in (Eqn. A.1.34) and $W(t)$ is defined in (Eqn. A.1.48).

$$Y_{trap}(t) = \alpha\{K(t) + W(t)\} \otimes \delta(t - \tau_{tis}) \quad (\text{Eqn. A.3.26})$$

i. Gradient of Model Parameters for Time-Averaged Tissue Response using the Generalized Feng Model as Input: A Trap

For the purposes of speeding up model fitting as well as estimating the covariance matrix of the impulse response model being fitted, it is useful to calculate the gradient of (Eqn. A.3.26) with respect to each of the model parameters. To this end, note that $\frac{\delta Y_{trap}(t)}{\delta \alpha}$ is given by (Eqn. A.3.27), which is a linear combination of two partial derivatives with respect to the amplitude α . However, the top partial derivative was evaluated previously and is given by (Eqn. A.3.15) above.

$$\frac{\delta Y_{trap}(t)}{\delta \alpha} = \frac{\delta}{\delta \alpha} [\alpha K(t) \otimes \delta(t - \tau_{tis})] + \frac{\delta}{\delta \alpha} [\alpha W(t) \otimes \delta(t - \tau_{tis})] \quad (\text{Eqn. A.3.27})$$

The superposition of partial derivatives in (Eqn. A.3.27) is due to the assumption of linearity in the response of the tissue to the injected tracer, and, as a result will also hold for the partial derivative of (Eqn. A.3.26) with respect to τ_{tis} . As a result, only the partial derivatives of (Eqn. A.3.28) with respect to the impulse response model parameters will be derived in this section; where $W(t)$ is determined in Appendix A.1.2 [(Eqn. A.1.48)], but is repeated here as (Eqn. A.3.29) for ease of calculation.

$$\alpha W(t) \otimes \delta(t - \tau_{tis}) \quad (\text{Eqn. A.3.28})$$

$$\left\{ -\mathbf{a}_0 t e^{-r_1 t} \mathbf{u}(t) - \frac{2a_0}{r_1} e^{-r_1 t} \mathbf{u}(t) + \frac{2a_0}{r_1} \mathbf{u}(t) - \mathbf{a}_0 t \mathbf{u}(t) \right\} \otimes \delta(t - [\tau_{bd} + \tau_{dblPk}]) \quad (\text{Eqn. A.3.29})$$

(Eqn. A.3.30) and (Eqn. A.3.31) give the gradients of (Eqn. A.3.27) with respect to the amplitude (α) and time-delay (τ_{tis}), respectively. In (Eqn. A.3.31), $M(t)$ is as defined in (Eqn. A.1.38) above, except the $\delta(t - \tau_{dblPk})$ in (Eqn. A.1.38) has now been included in the overall $\delta(t - [\tau_{bd} + \tau_{dblPk} + \tau_{tis}])$ term of (Eqn. A.3.31). To obtain the complete set of partial derivatives of (Eqn. A.3.27) with respect to the trap parameters, (Eqn. A.3.30)-thru-(Eqn. A.3.31) must be linearly combined with the corresponding partial derivatives in (Eqn. A.3.15) and (Eqn. A.3.16).

$$\frac{\delta[\alpha W(t)]}{\delta \alpha} = W(t) \otimes \delta(t - [\tau_{bd} + \tau_{dblPk} + \tau_{tis}]) \quad (\text{Eqn. A.3.30})$$

$$\frac{\delta[\alpha W(t)]}{\delta \tau_{tis}} = [-\alpha M(t)] \otimes \delta(t - [\tau_{bd} + \tau_{dblPk} + \tau_{tis}]) \quad (\text{Eqn. A.3.31})$$

A.4 SIMULTANEOUS ESTIMATION OF THE IMAGE-BASED INPUT FUNCTION AND TISSUE RESPONSE MODELS

A primary means of evaluating [¹⁸F]ML-10 performance in this dissertation involves estimation of the parameters of the impulse response function (IRF) of the target tissue. To this end, knowledge of the input radioactivity concentration into the tissue is required. However, as only an image-derived input function (IBIF) is available for modeling, this means that the IBIF itself must also be modeled. The joint log-likelihood function for a general IBIF and tissue model combination was derived in *Section 5.2* above, (*Eqn. 5.2.61*). The goal of this section is to derive the corresponding gradients of the joint-log likelihood function needed for efficient optimization.

A.4.1 The Joint Log-Likelihood Function

The general joint log-likelihood function for simultaneous estimation of the IBIF and tissue models was derived in *Section 5.2* above and is repeated here as (*Eqn. A.4.1*). As in *Section 5.2*, $M(\theta, \delta; \bar{t}_i) \triangleq [f(\theta; \bar{t}_i) \quad g(\theta, \delta; \bar{t}_i)]^T$ is a 2x1 column vector, where $f(\theta; \bar{t}_i)$ and $g(\theta, \delta; \bar{t}_i)$ denote the time-averaged values of the IBIF and tissue response models during the i^{th} frame, respectively, and N denotes the total number of PET frames acquired. θ and δ represent the

corresponding IBIF and tissue model parameter vectors, respectively. Furthermore, x_i denotes the 2x1 column vector containing the i^{th} input, u_i , and tumor tissue, v_i , sample pairs (i.e. $x_i \triangleq [u_i, v_i]^T$). (Eqn. A. 4.2) gives the form of the joint-covariance matrix for the i^{th} PET frame, where $\sigma_{1,i}^2$ and $\sigma_{2,i}^2$ are the input and tissue sample variances for the i^{th} PET frame, respectively.

$$\ell(\boldsymbol{\theta}, \boldsymbol{\delta}) = \begin{cases} -N \ln\{2\boldsymbol{\pi}\} - \frac{1}{2} \sum_{i=1}^N \ln\{|\boldsymbol{\Sigma}_i|\} - \\ -\frac{1}{2} \sum_{i=1}^N \left[[x_i - \mathbf{M}(\boldsymbol{\theta}, \boldsymbol{\delta}; \bar{\mathbf{t}}_i)]^T \boldsymbol{\Sigma}_i^{-1} [x_i - \mathbf{M}(\boldsymbol{\theta}, \boldsymbol{\delta}; \bar{\mathbf{t}}_i)] \right] \end{cases} \quad (\text{Eqn. A.4.1})$$

$$\boldsymbol{\Sigma}_i = \begin{bmatrix} \sigma_{1,i}^2 & \mathbf{0} \\ \mathbf{0} & \sigma_{2,i}^2 \end{bmatrix} \quad (\text{Eqn. A.4.2})$$

Following the typical convention in PET quantification to assume the measurement variances are proportional to the measured time-activity curve data (see *Chapter 2, Section 2.4.1*) the variances on the measured IBIF and tissue data are assumed to be of the form: $\sigma_{1,i}^2 = \alpha^2 u_i$ and $\sigma_{2,i}^2 = \beta^2 v_i$, respectively. α and β are unknown positive constants, and u_i and v_j are known, time-varying, weights that depend on the measured data but not the model parameters. With this measurement variance assumption, (Eqn. A. 4.2) takes the form of (Eqn. A. 4.3) below. Moreover, with using (Eqn. A. 4.3), the log-likelihood function in (Eqn. A. 4.1) can be re-written as in (Eqn. A. 4.4) below.

$$\boldsymbol{\Sigma}_i = \begin{bmatrix} \alpha^2 u_i & \mathbf{0} \\ \mathbf{0} & \beta^2 v_i \end{bmatrix} \quad (\text{Eqn. A.4.3})$$

$$\boldsymbol{\ell}(\boldsymbol{\theta}, \boldsymbol{\delta}) = \begin{cases} -N \ln\{2\pi\} - \frac{1}{2} \sum_{i=1}^N \ln\{\mathbf{u}_i \mathbf{v}_i\} - \frac{1}{2} \sum_{i=1}^N \ln\{\alpha^2\} - \frac{1}{2} \sum_{i=1}^N \ln\{\beta^2\} - \\ - \frac{1}{2} \sum_{i=1}^N [\mathbf{x}_i - \mathbf{M}(\boldsymbol{\theta}, \boldsymbol{\delta}; \bar{\mathbf{t}}_i)]^T \boldsymbol{\Sigma}_i^{-1} [\mathbf{x}_i - \mathbf{M}(\boldsymbol{\theta}, \boldsymbol{\delta}; \bar{\mathbf{t}}_i)] \end{cases} \quad (\text{Eqn. A.4.4})$$

Furthermore, by defining the diagonal matrices S_1 and S_2 as in (Eqn. A.4.5) and (Eqn. A.4.6), as well as eliminating all terms from (Eqn. A.4.4) that do not depend on the model parameters, (Eqn. A.4.4) can be re-written as (Eqn. A.4.7). Note that in (Eqn. A.4.7), \mathbf{u} , \mathbf{v} , $\mathbf{f}(\boldsymbol{\theta})$, and $\mathbf{g}(\boldsymbol{\theta}, \boldsymbol{\delta})$ are column vectors of the form: $\mathbf{u} = [u_1, \dots, u_N]^T$, $\mathbf{v} = [v_1, \dots, v_N]^T$, $\mathbf{f}(\boldsymbol{\theta}) = [f(\boldsymbol{\theta}; \bar{\mathbf{t}}_1), \dots, f(\boldsymbol{\theta}; \bar{\mathbf{t}}_N)]^T$, and $\mathbf{g}(\boldsymbol{\theta}, \boldsymbol{\delta}) = [g(\boldsymbol{\theta}, \boldsymbol{\delta}; \bar{\mathbf{t}}_1), \dots, g(\boldsymbol{\theta}, \boldsymbol{\delta}; \bar{\mathbf{t}}_N)]^T$.

$$S_1 = \begin{bmatrix} \mathbf{u}_1 & \mathbf{0} & \mathbf{0} & \mathbf{0} \\ \mathbf{0} & \mathbf{u}_2 & \vdots & \vdots \\ \vdots & \mathbf{0} & \ddots & \mathbf{0} \\ \mathbf{0} & \dots & \mathbf{0} & \mathbf{u}_N \end{bmatrix} \quad (\text{Eqn. A.4.5})$$

$$S_2 = \begin{bmatrix} \mathbf{v}_1 & \mathbf{0} & \mathbf{0} & \mathbf{0} \\ \mathbf{0} & \mathbf{v}_2 & \vdots & \vdots \\ \vdots & \mathbf{0} & \ddots & \mathbf{0} \\ \mathbf{0} & \dots & \mathbf{0} & \mathbf{v}_N \end{bmatrix} \quad (\text{Eqn. A.4.6})$$

$$\boldsymbol{\ell}(\boldsymbol{\theta}, \boldsymbol{\delta}) = \begin{cases} -\frac{N}{2} \ln\{\alpha^2\} - \frac{N}{2} \ln\{\beta^2\} - \frac{1}{2\alpha^2} [\mathbf{u} - \mathbf{f}(\boldsymbol{\theta})]^T S_1^{-1} [\mathbf{u} - \mathbf{f}(\boldsymbol{\theta})] - \\ - \frac{1}{2\beta^2} [\mathbf{v} - \mathbf{g}(\boldsymbol{\theta}, \boldsymbol{\delta})]^T S_2^{-1} [\mathbf{v} - \mathbf{g}(\boldsymbol{\theta}, \boldsymbol{\delta})] \end{cases} \quad (\text{Eqn. A.4.7})$$

From the form in (Eqn. A.4.7) the corresponding gradients with respect to all model parameters can be computed. The forms of the gradients with respect to the various model parameters are given in (Eqn. A.4.8). Note, the gradients $\nabla_{\boldsymbol{\theta}} f(\boldsymbol{\theta})$ were calculated in the previous

section for the Feng IBIF model and the generalized Feng IBIF model, as were the gradients corresponding to $\nabla_{\delta}g(\theta, \delta)$ for various tissue response models. As a result, the following sections focus on computing the components of $\nabla_{\theta}g(\theta, \delta)$ for the Feng and generalized Feng model. That is, computing the gradients of the tissue models with respect to the IBIF model parameters.

$$\begin{cases} \nabla_{\theta}\ell = [\mathbf{u} - \mathbf{f}(\theta)]^T \mathbf{S}_1^{-1} [\nabla_{\theta}\mathbf{f}(\theta)] + [\mathbf{v} - \mathbf{g}(\theta, \delta)]^T \mathbf{S}_2^{-1} [\nabla_{\theta}\mathbf{g}(\theta, \delta)] \\ \nabla_{\delta}\ell = [\mathbf{v} - \mathbf{g}(\theta, \delta)]^T \mathbf{S}_2^{-1} [\nabla_{\delta}\mathbf{g}(\theta, \delta)] \\ \nabla_{\alpha^2}\ell = -\frac{N}{2\alpha^2} + \frac{1}{2(\alpha^2)^2} [\mathbf{u} - \mathbf{f}(\theta)]^T \mathbf{S}_1^{-1} [\mathbf{u} - \mathbf{f}(\theta)] \\ \nabla_{\beta^2}\ell = -\frac{N}{2\beta^2} + \frac{1}{2(\beta^2)^2} [\mathbf{v} - \mathbf{g}(\theta, \delta)]^T \mathbf{S}_2^{-1} [\mathbf{v} - \mathbf{g}(\theta, \delta)] \end{cases} \quad (\text{Eqn. A.4.8})$$

A.4.2 Calculation of Additional Gradients: Feng Model

a. Reversible Kinetics

The system response function assuming the Feng IBIF model and reversible tracer kinetics was derived above in *Section A.3*, though it is repeated here as (*Eqn. A.4.9*). The corresponding gradients of (*Eqn. A.4.9*) with respect to the Feng IBIF model parameters are given in (*Eqn. A.4.10*) thru (*Eqn. A.4.14*).

$$\begin{aligned} Y(t) = & \left\{ \left[\frac{ab_0}{(-p_1+\beta)} \right] t e^{-p_1 t} \mathbf{u}(t) + \left[\frac{-ab_0}{(-p_1+\beta)^2} + \frac{ab_1}{(-p_1+\beta)} \right] e^{-p_1 t} \mathbf{u}(t) + \right. \\ & + \sum_{j=2}^N \left[\frac{ab_j}{(-p_j+\beta)} \right] e^{-p_j t} \mathbf{u}(t) + \left[\frac{ab_{N+1}}{\beta} \right] \mathbf{u}(t) - \left[\frac{-ab_0}{(-p_1+\beta)^2} + \right. \\ & \left. \left. + \frac{ab_1}{(-p_1+\beta)} + \sum_{j=2}^N \left[\frac{ab_j}{(-p_j+\beta)} \right] + \frac{ab_{N+1}}{\beta} \right] e^{-\beta t} \mathbf{u}(t) \right\} \otimes \delta(t - [\tau_{bd} + \tau_{tis}]) \end{aligned} \quad (\text{Eqn. A.4.9})$$

$$\begin{aligned} \frac{\partial Y(t)}{\partial b_0} = & \left\{ \left[\frac{\alpha}{(-p_1+\beta)} \right] t e^{-p_1 t} \mathbf{u}(t) + \left[\frac{-\alpha}{(-p_1+\beta)^2} + \left(\frac{\alpha}{p_1} \right) \frac{1}{(-p_1+\beta)} \right] e^{-p_1 t} \mathbf{u}(t) + \right. \\ & \left. - \left[\frac{\alpha}{\beta p_1} \right] \mathbf{u}(t) + \right. \\ & \left. + \left[\frac{\alpha}{(-p_1+\beta)^2} - \left(\frac{\alpha}{p_1} \right) \frac{1}{(-p_1+\beta)} + \frac{\alpha}{\beta p_1} \right] e^{-\beta t} \mathbf{u}(t) \right\} \otimes \delta(t - [\tau_{bd} + \tau_{tis}]) \end{aligned} \quad (\text{Eqn. A.4.10})$$

$$\begin{aligned} \frac{\partial Y(t)}{\partial b_i} = & \left\{ \left[\left(-\frac{p_i}{p_1} \right) \frac{\alpha}{(-p_1+\beta)} \right] e^{-p_1 t} \mathbf{u}(t) + \left[\frac{\alpha}{(-p_i+\beta)} \right] e^{-p_i t} \mathbf{u}(t) - \right. \\ & \left. - \left[\frac{\alpha}{\beta} \left(-\frac{p_i}{p_1} + 1 \right) \right] \mathbf{u}(t) + \right. \\ & \left. + \left[\left(\frac{p_i}{p_1} \right) \frac{\alpha}{(-p_1+\beta)} - \frac{\alpha}{(-p_i+\beta)} + \frac{\alpha}{\beta} \left(-\frac{p_i}{p_1} + 1 \right) \right] e^{-\beta t} \mathbf{u}(t) \right\} \\ & \otimes \delta(t - [\tau_{bd} + \tau_{tis}]) \end{aligned} \quad (\text{Eqn. A.4.11})$$

$$\begin{aligned} \frac{\partial Y(t)}{\partial p_1} = & \left\{ \left[\frac{-ab_0}{(-p_1+\beta)} \right] t^2 e^{-p_1 t} \mathbf{u}(t) + \left[\frac{2ab_0}{(-p_1+\beta)^2} - \frac{ab_1}{(-p_1+\beta)} \right] t e^{-p_1 t} \mathbf{u}(t) + \right. \\ & \left[\frac{-2ab_0}{(-p_1+\beta)^3} - \left(\frac{ab_1}{p_1} \right) \frac{1}{(-p_1+\beta)} + \frac{ab_1}{(-p_1+\beta)^2} \right] e^{-p_1 t} \mathbf{u}(t) + \\ & \left. + \left[\frac{ab_1}{\beta p_1} \right] \mathbf{u}(t) + \left[\frac{2ab_0}{(-p_1+\beta)^3} + \right. \right. \\ & \left. \left. + \left(\frac{ab_1}{p_1} \right) \frac{1}{(-p_1+\beta)} - \frac{ab_1}{(-p_1+\beta)^2} - \frac{ab_1}{\beta p_1} \right] e^{-\beta t} \mathbf{u}(t) \right\} \otimes \delta(t - [\tau_{bd} + \tau_{tis}]) \end{aligned} \quad (\text{Eqn. A.4.12})$$

$$\begin{aligned} \frac{\partial Y(t)}{\partial p_i} = & \left\{ \left[\left(-\frac{b_i}{p_1} \right) \frac{\alpha}{(-p_1+\beta)} \right] e^{-p_1 t} \mathbf{u}(t) - \left[\frac{ab_i}{(-p_i+\beta)} \right] t e^{-p_i t} \mathbf{u}(t) + \right. \\ & \left. + \left[\frac{ab_i}{(-p_i+\beta)^2} \right] e^{-p_i t} \mathbf{u}(t) + \left[\frac{ab_i}{\beta p_1} \right] \mathbf{u}(t) + \right. \\ & \left. + \left[\left(\frac{b_i}{p_1} \right) \frac{\alpha}{(-p_1+\beta)} - \frac{ab_i}{(-p_i+\beta)^2} - \frac{ab_i}{\beta p_1} \right] e^{-\beta t} \mathbf{u}(t) \right\} \otimes \delta(t - [\tau_{bd} + \tau_{tis}]) \end{aligned} \quad (\text{Eqn. A.4.13})$$

$$\frac{\partial Y(t)}{\partial \tau_{bd}} = \{ \beta Y(t) - \alpha F(t) \} \otimes \delta(t - [\tau_{bd} + \tau_{tis}]) \quad (\text{Eqn. A.4.14})$$

b. Trapping

The system response function assuming the Feng IBIF model and irreversible tracer kinetics was derived above in *Section A.3*, though it is repeated here as (Eqn. A.4.15). The corresponding gradients of (Eqn. A.4.15) with respect to the Feng IBIF model parameters are given in (Eqn. A.4.16) thru (Eqn. A.4.20).

$$\begin{aligned}
 Y(t) = & \left\{ \left[\frac{-\alpha b_0}{p_1} \right] t e^{-p_1 t} \mathbf{u}(t) + \left[\frac{-\alpha b_0}{p_1^2} - \frac{\alpha b_1}{p_1} \right] e^{-p_1 t} \mathbf{u}(t) - \right. \\
 & - \sum_{j=2}^N \left[\frac{\alpha b_j}{p_j} \right] e^{-p_j t} \mathbf{u}(t) + [\alpha b_{N+1}] t \mathbf{u}(t) + \left[\frac{\alpha b_0}{p_1^2} + \right. \\
 & \left. \left. + \frac{\alpha b_1}{p_1} + \sum_{j=2}^N \left[\frac{\alpha b_j}{p_j} \right] \right] \mathbf{u}(t) \right\} \otimes \delta(t - [\tau_{bd} + \tau_{tis}])
 \end{aligned} \tag{Eqn. A.4.15}$$

$$\begin{aligned}
 \frac{\partial Y(t)}{\partial b_0} = & \left\{ - \left(\frac{\alpha}{p_1} \right) t e^{-p_1 t} \mathbf{u}(t) - \left[\frac{2\alpha}{p_1^2} \right] e^{-p_1 t} \mathbf{u}(t) + \right. \\
 & \left. + \left[\frac{2\alpha}{p_1^2} \right] \mathbf{u}(t) - \left(\frac{\alpha}{p_1} \right) t \mathbf{u}(t) \right\} \otimes \delta(t - [\tau_{bd} + \tau_{tis}])
 \end{aligned} \tag{Eqn. A.4.16}$$

$$\begin{aligned}
 \frac{\partial Y(t)}{\partial b_i} = & \left\{ \left(\frac{\alpha p_i}{p_1^2} \right) e^{-p_1 t} \mathbf{u}(t) - \frac{\alpha}{p_i} e^{-p_i t} \mathbf{u}(t) + \alpha \left[-\frac{p_i}{p_1^2} + \frac{1}{p_i} \right] \mathbf{u}(t) - \right. \\
 & \left. - \alpha \left(-\frac{p_i}{p_1} + 1 \right) t \mathbf{u}(t) \right\} \otimes \delta(t - [\tau_{bd} + \tau_{tis}]); \quad i = 2, \dots, N
 \end{aligned} \tag{Eqn. A.4.17}$$

$$\begin{aligned}
 \frac{\partial Y(t)}{\partial p_1} = & \left\{ \frac{\alpha b_0}{p_1} t^2 e^{-p_1 t} \mathbf{u}(t) + \alpha \left[\frac{2b_0}{p_1^2} + \frac{b_1}{p_1} \right] t e^{-p_1 t} \mathbf{u}(t) + \right. \\
 & \left. \alpha \left[\frac{2b_0}{p_1^3} + \frac{2b_1}{p_1^2} \right] e^{-p_1 t} \mathbf{u}(t) + \right. \\
 & \left. + \alpha \left[-\frac{2b_0}{p_1^3} - \frac{2b_1}{p_1^2} \right] \mathbf{u}(t) + \left(\frac{\alpha b_1}{p_1} \right) t \mathbf{u}(t) \right\} \otimes \delta(t - [\tau_{bd} + \tau_{tis}])
 \end{aligned} \tag{Eqn. A.4.18}$$

$$\frac{\partial Y(t)}{\partial p_i} = \left\{ \left(\frac{\alpha b_i}{p_1^2} \right) e^{-p_1 t} \mathbf{u}(t) + \left(\frac{\alpha b_i}{p_i} \right) t e^{-p_i t} \mathbf{u}(t) + \left(\frac{\alpha b_i}{p_i^2} \right) e^{-p_i t} \mathbf{u}(t) - \right. \\ \left. - \left[\frac{\alpha b_i}{p_1^2} + \frac{\alpha b_i}{p_i^2} \right] \mathbf{u}(t) + \left(\frac{\alpha b_i}{p_1} \right) t \mathbf{u}(t) \right\} \otimes \delta(t - [\tau_{bd} + \tau_{tis}]); \quad i = 2, \dots, N \quad (\text{Eqn. A.4.19})$$

$$\frac{\partial Y(t)}{\partial \tau_{bd}} = -\alpha F(t) \otimes \delta(t - [\tau_{bd} + \tau_{tis}]) \quad (\text{Eqn. A.4.20})$$

A.4.3 Calculation of Additional Gradients: Generalized Feng Model

As in *Section A.3*, focus in this section will be on evaluating the gradient of the convolution of the second peak of the generalized Feng model only. That is, on evaluating $[M(t; \theta) \otimes \alpha e^{-\beta t} u(t)]$, where $M(t; \theta)$ is as defined in (*Eqn. A. 1.43*); though here the specific dependence of $M(t)$ on the model parameters θ is made explicit by writing $M(t; \theta)$. The complete gradients with respect to the generalized Feng model can be obtained by summing the corresponding gradients of the Feng model and the gradients of the second peak as demonstrated for the IBIF model parameter θ_i in (*Eqn. A. 4.21*), where $Y(t)$ is as defined in (*Eqn. A. 3.18*) above.

$$\frac{\partial Y(t; \theta, \delta)}{\partial \theta_i} = \left\{ \frac{\partial [(F(t; \theta) \otimes \alpha e^{-\beta t} u(t)) \otimes \delta(t - [\tau_{bd} + \tau_{tis}])]}{\partial \theta_i} + \right. \\ \left. + \frac{\partial [(M(t; \theta) \otimes \alpha e^{-\beta t} u(t)) \otimes \delta(t - [\tau_{bd} + \tau_{tis}])]}{\partial \theta_i} \right\} \quad (\text{Eqn. A.4.21})$$

a. Reversible Kinetics

For the case of reversible kinetics, the bottom equation of (Eqn. A.4.21), denoted as $J(\theta, \delta)$ in (Eqn. A.4.22) will take the form of (Eqn. A.4.23). This equation is slightly modified from the version that was derived in Section A.2, where it appears as (Eqn. A.2.20).

$$J(\theta, \delta) = \left(M(t; \theta) \otimes \alpha e^{-\beta t} \mathbf{u}(t) \right) \otimes \delta(t - [\tau_{bd} + \tau_{dblPk} + \tau_{tis}]) \quad (\text{Eqn. A.4.22})$$

$$J(\theta, \delta) = \alpha \left\{ \left[\frac{r_1 a_0}{(-r_1 + \beta)} \right] t e^{-r_1 t} \mathbf{u}(t) + \left[\frac{-r_1 a_0}{(-r_1 + \beta)^2} + \frac{a_0}{(-r_1 + \beta)} \right] e^{-r_1 t} \mathbf{u}(t) - \left[\frac{a_0}{\beta} \right] \mathbf{u}(t) - \left[\frac{-r_1 a_0}{(-r_1 + \beta)^2} + \frac{a_0}{(-r_1 + \beta)} - \frac{a_0}{\beta} \right] e^{-\beta t} \mathbf{u}(t) \right\} \otimes \delta(t - [\tau_{bd} + \tau_{dp} + \tau_{tis}]) \quad (\text{Eqn. A.4.23})$$

The resulting gradients with respect to the IBIF model parameters: a_0 , r_1 , and τ_{dblPk} are given below as (Eqn. A.4.24), (Eqn. A.4.25), and (Eqn. A.4.26), respectively. Note the bulk time delay, τ_{bd} also appears in (Eqn. A.4.23), because τ_{bd} describes the overall delay on the IBIF model. (Eqn. A.4.27) gives the gradient of $J(\theta, \delta)$ with respect to τ_{bd} .

$$\frac{\delta J(\theta, \delta)}{\delta a_0} = \left\{ \left[\frac{\alpha r_1}{(-r_1 + \beta)} \right] t e^{-r_1 t} + \left[\frac{-\alpha r_1}{(-r_1 + \beta)^2} + \frac{\alpha}{(-r_1 + \beta)} \right] e^{-r_1 t} - \left[\frac{\alpha}{\beta} \right] \mathbf{u}(t) - \left[\frac{-\alpha r_1}{(-r_1 + \beta)^2} + \frac{\alpha}{(-r_1 + \beta)} - \frac{\alpha}{\beta} \right] e^{-\beta t} \right\} \otimes \delta(t - [\tau_{bd} + \tau_{dp} + \tau_{tis}]) \quad (\text{Eqn. A.4.24})$$

$$\frac{\delta J(\theta, \delta)}{\delta r_1} = \left\{ \left[\frac{-\alpha a_0 r_1}{(-r_1 + \beta)} t^2 e^{-r_1 t} + \frac{2\alpha a_0 r_1}{(-r_1 + \beta)^2} t e^{-r_1 t} - \frac{2\alpha a_0 r_1}{(-r_1 + \beta)^3} e^{-r_1 t} + \frac{2\alpha a_0 r_1}{(-r_1 + \beta)^3} e^{-\beta t} \right] \otimes \delta(t - [\tau_{bd} + \tau_{dp} + \tau_{tis}]) \right\} \quad (\text{Eqn. A.4.25})$$

$$\frac{\delta J(\theta, \delta)}{\delta \tau_{dblPk}} = \left\{ \beta \left(M(t; \theta) \otimes \alpha e^{-\beta t} \mathbf{u}(t) \right) - \alpha M(t; \theta) \right\} \otimes \delta(t - [\tau_{bd} + \tau_{dp} + \tau_{tis}]) \quad (\text{Eqn. A.4.26})$$

$$\frac{\delta J(\theta, \delta)}{\delta \tau_{bd}} = \left\{ \beta Y(t; \theta, \delta) - \alpha (F(t; \theta) + M(t; \theta)) \right\} \otimes \delta(t - [\tau_{bd} + \tau_{tis}]) \quad (\text{Eqn. A.4.27})$$

b. Trapping

The system response function for the additional second order pole component of the generalized Feng IBIF model assuming irreversible tracer kinetics was derived above in *Section A.3*, though it is repeated here as (*Eqn. A.4.28*). The corresponding gradients of (*Eqn. A.4.28*) with respect to the additional second order pole parameters of the generalized Feng model are given in (*Eqn. A.4.29*) thru (*Eqn. A.4.31*). Note the bulk time delay, τ_{bd} also appears in this equation (*Eqn. A.4.28*), because τ_{bd} describes the overall delay on the IBIF model. (*Eqn. A.4.32*) gives the gradient with respect to τ_{bd} .

$$M(t; \theta, \delta) \otimes \alpha \mathbf{u}(t) = \left\{ -\mathbf{a}_0 t e^{-r_1 t} \mathbf{u}(t) - \frac{2\mathbf{a}_0}{r_1} e^{-r_1 t} \mathbf{u}(t) + \frac{2\mathbf{a}_0}{r_1} \mathbf{u}(t) - \mathbf{a}_0 t \mathbf{u}(t) \right\} \otimes \delta(t - [\tau_{bd} + \tau_{dblPk}]) \quad (\text{Eqn. A.4.28})$$

$$\frac{\delta [M(t; \theta, \delta) \otimes \alpha \mathbf{u}(t)]}{\delta a_0} = \left\{ -\alpha t e^{-r_1 t} \mathbf{u}(t) - \frac{2\alpha}{r_1} e^{-r_1 t} \mathbf{u}(t) + \frac{2\alpha}{r_1} \mathbf{u}(t) - \alpha t \mathbf{u}(t) \right\} \otimes \delta(t - [\tau_{bd} + \tau_{dblPk} + \tau_{tis}]) \quad (\text{Eqn. A.4.29})$$

$$\frac{\delta[M(t;\theta,\delta)\otimes\alpha\mathbf{u}(t)]}{\delta r_1} = \left\{ \alpha a_0 t^2 e^{-r_1 t} \mathbf{u}(t) + \frac{2\alpha a_0}{r_1} t e^{-r_1 t} \mathbf{u}(t) + \right. \\ \left. + \frac{2\alpha a_0}{r_1^2} e^{-r_1 t} \mathbf{u}(t) - \right. \\ \left. - \frac{2\alpha a_0}{r_1^2} \mathbf{u}(t) \right\} \otimes \delta(t - [\tau_{bd} + \tau_{dblPk} + \tau_{tis}]) \quad (\text{Eqn. A.4.30})$$

$$\frac{\delta[M(t;\theta,\delta)\otimes\alpha\mathbf{u}(t)]}{\delta \tau_{dp}} = -\alpha M(t; \theta, \delta) \otimes \delta(t - [\tau_{bd} + \tau_{dp} + \tau_{tis}]) \quad (\text{Eqn. A.4.31})$$

$$\frac{\delta[(F(t;\theta,\delta)+M(t;\theta,\delta))\otimes\alpha\mathbf{u}(t)]}{\delta \tau_{bd}} = -\alpha(F(t; \theta, \delta) + M(t; \theta, \delta)) \otimes \delta(t - [\tau_{bd} + \tau_{tis}]) \quad (\text{Eqn. A.4.32})$$

BIBLIOGRAPHY

- [1] D. N. Louis *et al.*, "The 2007 WHO classification of tumours of the central nervous system," *Acta Neuropathol*, vol. 114, no. 2, pp. 97-109, Aug 2007.
- [2] Q. T. Ostrom *et al.*, "CBTRUS statistical report: Primary brain and central nervous system tumors diagnosed in the United States in 2006-2010," *Neuro Oncol*, vol. 15 Suppl 2, pp. ii1-56, Nov 2013.
- [3] Q. T. Ostrom *et al.*, "CBTRUS Statistical Report: Primary brain and other central nervous system tumors diagnosed in the United States in 2010-2014," *Neuro Oncol*, vol. 19, no. suppl_5, pp. v1-v88, Nov 6 2017.
- [4] R. Stupp *et al.*, "Radiotherapy plus concomitant and adjuvant temozolomide for glioblastoma," *N Engl J Med*, vol. 352, no. 10, pp. 987-96, Mar 10 2005.
- [5] R. Stupp *et al.*, "Effects of radiotherapy with concomitant and adjuvant temozolomide versus radiotherapy alone on survival in glioblastoma in a randomised phase III study: 5-year analysis of the EORTC-NCIC trial," *Lancet Oncol*, vol. 10, no. 5, pp. 459-66, May 2009.
- [6] J. P. Thakkar *et al.*, "Epidemiologic and molecular prognostic review of glioblastoma," *Cancer Epidemiol Biomarkers Prev*, vol. 23, no. 10, pp. 1985-96, Oct 2014.
- [7] E. A. Eisenhauer *et al.*, "New response evaluation criteria in solid tumours: revised RECIST guideline (version 1.1)," *Eur J Cancer*, vol. 45, no. 2, pp. 228-47, Jan 2009.
- [8] P. Y. Wen *et al.*, "Updated response assessment criteria for high-grade gliomas: response assessment in neuro-oncology working group," *J Clin Oncol*, vol. 28, no. 11, pp. 1963-72, Apr 10 2010.
- [9] L. C. Hygino da Cruz, Jr., I. Rodriguez, R. C. Domingues, E. L. Gasparetto, and A. G. Sorensen, "Pseudoprogression and pseudoresponse: imaging challenges in the assessment of posttreatment glioma," (in eng), *AJNR. American journal of neuroradiology*, Review vol. 32, no. 11, pp. 1978-85, Dec 2011.

- [10] M. J. van den Bent, M. A. Vogelbaum, P. Y. Wen, D. R. Macdonald, and S. M. Chang, "End point assessment in gliomas: novel treatments limit usefulness of classical Macdonald's Criteria," (in eng), *Journal of clinical oncology : official journal of the American Society of Clinical Oncology*, vol. 27, no. 18, pp. 2905-8, Jun 20 2009.
- [11] A. A. Brandes *et al.*, "Disease progression or pseudoprogression after concomitant radiochemotherapy treatment: pitfalls in neurooncology," (in eng), *Neuro-oncology*, Review vol. 10, no. 3, pp. 361-7, Jun 2008.
- [12] J. C. Easaw *et al.*, "Canadian recommendations for the treatment of recurrent or progressive glioblastoma multiforme," (in eng), *Current oncology*, vol. 18, no. 3, pp. e126-36, Jun 2011.
- [13] M. J. Oborski, C. M. Laymon, F. S. Lieberman, and J. M. Mountz, "Distinguishing pseudoprogression from progression in high-grade gliomas: a brief review of current clinical practice and demonstration of the potential value of 18F-FDG PET," *Clin Nucl Med*, vol. 38, no. 5, pp. 381-4, May 2013.
- [14] W. Chen, "Clinical applications of PET in brain tumors," *J Nucl Med*, vol. 48, no. 9, pp. 1468-81, Sep 2007.
- [15] M. Defrise, D. W. Townsend, and R. Clack, "Three-dimensional image reconstruction from complete projections," *Phys Med Biol*, vol. 34, no. 5, pp. 573-87, May 1989.
- [16] G. Brix *et al.*, "Performance evaluation of a whole-body PET scanner using the NEMA protocol. National Electrical Manufacturers Association," *J Nucl Med*, vol. 38, no. 10, pp. 1614-23, Oct 1997.
- [17] G. Delso *et al.*, "Performance measurements of the Siemens mMR integrated whole-body PET/MR scanner," *J Nucl Med*, vol. 52, no. 12, pp. 1914-22, Dec 2011.
- [18] A. M. Karlberg, O. Saether, L. Eikenes, and P. E. Goa, "Quantitative comparison of PET performance-Siemens Biograph mCT and mMR," *EJNMMI Phys*, vol. 3, no. 1, p. 5, Dec 2016.
- [19] M. Reivich *et al.*, "The [18F]fluorodeoxyglucose method for the measurement of local cerebral glucose utilization in man," *Circ Res*, vol. 44, no. 1, pp. 127-37, Jan 1979.
- [20] L. Sokoloff *et al.*, "The [14C]deoxyglucose method for the measurement of local cerebral glucose utilization: theory, procedure, and normal values in the conscious and anesthetized albino rat," *J Neurochem*, vol. 28, no. 5, pp. 897-916, May 1977.
- [21] N. Ginovart, "Imaging the dopamine system with in vivo [11C]raclopride displacement studies: understanding the true mechanism," *Mol Imaging Biol*, vol. 7, no. 1, pp. 45-52, Jan-Feb 2005.

- [22] L. W. Kracht *et al.*, "Methyl-[11C]- l-methionine uptake as measured by positron emission tomography correlates to microvessel density in patients with glioma," *Eur J Nucl Med Mol Imaging*, vol. 30, no. 6, pp. 868-73, Jun 2003.
- [23] N. A. Lassen and W. Perl, *Tracer kinetic methods in medical physiology*. New York: Raven Press, 1979, pp. ix, 189 p.
- [24] H. H. Coenen *et al.*, "Consensus nomenclature rules for radiopharmaceutical chemistry - Setting the record straight," *Nucl Med Biol*, vol. 55, pp. v-xi, Dec 2017.
- [25] C. S. Levin and E. J. Hoffman, "Calculation of positron range and its effect on the fundamental limit of positron emission tomography system spatial resolution," *Phys Med Biol*, vol. 44, no. 3, pp. 781-99, Mar 1999.
- [26] M. Defrise, P. E. Kinahan, and C. Michel, "Image Reconstruction Algorithms in PET," in *Positron emission tomography: Basic Science and Clinical Practice*, P. E. Valk, D. L. Bailey, D. W. Townsend, and M. N. Maisey, Eds. London: Springer-Verlag, 2004, pp. 91-114.
- [27] S. R. Meikle and R. D. Badawi, "Quantitative Techniques in PET," in *Positron emission tomography: Basic Science and Clinical Practice*, P. E. Valk, D. L. Bailey, D. W. Townsend, and M. N. Maisey, Eds. London: Springer-Verlag, 2004, pp. 115-146.
- [28] B. Bendriem and D. W. Townsend, *The theory and practice of 3D PET* (Developments in nuclear medicine, no. 32). Dordrecht ; Boston: Kluwer Academic, 1998, pp. xvi, 167 p.
- [29] C.-M. Kao, P. La Riviere, and X. Pan, "Basics of Imaging Theory and Statistics," in *Emission Tomography: The Fundamentals of PET and SPECT*, M. N. Wernick and J. N. Aarsvold, Eds. London: Elsevier Academic Press, 2004, pp. 103-126.
- [30] P. E. Kinahan, M. Defrise, and R. Clackdoyle, "Analytic Reconstruction Methods," in *Emission Tomography: The Fundamentals of PET and SPECT*, M. N. Wernick and J. N. Aarsvold, Eds. London: Elsevier Academic Press, 2004, pp. 421-442.
- [31] J. L. Prince and J. M. Links, *Medical imaging signals and systems*, 2. ed. pp. xvii, 519 p.
- [32] D. S. Lalush and M. N. Wernick, "Iterative Image Reconstuction," in *Emission Tomography: The Fundamentals of PET and SPECT*, M. N. Wernick and J. N. Aarsvold, Eds. London: Elsevier Academic Press, 2004, pp. 443-472.
- [33] M. E. Kamasak, C. A. Bouman, E. D. Morris, and K. Sauer, "Direct reconstruction of kinetic parameter images from dynamic PET data," *IEEE Trans Med Imaging*, vol. 24, no. 5, pp. 636-50, May 2005.
- [34] T. Beyer *et al.*, "A combined PET/CT scanner for clinical oncology," *Journal of Nuclear Medicine*, vol. 41, no. 8, pp. 1369-1379, Aug 2000.

- [35] K. J. Lacroix, B. M. W. Tsui, B. H. Hasegawa, and J. K. Brown, "INVESTIGATION OF THE USE OF X-RAY CT IMAGES FOR ATTENUATION COMPENSATION IN SPECT," *Ieee Transactions on Nuclear Science*, vol. 41, no. 6, pp. 2793-2799, Dec 1994.
- [36] S. C. Blankespoor *et al.*, "Attenuation correction of SPECT using X-ray CT on an emission-transmission CT system: Myocardial perfusion assessment," *Ieee Transactions on Nuclear Science*, vol. 43, no. 4, pp. 2263-2274, Aug 1996.
- [37] P. E. Kinahan, D. W. Townsend, T. Beyer, and D. Sashin, "Attenuation correction for a combined 3D PET/CT scanner," *Medical Physics*, vol. 25, no. 10, pp. 2046-2053, Oct 1998.
- [38] C. Burger, G. Goerres, S. Schoenes, A. Buck, A. H. R. Lonn, and G. K. von Schulthess, "PET attenuation coefficients from CT images: experimental evaluation of the transformation of CT into PET 511-keV attenuation coefficients," *European Journal of Nuclear Medicine and Molecular Imaging*, vol. 29, no. 7, pp. 922-927, Jul 2002.
- [39] C. Y. Bai, L. Shao, A. J. Da Silva, and Z. Zhao, "A generalized model for the conversion from CT numbers to linear attenuation coefficients," *Ieee Transactions on Nuclear Science*, vol. 50, no. 5, pp. 1510-1515, Oct 2003.
- [40] P. E. Kinahan, B. H. Hasegawa, and T. Beyer, "X-ray-based attenuation correction for positron emission tomography/computed tomography scanners," *Seminars in Nuclear Medicine*, vol. 33, no. 3, pp. 166-179, Jul 2003.
- [41] H. Zaidi and B. Hasegawa, "Determination of the attenuation map in emission tomography," *Journal of Nuclear Medicine*, vol. 44, no. 2, pp. 291-315, Feb 2003.
- [42] J. P. J. Carney, D. W. Townsend, V. Rappoport, and B. Bendriem, "Method for transforming CT images for attenuation correction in PET/CT imaging," *Medical Physics*, vol. 33, no. 4, pp. 976-983, Apr 2006.
- [43] W. T. Dixon, "SIMPLE PROTON SPECTROSCOPIC IMAGING," (in English), *Radiology*, Article vol. 153, no. 1, pp. 189-194, 1984.
- [44] A. Martinez-Moller *et al.*, "Tissue Classification as a Potential Approach for Attenuation Correction in Whole-Body PET/MRI: Evaluation with PET/CT Data," *Journal of Nuclear Medicine*, vol. 50, no. 4, pp. 520-526, Apr 2009.
- [45] I. Bezrukov, F. Mantlik, H. Schmidt, B. Schoelkopf, and B. J. Pichler, "MR-Based PET Attenuation Correction for PET/MR Imaging," *Seminars in Nuclear Medicine*, vol. 43, no. 1, pp. 45-59, Jan 2013.
- [46] G. Wagenknecht, H.-J. Kaiser, F. M. Mottaghy, and H. Herzog, "MRI for attenuation correction in PET: methods and challenges," *Magnetic Resonance Materials in Physics Biology and Medicine*, vol. 26, no. 1, pp. 99-113, Feb 2013.

- [47] J. Du and G. M. Bydder, "Qualitative and quantitative ultrashort-TE MRI of cortical bone," *Nmr in Biomedicine*, vol. 26, no. 5, pp. 489-506, May 2013.
- [48] C. Catana *et al.*, "Toward Implementing an MRI-Based PET Attenuation-Correction Method for Neurologic Studies on the MR-PET Brain Prototype," *Journal of Nuclear Medicine*, vol. 51, no. 9, pp. 1431-1438, Sep 1 2010.
- [49] V. Keereman, Y. Fierens, T. Broux, Y. De Deene, M. Lonneux, and S. Vandenberghe, "MRI-Based Attenuation Correction for PET/MRI Using Ultrashort Echo Time Sequences," *Journal of Nuclear Medicine*, vol. 51, no. 5, pp. 812-818, May 1 2010.
- [50] A. Santos Ribeiro, E. R. Kops, H. Herzog, and P. Almeida, "Skull segmentation of UTE MR images by probabilistic neural network for attenuation correction in PET/MR," *Nuclear Instruments & Methods in Physics Research Section a-Accelerators Spectrometers Detectors and Associated Equipment*, vol. 702, pp. 114-116, Feb 21 2013.
- [51] D. J. Tyler, M. D. Robson, R. M. Henkelman, I. R. Young, and G. M. Bydder, "Magnetic resonance imaging with ultrashort TE (UTE) PULSE sequences: Technical considerations," *Journal of Magnetic Resonance Imaging*, vol. 25, no. 2, pp. 279-289, Feb 2007.
- [52] J. Ouyang, S. Y. Chun, Y. Petibon, A. A. Bonab, N. Alpert, and G. El Fakhri, "Bias Atlases for Segmentation-Based PET Attenuation Correction Using PET-CT and MR," *Ieee Transactions on Nuclear Science*, vol. 60, no. 5, pp. 3373-3382, Oct 2013.
- [53] V. Keereman, P. Mollet, Y. Berker, V. Schulz, and S. Vandenberghe, "Challenges and current methods for attenuation correction in PET/MR," *Magnetic Resonance Materials in Physics Biology and Medicine*, vol. 26, no. 1, pp. 81-98, Feb 2013.
- [54] C. Messiou *et al.*, "Quantifying sclerotic bone metastases with 2D ultra short TE MRI: A feasibility study," *Cancer Biomarkers*, vol. 7, no. 4-5, pp. 211-218, 2010 2010.
- [55] P. Khateri, H. S. Rad, A. Fathi, and M. R. Ay, "Generation of attenuation map for MR-based attenuation correction of PET data in the head area employing 3D short echo time MR imaging," *Nuclear Instruments & Methods in Physics Research Section a-Accelerators Spectrometers Detectors and Associated Equipment*, vol. 702, pp. 133-136, Feb 21 2013.
- [56] D. Izquierdo-Garcia *et al.*, "An SPM8-based approach for attenuation correction combining segmentation and nonrigid template formation: application to simultaneous PET/MR brain imaging," *J Nucl Med*, vol. 55, no. 11, pp. 1825-30, Nov 2014.
- [57] C. Burger, G. Goerres, S. Schoenes, A. Buck, A. H. Lonn, and G. K. Von Schulthess, "PET attenuation coefficients from CT images: experimental evaluation of the transformation of CT into PET 511-keV attenuation coefficients," *Eur J Nucl Med Mol Imaging*, vol. 29, no. 7, pp. 922-7, Jul 2002.

- [58] C. N. Ladefoged *et al.*, "A multi-centre evaluation of eleven clinically feasible brain PET/MRI attenuation correction techniques using a large cohort of patients," *Neuroimage*, vol. 147, pp. 346-359, Feb 15 2017.
- [59] F. L. Andersen *et al.*, "Combined PET/MR imaging in neurology: MR-based attenuation correction implies a strong spatial bias when ignoring bone," *Neuroimage*, vol. 84, pp. 206-216, Jan 2014.
- [60] C. Laymon *et al.*, "Comparison of MR-based with 511-keV transmission-based attenuation correction in neuro FDG PET/MR," *Journal of Nuclear Medicine*, vol. 55, no. supplement 1, p. 2098, May 1, 2014 2014.
- [61] D. Izquierdo-Garcia *et al.*, "An SPM8-Based Approach for Attenuation Correction Combining Segmentation and Nonrigid Template Formation: Application to Simultaneous PET/MR Brain Imaging," *Journal of Nuclear Medicine*, Article vol. 55, no. 11, pp. 1825-1830, Nov 2014.
- [62] C. N. Ladefoged *et al.*, "A multi-centre evaluation of eleven clinically feasible brain PET/MRI attenuation correction techniques using a large cohort of patients," *Neuroimage*, vol. 147, pp. 346-359, Feb 2017.
- [63] C. M. Laymon *et al.*, "Image-Based 2D Re-Projection for Attenuation Substitution in PET Neuroimaging," *Molecular Imaging and Biology*, journal article February 27 2018.
- [64] C. C. Watson, "New, faster, image-based scatter correction for 3D PET," in *1999 IEEE Nuclear Science Symposium. Conference Record. 1999 Nuclear Science Symposium and Medical Imaging Conference (Cat. No.99CH37019)*, 1999, vol. 3, pp. 1637-1641 vol.3.
- [65] C. C. Watson, D. Newport, M. E. Casey, R. A. deKemp, R. S. Beanlands, and M. Schmand, "Evaluation of simulation-based scatter correction for 3-D PET cardiac imaging," *IEEE Transactions on Nuclear Science*, vol. 44, no. 1, pp. 90-97, 1997.
- [66] G. F. Knoll, *Radiation detection and measurement*, 4th ed. Hoboken, N.J.: John Wiley, 2010, pp. xxvi, 830 p.
- [67] B. Pawelke, "Metabolite analysis in positron emission tomography studies: examples from food sciences," *Amino Acids*, vol. 29, no. 4, pp. 377-88, Dec 2005.
- [68] J. C. Price *et al.*, "Analyses of [(18)F]altanserin bolus injection PET data. II: consideration of radiolabeled metabolites in humans," *Synapse*, vol. 41, no. 1, pp. 11-21, Jul 2001.
- [69] C. Schiepers, W. Chen, M. Dahlbom, T. Cloughesy, C. K. Hoh, and S. C. Huang, "18F-fluorothymidine kinetics of malignant brain tumors," *Eur J Nucl Med Mol Imaging*, vol. 34, no. 7, pp. 1003-11, Jul 2007.
- [70] L. Horky, M. Muzi, J. Bruyere, M. Kijewski, and M.-A. Park, "Sep-Pak analysis is necessary for analyzing serial brain FLT-PET/CT images in glioblastoma multiforme

- (GBM) patients undergoing treatment," *Journal of Nuclear Medicine*, vol. 53, no. supplement 1, pp. 1255-1255, 2012.
- [71] P. Zanotti-Fregonara, K. Chen, J. S. Liow, M. Fujita, and R. B. Innis, "Image-derived input function for brain PET studies: many challenges and few opportunities," *J Cereb Blood Flow Metab*, vol. 31, no. 10, pp. 1986-98, Oct 2011.
- [72] R. Buchert *et al.*, "PET Pharmacokinetic Course Manual," in *PET Pharmacokinetics Course 2016, Yale University, New Haven, Connecticut, USA*, J. van den Hoff and R. P. Maguire, Eds., ed. .
- [73] S. M. Kay, *Intuitive probability and random processes using MATLAB*. New York: Springer, 2006, pp. xviii, 833 p.
- [74] A. Papoulis and S. U. Pillai, *Probability, random variables, and stochastic processes*, 4th ed. Boston: McGraw-Hill, 2002, pp. x, 852 p.
- [75] M. Soret, S. L. Bacharach, and I. Buvat, "Partial-volume effect in PET tumor imaging," *J Nucl Med*, vol. 48, no. 6, pp. 932-45, Jun 2007.
- [76] K. Erlandsson, I. Buvat, P. H. Pretorius, B. A. Thomas, and B. F. Hutton, "A review of partial volume correction techniques for emission tomography and their applications in neurology, cardiology and oncology," *Phys Med Biol*, vol. 57, no. 21, pp. R119-59, Nov 7 2012.
- [77] C. C. Meltzer, J. P. Leal, H. S. Mayberg, H. N. Wagner, Jr., and J. J. Frost, "Correction of PET data for partial volume effects in human cerebral cortex by MR imaging," *J Comput Assist Tomogr*, vol. 14, no. 4, pp. 561-70, Jul-Aug 1990.
- [78] H. W. Muller-Gartner *et al.*, "Measurement of radiotracer concentration in brain gray matter using positron emission tomography: MRI-based correction for partial volume effects," *J Cereb Blood Flow Metab*, vol. 12, no. 4, pp. 571-83, Jul 1992.
- [79] O. G. Rousset, Y. Ma, and A. C. Evans, "Correction for partial volume effects in PET: principle and validation," *J Nucl Med*, vol. 39, no. 5, pp. 904-11, May 1998.
- [80] S. Ashrafinia *et al.*, "Generalized PSF modeling for optimized quantitation in PET imaging," *Phys Med Biol*, vol. 62, no. 12, pp. 5149-5179, Jun 21 2017.
- [81] B. W. Jakoby, Y. Bercier, C. C. Watson, B. Bendriem, and D. W. Townsend, "Performance Characteristics of a New LSO PET/CT Scanner With Extended Axial Field-of-View and PSF Reconstruction," *IEEE Transactions on Nuclear Science*, vol. 56, no. 3, pp. 633-639, 2009.
- [82] P. Therasse *et al.*, "New guidelines to evaluate the response to treatment in solid tumors. European Organization for Research and Treatment of Cancer, National Cancer Institute of the United States, National Cancer Institute of Canada," *J Natl Cancer Inst*, vol. 92, no. 3, pp. 205-16, Feb 02 2000.

- [83] A. B. Miller, B. Hoogstraten, M. Staquet, and A. Winkler, "Reporting results of cancer treatment," *Cancer*, vol. 47, no. 1, pp. 207-14, Jan 01 1981.
- [84] A. Skladanowski and J. Konopa, "Adriamycin and daunomycin induce programmed cell death (apoptosis) in tumour cells," *Biochem Pharmacol*, vol. 46, no. 3, pp. 375-82, Aug 3 1993.
- [85] S. H. Kaufmann and W. C. Earnshaw, "Induction of apoptosis by cancer chemotherapy," *Exp Cell Res*, vol. 256, no. 1, pp. 42-9, Apr 10 2000.
- [86] W. Gunther, E. Pawlak, R. Damasceno, H. Arnold, and A. J. Terzis, "Temozolomide induces apoptosis and senescence in glioma cells cultured as multicellular spheroids," (in eng), *British journal of cancer*, vol. 88, no. 3, pp. 463-9, Feb 10 2003.
- [87] M. S. Ricci and W. X. Zong, "Chemotherapeutic approaches for targeting cell death pathways," *Oncologist*, vol. 11, no. 4, pp. 342-57, Apr 2006.
- [88] F. G. Blankenberg, "In vivo detection of apoptosis," (in eng), *Journal of nuclear medicine : official publication, Society of Nuclear Medicine*, vol. 49 Suppl 2, pp. 81S-95S, Jun 2008.
- [89] M. De Saint-Hubert, M. Bauwens, A. Verbruggen, and F. M. Mottaghy, "Apoptosis imaging to monitor cancer therapy: the road to fast treatment evaluation?," *Curr Pharm Biotechnol*, vol. 13, no. 4, pp. 571-83, Mar 2012.
- [90] T. Belhocine *et al.*, "Increased uptake of the apoptosis-imaging agent (99m)Tc recombinant human Annexin V in human tumors after one course of chemotherapy as a predictor of tumor response and patient prognosis," *Clin Cancer Res*, vol. 8, no. 9, pp. 2766-74, Sep 2002.
- [91] A. M. Allen *et al.*, "Assessment of response of brain metastases to radiotherapy by PET imaging of apoptosis with (1)(8)F-ML-10," (in eng), *European journal of nuclear medicine and molecular imaging*, vol. 39, no. 9, pp. 1400-8, Sep 2012.
- [92] T. Z. Belhocine *et al.*, "(99m)Tc-Annexin A5 quantification of apoptotic tumor response: a systematic review and meta-analysis of clinical imaging trials," *Eur J Nucl Med Mol Imaging*, vol. 42, no. 13, pp. 2083-97, Dec 2015.
- [93] Y. Suzuki, T. Inoue, M. Murai, M. Suzuki-Karasaki, T. Ochiai, and C. Ra, "Depolarization potentiates TRAIL-induced apoptosis in human melanoma cells: role for ATP-sensitive K⁺ channels and endoplasmic reticulum stress," *Int J Oncol*, vol. 41, no. 2, pp. 465-75, Aug 2012.
- [94] D. R. Green, *Means to an end : apoptosis and other cell death mechanisms*. Cold Spring Harbor, N.Y.: Cold Spring Harbor Laboratory Press, 2011, pp. xii, 220 p.

- [95] B. Fadeel and D. Xue, "The ins and outs of phospholipid asymmetry in the plasma membrane: roles in health and disease," *Crit Rev Biochem Mol Biol*, vol. 44, no. 5, pp. 264-77, Sep-Oct 2009.
- [96] S. K. Sahu, G. K. Aradhyam, and S. N. Gummadi, "Calcium binding studies of peptides of human phospholipid scramblases 1 to 4 suggest that scramblases are new class of calcium binding proteins in the cell," *Biochim Biophys Acta*, vol. 1790, no. 10, pp. 1274-81, Oct 2009.
- [97] S. Elmore, "Apoptosis: a review of programmed cell death," *Toxicol Pathol*, vol. 35, no. 4, pp. 495-516, Jun 2007.
- [98] G. J. Kemerink *et al.*, "Safety, biodistribution, and dosimetry of ^{99m}Tc-HYNIC-annexin V, a novel human recombinant annexin V for human application," *J Nucl Med*, vol. 44, no. 6, pp. 947-52, Jun 2003.
- [99] G. Koopman, C. P. Reutelingsperger, G. A. Kuijten, R. M. Keehnen, S. T. Pals, and M. H. van Oers, "Annexin V for flow cytometric detection of phosphatidylserine expression on B cells undergoing apoptosis," *Blood*, vol. 84, no. 5, pp. 1415-20, Sep 01 1994.
- [100] S. J. Martin *et al.*, "Early redistribution of plasma membrane phosphatidylserine is a general feature of apoptosis regardless of the initiating stimulus: inhibition by overexpression of Bcl-2 and Abl," *J Exp Med*, vol. 182, no. 5, pp. 1545-56, Nov 01 1995.
- [101] O. Ozdemir, Y. Ravindranath, and S. Savasan, "Cell-mediated cytotoxicity evaluation using monoclonal antibody staining for target or effector cells with annexinV/propidium iodide colabeling by fluorosphere-adjusted counts on three-color flow cytometry," *Cytometry A*, vol. 56, no. 1, pp. 53-60, Nov 2003.
- [102] F. G. Blankenberg, "Imaging the molecular signatures of apoptosis and injury with radiolabeled annexin V," (in eng), *Proceedings of the American Thoracic Society*, vol. 6, no. 5, pp. 469-76, Aug 15 2009.
- [103] F. G. Blankenberg and H. W. Strauss, "Will imaging of apoptosis play a role in clinical care? A tale of mice and men," *Apoptosis*, vol. 6, no. 1-2, pp. 117-23, Feb-Apr 2001.
- [104] F. G. Blankenberg, "Recent advances in the imaging of programmed cell death," *Curr Pharm Des*, vol. 10, no. 13, pp. 1457-67, 2004.
- [105] C. M. Lahorte *et al.*, "Biodistribution and dosimetry study of ¹²³I-rh-annexin V in mice and humans," *Nucl Med Commun*, vol. 24, no. 8, pp. 871-80, Aug 2003.
- [106] G. J. Kemerink *et al.*, "Biodistribution and dosimetry of ^{99m}Tc-BTAP-annexin-V in humans," *Eur J Nucl Med*, vol. 28, no. 9, pp. 1373-8, Sep 2001.
- [107] H. Kurihara *et al.*, "Imaging and dosimetry of ^{99m}Tc EC annexin V: preliminary clinical study targeting apoptosis in breast tumors," *Appl Radiat Isot*, vol. 66, no. 9, pp. 1175-82, Sep 2008.

- [108] T. Belhocine, N. Steinmetz, A. Green, and P. Rigo, "In vivo imaging of chemotherapy-induced apoptosis in human cancers," *Ann N Y Acad Sci*, vol. 1010, pp. 525-9, Dec 2003.
- [109] R. L. Haas *et al.*, "In vivo imaging of radiation-induced apoptosis in follicular lymphoma patients," *Int J Radiat Oncol Biol Phys*, vol. 59, no. 3, pp. 782-7, Jul 01 2004.
- [110] M. Kartachova, R. L. Haas, R. A. Olmos, F. J. Hoebbers, N. van Zandwijk, and M. Verheij, "In vivo imaging of apoptosis by ^{99m}Tc-Annexin V scintigraphy: visual analysis in relation to treatment response," *Radiother Oncol*, vol. 72, no. 3, pp. 333-9, Sep 2004.
- [111] S. Rottey, G. Slegers, S. Van Belle, I. Goethals, and C. Van de Wiele, "Sequential ^{99m}Tc-hydrazinonicotinamide-annexin V imaging for predicting response to chemotherapy," *J Nucl Med*, vol. 47, no. 11, pp. 1813-8, Nov 2006.
- [112] M. Kartachova, N. van Zandwijk, S. Burgers, H. van Tinteren, M. Verheij, and R. A. Valdes Olmos, "Prognostic significance of ^{99m}Tc Hynic-rh-annexin V scintigraphy during platinum-based chemotherapy in advanced lung cancer," *J Clin Oncol*, vol. 25, no. 18, pp. 2534-9, Jun 20 2007.
- [113] M. S. Kartachova, R. A. Valdes Olmos, R. L. Haas, F. J. Hoebbers, M. van Herk, and M. Verheij, "^{99m}Tc-HYNIC-rh-annexin-V scintigraphy: visual and quantitative evaluation of early treatment-induced apoptosis to predict treatment outcome," *Nucl Med Commun*, vol. 29, no. 1, pp. 39-44, Jan 2008.
- [114] F. J. Hoebbers *et al.*, "^{99m}Tc Hynic-rh-Annexin V scintigraphy for in vivo imaging of apoptosis in patients with head and neck cancer treated with chemoradiotherapy," *Eur J Nucl Med Mol Imaging*, vol. 35, no. 3, pp. 509-18, Mar 2008.
- [115] S. Rottey *et al.*, "^{99m}Tc-HYNIC Annexin-V imaging of tumors and its relationship to response to radiotherapy and/or chemotherapy," *Q J Nucl Med Mol Imaging*, vol. 51, no. 2, pp. 182-8, Jun 2007.
- [116] D. Loose, H. Vermeersch, F. De Vos, P. Deron, G. Slegers, and C. Van de Wiele, "Prognostic value of ^{99m}Tc-HYNIC annexin-V imaging in squamous cell carcinoma of the head and neck," *Eur J Nucl Med Mol Imaging*, vol. 35, no. 1, pp. 47-52, Jan 2008.
- [117] C. van de Wiele *et al.*, "Quantitative tumor apoptosis imaging using technetium-^{99m}-HYNIC annexin V single photon emission computed tomography," *J Clin Oncol*, vol. 21, no. 18, pp. 3483-7, Sep 15 2003.
- [118] H. Vermeersch *et al.*, "^{99m}Tc-HYNIC Annexin-V imaging of primary head and neck carcinoma," *Nucl Med Commun*, vol. 25, no. 3, pp. 259-63, Mar 2004.
- [119] A. Cohen, A. Shirvan, G. Levin, H. Grimberg, A. Reshef, and I. Ziv, "From the Gla domain to a novel small-molecule detector of apoptosis," (in eng), *Cell research*, vol. 19, no. 5, pp. 625-37, May 2009.

- [120] A. A. Neves and K. M. Brindle, "Imaging cell death," (in eng), *Journal of nuclear medicine : official publication, Society of Nuclear Medicine*, vol. 55, no. 1, pp. 1-4, Jan 2014.
- [121] X. Bao *et al.*, "The preclinical study of predicting radiosensitivity in human nasopharyngeal carcinoma xenografts by 18F-ML-10 animal- PET/CT imaging," *Oncotarget*, vol. 7, no. 15, pp. 20743-52, Apr 12 2016.
- [122] E. Demirci *et al.*, "Preclinical Evaluation of 18F-ML-10 to Determine Timing of Apoptotic Response to Chemotherapy in Solid Tumors," *Mol Imaging*, vol. 16, p. 1536012116685941, Jan 01 2017.
- [123] F. Hyafil *et al.*, "Detection of Apoptotic Cells in a Rabbit Model with Atherosclerosis-Like Lesions Using the Positron Emission Tomography Radiotracer [18F]ML-10," *Mol Imaging*, vol. 14, pp. 433-42, 2015.
- [124] A. Reshef *et al.*, "Molecular imaging of neurovascular cell death in experimental cerebral stroke by PET," *J Nucl Med*, vol. 49, no. 9, pp. 1520-8, Sep 2008.
- [125] M. Bauwens, M. De Saint-Hubert, J. Cleynhens, C. Vandeputte, J. Li, and E. Devos, "In vitro and in vivo comparison of 18F and 123I-labeled ML10 with 68Ga-Cys2-AnxA5 for molecular imaging of apoptosis," *Q J Nucl Med Mol Imaging*, vol. 57, no. 2, pp. 187-200, Jun 2013.
- [126] M. Kadirvel *et al.*, "Detection of apoptosis by PET/CT with the diethyl ester of [(1)(8)F]ML-10 and fluorescence imaging with a dansyl analogue," *Bioorg Med Chem*, vol. 22, no. 1, pp. 341-9, Jan 01 2014.
- [127] M. Medoc *et al.*, "In Vivo Evaluation of Radiofluorinated Caspase-3/7 Inhibitors as Radiotracers for Apoptosis Imaging and Comparison with [18F]ML-10 in a Stroke Model in the Rat," *Mol Imaging Biol*, vol. 18, no. 1, pp. 117-26, Feb 2016.
- [128] T. H. Witney *et al.*, "A Systematic Comparison of 18F-C-SNAT to Established Radiotracer Imaging Agents for the Detection of Tumor Response to Treatment," *Clin Cancer Res*, vol. 21, no. 17, pp. 3896-905, Sep 01 2015.
- [129] J. Høglund *et al.*, "18F-ML-10, a PET tracer for apoptosis: first human study," (in eng), *Journal of nuclear medicine : official publication, Society of Nuclear Medicine*, vol. 52, no. 5, pp. 720-5, May 2011.
- [130] C. Shaha, R. Tripathi, and D. P. Mishra, "Male germ cell apoptosis: regulation and biology," *Philos Trans R Soc Lond B Biol Sci*, vol. 365, no. 1546, pp. 1501-15, May 27 2010.
- [131] C. J. Galban *et al.*, "Prospective analysis of parametric response map-derived MRI biomarkers: identification of early and distinct glioma response patterns not predicted by standard radiographic assessment," *Clin Cancer Res*, vol. 17, no. 14, pp. 4751-60, Jul 15 2011.

- [132] T. C. Kwee *et al.*, "Comparison of apparent diffusion coefficients and distributed diffusion coefficients in high-grade gliomas," *J Magn Reson Imaging*, vol. 31, no. 3, pp. 531-7, Mar 2010.
- [133] B. Ma *et al.*, "Voxel-by-voxel functional diffusion mapping for early evaluation of breast cancer treatment," *Inf Process Med Imaging*, vol. 21, pp. 276-87, 2009.
- [134] M. J. Oborski, C. M. Laymon, F. S. Lieberman, J. Drappatz, R. L. Hamilton, and J. M. Mountz, "First use of (18)F-labeled ML-10 PET to assess apoptosis change in a newly diagnosed glioblastoma multiforme patient before and early after therapy," (in eng), *Brain and behavior*, vol. 4, no. 2, pp. 312-5, Mar 2014.
- [135] M. J. Oborski, C. M. Laymon, F. S. Lieberman, Y. X. Qian, J. Drappatz, and J. M. Mountz, "F-18 ML-10 PET: Initial Experience in Glioblastoma Multiforme Therapy Response Assessment," (in English), *Tomography*, Article vol. 2, no. 4, pp. 317-324, Dec 2016.
- [136] M. J. Oborski, C. M. Laymon, Y. Qian, F. S. Lieberman, A. D. Nelson, and J. M. Mountz, "Challenges and Approaches to Quantitative Therapy Response Assessment in Glioblastoma Multiforme Using the Novel Apoptosis Positron Emission Tomography Tracer F-18 ML-10," (in eng), *Translational oncology*, vol. 7, no. 1, pp. 111-9, Feb 2014.
- [137] C. M. Laymon *et al.*, "Image-Based 2D Re-Projection for Attenuation Substitution in PET Neuroimaging," *Mol Imaging Biol*, Feb 27 2018.
- [138] K. P. Wong, D. Feng, S. R. Meikle, and M. J. Fulham, "Simultaneous estimation of physiological parameters and the input function--in vivo PET data," *IEEE Trans Inf Technol Biomed*, vol. 5, no. 1, pp. 67-76, Mar 2001.
- [139] K. B. Contractor, L. M. Kenny, C. R. Coombes, F. E. Turkheimer, E. O. Aboagye, and L. Rosso, "Evaluation of limited blood sampling population input approaches for kinetic quantification of [18F]fluorothymidine PET data," *EJNMMI Res*, vol. 2, p. 11, Mar 24 2012.
- [140] D. Vriens, L. F. de Geus-Oei, W. J. Oyen, and E. P. Visser, "A curve-fitting approach to estimate the arterial plasma input function for the assessment of glucose metabolic rate and response to treatment," *J Nucl Med*, vol. 50, no. 12, pp. 1933-9, Dec 2009.
- [141] K. Wakita *et al.*, "Simplification for measuring input function of FDG PET: investigation of 1-point blood sampling method," *J Nucl Med*, vol. 41, no. 9, pp. 1484-90, Sep 2000.
- [142] P. Zanotti-Fregonara *et al.*, "Population-based input function and image-derived input function for [(1)(1)C](R)-rolipram PET imaging: methodology, validation and application to the study of major depressive disorder," *Neuroimage*, vol. 63, no. 3, pp. 1532-41, Nov 15 2012.

- [143] K. W. Chen, S. C. Huang, and D. C. Yu, "The effects of measurement errors in the plasma radioactivity curve on parameter estimation in positron emission tomography," *Phys Med Biol*, vol. 36, no. 9, pp. 1183-200, Sep 1991.
- [144] Y. Cheng and I. S. Yetik, "Propagation of Blood Function Errors to the Estimates of Kinetic Parameters with Dynamic PET," *Int J Biomed Imaging*, vol. 2011, p. 234679, 2011.
- [145] D. Feng and X. Wang, "A computer simulation study on the effects of input function measurement noise in tracer kinetic modeling with positron emission tomography (PET)," *Comput Biol Med*, vol. 23, no. 1, pp. 57-68, Jan 1993.
- [146] R. H. Huesman and B. M. Mazoyer, "Kinetic data analysis with a noisy input function," *Phys Med Biol*, vol. 32, no. 12, pp. 1569-79, Dec 1987.
- [147] P. Zanotti-Fregonara *et al.*, "Comparison of eight methods for the estimation of the image-derived input function in dynamic [(18)F]-FDG PET human brain studies," *J Cereb Blood Flow Metab*, vol. 29, no. 11, pp. 1825-35, Nov 2009.
- [148] E. Croteau *et al.*, "Image-derived input function in dynamic human PET/CT: methodology and validation with 11C-acetate and 18F-fluorothioheptadecanoic acid in muscle and 18F-fluorodeoxyglucose in brain," *Eur J Nucl Med Mol Imaging*, vol. 37, no. 8, pp. 1539-50, Aug 2010.
- [149] E. K. Fung and R. E. Carson, "Cerebral blood flow with [15O]water PET studies using an image-derived input function and MR-defined carotid centerlines," *Phys Med Biol*, vol. 58, no. 6, pp. 1903-23, Mar 21 2013.
- [150] J. E. Mourik *et al.*, "Image-derived input functions for PET brain studies," *Eur J Nucl Med Mol Imaging*, vol. 36, no. 3, pp. 463-71, Mar 2009.
- [151] D. Feng, S. C. Huang, and X. Wang, "Models for computer simulation studies of input functions for tracer kinetic modeling with positron emission tomography," *Int J Biomed Comput*, vol. 32, no. 2, pp. 95-110, Mar 1993.
- [152] U. Simoncic and R. Jeraj, "Cumulative input function method for linear compartmental models and spectral analysis in PET," *J Cereb Blood Flow Metab*, vol. 31, no. 2, pp. 750-6, Feb 2011.
- [153] Y. Bard, *Nonlinear parameter estimation*. New York,: Academic Press, 1974, pp. x, 341 p.
- [154] J. A. Jacquez, *Compartmental analysis in biology and medicine*. , 3 ed. Ann Arbor, Michigan: BioMedware, 1996.
- [155] S. M. Kay, *Fundamentals of Statistical Signal Processing, Volume I: Estimation Theory* (Prentice Hall signal processing series). Englewood Cliffs, N.J.: Prentice-Hall PTR, 1993.

- [156] H. L. Van Trees, K. L. Bell, and Z. Tian, *Detection, estimation, and modulation theory / Harry L. Van Trees, Kristine L. Bell, with Zhi Tian*, Second edition. ed. Hoboken, N.J.: John Wiley & Sons, Inc., 2013, pp. xxi, 1151 pages.
- [157] R. M. Lambrecht and A. Rescigno, *Tracer kinetics and physiologic modeling : theory to practice : proceedings of seminar held at St. Louis, Missouri, June 6, 1983* (Lecture notes in biomathematics, no. 48). Berlin ; New York: Springer, 1983, pp. viii, 509.
- [158] R. P. Beyer, "Fitting smooth curves to noisy indicator-dilution and other unimodal data," *Comput Biomed Res*, vol. 25, no. 2, pp. 144-52, Apr 1992.
- [159] L. F. de Geus-Oei *et al.*, "Comparison of image-derived and arterial input functions for estimating the rate of glucose metabolism in therapy-monitoring 18F-FDG PET studies," *J Nucl Med*, vol. 47, no. 6, pp. 945-9, Jun 2006.
- [160] H. Guo, R. A. Renaut, and K. Chen, "An input function estimation method for FDG-PET human brain studies," *Nucl Med Biol*, vol. 34, no. 5, pp. 483-92, Jul 2007.
- [161] K. P. Burnham, D. R. Anderson, and K. P. Burnham, *Model selection and multimodel inference : a practical information-theoretic approach*, 2nd ed. New York: Springer, 2002, pp. xxvi, 488 p.
- [162] D. H. Anderson, *Compartmental Modeling and Tracer Kinetics*, Berlin, Heidelberg: Springer Berlin Heidelberg, 1983.
- [163] K. Godfrey, *Compartmental models and their application*. London ; New York: Academic Press, 1983, pp. xiv, 293 p.
- [164] R. N. Gunn, S. R. Gunn, and V. J. Cunningham, "Positron emission tomography compartmental models," *J Cereb Blood Flow Metab*, vol. 21, no. 6, pp. 635-52, Jun 2001.
- [165] C.-T. Chen, *Linear system theory and design*, Fourth edition. ed. (The Oxford series in electrical and computer engineering). New York: Oxford University Press, 2013, pp. xiii, 386 pages.
- [166] K. Herholz, J. Rudolf, and W. D. Heiss, "FDG transport and phosphorylation in human gliomas measured with dynamic PET," *J Neurooncol*, vol. 12, no. 2, pp. 159-65, Feb 1992.
- [167] N. Kimura, Y. Yamamoto, R. Kameyama, T. Hatakeyama, N. Kawai, and Y. Nishiyama, "Diagnostic value of kinetic analysis using dynamic 18F-FDG-PET in patients with malignant primary brain tumor," *Nucl Med Commun*, vol. 30, no. 8, pp. 602-9, Aug 2009.
- [168] M. Muzi *et al.*, "Kinetic analysis of 3'-deoxy-3'-18F-fluorothymidine in patients with gliomas," *J Nucl Med*, vol. 47, no. 10, pp. 1612-21, Oct 2006.

- [169] C. Schiepers *et al.*, "Kinetics of 3'-deoxy-3'-18F-fluorothymidine during treatment monitoring of recurrent high-grade glioma," *J Nucl Med*, vol. 51, no. 5, pp. 720-7, May 2010.
- [170] R. B. Innis *et al.*, "Consensus nomenclature for in vivo imaging of reversibly binding radioligands," *J Cereb Blood Flow Metab*, vol. 27, no. 9, pp. 1533-9, Sep 2007.
- [171] V. J. Cunningham and T. Jones, "Spectral analysis of dynamic PET studies," *J Cereb Blood Flow Metab*, vol. 13, no. 1, pp. 15-23, Jan 1993.
- [172] A. Bertoldo, P. Vicini, G. Sambuceti, A. A. Lammertsma, O. Parodi, and C. Cobelli, "Evaluation of compartmental and spectral analysis models of [18F]FDG kinetics for heart and brain studies with PET," *IEEE Trans Biomed Eng*, vol. 45, no. 12, pp. 1429-48, Dec 1998.
- [173] K. Schmidt, "Which linear compartmental systems can be analyzed by spectral analysis of PET output data summed over all compartments?," *J Cereb Blood Flow Metab*, vol. 19, no. 5, pp. 560-9, May 1999.
- [174] F. Turkheimer, R. M. Moresco, G. Lucignani, L. Sokoloff, F. Fazio, and K. Schmidt, "The use of spectral analysis to determine regional cerebral glucose utilization with positron emission tomography and [18F]fluorodeoxyglucose: theory, implementation, and optimization procedures," *J Cereb Blood Flow Metab*, vol. 14, no. 3, pp. 406-22, May 1994.
- [175] J. J. DiStefano, 3rd, "Optimized blood sampling protocols and sequential design of kinetic experiments," *Am J Physiol*, vol. 240, no. 5, pp. R259-65, May 1981.
- [176] D. Bertsimas and J. N. Tsitsiklis, *Introduction to linear optimization* (Athena Scientific series in optimization and neural computation). Belmont, Mass.: Athena Scientific, 1997, pp. xv, 587 p.
- [177] D. G. Luenberger and Y. Ye, *Linear and nonlinear programming*, 4th ed. (International series in operations research and management science). Switzerland: Springer International Publishing, 2016, pp. xiii, 546 p.
- [178] F. Turkheimer *et al.*, "Estimation of component and parameter distributions in spectral analysis," *J Cereb Blood Flow Metab*, vol. 18, no. 11, pp. 1211-22, Nov 1998.
- [179] S. M. Ross, *Simulation*, Fifth edition. ed. Amsterdam: Academic Press, 2013, pp. xii, 310 pages.
- [180] B. Efron, "Bootstrap Methods: Another Look at the Jackknife," *The Annals of Statistics*, vol. 7, no. 1, pp. 1-26, 1979.
- [181] J. V. Beck and K. J. Arnold, *Parameter estimation in engineering and science* (Wiley series in probability and mathematical statistics). New York: Wiley, 1977, pp. xix, 501 p.

- [182] M. Muzi, D. A. Mankoff, J. R. Grierson, J. M. Wells, H. Vesselle, and K. A. Krohn, "Kinetic modeling of 3'-deoxy-3'-fluorothymidine in somatic tumors: mathematical studies," *J Nucl Med*, vol. 46, no. 2, pp. 371-80, Feb 2005.
- [183] J. B. Bassingthwaite and M. Chaloupka, "Sensitivity functions in the estimation of parameters of cellular exchange," *Fed Proc*, vol. 43, no. 2, pp. 181-4, Feb 1984.
- [184] S. M. Kay, *Fundamentals of Statistical Signal Processing, Volume II: Detection Theory* (Prentice Hall signal processing series). Englewood Cliffs, N.J.: Prentice-Hall PTR, 1998.
- [185] D. A. Hamstra *et al.*, "Functional diffusion map as an early imaging biomarker for high-grade glioma: correlation with conventional radiologic response and overall survival," (in eng), *Journal of Clinical Oncology*, vol. 26, no. 20, pp. 3387-94, Jul 10 2008.
- [186] V. W. Pike, "Positron-emitting radioligands for studies in vivo-probes for human psychopharmacology," *J Psychopharmacol*, vol. 7, no. 2, pp. 139-58, Jan 1993.
- [187] V. W. Pike, "PET radiotracers: crossing the blood-brain barrier and surviving metabolism," *Trends Pharmacol Sci*, vol. 30, no. 8, pp. 431-40, Aug 2009.
- [188] C. A. Mathis, N. S. Mason, B. J. Lopresti, and W. E. Klunk, "Development of positron emission tomography beta-amyloid plaque imaging agents," *Semin Nucl Med*, vol. 42, no. 6, pp. 423-32, Nov 2012.
- [189] R. N. Waterhouse, "Determination of lipophilicity and its use as a predictor of blood-brain barrier penetration of molecular imaging agents," *Mol Imaging Biol*, vol. 5, no. 6, pp. 376-89, Nov-Dec 2003.
- [190] S. G. Hasselbalch, G. M. Knudsen, S. Holm, L. P. Hageman, B. Capaldo, and O. B. Paulson, "Transport of D-glucose and 2-fluorodeoxyglucose across the blood-brain barrier in humans," *J Cereb Blood Flow Metab*, vol. 16, no. 4, pp. 659-66, Jul 1996.
- [191] R. Ullrich *et al.*, "Glioma proliferation as assessed by 3'-fluoro-3'-deoxy-L-thymidine positron emission tomography in patients with newly diagnosed high-grade glioma," *Clin Cancer Res*, vol. 14, no. 7, pp. 2049-55, Apr 1 2008.
- [192] A. M. Spence *et al.*, "NCI-sponsored trial for the evaluation of safety and preliminary efficacy of 3'-deoxy-3'-[18F]fluorothymidine (FLT) as a marker of proliferation in patients with recurrent gliomas: preliminary efficacy studies," *Mol Imaging Biol*, vol. 11, no. 5, pp. 343-55, Sep-Oct 2009.
- [193] J. Logan, "Graphical analysis of PET data applied to reversible and irreversible tracers," *Nucl Med Biol*, vol. 27, no. 7, pp. 661-70, Oct 2000.
- [194] C. S. Patlak and R. G. Blasberg, "Graphical evaluation of blood-to-brain transfer constants from multiple-time uptake data. Generalizations," *J Cereb Blood Flow Metab*, vol. 5, no. 4, pp. 584-90, Dec 1985.

- [195] C. S. Patlak, R. G. Blasberg, and J. D. Fenstermacher, "Graphical evaluation of blood-to-brain transfer constants from multiple-time uptake data," *J Cereb Blood Flow Metab*, vol. 3, no. 1, pp. 1-7, Mar 1983.
- [196] A. M. Allen *et al.*, "Assessment of response of brain metastases to radiotherapy by PET imaging of apoptosis with (1)(8)F-ML-10," (in eng), *Eur J Nucl Med Mol Imaging*, vol. 39, no. 9, pp. 1400-8, Sep 2012.
- [197] M. J. Oborski, C. M. Laymon, Y. Qian, F. S. Lieberman, A. D. Nelson, and J. M. Mountz, "Challenges and Approaches to Quantitative Therapy Response Assessment in Glioblastoma Multiforme Using the Novel Apoptosis Positron Emission Tomography Tracer F-18 ML-10," *Transl Oncol*, vol. 7, no. 1, pp. 111-9, Feb 2014.
- [198] B. A. Moffat *et al.*, "Functional diffusion map: a noninvasive MRI biomarker for early stratification of clinical brain tumor response," *Proc Natl Acad Sci U S A*, vol. 102, no. 15, pp. 5524-9, Apr 12 2005.
- [199] B. M. Ellingson *et al.*, "Volumetric analysis of functional diffusion maps is a predictive imaging biomarker for cytotoxic and anti-angiogenic treatments in malignant gliomas," *J Neurooncol*, vol. 102, no. 1, pp. 95-103, Mar 2011.
- [200] B. M. Ellingson *et al.*, "Validation of functional diffusion maps (fDMs) as a biomarker for human glioma cellularity," *J Magn Reson Imaging*, vol. 31, no. 3, pp. 538-48, Mar 2010.
- [201] F. Blankenberg, "To scan or not to scan, it is a question of timing: technetium-99m-annexin V radionuclide imaging assessment of treatment efficacy after one course of chemotherapy," *Clin Cancer Res*, vol. 8, no. 9, pp. 2757-8, Sep 2002.
- [202] T. Belhocine, N. Steinmetz, C. Li, A. Green, and F. G. Blankenberg, "The imaging of apoptosis with the radiolabeled annexin V: optimal timing for clinical feasibility," *Technol Cancer Res Treat*, vol. 3, no. 1, pp. 23-32, Feb 2004.
- [203] S. Hu *et al.*, "Longitudinal PET imaging of doxorubicin-induced cell death with 18F-Annexin V," (in eng), *Molecular imaging and biology : MIB : the official publication of the Academy of Molecular Imaging*, vol. 14, no. 6, pp. 762-70, Dec 2012.
- [204] G. Madelin, J. S. Lee, R. R. Regatte, and A. Jerschow, "Sodium MRI: methods and applications," *Prog Nucl Magn Reson Spectrosc*, vol. 79, pp. 14-47, May 2014.
- [205] T. Henzler *et al.*, "Imaging of tumor viability in lung cancer: initial results using ²³Na-MRI," *Rofo*, vol. 184, no. 4, pp. 340-4, Apr 2012.
- [206] R. Ouwerkerk, K. B. Bleich, J. S. Gillen, M. G. Pomper, and P. A. Bottomley, "Tissue sodium concentration in human brain tumors as measured with ²³Na MR imaging," *Radiology*, vol. 227, no. 2, pp. 529-37, May 2003.

- [207] J. Kurhanewicz, D. B. Vigneron, and S. J. Nelson, "Three-dimensional magnetic resonance spectroscopic imaging of brain and prostate cancer," *Neoplasia*, vol. 2, no. 1-2, pp. 166-189, Jan-Apr 2000.
- [208] B. Hamans, A. C. Navis, A. Wright, P. Wesseling, A. Heerschap, and W. Leenders, "Multivoxel (1)H MR spectroscopy is superior to contrast-enhanced MRI for response assessment after anti-angiogenic treatment of orthotopic human glioma xenografts and provides handles for metabolic targeting," *Neuro Oncol*, vol. 15, no. 12, pp. 1615-24, Dec 2013.
- [209] J. Oh *et al.*, "Survival analysis in patients with glioblastoma multiforme: predictive value of choline-to-N-acetylaspartate index, apparent diffusion coefficient, and relative cerebral blood volume," *J Magn Reson Imaging*, vol. 19, no. 5, pp. 546-54, May 2004.
- [210] F. Raschke, G. A. Fellows, A. J. Wright, and F. A. Howe, "(1) H 2D MRSI tissue type analysis of gliomas," *Magn Reson Med*, vol. 73, no. 4, pp. 1381-9, Apr 2015.
- [211] S. Saraswathy *et al.*, "Evaluation of MR markers that predict survival in patients with newly diagnosed GBM prior to adjuvant therapy," *J Neurooncol*, vol. 91, no. 1, pp. 69-81, Jan 2009.
- [212] L. G. Strauss, A. Dimitrakopoulou-Strauss, and U. Haberkorn, "Shortened PET data acquisition protocol for the quantification of 18F-FDG kinetics," *J Nucl Med*, vol. 44, no. 12, pp. 1933-9, Dec 2003.
- [213] T. Torizuka *et al.*, "Short dynamic FDG-PET imaging protocol for patients with lung cancer," *Eur J Nucl Med*, vol. 27, no. 10, pp. 1538-42, Oct 2000.
- [214] A. J. Reader and J. Verhaeghe, "4D image reconstruction for emission tomography," *Phys Med Biol*, vol. 59, no. 22, pp. R371-418, Nov 21 2014.
- [215] G. Wang and J. Qi, "Direct estimation of kinetic parametric images for dynamic PET," *Theranostics*, vol. 3, no. 10, pp. 802-15, Nov 20 2013.